Development of Silicon Detectors for the High Luminosity LHC

Dissertation

zur Erlangung des Doktorgrades

an der Fakultät für Mathematik, Informatik
und Naturwissenschaften

Fachbereich Physik

der Universität Hamburg

vorgelegt von

Thomas Valentin Eichhorn

aus Lahr im Schwarzwald

Hamburg

2015

ABSTRACT

The *Large Hadron Collider* (LHC) at CERN will be upgraded to a *High Luminosity LHC* in the year 2022, increasing the instantaneous luminosity by a factor of five. This will have major impacts on the experiments at the LHC, such as the *Compact Muon Solenoid* (CMS) experiment, and especially for their inner silicon tracking systems. Among other things, the silicon sensors used therein will be exposed to unprecedented levels of radiation damage, necessitating a replacement of the entire tracking detector. In order to maintain the excellent current performance, a new tracking detector has to be equipped with sensors of increased radiation hardness and higher granularity. The CMS experiment is undertaking an extensive R&D campaign in the search for the future silicon sensor technology baseline to be used in this upgrade. This thesis presents two methods suitable for use in this search: finite element *TCAD simulations* and *test beam measurements*.

The simulations are focussed on the interstrip capacitance between sensor strips and are compared to measurements before and after the inclusion of radiation damage effects. A geometrical representation of the strip sensors used in the campaign has been found, establishing the predictive power of simulations.

The test beam measurements make use of the high-precision pixel telescopes available at the DESY-II test beam facility. The performance of these telescopes has been assessed and their achievable pointing resolution has been found to be below $2\,\mu\text{m}$. Thin, epitaxial silicon is a candidate material for usage in radiation hard sensors for the future CMS tracking detector. Sample strip sensors of this material have been irradiated to fluences of up to $1.3 \times 10^{16}\,\text{n}_{\text{eq}}/\text{cm}^2$ with $800\,\text{MeV}$ or $23\,\text{GeV}$ protons. Test beam measurements with $5\,\text{GeV}$ electrons have been performed to investigate the radiation hardness of epitaxial sensors using the pixel beam telescopes. The epitaxial *device under test* (DUT) has been integrated into the telescope and its software analysis framework. An alignment of DUT and telescope planes has been performed and traversing particle tracks reconstructed for the sensor analysis. Results show that the achievable resolution in the epitaxial silicon strip sensors is at the binary level. The measured charge collection efficiency for p-bulk sensors amounts to $80\,\%$ of pre-irradiation levels for fluences of $3 \times 10^{15}\,\text{n}_{\text{eq}}/\text{cm}^2$ and to over $65\,\%$ for $\Phi = 1.3 \times 10^{16}\,\text{n}_{\text{eq}}/\text{cm}^2$. Signal-to-noise levels at these fluence levels are 7.4 and 3.8, respectively. With particle tracks of various inclinations, the sharing of charge between sensor strips is investigated. Indications of possible charge losses at the sensor surface are described and evidence of commencing charge multiplication effects is presented. Sensors are also compared to thicker, non epitaxial sensors irradiated to the same fluence. From the obtained results, acquired from the first test beam measurements of irradiated epitaxial sensors ever performed, a complete picture of this material has been gained. It can be concluded that thin, p-bulk epitaxial silicon is sufficiently radiation hard for usage as an outer pixel detector sensor material.

ZUSAMMENFASSUNG

Der *Large Hadron Collider* (LHC) am CERN wird im Jahr 2022 zum *High Luminosity LHC* (HL-LHC) erweitert, indem die instantane Luminosität um den Faktor fünf erhöht wird. Dies hat erhebliche Auswirkungen auf die Experimente am LHC, wie zum Beispiel das CMS Experiment, insbesonders auf deren Spurdetektoren. Die dort verwendeten Siliziumsensoren werden erheblichen Strahlenschädigungen ausgesetzt, wodurch ein Komplettaustausch des Detektors notwendig wird. Um die gegenwärtige, ausgezeichnete Leistung des Spurdetektors auch im HL-LHC beibehalten zu können, muss dieser mit noch strahlenhärteren Sensoren ausgestattet werden, die zudem noch eine erhöhte Granularität aufweisen. Eine Forschungskampagne innerhalb des CMS Experimentes sucht derzeit nach einer geeigneten Technologie für die zukünftigen Siliziumsensoren. Die vorliegende Arbeit ist Teil dieses Projektes und benutzt zwei Methoden zur Untersuchung von Sensoreigenschaften: *TCAD Simulationen* und *Teststrahlmessungen*.

Die Simulationen beschränken sich auf die Zwischenstreifenkapazität in Streifensensoren und werden mit Messungen vor und nach Bestrahlung verglichen. Es wurde eine Struktur gefunden, die den in dieser Kampagne verwendeten Sensoren entspricht, und dadurch die Vorhersagefähigkeit von Simulationen erhöht.

Für die durchgeführten Teststrahlmessungen wurden die Präzisionsteleskope verwendet, die am DESY-II Teststrahl zur Verfügung stehen. Systematische Untersuchungen dieser Teleskope wurden durchgeführt und resultieren in einer Vorhersagegenauigkeit von unter $2\,\mu\mathrm{m}$ am Punkt des Testsensors. Dünnes, epitaktisch gewachsenes Silizium könnte ein geeignetes strahlenhartes Sensormaterial für den zukünftigen CMS Spurdetektor sein. Sensoren dieses Materials wurden mit 800 MeV oder 23 GeV Protonen bis zu Fluenzen von $1,3 \times 10^{16}\,\mathrm{n_{eq}/cm^2}$ bestrahlt. Um die Strahlenhärte von epitaktischen Sensoren zu bestimmen, wurden sie unter Verwendung der Teleskope mit 5 GeV Elektronen im DESY-II Teststrahl vermessen. Die Sensoren wurden in die Teleskope und in deren Auslese- und Analysesoftware integriert. Eine Präzisionsausrichtung von Sensoren und Teleskop wurde durchgeführt und durchquerende Teilchenspuren zur Sensoranalyse rekonstruiert. Die Analyseergebnisse zeigen, dass die epitaktischen Sensoren eine binäre Auflösung erreichen. Die gemessene Ladungssammlungseffizienz für p-Typ Sensoren beträgt für eine Fluenz von $3 \times 10^{15}\,\mathrm{n_{eq}/cm^2}$ 80 % des vor der Bestrahlung gemessenen Wertes. Für Fluenzen der Größe $\Phi = 1,3 \times 10^{16}\,\mathrm{n_{eq}/cm^2}$ beträgt dieser Wert 65 %. Mit Teilchenspuren aus verschiedenen Einfallswinkeln wird die Ladungsteilung zwischen Streifen untersucht, Indizien von Ladungsverlusten an der Sensoroberfläche werden beschrieben und Anzeichen von beginnender Ladungsmultiplikation aufgezeigt. Die epitaktischen Sensoren werden außerdem mit dickeren, nicht epitaktischen Sensoren gleicher Fluenz verglichen. Aus den gewonnen Daten kann die Schlussfolgerung gezogen werden, dass dünnes, epitaktisch gewachsenes p-Typ Silizium ausreichend strahlenhart für einen Einsatz als Sensormaterial in den äußeren Lagen des Pixeldetektors ist.

*Do not go where the path may lead, go instead
where there is no path and leave a trail.*

— Ralph Waldo Emerson

CONTENTS

LIST OF FIGURES

LIST OF TABLES

ACRONYMS

ACONITE   ATLAS Copy of National Instruments based Telescope

ADC   Analogue-to-digital converter

ALiBaVa   A Liverpool Barcelona Valencia readout system

ATLAS   A Toroidal LHC Apparatus

CERN   European Organization for Nuclear Research

CBC   CMS Binary Chip

CMOS   Complementary metal-oxide-semiconductor

CMS   Compact Muon Solenoid

DAF   Deterministic annealing filter

DAQ   Data acquisition

DATURA   DESY Advanced Telescope Using Readout Acceleration

DESY   Deutsches Elektronen-Synchrotron

DUT   Device under test

Epi   Epitaxial silicon

FEA   Finite element analysis

FIR   Finite impulse response

FPGA   Field programmable gate array

Fth   Float-zone silicon thinned

FZ   Float-zone silicon

GEAR   Geometry API for Reconstruction

HL-LHC   High Luminosity Large Hadron Collider

ILC   International Linear Collider

JTAG   Joint Test Action Group

LCIO   Linear Collider Input/Output

LHC   Large Hadron Collider

LHCb   LHC beauty experiment

MCz	Magnetic Czochralski silicon
MIMOSA 26	Minimum Ionising MOS Active Pixel Sensor
MIP	Minimum ionising particle
MPV	Most probable value
NIEL	Non ionising energy loss
PCB	Printed circuit board
PETRA	Positronen-Elektronen Tandem Ring Anlage
PKA	Primary knock on atom
PMT	Photomultiplier tube
ROC	Readout chip
SHV	Safe high voltage
SNR	Signal-to-noise ratio
SUSY	Supersymmetry
TCAD	Technology computer-aided design
TDC	Time-to-digital converter
TLU	Trigger logic unit

INTRODUCTION

1.1 SCOPE OF THIS WORK

The *Large Hadron Collider* (LHC) is the largest particle accelerator ever built. During its first years of operation from 2010 to 2013, its experiments have made remarkable achievements, the discovery of the theorised Higgs particle perhaps being the most famous. This discovery resulted in the Nobel Prize in Physics for 2013 being awarded to François Englert and Peter Higgs.

With all particles postulated by the Standard Model of particle physics now found, the success story of the LHC will be continued throughout the next decade. A *high luminosity* upgrade towards a *High Luminosity LHC* (HL-LHC) aims to push the frontiers of science even further. This upgrade will increase the instantaneous luminosity by a factor of five and will have a major impact on the experiments at the LHC, one of which is the *Compact Muon Solenoid* (CMS) experiment.

The CMS experiment uses a multi-purpose cylindrical detector to measure particles produced in the LHC's collisions. The innermost detector part is the *tracker* detector. It encompasses almost $200\,\mathrm{m}^2$ of active silicon sensors. After the upgrade to the HL-LHC, the CMS tracker will experience unprecedented levels of radiation damage and an increased occupancy. Radiation damage causes a multitude of defects in silicon sensors, greatly affecting their properties and degrading their performance. An increased occupancy leads to inefficiencies in the reconstruction of particle tracks, which is one of the main responsibilities of the tracker.

To maintain the excellent tracking performance, the CMS experiment is developing an all-new tracker detector, which will be installed in the *Phase-II Upgrade* in 2022. A new tracker will include sensors with increased radiation hardness and a higher granularity, while reducing the material budget. By utilising a new module design, the tracker will furthermore contribute to the Level-1 trigger. To find the technological baseline for these sensors, a large R&D campaign is ongoing. Within the campaign, a wide range of sensor structures has been produced and investigated.

This thesis begins with a description of the current LHC and its experiments, especially the CMS experiment. The high luminosity upgrade is explained, with its physics research motivation and the consequences for the CMS tracker detector. The first chapter concludes with a summary of the aforementioned campaign to find the optimal silicon sensor technology for the upgraded tracker sensors.

Chapter two follows up on silicon tracking detectors in general. The basics of semiconductor sensors and the underlying physics are described, together with

an overview of the production techniques used in industry to manufacture silicon sensors. The radiation damage sustained by silicon sensors in a collider experiment is then explained, including the effects on a sensor's performance.

In this work, two main investigative techniques of sensor development are utilised: TCAD simulations and test beam measurements. The third chapter introduces these methods in detail, starting with aspects of the simulations. After that, the properties of the DESY-II test beam are highlighted and the pixel beam telescopes used therein are illustrated. This is followed by a brief overview of the software analysis framework used for the analysis and reconstruction of the data obtained from the telescopes. A beam telescope's figure of merit is the resolution it can achieve. This and other performance aspects are detailed thereafter. The chapter concludes with a description of the irradiation centres used for the sensors analysed in this work.

In chapter four, the results of undertaken TCAD simulations are shown. Together with other collaborators, a multitude of simulations were performed to provide input to the aforementioned R&D campaign. To validate simulation results, a comparison with measurements is necessary. This comparison was performed with strip sensors of various geometries, where the exact processing properties were not entirely known. By approximating the simulated interstrip capacitance to measurements, a suitable simulation structure was found, allowing a comparison of other sensor properties between simulations and measurements. Several models to include radiation damage in simulations are discussed and the interstrip capacitance is again compared with results obtained from irradiated sensors.

Chapter five presents investigations on the radiation hardness of epitaxial silicon. Sensors of this material were irradiated up to the highest fluences expected after a lifetime operation in the innermost layer of the CMS tracker at the HL-LHC and their performance measured extensively by the pixel beam telescopes in the DESY-II test beam. The analysis steps performed are explained in detail, together with the changes and modifications to the telescope analysis framework. Results on the sensor's resolution and noise are then presented, followed by an evaluation of the charge collection efficiency and the signal-to-noise ratio. Finally, investigations into charge sharing are presented, together with measurements of the sensor current. The results obtained from epitaxial silicon are then compared to those obtained from other materials. A summary of measurements and results is given and the feasibility of using epitaxial sensors as a radiation hard tracking detector material discussed.

In chapter six, results presented in this thesis are summarised and an outlook of future developments in the field of radiation hard silicon sensors is given.

1.2 THE LARGE HADRON COLLIDER

The *Large Hadron Collider* (LHC) is a circular particle accelerator with a circumference of almost 27 km. It is located at the *European Organization for Nuclear Research* (CERN) in Geneva, Switzerland. To this day, it is the largest and most powerful particle accelerator. Opposing particle beams from protons or lead nuclei are each accelerated to an energy of 7 TeV in the beam pipes in the LHC's underground tunnels. The beams are brought into collision at four main interaction points. Around these interaction points, the major experiments have been set up. These are:

- ALICE — *A Large Ion Collider Experiment*
- ATLAS — *A Toroidal LHC ApparatuS*
- CMS — *Compact Muon Solenoid*
- LHCb — *LHC beauty experiment*

Both the ATLAS and CMS experiments are multi-purpose experiments and were constructed to answer open questions in particle physics, one famously being the existence of the theorised Higgs particle, which was confirmed in July 2013. Other research goals of ATLAS and CMS are the search for supersymmetric particles and physics beyond the Standard Model. Although they share the same physics goals, the two experiments are constructed in a diverse manner, as to be able to validate each other's results independently. This is also achieved by using different algorithms and methods for later data analysis.

ALICE has been built to study the collisions of heavy ions (lead nuclei) and look for evidence of the quark-gluon plasma. This is a state of matter where quarks and gluons are no longer confined inside hadrons. Studying this is essential for further understanding of *quantum chromodynamics* (QCD) and can give insights to very early stages of our universe, before particles were formed.

LHCb is a detector focussed on studying the physics of b-quarks, especially the CP violation in b-hadrons. This can help in understanding the matter/antimatter asymmetry of the universe. Contrary to the other three main experiments, the LHCb detector is built as a forward detector, focussing on collision products close to the beam.

An overview of the LHC and the location of the four main experiments can be seen in figure 1.1.

1.2.1 *The Accelerator Complex*

Before particles can be collided in the main LHC synchrotron, they have to be pre-accelerated by several smaller accelerators. This is due to the specific design of the
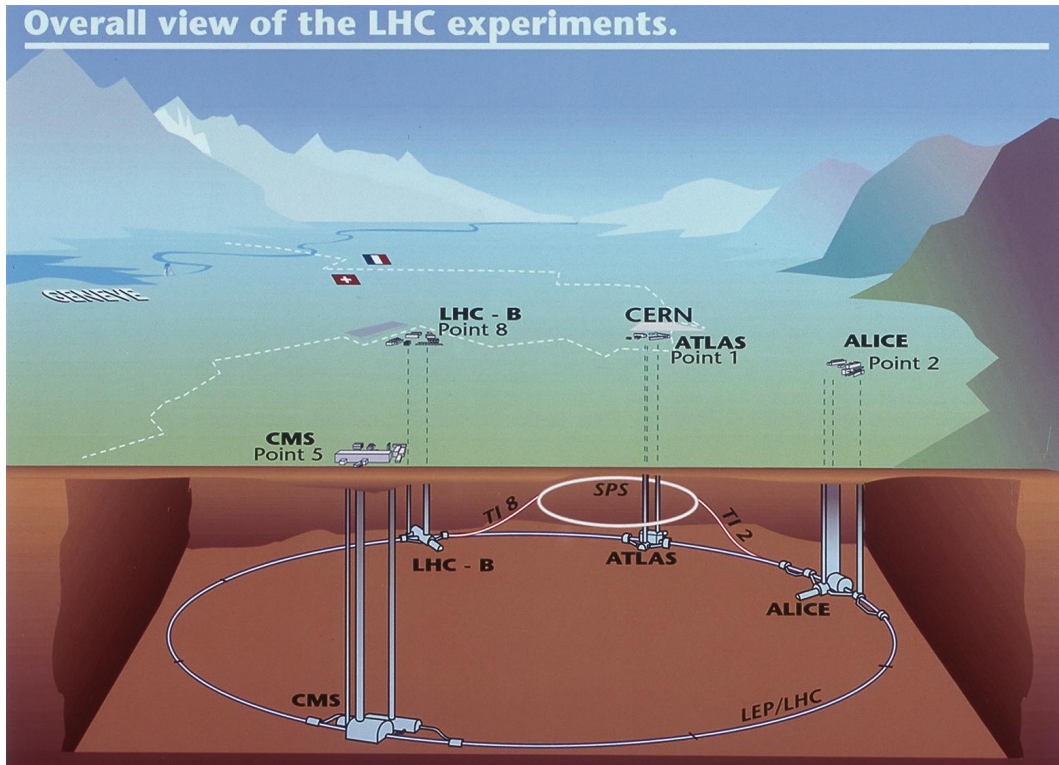
Figure 1.1: The LHC and its main experiments. [25]

LHC cavities and magnets.

Hydrogen atoms are stripped of their electron and are passed by the LINAC 2 into the *PS Booster*. At this stage, the proton energy is comparatively low at 50 MeV. The PS Booster accelerates the protons to 1.4 GeV before injecting them into the *Proton Synchrotron* (PS), where they are accelerated to 25 GeV. The PS feeds protons into the *Super Proton Synchrotron* (SPS) and also to some smaller experiments. Within the SPS, the proton energy is increased to 450 GeV, before injecting the protons into the LHC ring. The injection is done both clockwise and anticlockwise, to obtain two beams. The LHC finally accelerates the proton beams to their nominal energy of 7 TeV. This acceleration scheme is shown in figure 1.2, including other miscellaneous experiments located at CERN.

1.2.2   *The Physics Goals*

As previously stated, the LHC was constructed to answer open questions in particle physics. This means not only looking into the smallest and most fundamental objects in nature, but also looking very far back in time, right after the Big Bang. The current understanding of particle physics is nested inside a collection of theories called the Standard Model. This model introduces quarks as the building blocks of nature and defines forces as the exchange of carrier particles.
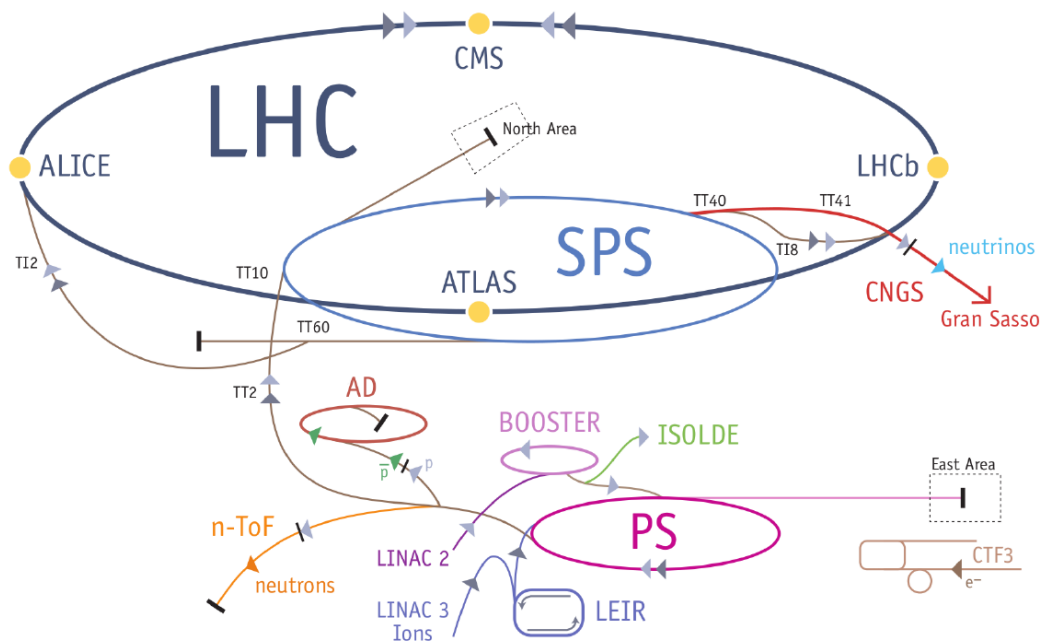
Figure 1.2: The LHC accelerator complex. Protons are accelerated in the LINAC 2 and are passed to the LHC via the Booster, PS and SPS accelerators. The protons reach their nominal energy of 7 TeV only in the LHC. [82]

All particles within the Standard Model can be counted to either the *fermions* or the *bosons*, depending if they have half-integer or integer spin. Fermions are divided into quarks and leptons, with the distinction that former interact via the strong force, whereas the latter do not. The bosons act as force carriers.

Despite being a very powerful theory, the Standard Model cannot account for several observed phenomena, for example the existence of dark matter or the absence of antimatter in the universe. It also cannot explain the origin of mass, or why some particles have mass and some have none at all. A possible solution for this could be the Higgs mechanism [67]. This mechanism postulates that space is filled by a Higgs field, which particles interact with. This interaction then gives particles their mass, with the amount of mass depending on the strength of the interaction. A particle associated with this field, the Higgs boson, was discovered at the LHC and announced in July 2012 [28].

A further shortcoming of the Standard Model is that it cannot describe nature's fundamental forces — the strong and the weak force as well as the electromagnetic and gravitational force — in a unified way. A possibility for this lies in a theory called supersymmetry. Supersymmetry hypothesises more massive partners to the known Standard Model particles. With these supersymmetric particles, a unification of forces in a single theory could be possible. Evidence of these particles could be found with the LHC [36].

Regular operation of the LHC began in 2010, with a centre of mass energy of $\sqrt{s} = 7$ TeV. The energy was increased to $\sqrt{s} = 8$ TeV in 2012. At the beginning

of the year 2013, *Run 1* was completed and the LHC entered its first long shutdown [57]. During this shutdown, several accelerator components undergo maintenance. Furthermore, consolidation and upgrade activities are performed. The shutdown will be completed in 2015 when operations will recommence. This *Run 2* will provide collisions with the centre of mass energy increased to $\sqrt{s} = 13\,\text{TeV}$.

1.3 THE COMPACT MUON SOLENOID EXPERIMENT

The *Compact Muon Solenoid* (CMS) experiment [27] uses a cylindrical particle detector to measure a wide range of particles produced in the LHC's collisions. The entire detector is around 28 m long, 15 m wide and weighs about 14000 t. Its name origins from the fact that despite its weight, the detector is fairly small and compact, especially compared with the ATLAS detector. The superconducting 3.8 T solenoid magnet and the muon systems make up the remainder of the experiment's name. A schematic of the detector is displayed in figure 1.3. The CMS detector is comprised of many individual detector layers, each fulfilling an individual task in detecting and measuring the traversing particles. Each subdetector consists of a cylindrical component, called the barrel, and an endcap component on either side. The subdetectors are described in the following, an overview of each subdetector and its task in reconstructing particles can be seen in figure 1.4.
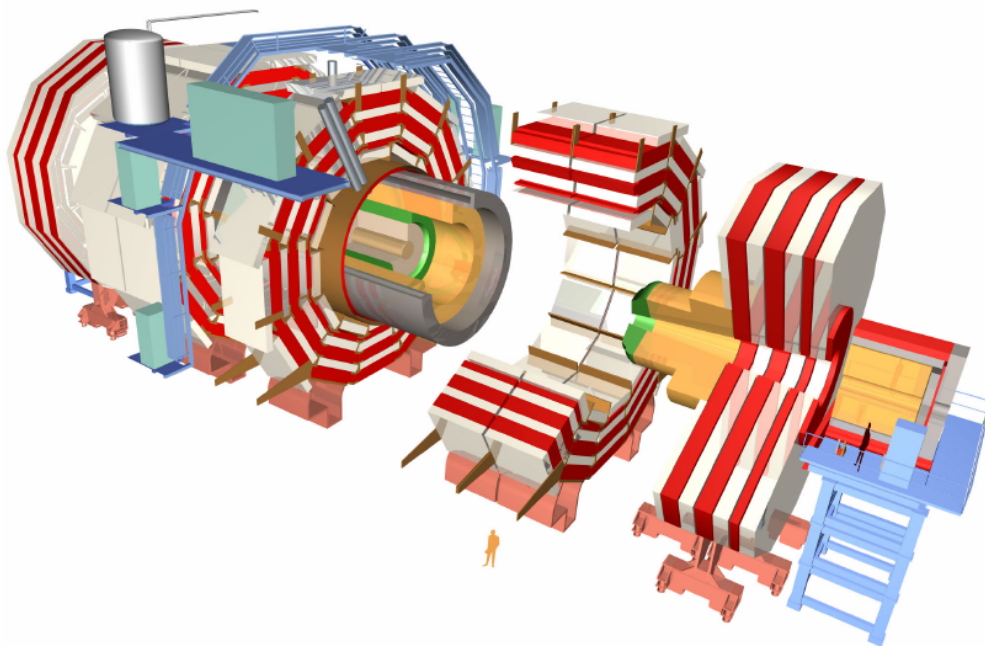
Figure 1.3: The CMS detector [25]. From the inside: the silicon tracker is displayed in light brown. The electromagnetic calorimeter is shown in green and the hadronic calorimeter in yellow. The solenoid is grey, the muon chambers white and the iron return yokes red.

The right-handed coordinate system used within the CMS experiment has the origin centred at the nominal collision point within the experiment. The x axis points radially inward towards the centre of the LHC ring. The y axis points vertically upward, the z axis West towards the Jura mountains. CMS measures the azimuthal angle ϕ from the x axis in the x-y plane. The radial coordinate in this plane is denoted by r and the polar angle θ is measured from the z axis, with the pseudorapidity η defined as $\eta = -\ln\tan\theta/2$ [27].
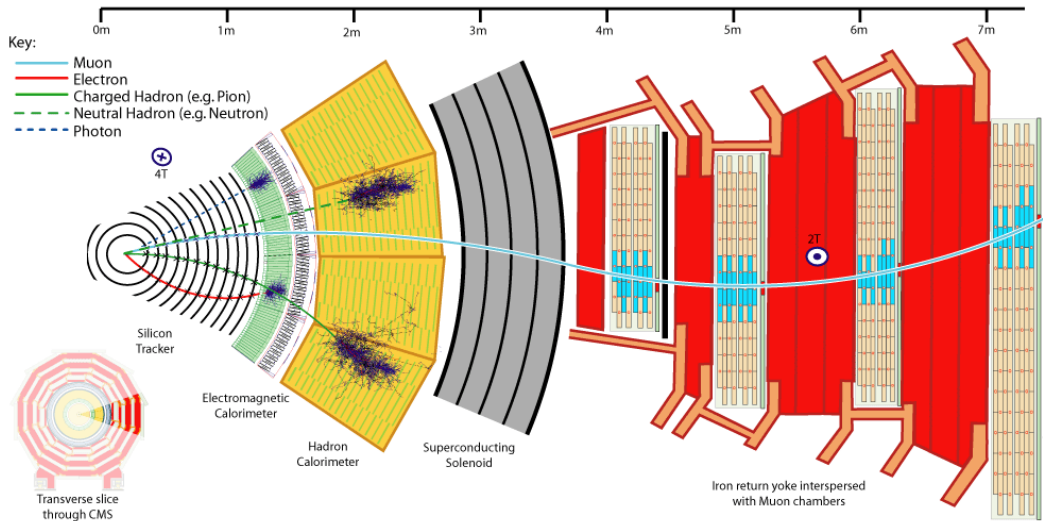
Figure 1.4: CMS subdetectors and their role in identifying particles [25]. Photons are only measured in the electromagnetic calorimeter, neutral hadrons only in the hadronic calorimeter. Electrons and charged hadrons leave a trace in the tracker and are measured in the electromagnetic or hadronic calorimeter, respectively. Muons are also seen by the tracker and are detected in the muon chambers. The trajectories of charged particles are curved due to the magnetic field.

1.3.1 *Pixel Detector*

After a collision of two beam bunches at the interaction point in the centre of the CMS detector, any particles emerging from the collision and travelling outwards will first pass through the innermost subdetector, the tracker. In most high-energy particle physics experiments, a central tracking detector surrounds the inner interaction point. Examples are not only the CMS experiment described here, but also other collider experiments, such as H1 [1] and ZEUS [137] at HERA, or CDF [16] and DØ [107] at Tevatron. The CMS tracker is divided into two parts, the inner part being the pixel detector, the outer part the silicon strip tracker. Comprising almost 200 m^2 of active silicon, the CMS tracker is the largest all-silicon tracker ever built. A schematic drawing showing all subsections of the pixel and strip tracker is shown in figure 1.5.

The pixel detector contains 65 million pixels and measures the path of emerging particles as precisely as possible. The pixel detector has to be as close as possi-
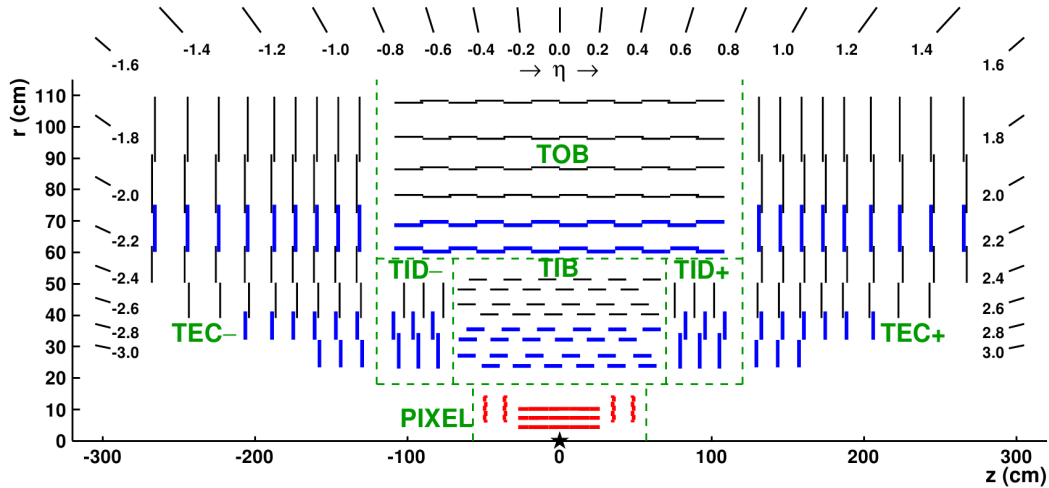
Figure 1.5: Schematic of the CMS tracker detector. The tracker is symmetric to the horizontal line at $r = 0\,\mathrm{cm}$, the interaction point at $z = 0\,\mathrm{cm}$ is indicated by a star. Module positions are represented by lines, with double-sided modules indicated in blue and pixel modules displayed in red. Image from [29].

ble to the interaction point, to be able to resolve secondary and tertiary vertices of long-lived particles, such as heavy quarks and τ-leptons. To accomplish this, it currently has three barrel detector layers at $4.4\,\mathrm{cm}$, $7.3\,\mathrm{cm}$ and $10.2\,\mathrm{cm}$ distance from the beam pipe, together with an endcap disc containing two detector layers at either end. The pixels have a cell size of $150\,\mathrm{\mu m}$ by $100\,\mathrm{\mu m}$ to keep their occupancy below a level of 10^{-4}. The sensors are processed in *n-in-n* technology, with a high-resistivity n-bulk and an n-doped implant of high concentration and are bump bonded to the readout chip. The pixel detector achieves a spatial hit resolution of under $10\,\mathrm{\mu m}$ perpendicular to the magnetic field in the barrel [26].

Challenges to the pixel detector result from the high number of channels, which puts constraints on powering and cooling. An advantage of using so many channels is the aforementioned excellent spatial resolution. Being so close to the beam pipe, the pixel detector experiences an intense amount of radiation from traversing particles [29]. At the design luminosity of $10^{34}\,\mathrm{cm^{-2}s^{-1}}$, the innermost layer of the pixel detector will be exposed to a particle fluence of $3 \times 10^{14}\,\mathrm{n_{eq}/cm^2}$ per year [33].

1.3.2 *Strip Tracker*

Further outwards from the pixel detector, the strip tracker is located. In order to reduce the amount of material used, the power consumption and the overall cost, this part of the tracker uses strip sensors. The inner parts of the strip tracker are the *Tracker Inner Barrel* (TIB) and *Tracker Inner Disc* (TID). The former has four layers of strips running parallel to the direction of the beam, the latter is comprised of three endcap discs at either side with radial strips. The two inner layers of the

TIB feature double-sided sensors[1] with a cell size of $10\,cm \times 80\,\mu m$. Sensors in the two outer layers of the TIB have a cell size of $10\,cm \times 120\,\mu m$. All TIB sensors have a thickness of $320\,\mu m$. Hit resolutions vary from $16\,\mu m$ to $28\,\mu m$ in the barrel, with occupancies below $3\,\%$ [26, 76].

The *Tracker Outer Barrel* (TOB) surrounds the TIB and the TID and spans radii from $55\,cm$ to $110\,cm$. It is composed of six module layers, with cell sizes increased to $20\,cm \times 120\,\mu m$ and $20\,cm \times 180\,\mu m$. The sensor thickness is increased to $500\,\mu m$ to increase signal amplitudes. Hit resolutions achieved here range from $18\,\mu m$ to $47\,\mu m$ [29].

On each side, a *Tracker End Cap* (TEC) surrounds the TOB detector. Each endcap is composed of nine discs, with strips running in radial direction. Cell sizes vary from $97\,\mu m \times 25\,cm$ to $184\,\mu m \times 25\,cm$. The inner four discs employ sensors of $320\,\mu m$ thickness, in the outer five discs this is increased to $500\,\mu m$.

All together, the strip tracker contains 15200 sensor modules, with about 10 million strips and extends outwards to a radius of $110\,cm$. The strip tracker is read out by 80000 readout chips. As for the pixel detector, a major challenge to the strip tracker is the intense radiation it is exposed to. Expected fluences in the strip tracker for an integrated luminosity of $500\,fb^{-1}$ range from $1.6 \times 10^{14}\,n_{eq}/cm^2$ in the inner layer to $0.2 \times 10^{14}\,n_{eq}/cm^2$ in the outer layer [27]. Whereas the layers of the pixel detector provide real 3D data, strip sensors lose the information from one dimension. To accommodate for this, the strip directions in the different layers are slightly rotated.

In the first long shutdown after Run 1, ending in 2015, extensive maintenance is performed on the strip tracker to enable operation at temperatures below $0\,°C$ and to mitigate radiation damage effects [20]. The cooling system is refurbished, the dry gas supply is augmented and the humidity sealing is improved.

Both pixel detector and strip tracker are designed to measure the particles' vertex and map their path as precisely as possible without deflecting or slowing them down, as the particle energy is determined by subdetectors located further outwards. This requires the pixel and strip tracker detectors to be as lightweight as possible. Besides the vertex, the pixel and strip detectors can determine the charge and the momentum of the traversing particles. This is due to the magnetic field within the CMS experiment.

1.3.3 *Calorimeters, Solenoid and Muon System*

Whereas the pixel and strip tracker detectors rely on thin silicon sensors as a detector material to measure a particles trajectory, the calorimeters utilise heavy absorber materials to stop a particle and determine its energy. The superconduct-

---

1 Double-sided means that a second strip detector module is mounted back-to-back to the first module. They are rotated by a *stereo* angle of 100 mrad.

ing solenoid magnet, in part namesake of the CMS experiment, is a vital feature for particle identification and surrounds both calorimeters. The outer muon system encompasses the inner detector parts.

1.3.3.1 *Electromagnetic Calorimeter*

The *electromagnetic calorimeter* (ECAL) detects electrons, positrons, and photons and measures their energy by completely stopping them. It consists of 76200 lead tungstate ($PbWO_4$) crystals, which act both as absorbers and scintillators. Electrons and photons induce scintillating light by depositing their energy when passing through a crystal. Photodetectors are mounted on the back of these crystals to detect this scintillation light, with a wavelength of around 420 nm. Similar to the tracker detector, the ECAL is composed of a barrel detector part and an endcap on either side. The relative energy resolution has been measured to be

$$\left(\frac{\sigma}{E}\right)^2 = \left(\frac{2.8\,\%}{\sqrt{E}}\right)^2 + \left(\frac{0.12}{E}\right)^2 + (0.30\,\%)^2 \,, \tag{1.1}$$

with the energy E in GeV [27]. The spatial precision is increased by preshower detectors in front of the endcaps, which also aid in identifying neutral pions.

1.3.3.2 *Hadron Calorimeter*

The *hadronic calorimeter* (HCAL) is a sampling calorimeter responsible for detecting hadrons such as protons, neutrons, or pions and measuring their energy. Incoming particles create secondary particle showers when hitting the heavy absorber plates. With the shower passing through the scintillators, these emit light which can in turn be read out by hybrid photo diodes.

The HCAL is positioned between the ECAL and the magnet coil, which place constraints on its size. It is built from alternating layers of plastic scintillators and brass or steel absorbers and is subdivided into a barrel and two endcaps. A further barrel detector part (HO) is located outside the solenoid magnet, additionally two forward calorimeters (HF) are located at $z = \pm 11.2$ m.

The HCAL is segmented into *towers* in η-ϕ direction. In the barrel (HB) they are of size 0.087×0.087, in the endcaps (HE), the towers are of the same size, except for $|\eta| \geqslant 1.6$, where they are 0.17×0.17. The total absorber thickness increases from 5.82 interaction lengths (λ_I) at $\eta = 0$ to $10.6\,\lambda_I$ at $|\eta| = 1.3$ in the HB. The HE calorimeter has a total length of about $10\,\lambda_I$ [27].

1.3.3.3 *Solenoid*

The superconducting solenoid magnet is the central part of the CMS detector, separating the tracker and the calorimeters from the muon system. On the inside the

magnetic field is 3.8 T strong, on the outside almost 2 T, concentrated by the iron return yoke. All particles, except muons and neutrinos, should be absorbed before the solenoid.

1.3.3.4 *Muon System*

The detection of muons is an important part of identifying interesting processes expected at the LHC. The predicted decay of a Standard Model Higgs boson into ZZ or ZZ*, which in turn decay into four leptons is considered *gold plated* if all leptons concerned are muons [27]. As also implied by the experiment's name, the detection of muons is of central importance to the CMS experiment.

The muon system has three elementary functions: to identify muons, measure their momentum, and triggering. Good muon momentum resolution and triggering capability stem from the solenoid magnet and its flux return yoke. The muon system utilises three different techniques to detect muons. In the barrel region drift tube chambers are used, up to a pseudorapidity of $|\eta| = 1.2$. Cathode strip chambers are used in the endcap discs ranging from $|\eta| = 0.9$ to $|\eta| = 2.4$. Both systems are complemented by resistive plate chambers, which provide a fast and independent trigger.

1.4 A FUTURE HIGH LUMINOSITY LHC AND ITS REQUIREMENTS

The LHC and its experiments have been designed and built with a run time up to the year 2022 in mind, at which the design instantaneous luminosity of $L = 10^{34} \text{cm}^{-2}\text{s}^{-1}$ will be reached, with a centre of mass energy of $\sqrt{s} = 14 \text{ TeV}$. With modifications to the accelerator complex and the LHC itself, an even higher luminosity can be achieved. In a collider experiment, the instantaneous luminosity L can be written as

$$L = \frac{n \cdot N_1 \cdot N_2 \cdot f}{A} , \tag{1.2}$$

with the number of bunches in the beam denoted by n, the amounts of particles in the colliding bunches N_1 and N_2, the collision rate f and the cross section of the bunches A. By integrating the instantaneous luminosity over time

$$\int L dt \tag{1.3}$$

a measure of the number of collisions delivered to the experiments can be calculated. At the end of the design run time in 2022, approximately 500 fb^{-1} will have been delivered to the ATLAS and CMS experiments.

It is planned to increase the instantaneous luminosity of the LHC after the year 2022 by a factor of five [132] to $5 \times 10^{34} \text{cm}^{-2}\text{s}^{-1}$ [113]. This will not only necessitate changes to the LHC [55], but will also have major impacts on the experiments.

The reasons for upgrading the LHC and the resulting changes to the CMS experiment are discussed in the following.

1.4.1   *The Physics Case*

The motivation to continue and upgrade the operation of the LHC and its experiments stems from the physics possibilities. With an increased luminosity, the LHC is able to provide more statistics for physics studies beyond those currently possible. With the discovery of a Higgs-like particle [28] in 2012, a primary goal of any future LHC operation will be to assess this particle's properties. Especially Higgs physics in rare decay channels will benefit greatly from increased statistics.

Other physics cases for an upgrade are improvements on Standard Model parameter measurements [61], which will also greatly benefit from improved statistics. Physics beyond the Standard Model could also be discovered with the HL-LHC, for example supersymmetry. If found, the HL-LHC could then determine SUSY parameters and perform *sparticle* spectroscopy. Additionally, with a High Luminosity LHC, other rare processes, such as Higgs pair productions can be investigated [64].

1.4.2   *Preceding Upgrades*

Before the actual upgrade to the HL-LHC takes place, several other minor upgrades to the LHC and the CMS experiment are foreseen. These are necessary to replace components that have suffered from radiation damage and to repair defective parts. Furthermore, the increased luminosity will lead to inefficiencies, especially in the pixel detector of the CMS experiment. These issues are addressed in the so-called Phase-I Upgrade [44], scheduled to take place in the technical stop of 2016/2017.

Within this upgrade, the present pixel detector will be replaced with one capable of maintaining an excellent tracking performance, especially at luminosities of $2 \times 10^{34}\,\mathrm{cm^2 s^{-1}}$ and in an environment of increased pileup[2]. The upgraded pixel detector will continue to use the current n-in-n sensor technology, as it has been shown to be sufficiently radiation hard [104], but will use an upgraded *readout chip* (ROC).

The new ROC will feature more buffer cells to prevent overflows at higher hit occupancies and will move to a faster, digital readout, significantly reducing data losses. The analogue performance will also be enhanced by a reduction of internal cross-talk and time-walk effects. The performance of the design changes has been studied in detail with a precision tracking telescope at the DESY test beam facilities [121]. Furthermore, a fourth barrel detector layer will be added to the pixel

---

2 Pileup describes the number of interactions per bunch crossing.

detector, improving tracking efficiency and seed resolution. This also necessitates upgrades to the cooling, powering and the support structure. More details can be found in [44].

1.4.3 *Impacts on the Pixel and Tracker Detectors*

The even more intense particle flux expected from a High Luminosity LHC will have severe impacts on the tracking system of CMS. Nevertheless, to benefit from the increase in luminosity, the performance of the CMS tracker has to be kept at its current level. In the following, the challenges for the inner detectors will be explained, together with the proposed changes and improvements to the detectors.

1.4.3.1 *Radiation Damage*

The intense flux of particles traversing the pixel and tracker detectors will lead to unprecedented levels of radiation damage of over $10^{16}\,\mathrm{n_{eq}/cm^2}$ in some areas. To cope with these levels of radiation, new radiation hard sensors are necessary, as well as suitable readout electronics and services. Figure 1.6 shows the expected radial dependence of the fluence in the CMS tracker for a future High Luminosity LHC. Because of these high fluence levels, an entirely new, even more radiation hard tracker has to be developed.
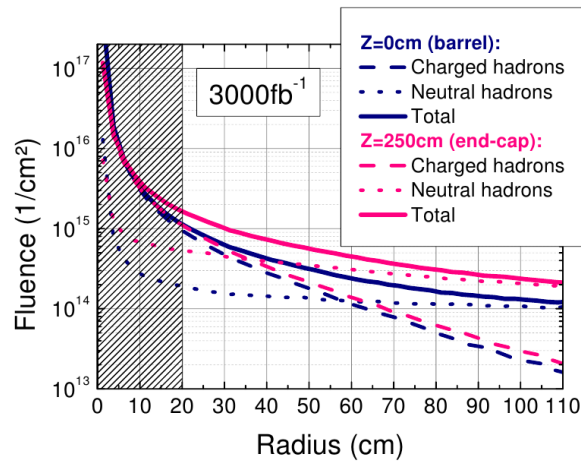
Figure 1.6: Simulated radial dependence of the expected particle fluence for a future HL-LHC, for a barrel and an endcap scenario. The layout of the current CMS tracker is assumed, together with an integrated luminosity of $3000\,\mathrm{fb^{-1}}$. The pixel detector extends from the beam pipe outwards to a radius of $20\,\mathrm{cm}$. The strip tracker occupies the region from $20\,\mathrm{cm}$ to $110\,\mathrm{cm}$. Image from [43], with data from [98].

To reduce the leakage current expected from highest fluence levels, the cooling system installed in the tracker will also be upgraded. While the current tracker uses a fluorocarbon system, with an operating temperature of $4\,°\mathrm{C}$, a future HL-

LHC CMS tracker will have to be operated at temperatures below $-20\,°C$. To achieve this, the cooling system will be changed to an evaporative CO_2 system, delivering more cooling power.

1.4.3.2   *A New Tracker Concept*

An increase in particles will also lead to a higher occupancy in the sensors, leading to a higher number of pileup events between 100 and 200, resulting in inefficiencies in event reconstruction. This can be counterbalanced by increasing the sensor granularity. A reduction of material in the tracking volume, compared with the current tracker, will reduce the rate of secondary interactions and improve tracking performance for low transverse momenta. The increased luminosity will furthermore lead to a rise in the CMS trigger rate, challenging the event selection. Providing tracking information input to the Level-1 trigger can reduce the trigger rate, while preserving physics performance capabilities. A major difficulty in the implementation of tracking triggers at Level-1 is the tracker data volume, which is too large to be transferred from the tracker to an external decision logic. This therefore necessitates on-detector data reduction [65]. The new, upgraded CMS tracker design is based on so-called p_T-*modules*, which provide this functionality. These modules consist of two silicon sensors separated by a small gap in a sandwich configuration. Both sensors are read out by the same readout chip, which also provides a simple p_T discrimination for the Level-1 trigger, based on the track bending in the 3.8 T magnetic field of the CMS solenoid. An illustration of this principle is shown in figure 1.7.
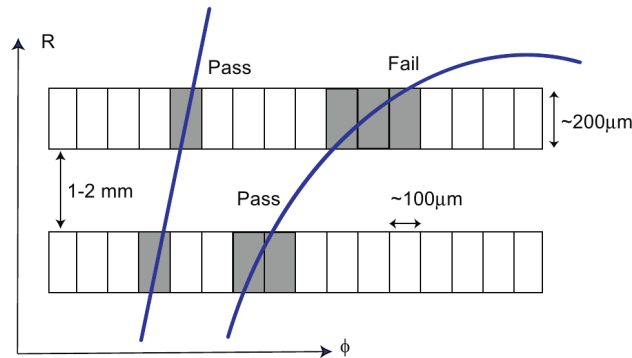
Figure 1.7: Schematic illustration of selecting high p_T tracks from hits in stacked layers. Image from [65].

Two basic types of modules are proposed for usage in the future tracker: *PS modules* and *2S modules* [93]. The former consists of a pixel sensor and a strip sensor and would be used in the inner parts of the tracker, where the expected track density is higher. Outer parts of the tracker would be equipped with the latter module type, which employs two identical strip sensors. A schematic image of the proposed baseline layout can be seen in figure 1.8.
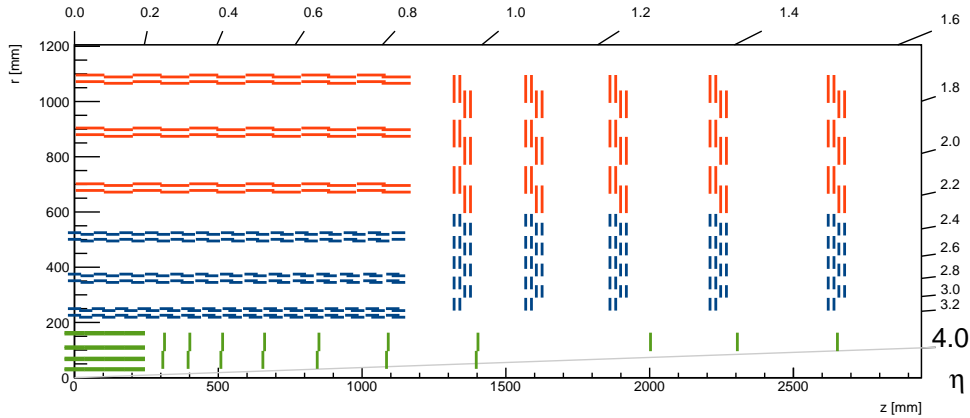
Figure 1.8: Baseline layout of the CMS tracker for the HL-LHC. Red lines show proposed positions of 2S modules, blue those of PS modules. Possible positions of pixel sensor modules are shown in green. Image from [123].

Figure 1.9 shows sketches of the PS and 2S modules. The 2S module consists of two silicon strip sensors, which are read out at both edges by a common set of front-end chips. The sensor area is $10\,\mathrm{cm} \times 10\,\mathrm{cm}$, with a strip length of $5\,\mathrm{cm}$ and $90\,\mu\mathrm{m}$ pitch. For the PS module, the upper strip sensor has $2.5\,\mathrm{cm}$ long strips, with a pitch of $100\,\mu\mathrm{m}$. The pixels in the lower pixel sensor are $1.5\,\mathrm{mm}$ long and $100\,\mu\mathrm{m}$ wide. Both sensors in the PS module have an area of $5\,\mathrm{cm} \times 10\,\mathrm{cm}$. The 2S and PS modules both have DC-DC power converters, optoelectronic connectors [5] and GigaBit Transceivers [95] included on the service hybrid.
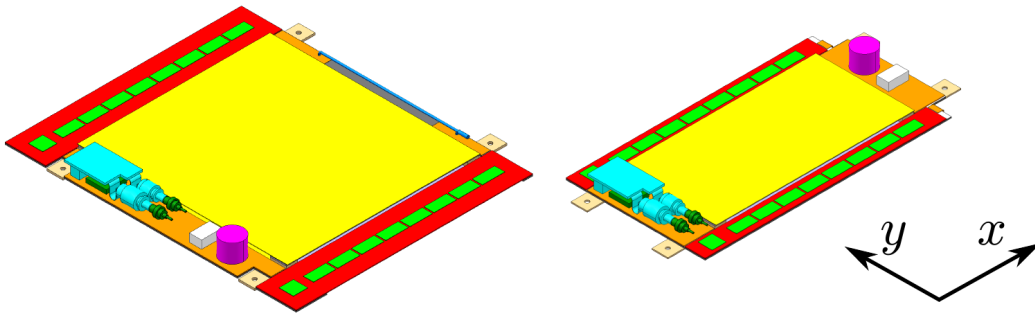
Figure 1.9: Sketch of p_T-module designs. Left: the 2S module with two strip sensors. Right: the PS module with a strip sensor above a pixel sensor. Hybrids are shown in red, sensors in yellow and front-end chips in green. Image from [92].

1.4.4 *The HPK Campaign*

The CMS Tracker Collaboration has started an extensive campaign to identify not only properties and production processes of various silicon materials, but also to provide a technological baseline for future sensors [69]. The campaign focus lies on determining radiation damage effects and annealing behaviour. Different sensor geometries and materials are being evaluated and compared to find the sensor

suited best for the HL-LHC. A single vendor, Hamamatsu Photonics K.K., has been chosen and measurement techniques have been fixed to ensure comparability of results between participating institutes.

1.4.4.1 *Materials*

Three different silicon base materials have been selected: *Float Zone* (FZ), *Magnetic Czochralski* (MCz) and *Epitaxial Silicon* (Epi). The basic production processes behind each of these materials, including the difference between thinned and deep-diffused Float Zone, is explained in chapter 2.2 in detail. Wafers from each base material are fabricated as both p-bulk and n-bulk silicon, with a crystal orientation of $\langle 100 \rangle$. An overview of the delivered materials and some of their properties is given in table 1.1.

Table 1.1: Overview of the HPK campaign materials. The bulk resistivity differs for n- and p-bulk non-epitaxial material.

Material type	Abbreviation	Physical thickness in μm	Active thickness in μm	Mean oxygen content in $10^{17}\,\mathrm{cm}^{-3}$	Bulk resistivity in kΩcm
Deep-diffused Float Zone	FZ120	320	120	5	n: $1.2 - 2.4$ p: $3 - 8$
Deep-diffused Float Zone	FZ200	320	200	3	n: $1.2 - 2.4$ p: $3 - 8$
Deep-diffused Float Zone	FZ320	320	320	1	n: $1.2 - 2.4$ p: $3 - 8$
Thinned Float Zone	Fth200	200	200	1	n: $1.2 - 2.4$ p: $3 - 8$
Magnetic Czochralski	MCz200	200	200	4	n: > 0.5 p: > 2
Epitaxial	Epi70	320	70	1	$0.5 - 2$
Epitaxial	Epi100	320	100	1	$0.5 - 2$

1.4.4.2 *Structures*

The wafers contain a wide range of different structures to investigate material and structure properties. An overview can be found in figure 1.10. Within this work, the *multi-geometry silicon strip detector* (MSSD) and the *Baby Additional* (Baby_Add) sensors have been used. Details on their geometry is given in chapters 4 and 5, respectively. Further important structures included on the wafer are a variety of diodes, several layouts of pixel and strip sensors, test structures and strip sensors

with novel readout schemes.

The diodes are used to evaluate changes to sensor bulk properties with irradiation. Information on these changes can be gained by qualification measurements, such as current or capacitance against applied voltage. Openings in the front and back side metallisation allow usage of *Transient Current Technique* (TCT) measurements, in which laser pulses are used to assess carrier trapping times, electric fields and charge collection efficiencies.

Various layouts of *Multi-geometry-Pixel* (MPix) structures are used to evaluate biasing schemes, such as punch-through biasing or polysilicon biasing. The pixel sensor structures are also used as prototypes for new module designs [69]. Investigations into strip sensor properties are performed on *Baby Standard* (Baby_Std) strip sensors. Charge collection efficiencies and strip parameters, such as capacitances, resistances and currents are measured before and after all irradiation steps.

The *Baby_PA* sensor realises a novel sensor design, with an integrated pitch adapter included in the first metal layer of the sensor. A further design study included is the *Baby_Strixel* sensor. This design features short, staggered strips with routing lines between readout strips. Select wafers are produced with a second metal layer on top, integrating a pitch adapter and routing structures in an aim to reduce the overall material budget. The feasibility of these designs is evaluated within the HPK campaign.
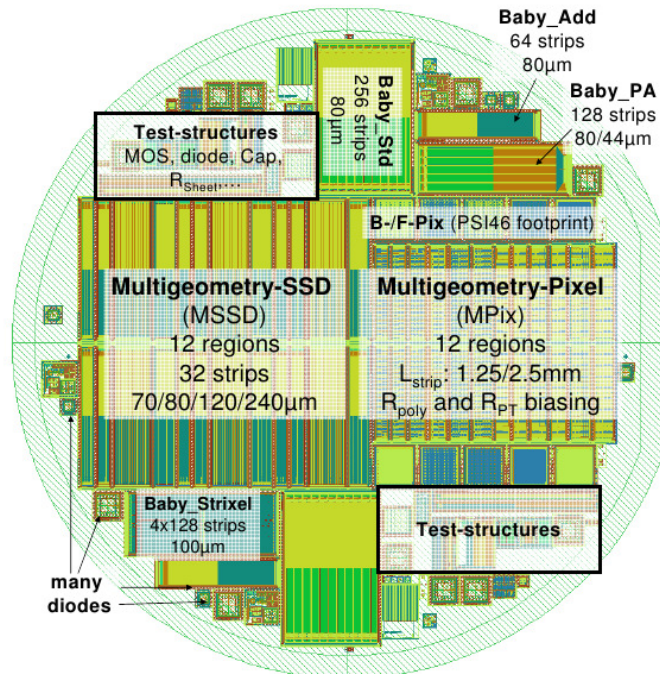
Figure 1.10: Schematic layout of the HPK campaign wafer. The wafer contains various devices, such as diodes and small strip sensors. Multi-geometry strip and pixel sensors are included together with test structures and sensors with novel readout schemes. Image from [43].

1.4.4.3 *Irradiations and Qualifications*

To verify the performance of the different sensor structures after the fluence expected from the entire High Luminosity LHC runtime, samples were irradiated to several fluence levels. These levels correspond to those expected for sensors at certain radii in the CMS tracker and are listed in table 1.2. An overview of the radial dependence of the fluence levels can be found in figure 1.6. The irradiation centres are described in 3.7.

Table 1.2: Overview of the irradiation steps performed within the HPK campaign.

Proton fluence	Neutron fluence	Corresponding radial
in 10^{14} n_{eq}/cm^2		position in cm
3	4	40
10	5	20
15	6	15
30	7	10
130	10	5

All sensor structures are measured prior to any irradiation. The exact specifications for all measurements have been agreed upon by participating institutes. Following that, they are irradiated with either protons or neutrons, undergo an annealing of ten minutes at $60\,^\circ$C and are then remeasured. Afterwards, they are irradiated with the missing particle type, followed by a further annealing step before they are measured again. With this procedure, the combined radiation environment of charged and neutral hadrons can be reproduced. Measurements are stored on a central database for comparability.

SEMICONDUCTOR TRACKING DETECTORS

With technological advances in science and industry, semiconductor sensors have seen an increasing popularity in particle physics. Of the materials considered semiconductors, mainly silicon, germanium and diamond sensors are used to build tracking detectors. As the name suggests, tracking detectors are used to gain information on the track and momentum of charged particles traversing them. The quality and the performance of the track and vertex reconstruction are vital for all particle physics experiments and thus must be ensured over the experiment's entire running time. In this chapter, the main physics processes behind semiconductor sensors are described, along with their basic properties and attributes. The production technologies used in the manufacturing of silicon sensors are also introduced. Finally, the effects of radiation damage in silicon are highlighted. Broader overviews over the entire theoretical background are given, for example in [66], [83], [87] and [122].

2.1 SILICON AS A SENSOR MATERIAL

Silicon is by far the most popular semiconductor sensor material. Its advantages include a high signal level due to the small band gap of $E_g = 1.12\,\text{eV}$ at $300\,\text{K}$ [83], excellent spatial resolution in the order of micrometres and fast signal collection in the nanosecond regime. With an ionisation energy of $3.6\,\text{eV}$ required to produce a single electron-hole pair [122], silicon sensors have an energy resolution almost ten times better than that of gaseous detectors [66]. Silicon sensors also show some intrinsic radiation hardness, which can be increased with different design techniques. In the following, the basic working principles of silicon semiconducting sensors are explained, together with aspects of their operation in high-energy physics.

2.1.1 *Working Principle*

In a solid crystal, the atoms form a lattice structure with the effect that their atomic orbitals begin to overlap. With an increasing number of atoms, the energy levels become increasingly dense, eventually forming a continuous band structure. The band with the highest energy level that is still fully occupied by electrons is called the *valence band*, the band lowest in energy with free states is referred to as the *conduction band*. The structure of these bands alters a material's conductivity and allows the categorisation of materials into *conductors*, *semiconductors* and *insulators*, as shown in figure 2.1. Electrical conductivity is caused by movement of electrons in the conduction band. If an electron moves from a state within the valence band to a state in the conduction band, it creates a vacancy in the valence band,

which is called a *hole*. In conductors, the Fermi energy[1] lies within the conduction band, leading to a large concentration of free electrons in this band, also at low temperatures. Due to the high electron concentration in the conduction band, the conductivity in these materials is high. In contrast, in insulators the Fermi energy is below the conduction band. Due to the large *band gap* between valence and conduction bands, electrons can not be excited from the former to the latter. This results in insulators being non-conductive. In semiconductors at low temperatures, the conduction band is also not occupied by electrons, with the Fermi energy located beneath the conduction band. The band gap however is significantly smaller than in insulators. Because of this, from certain temperatures onwards, electrons can be excited from the valence band to the conduction band. The conductivity of a semiconductor is therefore dependent on its temperature.
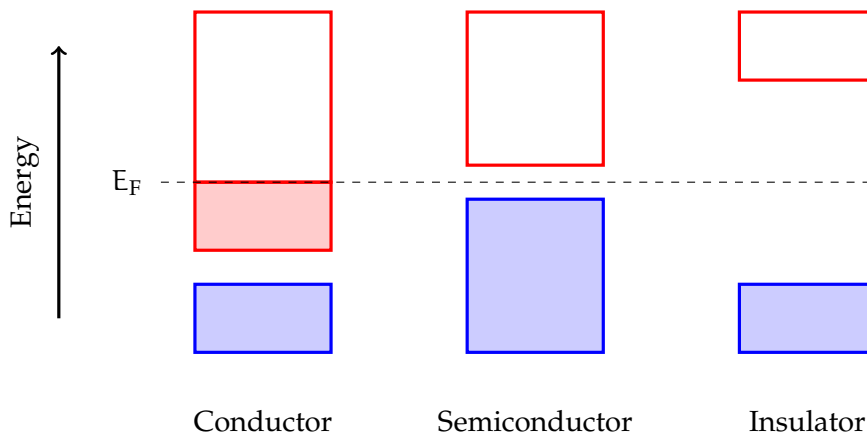
Figure 2.1: Schematic classification of solids into conductors, semiconductors and insulators, according to their band structure. Filled colours denote occupied states. The valence bands are shown in blue, the conduction bands in red. At a temperature of $T = 0\,K$, all states below the Fermi energy E_F are occupied, all above free.

Intrinsic silicon follows the general behaviour of a semiconductor, acting as an insulator at low temperatures and showing conducting properties at higher temperatures. Both bands are separated by the band gap, which is $1.12\,eV$, as stated above.

2.1.1.1 *Doping*

By adding artificial impurities to the silicon crystal (*doping*), additional states in the band gap can be created, altering the electrical conductivity. By adding elements from the third group in the periodic table of elements (e.g. boron) to the group-IV silicon, *p-type* material is created. Likewise, by adding group-V elements such as phosphorus, *n-type* material is produced. In both cases, a silicon atom is replaced by an impurity atom. Due to the different valence electron configuration of these

---

1 The Fermi energy denotes the energy at which the occupancy probability of a state is 1/2, as described by the Fermi–Dirac function $F(E) = 1 / \left(1 + \exp\left(\frac{E - E_F}{k_B T}\right)\right)$.

impurity atoms, additional free charge carriers are introduced. With three valence electrons, group-III elements lack an electron compared with the surrounding silicon atoms. This effectively introduces a hole. Likewise, an impurity atom from the fifth group introduces an additional free electron. In both cases, the additional free charge carriers can be used for electrical conductance. By introducing additional holes (p-type) or electrons (n-type), the dopants act as acceptors or donors, respectively. Acceptor states can be occupied by valence band electrons, creating holes in the band. Due to this process, the majority charge carriers in p-type material are holes. Likewise, in n-bulk silicon, the donor states create excess electrons. Accordingly, here the majority charge carriers are electrons. An overview of states created by doping is shown in figure 2.2.
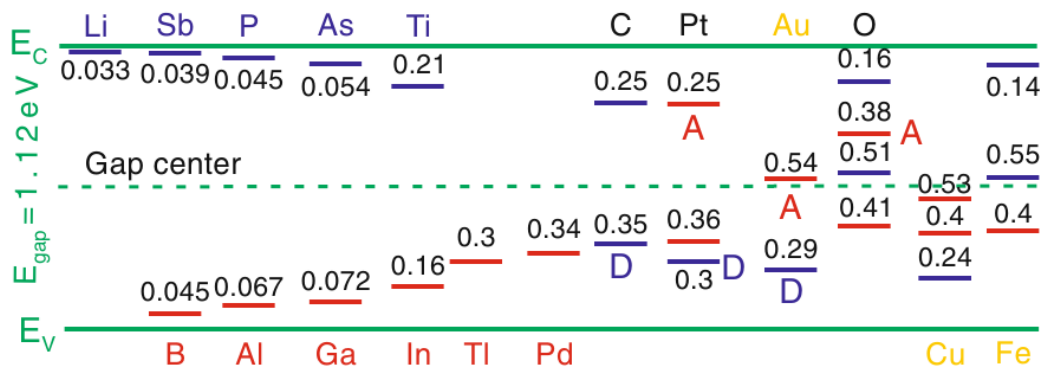
Figure 2.2: States in the silicon band gap created by different dopants. Acceptor states are displayed in red, donor states in blue. Image from [66].

To utilise silicon as a detector material, it must be sensitive to the amount of charge carriers in a signal. These charge carriers are created by means of ionisation by a traversing particle, as is explained in section 2.1.2.6, and can amount to only $\sim 10^3$ charge carriers. In intrinsic silicon, however, the amount of free charge carriers is of the order of $\sim 10^9$. Therefore, the amount of free charge carriers in a silicon sensor has to be reduced vastly. This process is called depletion and is achieved by application of reverse bias voltage to a so-called *pn-junction*.

2.1.1.2   *The pn-Junction*

If p-doped material and n-doped material are brought together, a pn-junction is created. In p-type material, the Fermi energy is slightly above the acceptor level, which in turn is above the energy of the valence band E_V. In n-type material, the situation is different, with the Fermi energy located slightly below the donor level, which is located beneath the conduction band, the lower limit of which is E_C. A schematic of these levels is shown in figure 2.3. At the junction between both materials, an equilibrium of charge carriers begins to form. Due to the different Fermi levels in both materials, the majority charge carriers in one material diffuse into the other material and vice versa. This is shown in figure 2.4.
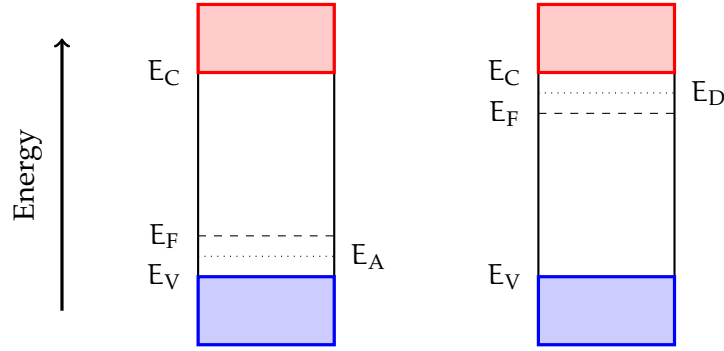
Figure 2.3: Location of the Fermi energy E_F for p-doped (left) and n-doped (right) silicon. E_C and E_V denote the lower and upper edges of the conduction and valence bands, respectively. Dotted lines indicate the position of the acceptor and donor levels.
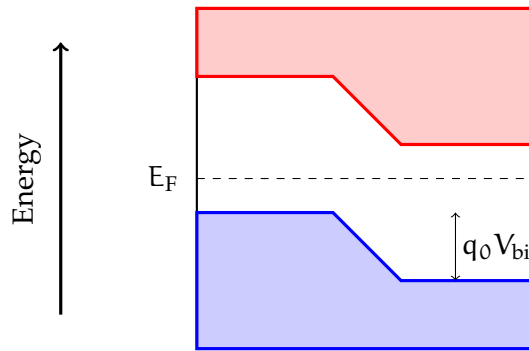
Figure 2.4: Band scheme in the pn-junction, after p- and n-doped materials have been brought into contact. Conduction and valence bands are shifted by the value of the built-in voltage V_{bi} [66].

The electrons diffusing from the n-region leave a positive charge behind and recombine with holes in the p-region. The holes diffusing from the p-region into the n-material behave accordingly. The resulting holes in the n-region and electrons in the p-region create an electric field, which counteracts the diffusion process until equilibrium is reached. In the state of equilibrium, a space charge region depleted of free charge carriers at the pn-junction has been created. The depleted region consists of a negatively charged area of size d_p at the p-doped side of the junction and a positively charged area of size d_n at the n-doped side of the junction. The space charge region as a whole is charge neutral, the charge density $\rho(x)$ is [83]:

$$\rho(x) = \begin{cases} 0 & \text{for } x < -d_p \\ -q_0 N_A & \text{for } -d_p \leqslant x \leqslant 0 \\ q_0 N_D & \text{for } 0 \leqslant x \leqslant d_n \\ 0 & \text{for } d_n < x \end{cases} \quad , \tag{2.1}$$

with the elementary charge q_0 and the doping densities of acceptors and donors, N_A and N_D, respectively. By integrating Poisson's equation

$$\frac{d^2 V}{dx^2} = -\frac{\rho(x)}{\epsilon_o \epsilon_r},$$

(2.2)

the electric field within the sensor can be calculated from the electrostatic potential $V(x)$:

$$E(x) = -\frac{dV(x)}{dx} = \begin{cases} -\frac{q_0 N_A}{\epsilon_o \epsilon_r} \cdot (x + d_p) & \text{for } -d_p \leqslant x \leqslant 0 \\ \frac{q_0 N_D}{\epsilon_o \epsilon_r} \cdot (x - d_n) & \text{for } 0 \leqslant x \leqslant d_n \end{cases},$$

(2.3)

with the vacuum permittivity ϵ_o and the relative permittivity ϵ_r. Further integration leads to:

$$V(x) = \begin{cases} -\frac{q_0 N_A}{2\epsilon_o \epsilon_r} \cdot (x + d_p)^2 & \text{for } -d_p \leqslant x \leqslant 0 \\ \frac{q_0 N_D}{2\epsilon_o \epsilon_r} \cdot (x - d_n)^2 & \text{for } 0 \leqslant x \leqslant d_n \end{cases},$$

(2.4)

so that the potential difference V_{bi} between the borders of the space charge region amounts to:

$$V_{bi} = \frac{q_0}{2\epsilon_o \epsilon_r} \cdot |N_{eff}| \cdot d^2,$$

(2.5)

with effective doping concentration $N_{eff} = N_D - N_A$. The effective doping concentration can also be used to determine the sensor bulk resistivity ρ, which can be expressed as

$$\rho = \frac{1}{q_0 \mu |N_{eff}|},$$

(2.6)

with the mobility of the majority charge carriers μ [122]. From equation 2.5 the width of the space charge region can be calculated to:

$$d = d_p + d_n = \sqrt{\frac{2\epsilon_o \epsilon_r \cdot (N_A + N_D)}{q_0 N_A N_D} \cdot V_{bi}}.$$

(2.7)

The built-in voltage V_{bi} is generally in the order of millivolts [83], with only a few micrometres depleted of charge carriers[2]. However, if an external bias voltage V_{bias} is applied to the pn-junction, the space charge region is enlarged or reduced, depending on the voltage polarity. Equation 2.7 then reads:

$$d = \sqrt{\frac{2\epsilon_o \epsilon_r \cdot (N_A + N_D)}{q_0 N_A N_D} \cdot (V_{bi} - V_{bias})}.$$

(2.8)

---

2 For very thin sensors this can be a substantial amount of the sensor.

If the higher bias potential is attached to the p-doped section of a pn-junction and the lower bias potential to the n-doped section, the pn-junction is operated in *forward direction*. From equation 2.8 one can see that the reciprocal case, with higher potential at the n-side and lower potential at the p-side, can enlargen the space charge region. This mode is called *reverse bias* and is generally the modus operandi for silicon sensors.

The performance of silicon sensors can be put into comparison when looking at some distinctive basic sensor properties: a sensor's depletion voltage, its capacitance and leakage current. These elementary characteristics are discussed in the following.

2.1.1.3   *Capacitance and Depletion Voltage*

The depletion voltage V_{depl} of a sensor is the applied bias voltage in reverse direction, at which the entire sensor volume is depleted of free charge carriers. From equation 2.8 one can obtain the expression

$$V_{depl} = \frac{q_0 D^2 \cdot |N_{eff}|}{2\epsilon_0 \epsilon_r} \, ,$$

(2.9)

for a sensor of thickness D, assuming that the depletion voltage is large compared with the built-in voltage V_{bi}. As the space charge region acts as a parallel plate capacitor, the bulk capacitance is directly related to the thickness d of the depleted region:

$$C_{bulk} \propto \frac{\epsilon_0 \epsilon_r}{d} \, .$$

(2.10)

This leads to the expression

$$C_{bulk} \propto \begin{cases} \sqrt{\frac{q_0 \epsilon_0 \epsilon_r \cdot |N_{eff}|}{2V_{bias}}} & \text{for } V_{bias} \leqslant V_{depl} \\ \frac{\epsilon_0 \epsilon_r}{D} & \text{for } V_{bias} > V_{depl} \end{cases}$$

(2.11)

for the bulk capacitance C_{bulk}, from which can be seen that the capacitance decreases with applied bias voltage until depletion is reached. Reciprocally, from measuring the bulk capacitance of a sensor for different bias voltages, the depletion voltage can be calculated. In most cases this is done by plotting the inverse square bulk capacitance against the applied bias voltage, as is illustrated in figure 2.5.

2.1.1.4   *Leakage Current*

In an ideal sensor, the flow of current is given by the *Shockley equation*, which describes the diffusion current densities of electrons J_n and holes J_p [127]:

$$J_n = \frac{q_0 D_n n_{p0}}{L_n} \left(\exp\left(\frac{q_0 V}{k_B T} \right) - 1 \right)$$

(2.12)
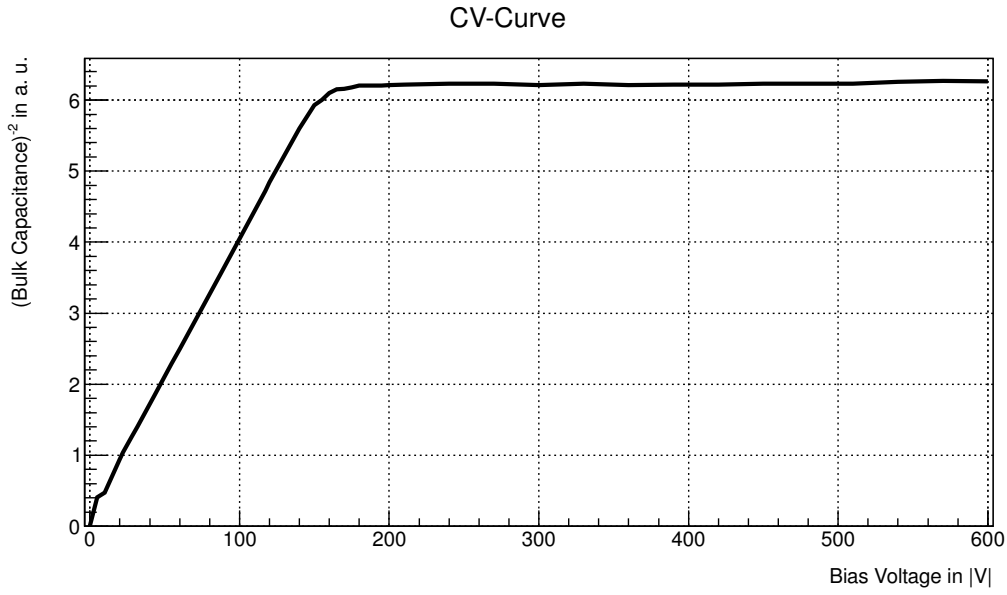
Figure 2.5: Simulated example CV-curve to determine the depletion voltage of a silicon sensor. At approximately 170 V the inverted square bulk capacitance levels off, indicating that the entire bulk is depleted of free charge carriers at this bias voltage.

and

$$J_p = \frac{q_0 D_p p_{n0}}{L_p} \left(\exp\left(\frac{q_0 V}{k_B T} \right) - 1 \right) . \tag{2.13}$$

Here, the diffusion length for electrons and holes is $L_{n,p} = \sqrt{D_{n,p} \tau_{n,p}}$, with diffusion coefficients D_n and D_p, and carrier lifetimes τ_n and τ_p. p_{n0} is the hole density on the n-side in equilibrium, n_{p0} the density of electrons on the p-side. The ideal current voltage characteristics are obtained by summation of J_n and J_n to the diffusion current J_d:

$$J_d = J_n + J_p = J_0 \left(\exp\left(\frac{q_0 V}{k_B T} \right) \right) , \tag{2.14}$$

with the saturation current density J_0 defined as

$$J_0 = \frac{q_0 D_n n_i^2}{L_n N_A} + \frac{q_0 D_p n_i^2}{L_p N_D} . \tag{2.15}$$

In equation 2.15, n_i is the free charge carrier concentration, N_A and N_D are the doping densities of acceptors and donors, respectively.

When reverse bias voltage is applied to a sensor, the resulting current flow is called the leakage current J_{leak}. The leakage current is an important detector parameter, as it has a large impact on the sensor's noise and its power consumption.

In diodes, it consists of two main components, the diffusion current introduced above and the generation current J_{gen}:

$$J_{leak} = J_d + J_{gen} \qquad (2.16)$$

The generation current is caused by the creation of electron-hole pairs from defects near the middle of the silicon band gap. These defects are created for example by processing steps during the sensor fabrication or are induced by radiation. As only defects in the depleted sensor area contribute to J_{gen}, a dependence on the depletion width d and therefore on the bias voltage is observed:

$$J_{gen} \propto d \propto \sqrt{V} \qquad \text{for} \qquad V \leqslant V_{dep}. \qquad (2.17)$$

J_{gen} saturates for voltages near the depletion voltage and can be expressed by the generation life time τ_g [127]:

$$J_{gen} = \frac{q_0 n_i d\left(V\right)}{\tau_g}. \qquad (2.18)$$

In most application scenarios of silicon detectors, J_{gen} dominates the leakage current. However, at high temperatures the diffusion current J_d can be of substantial size. Further contributions to the leakage current come from states at the silicon - silicon dioxide interface or from surface effects. Especially in segmented sensors, the surface generation current can amount to significant size. The surface current density J_{surf} is expressed by

$$J_{surf} = q_0 n_i S_0, \qquad (2.19)$$

with the *surface generation velocity* S_0 expressed as [138]

$$S_0 = \sigma_{eff} v_{th} \pi k_B T D_{it} \qquad (2.20)$$

for a homogeneous distribution of interface states. Here σ_{eff} is the effective capture cross section, v_{th} the average thermal velocity of minority carriers and D_{it} the density of interface states.

Scaling a current measured at a temperature T_1 to a different temperature T_2 can be performed by

$$I(T_2) = I(T_1) \cdot \left(\frac{T_2}{T_1}\right)^2 \exp\left(\frac{-E_{eff}}{2k_B} \cdot \left(\frac{1}{T_2} - \frac{1}{T_1}\right)\right), \qquad (2.21)$$

with $E_{eff} = 1.21\,eV$, as found by Chilingarov [31].

2.1.2   *From the pn-Junction to a Segmented Sensor*

The pn-junction explained in the previous section is, in essence, a diode. The diode is the most simple semiconductor sensor. In case of an n-bulk diode, a thin layer of highly p-doped silicon is implanted into an n-doped silicon bulk. In the production process, a silicon dioxide layer forms on top of the p-doped implant. An aluminium layer is deposited on top, acting as an electric contact. On the opposite side of the n-doped bulk, a region of higher n-doping concentration limits the possible depletion region and assures connectivity with the aluminium backplane layer below. A p-type diode is constructed accordingly by exchanging the dopants. Typical bulk thicknesses are between $50\,\mu m$ and $500\,\mu m$ with implantation and silicon dioxide thicknesses usually below $2\,\mu m$. The bulk doping concentration is usually in the order of $\sim 10^{12}\,cm^{-3}$, the higher strip and backplane implantation concentrations can be up to $\sim 10^{18}\,cm^{-3}$. High doping concentrations are denoted by a plus sign, e.g. p^+ or n^+. The lateral extent of a diode sensor can reach a centimetre in size. While diodes are not used as sensors in high-energy physics detectors due to their lack of position sensitivity, they are used in many setups to investigate material properties and radiation damage effects.

2.1.2.1   *Strip Sensors*

A strip sensor is built in a similar way to a diode, with the main difference in the processing of the top side. In a diode, the implantation covers the entire top side of the sensor, except for a possible exterior guard ring structure (cf. 2.1.2.2), while in a strip sensor, the implantation is performed in individual strip segments. A silicon dioxide layer also encompasses the top side of the sensor, but the top side aluminium now solely runs over the individual strips. Each strip implantation creates a separate pn-junction with the surrounding bulk material. The distance between strip implant centres is called the sensor *pitch* and is usually between $\sim 50\,\mu m$ and $\sim 300\,\mu m$ in size.

At the end of the sensor, the strip implants are connected to an aluminium *DC pad*, which allows a direct contacting of the strips for testing purposes. Each aluminium strip can be contacted at an *AC pad*. A *bias ring*, consisting of an implant and an overlying aluminium strip surrounds the strips and, in p-in-n sensors, provides ground potential to the strip implants over the polysilicon *bias resistors*. The bias ring is surrounded by one or more *guard rings*. All aforementioned top side implants are of the same doping type - in case of an n-bulk sensor they are p^+-doped, in case of a p-bulk sensor they are n^+-doped. Beyond the guard rings at the edge of the sensor, an implant prevents high electric fields at the cut edges. The implant is of the same type as the back side doping, which connects the sensor to the aluminium back side, from which the bias voltage is applied. A schematic of a typical strip sensor can be seen in figure 2.6, a cut through the sensor illustrating its operation principle is shown in figure 2.7.
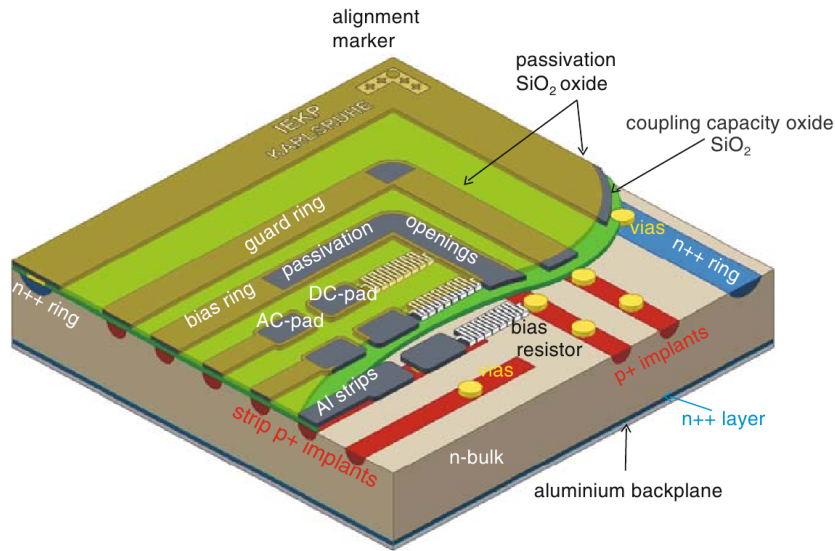
Figure 2.6: Schematic of an n-bulk silicon strip sensor and its main features. Image from [66].
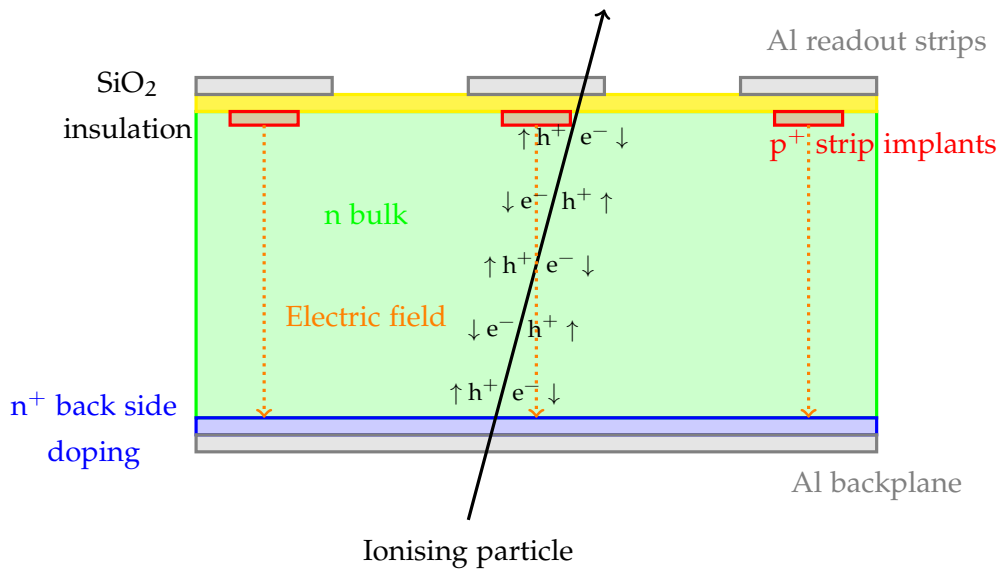
Figure 2.7: Working principle of an AC-coupled p-in-n silicon strip detector. Electron-hole pairs resulting from the ionisation of a traversing charged particle travel to the sensor electrodes. This schematic depicts a p-in-n sensor, in which the holes travel to the readout strips while the electrons are collected at the backplane. In an n-in-p sensor, this is reversed.

An ionising charged particle creates electron-hole pairs when traversing the sensor. The electric field within the sensor bulk separates the electrons and holes, which begin to drift to their respective electrodes. In the p-in-n sensor sketched in figures 2.6 and 2.7, holes travel towards the strips, whilst electrons are collected at the backplane. Charges collected at the strip implants capacitively couple to the aluminium readout strips. The AC pads thereof are wire bonded to a *readout chip* (ROC), where the intrinsic signal is shaped, amplified and measured. This *AC coupling* has the advantage that the sensor's leakage current does not flow through the readout chip. The signals from each individual strip give the sensor position resolution in one dimension. As the induced signal is independent of where along the strip it was created, no information on the secondary plane coordinate along the strips can be measured. An alternate operation method is called DC coupling. Here the aforementioned DC pads are directly connected to the readout chip. The technique is often used in pixel detector sensors, where the metallisation on top of an implant acts as a DC pad and is connected via *bump bonds* to the ROC.

2.1.2.2 *Strip Isolation Technologies and Guard Rings*

Silicon sensors featuring a p-type bulk have a major disadvantage when compared with n-bulk sensors due to the layer of silicon dioxide on the sensor top side, as this oxide layer can accumulate positive charges. This positive charge can attract electrons, forming an electron accumulation layer at the interface between silicon and silicon dioxide. This layer can then short the n-doped strip implants, rendering the strip sensor useless. Two main isolation techniques can be used to prevent this effect:

- *p-spray* isolation
  Here, a thin layer of p^+-doped silicon is implanted over the entire top side silicon surface, except for the n^+ implants. The p-spray layer prevents the accumulation of electrons.

- *p-stop* isolation
  In this case, one or more p^+ implants are placed between the n^+ strip implants. These p-stop implants prevent the shortening of the readout implants by cutting into the electron accumulation layer.

Guard rings are included in most diodes and strip sensors to shape the electric field inside the sensitive area [66]. Furthermore, they prevent a breakdown of the sensor due to effects of the sensor edge [87]. Beneath the aluminium guard ring structure, an implant of the same doping type as the strip implant is located and connected with a *via*. A via is a conductive connection between layers in a sensor.

2.1.2.3 *Pixel Sensors*

One of the main drawbacks of silicon strip sensors is that they only deliver a position measurement in one dimension. A further segmentation of the strips into a

pixelated structure leads to a *pixel sensor*, which is sensitive in two space dimensions. Depending on application area, the size of each pixel can be in the order of $\sim 10\,\mu m \times 10\,\mu m$. The readout chip is adapted to small input capacitances and in most cases is designed to operate with a direct DC coupling to the pixel implants.

Due to the increased segmentation in a pixel sensor, the wire bonding technique used to connect a strip sensor to the readout chip is no longer viable. In the case of *hybrid* pixel sensors, a readout chip of the same size and segmentation as the sensor is *bump bonded* to the sensor. Another possibility is to directly combine sensor and readout chip on the same silicon wafer to a *monolithic active pixel sensor* (MAPS) [66]. In both cases, the pixelation leads to a large number of readout channels and can necessitate large amounts of power and thus cooling for operation. This leads to complex engineering challenges for the support and supply structures during the construction of a pixel detector.

2.1.2.4 *Noise in Silicon Sensors*

In any silicon sensor, a variety of sources contribute to the sensor's noise. The exact contributions differ between sensor technology, operation conditions and readout strategies [66]. The main sources are the load capacitance C_d, the leakage current I_{leak}, and parallel and series resistances R_P and R_S. In general, noise is expressed as *equivalent noise charge* (ENC), giving the amount of electrons contributing to the noise. Contributions to the ENC are summed quadratically, as shown in equation 2.22:

$$\mathrm{ENC} = \sqrt{\mathrm{ENC}_C^2 + \mathrm{ENC}_{I_{leak}}^2 + \mathrm{ENC}_{R_P}^2 + \mathrm{ENC}_{R_S}^2}\,. \tag{2.22}$$

The noise stemming from the load capacitance C_d is the most significant contribution:

$$\mathrm{ENC}_C = a + b \cdot C_d\,. \tag{2.23}$$

The parameters a and b are specific to the used preamplifier in the readout chip. According to Hartmann [66], the slope b is mostly defined by the intrinsic chip voltage noise $u_{n,amp}$ and the peaking time of the shaper t_p:

$$b \sim \frac{u_{n,amp}}{t_p}\,. \tag{2.24}$$

Shot noise is contributed by the leakage current:

$$\mathrm{ENC}_{I_{leak}} = \frac{e}{2}\sqrt{\frac{I_{leak} \cdot t_p}{q_0}}\,, \tag{2.25}$$

with Euler's number e and the elementary charge q_0. *Parallel thermal noise* comes from the bias resistance R_P:

$$\text{ENC}_{R_P} = \frac{e}{q_0} \sqrt{\frac{k_B T \cdot t_p}{2R_P}}, \tag{2.26}$$

with the operation temperature T and Boltzmann's constant k_B. *Serial thermal noise* from the aluminium strip resistance R_S contributes the term

$$\text{ENC}_{R_S} = C_d \cdot \frac{e}{q_0} \sqrt{\frac{k_B T \cdot R_S}{6t_p}}. \tag{2.27}$$

From equations 2.22 to 2.27 it can be seen that for a minimal sensor noise ENC, the sensor design should aim to minimise the load capacitance C_d, the leakage current I_{leak} and the series resistance R_S. Parallel resistance R_P should be large.

2.1.2.5 *Interstrip Capacitance and Resistance*

The interstrip capacitance C_{int} is defined as the capacitance measured between two adjacent strips in a strip sensor. The capacitance value is measured between the AC pads of the concerned strips and is one of the main components of the capacitive load on the readout chip and therefore a large contributor to strip noise. Nevertheless, C_{int} is beneficial to a sensor's operation to some extent, as it is part responsible for the charge sharing between adjacent strips. Charge sharing, as is explained in following sections, can improve a sensor's position resolution to some extent.

The interstrip resistance R_{int} denotes the resistance between individual strips. To ensure the isolation of the strips towards each other, the value of R_{int} should be in the order of several $G\Omega$ [66]. The measurement of the interstrip resistance is very demanding: The sensor is biased to a certain bias voltage, with all strips at ground potential. Only a small measurement voltage of approximately 1 V can be applied to the strip measured, as to not distort the depletion layer. The resulting current difference in the nA regime at a neighbouring strip is then measured.

2.1.2.6 *Charge Creation and Charge Collection*

Charges are created in a semiconducting sensor by the interaction of traversing charged particles with the sensor matter. The charged particles hereby interact with shell electrons of the detector atoms, losing energy in the process. A particle's mean energy loss dE by traversing matter of thickness dx is described by the Bethe formula [100]:

$$-\frac{dE}{dx} = \frac{4\pi n z^2}{m_e c^2 \beta^2} \cdot \left(\frac{q_0^2}{4\pi\epsilon_0} \right)^2 \cdot \left[\ln\left(\frac{2m_e c^2 \beta^2}{I \cdot (1-\beta^2)} \right) - \beta^2 \right], \tag{2.28}$$

with the vacuum permittivity ϵ_0, elementary charge q_0, rest mass m_e, the speed of light c and β defined as $\beta = v/c$. The traversing particle has the velocity v and the charge $z \cdot q_0$. The electron density of the detector material is given by n and I is the mean excitation potential of the atoms.

Figure 2.8 shows the stopping power for a muon of positive charge in copper as a function of $\beta\gamma = p/Mc$, with the Lorentz factor $\gamma = 1/\sqrt{1-\beta^2}$. The energy loss as described by the Bethe equation can only be applied in the indicated Bethe region, at lower and higher energies, other processes, such as radiative losses, dominate.
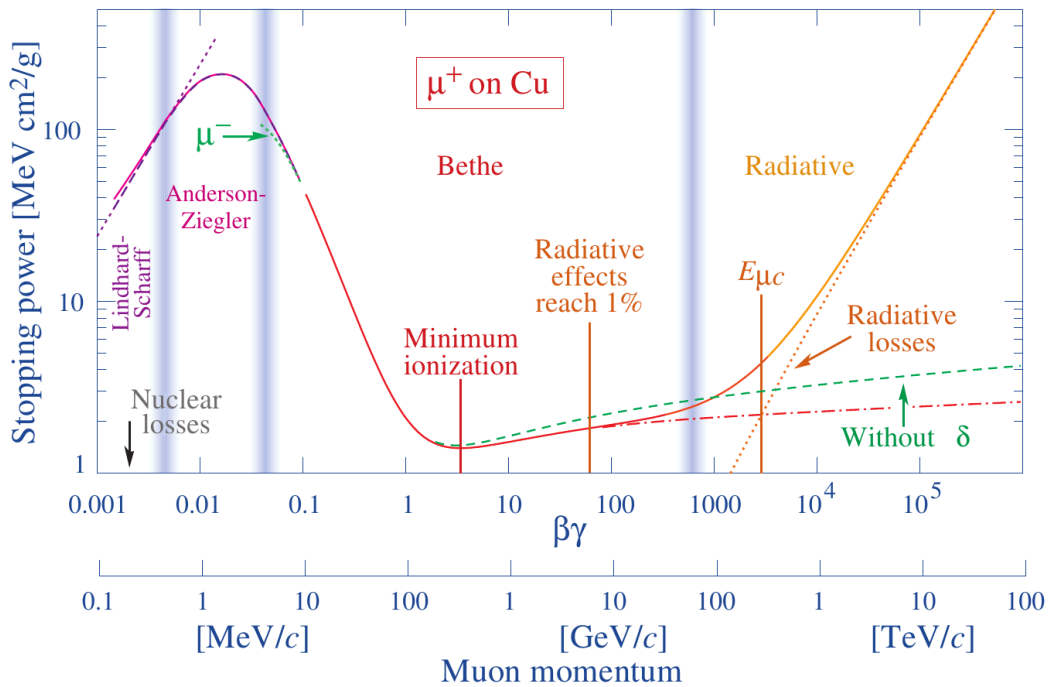
Figure 2.8: Mean stopping power of positively charged muons in copper. Particles with $\beta\gamma \approx 2-3$ are considered *minimum ionising particles*. Image from [100].

The energy losses of electrons traversing matter follow the same mechanisms as described above. Due to their small mass, *bremsstrahlung* losses also contribute to their energy loss, especially towards higher energies. Bremsstrahlung is the electromagnetic radiation emitted by the deceleration of a charged particle in the electric field of another particle. The calculated overall stopping power for electrons in silicon is shown in figure 2.9.

The actual energy loss distribution of a particle with a certain energy crossing a sensor is however not Gaussian. This is due to so-called δ-rays. These are created if the incident particle knocks an orbiting electron out of its orbit around an atom, transferring a high momentum to the electron. This electron can then ionise further atoms in the sensor bulk, inducing a large charge. These fluctuations in the energy loss distribution are described by the *Landau-Vavilov theory*. The Landau distribution resembles a Gaussian distribution, but has a long upper tail, to account for the transferring of large amounts of energy. Due to the tail, the distri-

Stopping Power for Electrons in Silicon
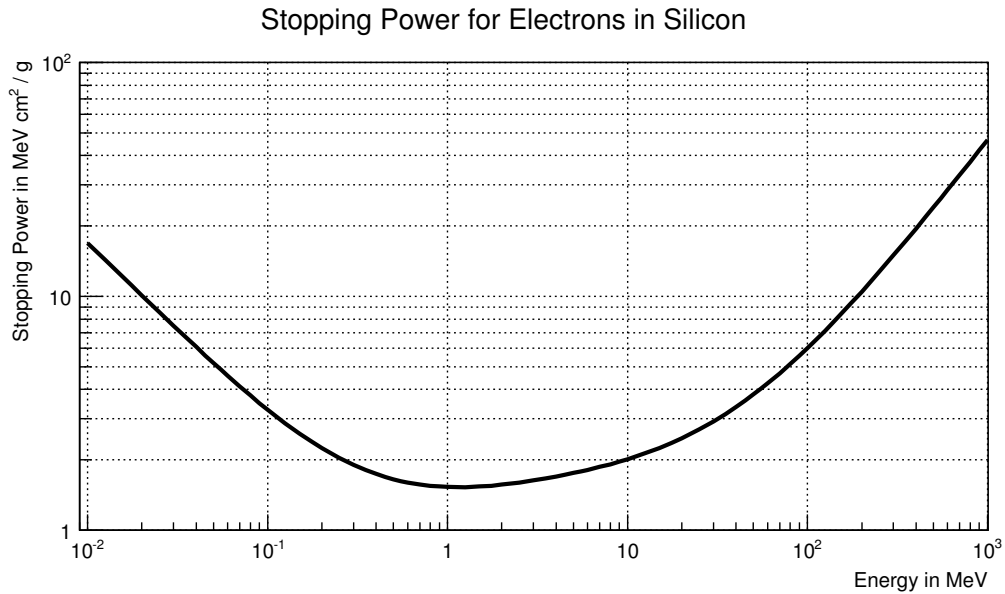
Figure 2.9: Stopping power of electrons in silicon. Plot created with data from [13].

bution has no meaningful mean or variance. The *most probable value* (MPV) is used instead.

For thin silicon sensors, the Landau-Vavilov theory however does not give correct predictions for the measured energy distributions, which are significantly wider than expected [15]. An example of this *straggling* is shown in figure 2.10 for 500 MeV pions in silicon of varying thickness.

The particle's energy that is lost in traversing a silicon sensor is mainly used to create electron-hole pairs in the sensor. In silicon, the ionisation energy of 3.6 eV is needed to produce a single electron-hole pair [122]. From figure 2.9 one can calculate a minimum energy loss of about 390 eV/μm for a MIP in silicon. This would result in 108 electron-hole pairs created per micrometre. However this number is reduced to 75 due to the Landau distribution of the deposited energy [66].

With the application of an electric field E, the created electrons and holes drift to the positive and negative electrodes, respectively. In an n-bulk sensor, the high potential is at the backplane and the low potential at the strip or pixel implants. In this case, electrons drift towards the backplane and holes are collected at the top side. In p-bulk sensors, this is the other way round: electrons are collected at the segmentations and holes drift towards the backplane. Ramo's theorem [109] states that the drift of a charge q with velocity $\vec{v}_{d_{e,h}}$ induces a current I_j at the readout electrode j of the form

$$I_j = q\vec{v}_{d_{e,h}} \cdot \vec{E}_{w_j} \, , \tag{2.29}$$
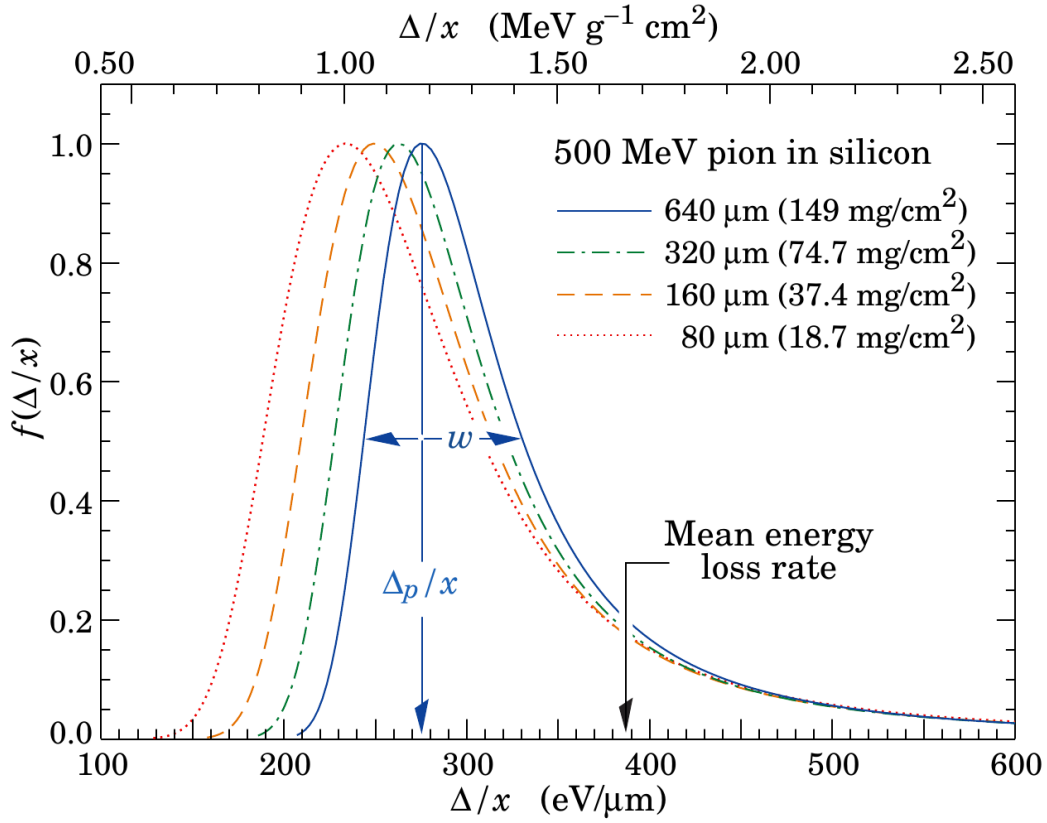
Figure 2.10: Straggling functions in silicon sensors of different thicknesses for $500\,\text{MeV}$ pions as a function of energy loss per distance. Functions are normalised to unity at the most probable value. Image from [100].

with the weighting field $\vec{E}_{w_j}$ of the electrode j. The weighting field itself is derived from the weighting potential Φ_{w_j}:

$$\vec{E}_{w_j} = -\frac{\partial \Phi_{w_j}}{\partial x}.$$ (2.30)

Φ_{w_j} is found by solving the Laplace equation $\Delta\Phi_{wj} = 0$ with unit potential at electrode j and zero potential at all other electrodes. The weighting potential differs substantially between detector electrode geometries. In the simplest case of a diode of thickness d, the weighting potential is linear, leading to a weighting field of the form $1/d$. Thus, the drift of n charge carriers induces a current of

$$I = \frac{n \cdot q \cdot v_{d_{e,h}}}{d}$$ (2.31)

in the sensor at full depletion.

2.1.2.7 *Charge Collection Efficiency*

For the actual real-world operation of a silicon sensor, the current flowing through the sensor is not the most important measurement, but rather the *collected charge*

Q. The charge Q is defined as the total current, induced by drifting charge carriers, integrated over time:

$$Q = \int_0^T I_e(t)\,dt + \int_0^T I_h(t)\,dt\,. \tag{2.32}$$

I_e and I_h are the currents induced by electrons and holes, respectively. With this definition of charge, the *charge collection efficiency* (CCE) can be defined:

$$CCE = \frac{Q}{Q_o}\,. \tag{2.33}$$

Here Q is defined as the charge collected by the sensor and $Q_o = qN_o$ as the charge deposited in the sensor by the N_0 charge carriers. Assuming a pad sensor, equation 2.32 can be expanded with equation 2.31. Following that, the integration over dt is substituted with an integration over $\frac{dx}{v_d}$, assuming the electron-hole pairs are created at x_o at zero time:

$$
\begin{aligned}
Q &= \int_0^T \frac{n_e(t) \cdot q \cdot v_{d_{e,h}}}{d}\,dt + \int_0^T -\frac{n_h(t) \cdot q \cdot v_{d_{e,h}}}{d}\,dt \\
&= \int_{x_0}^d \frac{n_e(t(x)) \cdot q}{d}\,dx + \int_{x_0}^0 -\frac{n_h(t(x)) \cdot q}{d}\,dx\,.
\end{aligned}
\tag{2.34}
$$

If $N_o = n_e(t) = n_h(t)$, then all deposited charge is collected, with CCE equalling 1. However, if the number of charge carriers decreases over time, less charge is collected than was deposited, leading to a CCE lower than 1. This can be caused by the trapping of charge carriers during their drift and is expressed by the trapping time $\tau_{e,h}$:

$$n_{e,h}(t) = n_{o_{e,h}} \cdot \exp\left(-\frac{t}{\tau_{e,h}}\right)\,. \tag{2.35}$$

Trapping is increased after introduction of defects due to radiation damage and is further discussed in section 2.3.3.3. It is worth noting that radiation damage effects can also increase the amount of charge carriers $n_e(t) = n_h(t)$ collected over the amount N_o that were generated. This effect, leading to a charge collection efficiency greater than 1 is called *charge multiplication*.

2.1.2.8 *Signal Identification and Clustering*

Charges collected at the individual channels of a silicon sensor are subject to *clustering* algorithms after being read out. These processes aim to reconstruct the trajectories of particles traversing the sensor, based on their charge deposition at each

channel. These signal charges have to be distinguished from the noise background, which depends on sensor type and readout mode.

Particles traversing the sensor can also incide at angles different from perpendicular incidence and therefore deposit charge beneath multiple segmentations, leading to signal charges on several channels. Likewise, a charge induced under one channel might diffuse to adjacent channels. Clustering algorithms are used to group charge distributions to assign them to single particle hits. In most algorithms, the channel registering the highest pulse height or exceeding a certain signal-to-noise cut is assigned as a *seed* of a cluster. Neighbouring channels can then, fulfilling certain criteria, be added to this cluster. A hit position x_{hit} can then be calculated from each cluster using a further algorithm, for example via *centre of gravity*:

$$x_{hit} = \frac{1}{Q} \sum_i q_i x_i \,.$$
(2.36)

The position x_i of each channel i in a cluster is weighted by its charge q_i. Division by the total charge of the cluster Q gives the centre of gravity position.

2.1.2.9   *The η-Distribution*

The η-distribution [12] is an important distribution to assess the performance of a sensor. η is generally defined as:

$$\eta = \frac{Q_{Left}}{Q_{Left} + Q_{Right}} \,.$$
(2.37)

The charges Q_{Left} and Q_{Right} can be defined in multiple ways and show the versatility of this distribution. For the clustered data of a segmented sensor, Q_{Left} and Q_{Right} can for example be defined as the charges measured on the channels left and right of a cluster seed. Alternatively, a particle track can be used as a basis for the calculation of η. Q_{Left} and Q_{Right} can then be defined as the charges on the channels to the left and to the right of the track impact point.

In both cases, η can give an insight to the charge distribution within the sensor. Entries around 0 or 1 stem from clusters (or tracks, etc.) where the majority of charge is collected at a single channel. Little or no charge is collected at neighbouring channels, thus the charge ratio η is very large (or very small). Entries towards the centre of the η-distribution come from charge sharing between channels. Entries below 0 or above 1 are indicative of opposite-sign noise. Generally, the distribution's mean is centred around 0.5, meaning there is no preferred side for charge collection. Shifts to either side can be caused by several effects:

- Magnetic field
  If the sensor is operated within a magnetic field, a shift in the η-distribution

can be caused by the Lorentz force, which acts on charges moving in a magnetic field. Charge carriers generated in the sensor bulk can thus also travel in a lateral direction. Since either electrons or holes are collected in a silicon sensor, the drift direction is always the same. The position of the collected charge is therefore shifted relative to, for example, the track impact point that generated the charge.

- Cross-talk
  Cross-talk effects in the sensor readout can result in charges being attributed to the wrong channels. An example of this effect occurring and how it is overcome is given in section 5.3.5.

2.1.2.10 *Sensor Resolution*

The achievable resolution from a sensor is one of its key performance figures, as it defines how precise the position of a traversing particle can be reconstructed. In a binary readout system, where no pulse height information is available, the *binary resolution* is given by:

$$\sigma^2 = \int_{-p/2}^{p/2} \frac{x^2}{p} dx = \frac{p^2}{12} \rightarrow \sigma = \frac{p}{\sqrt{12}} \, . \tag{2.38}$$

In equation 2.38 it is assumed that hits are randomly positioned between two strips (or pixels) with pitch p. The distance between measured position and true hit position then follows a Gaussian distribution with standard deviation σ^2. With pulse height information, as described previously, a hit can be positioned more precisely between strips or pixels, leading to an improved resolution.

Generally speaking, the resolution of a sensor can be measured with hits or tracks of known position $\vec{x}$. The distance to the hit position measured by the sensor $\vec{p}$ gives the residual distribution of this sensor. Assuming an even distribution of tracks or hits between sensor segmentations, this leads to a Gaussian residual distribution. The square root of the standard deviation is this sensor's resolution. If no information from the sensor in question has been used to reconstruct the hit or track position $\vec{x}$, then the distribution is said to be an *unbiased* residual distribution. If, for example, however the hit or track position has been reconstructed with information from the sensor in question, the distribution is said to be *biased*. In this case, the distribution's width no longer represents the sensor resolution.

2.2 SILICON PRODUCTION PROCESSES

While more than a quarter of the mass of the Earth's crust is made up from silicon, it is mostly found in the form of silicate minerals and silicon dioxide quartz sand. To create pure single-crystal silicon needed for a semiconductor sensor, several steps of purification and distillation are required [66]. These steps also include

melting processes, in which carbon in the form of coal or coke is introduced. At temperatures between 1500 °C and 2000 °C, carbon monoxide is formed with the oxygen in the silicon dioxide via the reactions

$$SiO_2 + 3C \rightarrow SiC + 2CO \qquad and \qquad 2SiC + SiO_2 \rightarrow 3Si + 2CO \,. \qquad (2.39)$$
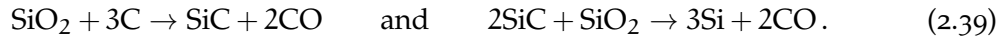
Remaining impurities are removed by addition of hydrochloric acid resulting in trichlorsilane

$$Si + 3HCl \rightarrow SiHCl_3 + H_2 \,, \qquad (2.40)$$

which is then further vaporised by hydrogen in a *chemical vapour deposition* (CVD) process at around 1000 °C:

$$SiHCl_3 + H_2 \rightarrow Si + 3HCl \,. \qquad (2.41)$$

The final pure silicon then grows on *slim rods* for several days, after which the dopant impurities can be added. Three main processes are available to purify the silicon ingots, from which the final wafers are cut.

2.2.1   *The Czochralski Process*

The Czochralski process [38] is the production method most commonly used in the semiconductor industry. High-purity silicon is melted into a quartz crucible where dopants are added to the melt. A rotating seed crystal is dipped into the melt and slowly drawn out again whilst being rotated. The silicon ingot is subsequently grown on the seed crystal. The quartz crucible accounts for a higher oxygen concentration than is obtained with other methods. The amount of O_2 can furthermore be adjusted by the rotation speed of the seed crystal. A drawback of this process is the comparatively high amount of further impurities, such as carbon and aluminium, beside oxygen in the crystal, resulting from the crucible and convection in the silicon melt. In the past, detector-grade silicon with resistivities greater 100 Ωcm could not be produced with the Czochralski process due to the high impurity content. However, this can be counteracted by application of a magnetic field during the growth process. The magnetic field not only reduces the amount of impurities, but also distributes them more homogeneously over the silicon crystal. A schematic of this *Magnetic Czochralski* (MCz) process is shown in figure 2.11a.

2.2.2   *Float Zone Silicon*

In the *Float Zone* (FZ) process [130], a polysilicon rod is suspended in vacuum or in an inert gas and contacted at the bottom with a seed crystal. With high-frequency

induction, a narrow part of the rod is melted. The melting zone is slowly moved upwards from the seed crystal, with the material at the bottom solidifying into a single crystal [87]. A schematic picture of the float zone growth process is shown in figure 2.11b. Foreign impurities, with a small solubility in silicon, move towards the top of the rod. Sufficient repetitions of the zone-melting result in very pure crystals of high resistivity. The vacuum or gaseous environment leads to a low oxygen concentration in Float Zone silicon of less than $1 \times 10^{16}\,\mathrm{cm}^{-3}$. An increase in oxygen concentration can be achieved by thermal diffusion of a thicker SiO_2 layer grown on the outside of the final wafer. The resulting material is then referred to as *Diffusion Oxygenated Float Zone* (DOFZ) silicon.

(a) The Czochralski method. Image from [66].

(b) Float Zone wafer growth. Image from [70].
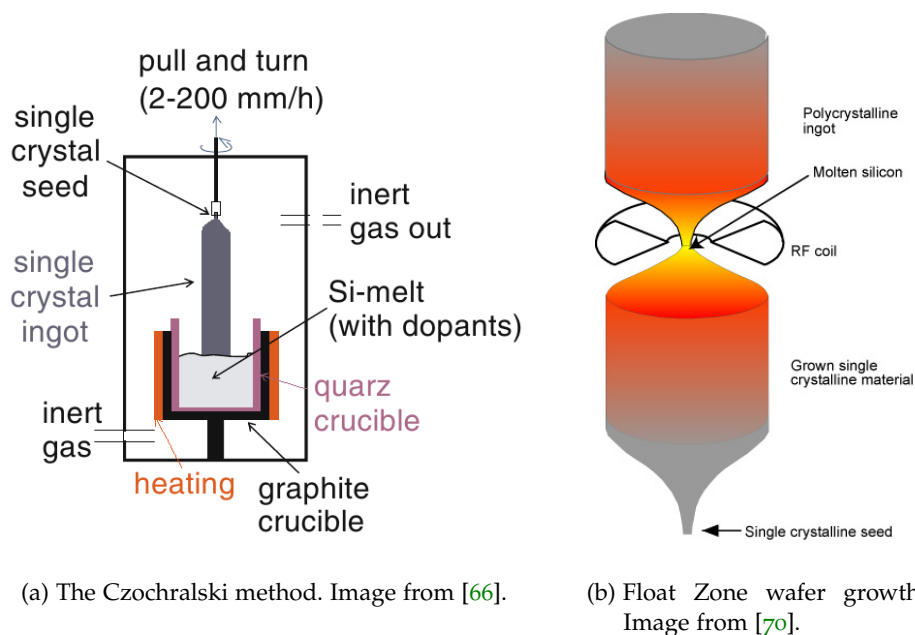
Figure 2.11: Schematics of different wafer growth techniques.

2.2.3 *Epitaxial Silicon Growth*

In the epitaxial silicon growth process, a thin layer is grown on a single-crystal substrate. In course of the growth process, the layer adopts the orientation of the substrate crystal. *Homoepitaxy* is the term used if layer and substrate are made from the same material, likewise *heteroepitaxy* is used to describe a process, in which an epitaxial layer is grown on a different substrate material. The most widely used growth method is the CVD process, in which at approximately 1200 °C, a gaseous silicon compound (here silicon tetrachloride) is decomposed by

$$SiCl_4 + 2H_2 \rightarrow Si + 4HCl, \tag{2.42}$$

with the resulting silicon growing on the crystal substrate. Doping of the epitaxial layer is achieved by adding gaseous compounds to the environment, such as

B_2H_6 or PH_3.

The epitaxial sensors used within the CMS HPK campaign (cf. section 1.4.4) are grown on an oxygen-rich Magnetic Czochralski substrate material. During the further processing, the oxygen diffuses into the epitaxial layer, resulting in a high oxygen content in the sensors. This has an effect on detector properties, which is discussed for example in [74].

2.2.4 *Further Processing*

The silicon ingot is sliced into thin discs called *wafers*. The typical wafer has a thickness of $300\,\mu m$ to $500\,\mu m$, but can be further thinned down by polishing. Smaller wafer thicknesses however have a reduced mechanical stability. A reduction of the active sensor thickness, while retaining the physical thickness, can be achieved by *deep diffusion* of the back side implant. The deep diffusion process intends to create a silicon sensor with a reduced active thickness. This is achieved by a diffusion of dopant atoms very far into the back side of the sensor at high temperatures. As the doping concentration in that part of the sensor is very high, the region can not be depleted of charge carriers and thus does not contribute to the active sensor volume. A drawback of deep diffusion is that the transition between the low-doped active sensor volume and the high doped back side is not as sharp as in conventional *wafer-bonding* and that additional defects can be introduced [74]. The deep-diffused sensors used in the HPK campaign are the first sensors used in high-energy physics which employ this technology.

In the wafer-bonding process, an implantation is performed on the sensor back side. Following that, the sensor material is bonded to a *handling wafer* with low resistivity. Due to the increased thickness, this method also improves mechanical stability.

All wafers then run through several further processing steps. In various oxidation, photolithographic, implantation and metallisation processes, the top and bottom side structures are produced. In a final step, the wafer is *diced*, that means the individual sensors are cut out of the wafer. A more detailed description can be found in [66].

2.3 RADIATION DAMAGE

In this section, the mechanisms and effects of radiation damage on silicon sensors and their performance are presented. The radiation damage stems from the extremely high particle flux the detectors are exposed to in the experiments. Generally, radiation damage effects in silicon can be categorised in two different types: bulk damage and surface damage. The former describes damages to the silicon bulk and is mainly caused by displacements of silicon atoms by charged hadrons

and neutrons. The latter is used for radiation induced damages in the silicon dioxide layer and at the Si-SiO$_2$ interface. Surface damage is primarily caused by ionising radiation.

2.3.1 *Bulk Damage*

Hadronic particles traversing the silicon bulk not only ionise it, but also interact with the atoms contained therein through the strong and electromagnetic forces [66]. These interactions can dislocate lattice atoms from their position, creating a cascade of *interstitial atoms* and *vacancies* in the silicon lattice. The initially displaced atom is referred to as the *primary knock on atom* (PKA). The interstitial atoms can recombine with a vacancy or form defects with other interstitial atoms or impurities in the sensor. The impurities originate from the sensor processing and manufacturing steps. Furthermore, not only interstitials can form defects, but also the vacancies. Defects can be categorised into two main groups depending on their size: *point defects* are small, local defects distributed throughout the silicon bulk. *Cluster defects* are spatial agglomerations of many defects. These clusters can have properties different from the individual defects they are composed of. Figure 2.12 shows a simulation of a damage cascade caused by a 1 MeV neutron. The initially displaced PKA displaces further silicon atoms and creates cluster defects along its path through the silicon.
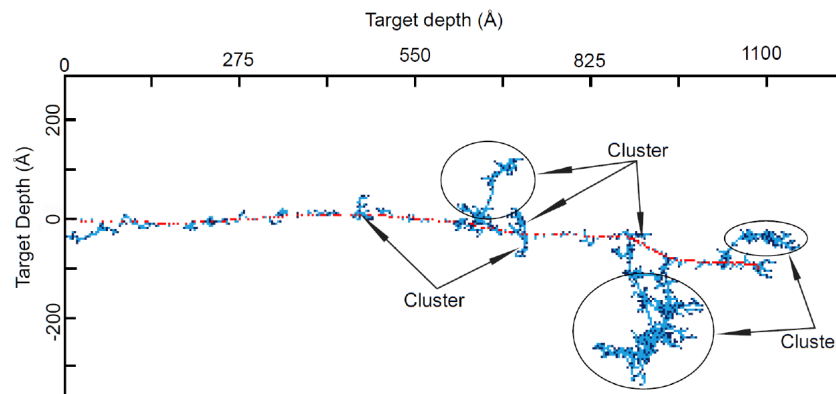
Figure 2.12: Simulation of a damage cascade created from a 1 MeV neutron. The PKA's track is shown in red, with displaced silicon atoms in blue. Image from [74].

2.3.1.1 *Defects*

The interstitial atoms (I) displaced by the PKA and the vacancies (V) created in the process can interact with other defects. In the following, a brief list of the most common defect reactions is given:

- V + I → Si
  A vacancy and an interstitial can recombine to restore the intrinsic silicon lattice structure.

- $V + V \rightarrow V_2$
  Two vacancies can be combined and form a double vacancy.

- $V_2 + V \rightarrow V_3$
  A double vacancy can then react with a further vacancy to form a triple vacancy V_3.

- $V + O \rightarrow VO$
  A vacancy can combine with an oxygen atom, forming a vacancy-oxygen complex.

- $I + I \rightarrow I_2$
  Two interstitials can be combined to form a double interstitial.

- $V + P \rightarrow VP$
  A vacancy can combine with a phosphorus atom. The phosphorus stems from the doping process.

More detailed descriptions of radiation induced defects in silicon and their properties can be found in [71] and [74].

2.3.1.2 NIEL Scaling

The *Non Ionising Energy Loss* (NIEL) scale describes the rate of energy lost by a particle traversing a material due to atomic displacements. The amount of defects created in the silicon bulk are assumed to scale linearly with the energy loss. The fraction of recoil energy deposited as displacements can be calculated by the *Lindhard partition function* $P(E_R)$, which leads to the damage function $D(E)$ [94]:

$$D(E) = \sum_{\nu} \sigma_{\nu}(E) \int_{E_d}^{E_R^{max}} f_{\nu}(E, E_R) P(E_R) dE_R ,\tag{2.43}$$

with the cross section σ_{ν} and probability $f_{\nu}(E, E_R)$ of a possible reaction ν. The probability depends on the incident particle's energy E and its recoil energy E_R. E_d and E_R^{max} are the threshold energy for displacements and the maximum recoil energy, respectively. The former amounts to $42\,eV$, the latter can be expressed as $4E m_p m_i / (m_p + m_i)^2$ with the particle mass m_p and the recoil atom mass m_i [4]. According to [71], values for $P(E_R)$ are for example $P \approx 50\,\%$ for $10\,MeV$ protons, $P \approx 42\,\%$ for $24\,GeV$ protons and $P \approx 43\,\%$ for $1\,MeV$ neutrons. With the damage function $D(E)$, which is shown for several particles and energies in figure 2.13, the hardness factor κ can be calculated, which relates the radiation damage of a particle with energy spectrum $\phi(E)$ to the damage created by $1\,MeV$ neutrons:

$$\kappa = \frac{\int D(E) \phi(E) dE}{D(E_n) \int \phi(E) dE} .\tag{2.44}$$
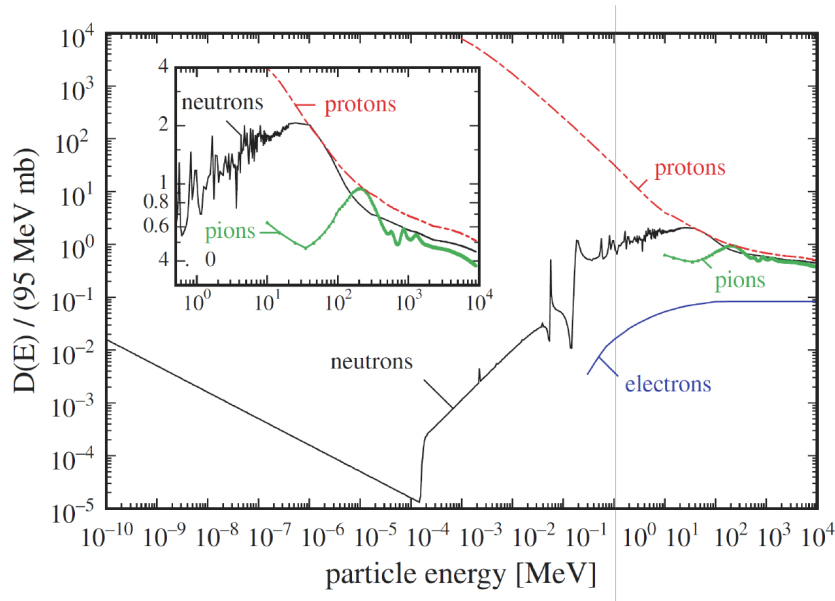
Figure 2.13: Damage functions $D(E)$ for different particles and energies, normalised to 1 MeV neutrons. The insert shows a zoomed excerpt of the spectrum towards higher energies. Image from [94].

The damage function for 1 MeV neutrons is $D(E_n) = 95\,\mathrm{MeV\,mb}$ [94]. Irradiation fluences Φ can thus be expressed as a 1 MeV neutron equivalent fluence Φ_{eq}:

$$\Phi_{eq}\left[n_{eq}/cm^2\right] = \kappa \cdot \Phi = \kappa \cdot \int \phi(E)\,dE\,. \qquad (2.45)$$

Violations to the NIEL scale have however been observed for certain macroscopic damages (cf. [71] and [53]). Furthermore, the scaling for example does not differentiate between point and cluster defects, but only accounts for the total displacement energy.

2.3.2 Surface Damage

Surface damage is primarily introduced by ionisation of the isolating silicon dioxide layer by traversing particles. Damages to additional layers, such as silicon nitride (Si_3N_4), are also counted as surface damage. Charge carriers generated by ionisation in the silicon bulk are generally collected by the backplane and segmentation electrodes. Carriers in the oxide layers however can not necessarily escape the region and can cause radiation damage in the oxide and in the interface between isolator and silicon bulk. Several effects are attributable to surface damage [138]:

- *Oxide trapped charges*
  Existing processing defects or new defects created by radiation damage in

the oxide can capture the charge carriers generated by ionisation. The later emission of the charge carriers however is suppressed due to the large band gap in SiO_2 of $E_g = 8.8\,eV$ [135]. The carriers thus act as positive or negative charges trapped within the oxide.

- *Fixed oxide charges*
  In the vicinity of the silicon - silicon dioxide interface, the atoms are highly disordered. Deep defects towards the band gap centre trap holes, forming fixed charges at the interface. A material dependent saturation occurs at a charge concentration of approximately $Q_f \sim 3 \times 10^{12}\,cm^{-2}$, as can be seen in figure 2.14.

- *Interface traps*
  Dangling silicon bonds at the $Si - SiO_2$ interface create energy levels in the silicon band gap [139]. These levels are near the centre of the band gap and are a major contributor to the surface generation current.
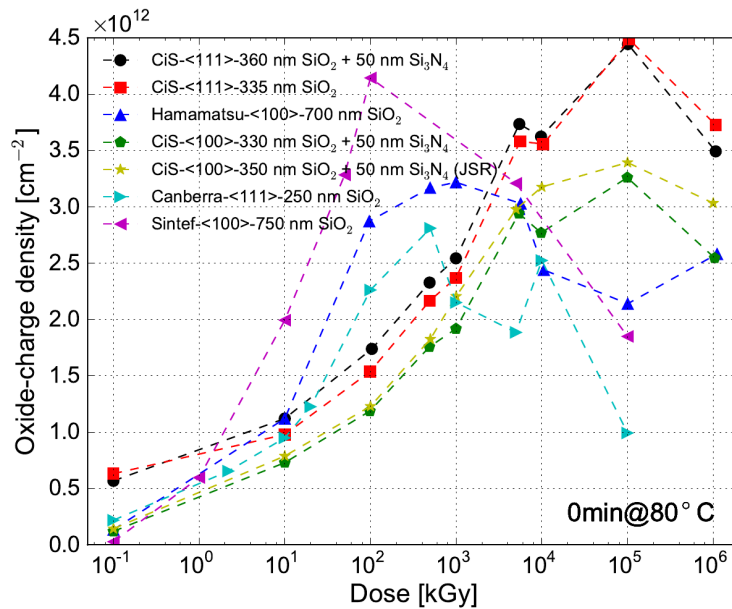
Figure 2.14: Dose dependence of the fixed oxide charge concentration for several materials. Image from [138].

The above effects can have great influence on the properties of segmented silicon sensors by increasing the depletion voltage and leakage current and may cause charge losses at the interface. They also greatly influence a sensor's interstrip capacitance, as is shown in chapter 4.

2.3.3 *Effect of Radiation Damage on Sensor Properties*

The aforementioned bulk and surface defects create additional states in the silicon band gap. These states have three main effects on the performance of a silicon sensor. Defects can increase the leakage current, they can change the space

charge distribution, influencing the depletion voltage of a sensor, and they can trap charges, which in turn changes the charge collection efficiency. An overview is given in figure 2.15. The impact of an individual defect depends on the band gap level it creates. States towards the centre of the band gap tend to generate leakage current. Acceptor and donor states towards either conduction or valence band can be ionised easily. This generates space charge and has an effect on the effective doping concentration. Energy states between band gap centre and either band gap edge can generate both current and space charge, as well as trap charges. Combinations of all three effects are also possible and are pronounced in cluster defects. Furthermore, annealing effects, which are discussed in 2.3.3.4, also have an influence on macroscopic sensor properties.
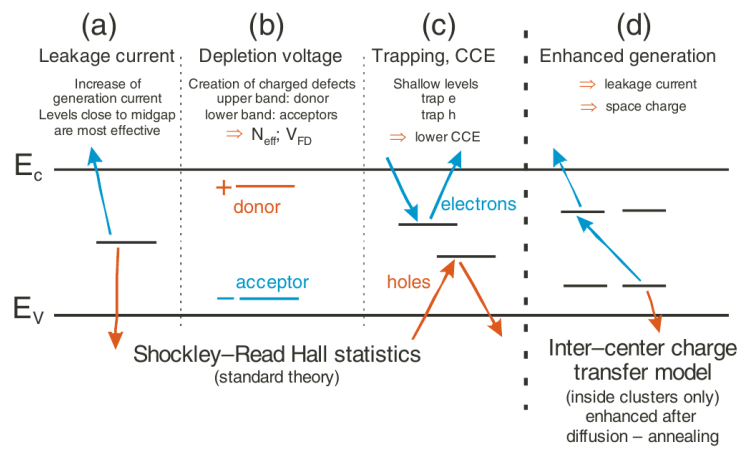
Figure 2.15: Defects in the silicon band gap and their effects. Image from [66].

2.3.3.1 Leakage Current

Defects located towards the centre of the band gap tend to generate leakage current. The leakage current of a sensor is generally measured at the depletion voltage or slightly above it. The leakage current greatly increases with fluence and can be parametrised, according to Moll [94] by:

$$\frac{\Delta I}{\text{Volume}} = \alpha \cdot \Phi_{eq}.$$

(2.46)

ΔI is the increase in leakage current measured after irradiation of a sensor with the equivalent fluence Φ_{eq}, compared with the current prior to irradiation. The current is scaled to the sensor volume and to a certain temperature. As can be seen in figure 2.16, the increase in current is proportional to the equivalent fluence, which is reflected in the scaling factor α. For currents scaled to $20\,°\text{C}$ and after an annealing time of $80\,\text{min}$ at $60\,°\text{C}$, α equals $(3.99 \pm 0.03) \times 10^{-17}$ A/cm [94].
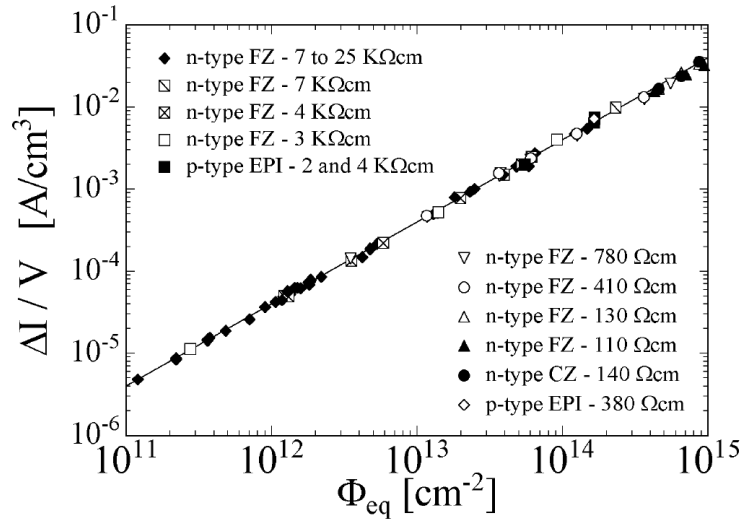
Figure 2.16: Scaling of current with fluence. Image from [94].

2.3.3.2   *Depletion Voltage*

A change in space charge is caused by defects located towards the centre of the band gap. As stated earlier, the space charge in a sensor defines the effective doping concentration and thus the depletion voltage of the device. Prior to irradiation, the effective doping concentration N_{eff} is given by the amount of donors and acceptors in the silicon bulk:

$$N_{eff} = N_D - N_A .$$ (2.47)

The depletion voltage V_{depl} is proportional to the absolute value of N_{eff}, as described in equation 2.9. Defects created by irradiation resulting in donor states increase the effective doping concentration and thus the depletion voltage. Acceptor states on the other hand decrease N_{eff}. In p-bulk material, N_{eff} is initially less than zero, so an increase in acceptors only increases the depletion voltage. N-bulk material, however has an N_{eff} value larger than zero. An increase in acceptor states therefore decreases V_{depl}, until at a certain fluence, enough acceptors have been created to cancel out the initial donor concentration. More acceptors therefore decrease N_{eff} below zero, increasing V_{depl} again. At this point, the n-bulk sensor behaves as p-bulk material and is said to be *type inverted*. Figure 2.17 illustrates this effect.

2.3.3.3   *Charge Collection Efficiency*

A critical aspect of radiation damage is the trapping of charge carriers and thus, the reduction of the charge collection efficiency (CCE). While a radiation induced rise in depletion voltage and leakage current can, to some extent, be compensated by applying higher bias voltage and reducing operation temperature, a reduction in CCE can not be counteracted directly. As detailed in section 2.1.2.7, the charge collection efficiency is one of the most important properties of a silicon sensor. A
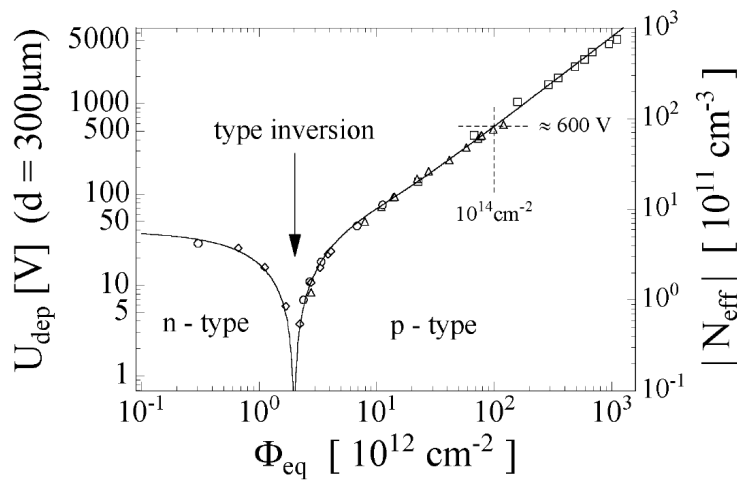
Figure 2.17: Type inversion in n-bulk silicon and increase of depletion voltage. Image from [94].

reduction of the CCE can be attributed to an increased trapping of charge carriers and an increase in trapping time. Since these effects reduce the distance charge carriers can travel before being trapped, utilising thinner sensors can mitigate the effect to some extent. No explicit defect responsible for trapping has been identified yet, although some candidates exist [74].

2.3.3.4 *Annealing*

Radiation induced defects in silicon sensors are not static, but evolve in a continuous process called *annealing*. Three basic processes have been identified [94]:

- *Dissociation*
  Defects of two components or more can dissociate into their individual constituents. This is possible if the binding energy of the complex is smaller than the energy of the absorbed phonon[3]. The new fragments can then build new defects, recombine or migrate through the lattice.

- *Migration*
  The mobility of a defect is dependent on the temperature. Assuming sufficient mobility, defects can become mobile and migrate through the lattice.

- *Complex formation*
  Mobile defects can interact with other defects or impurities. They can recombine or form new defect complexes.

These annealing processes are highly temperature dependent. This is especially important for detector usage scenarios where low-temperature operation periods are interrupted by maintenance and repair phases, which are carried out at room

---

3 *Phonons* are quanta of lattice vibrations [127].

temperature. It has been found that annealing influences both sensor leakage current and effective doping concentration, and thus the depletion voltage [94]. Annealing effects on charge collection efficiency have also been observed [47].

The leakage current has been measured to decrease with an increase of annealing time. The parameter α in equation 2.46 is described by Moll in [94] by the expression

$$\alpha(t) = \alpha_1 \exp\left(-\frac{t}{\tau_1}\right) + \alpha_0 - \beta \ln\left(\frac{t}{t_0}\right) \tag{2.48}$$

and allows to relate the leakage current, fluence and annealing. The parameters α_1, τ_1, α_0, β and t_0 have been fitted for several scenarios of annealing time and temperature. This is shown in figure 2.18.
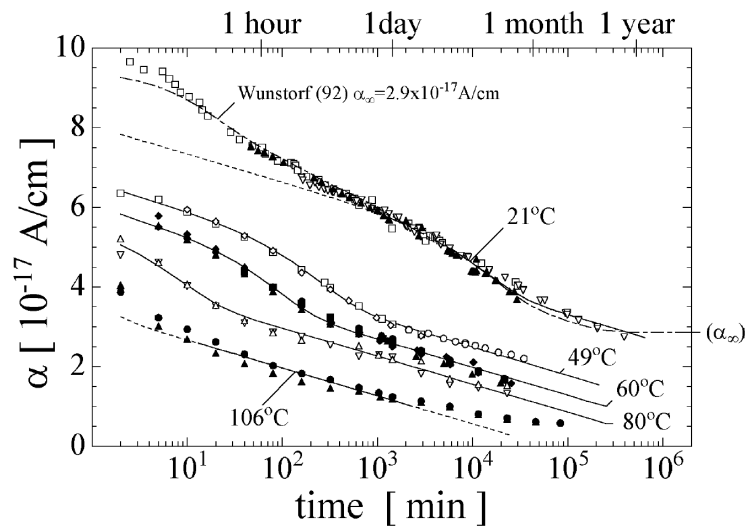
Figure 2.18: Annealing of the leakage current damage rate α for different annealing times and temperatures. Image from [94].

The annealing behaviour of the effective doping concentration N_{eff} and thus the depletion voltage is described by the *Hamburg Model*. Figure 2.19 shows the change of N_{eff} for an n-bulk diode after several annealing steps at 60 °C. N_{eff} decreases towards a minimum and then rises again beyond its initial value. The former step is called *beneficial annealing*, the latter *reverse annealing*.

This behaviour is described by three summable terms, the first of which denotes the *constant damage* [94]:

$$N_C = N_{C,0} \cdot \left(1 - \exp\left(-c\Phi_{eq}\right)\right) + g_c \Phi_{eq}. \tag{2.49}$$

The beneficial annealing is described by

$$N_A(\Phi, T, t) = \Phi_{eq} g_a \exp\left(-\frac{t}{\tau_a(T)}\right), \tag{2.50}$$
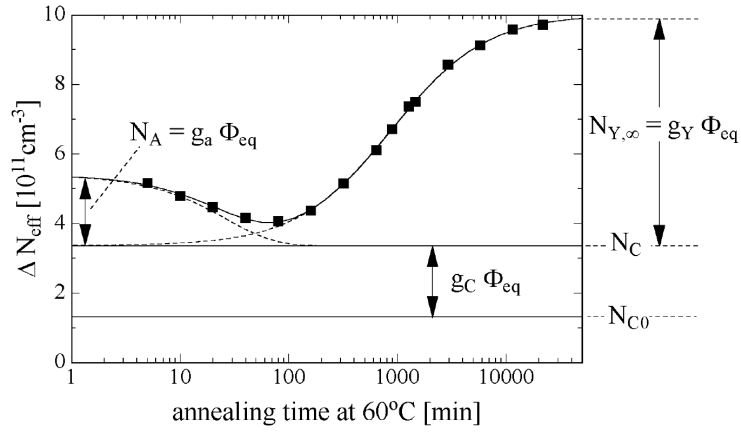
Figure 2.19: Annealing of the effective doping concentration. Image from [94].

the reverse annealing by

$$N_Y\left(\Phi, T, t\right) = \Phi_{eq} g_y \cdot \left(1 - \exp\left(\frac{-t}{\tau_y\left(T\right)}\right)\right) . \tag{2.51}$$

The total change ΔN_{eff} of the effective doping concentration N_{eff} can thus be written as:

$$\Delta N_{eff}\left(\Phi, T, t\right) = N_C + N_A\left(\Phi, T, t\right) + N_Y\left(\Phi, T, t\right) , \tag{2.52}$$

with parameters $\tau_a\left(T\right)$ and $\tau_y\left(T\right)$ to describe the short-term and reverse annealing, respectively. The constants g_c, g_a and g_y have been determined for a range of materials, together with the *removable donor concentration* $N_{C,0}$ [94].

EXPERIMENTAL METHODS AND TECHNIQUES

In this chapter, the experimental methods used within this thesis are described and discussed. The TCAD simulation framework used in chapter 4 is presented first, followed by the DESY-II test beam facility, in which the measurements from chapter 5 were performed. The latter made use of special pixel beam telescopes. They are also introduced in this chapter, together with their readout software. Following that, an assessment of the telescopes' performance is given, followed by an introduction to the ALiBaVa system, which has been used as a DAQ system for the sensors measured in chapter 5. The last part of this chapter describes the facilities used for sensor irradiations.

3.1 TCAD SIMULATIONS

Technology computer-aided design (TCAD) simulations are a highly versatile tool used in the development and in the analysis of semiconducting sensors. Numerous software packages are available and offer a wide range of common features. Within this thesis, the *Synopsys Sentaurus* package has been used [125]. Another important software suite is *Silvaco ATLAS* [118], which is used, among others, by collaborators within the CMS experiment. Both packages follow the standard *finite element analysis* (FEA) scheme of first creating a mesh-like grid structure followed by solving equations at each of these mesh points to then subsequently calculate the desired physical properties. In the following, the basic simulation steps are described.

3.1.1 *Structure Generation*

A simulation process starts off with the creation of a two- or three-dimensional structure that is to be simulated. The used materials are specified and placed, and material properties are defined. Properties are for example the amount of doping in silicon with a certain dopant. An alternative approach is to simulate the actual sensor fabrication and processing steps, that is the diffusion, implantation, etching, etc. The created structure is now meshed into a lattice. An example is shown in figure 3.1. A different mesh coarseness can be defined by the user for different areas or materials, as can be the used meshing techniques.

Within the meshing process, a compromise regarding the mesh size has to be reached. A finer mesh yields a greater solution accuracy, a more coarse mesh helps in numerical efficiency and reduces simulation time. The latter aspect is especially
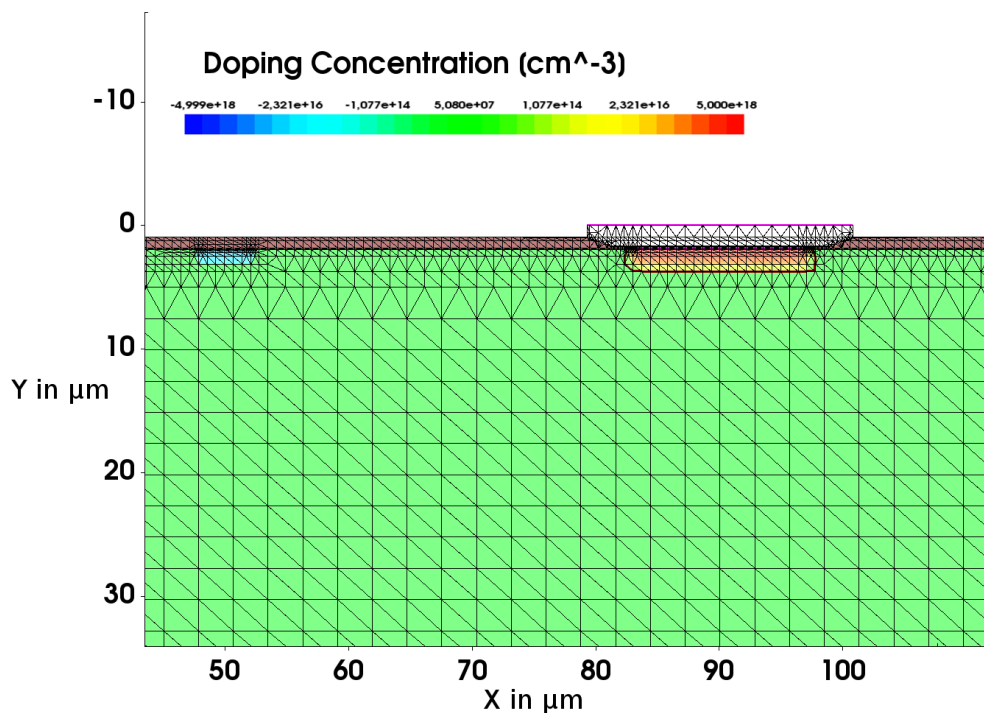
Figure 3.1: Example of an automatically generated mesh structure. The picture shows a zoomed view onto a strip of a p-bulk sensor. Below the colourless aluminium strip, the phosphorous strip implant is placed, with doping levels depicted in red and yellow. On the left, a boron p-stop implant can be seen in blue. The silicon dioxide at the sensor surface is brown. The meshing is homogeneous in the sensor bulk, with the mesh spacing growing tighter towards the top. The mesh size is especially small around the implants and at the Si-SiO$_2$ interface.

critical for three-dimensional simulations.

3.1.2 *Device Simulation*

After the meshing process is complete, the actual device simulation can commence. Environment variables, such as temperature, are set and the desired physical models are activated. These models for example allow the parametrisation of the charge carrier mobility, avalanche effects, or the saturation of the electric field. Readout electronics can be included in the simulation with a SPICE[1] model, allowing for comparison with different experimental measurements. Laser illuminations and traversing particles can also be added. Three major simulation modes can be selected. These are:

- Voltage ramping
  The voltage applied to an electrical contact is ramped up (or down) with

---

1 Simulation Program with Integrated Circuit Emphasis.

given start and end values. The used step sizes can also be specified. This simulation mode generally represents the IV-measurement of a sensor in a laboratory setup.

- Capacitive calculation
  In this simulation mode, a small-signal AC analysis is performed. Small sinusoidal signals are superimposed upon the DC bias voltage. From the device response, capacitances can be extracted.

- Time-dependent simulation
  Here a transient simulation is performed to assess the response of a device to traversing particles or laser illuminations at definable times. From a calculated state of equilibrium, the time is increased and the device equations are recomputed. This is done iteratively until a specified end time is reached.

With the simulation mode(s) selected, the simulator then calculates Poisson's equation

$$\frac{d^2 V(x)}{dx^2} = -\frac{\rho(x)}{\epsilon_r \epsilon_0} \, , \tag{3.1}$$

with the charge density $\rho(x)$ and permittivity $\epsilon_r \epsilon_0$ for each previously generated mesh point x. The carrier continuity equations

$$\nabla \cdot \vec{J}_n = q \cdot (R_{eff} + \frac{\partial n}{\partial t}) \tag{3.2}$$

for electrons, and

$$-\nabla \cdot \vec{J}_p = q \cdot (R_{eff} + \frac{\partial p}{\partial t}) \tag{3.3}$$

for holes are also calculated, with the current densities $\vec{J}_n$ and $\vec{J}_p$ for electrons and holes respectively. The electron and hole densities are denoted with n and p respectively, the effective recombination rate with R_{eff}. The iterative procedure used to solve these equations starts with an initial guess of the solution. Iterations continue until the corrections are small enough to satisfy predefined convergence criteria, or until a given number of iterations have been performed. From equations 3.1, 3.2 and 3.3, the user-specified physical quantities, such as electric fields, potentials, capacitances or carrier densities are then derived.

3.1.3 *Simulation Analysis*

Synopsys Sentaurus includes a variety of tools to analyse simulated data. Plot files can be created by the simulation at times and points selected by the user. These files contain the values of all specified physical properties at each mesh point. Figures 3.2 and 3.3 show an example. An n-bulk silicon sensor with five strips

has been simulated, with the sensor's charge carrier densities displayed over time. A MIP-like particle then traverses the sensor from the top right to the bottom left, creating electron-hole pairs. The electrons drift towards the upper backplane, whereas the holes are collected at the bottom strips. Due to the unequal mobility, the electrons are collected much faster.
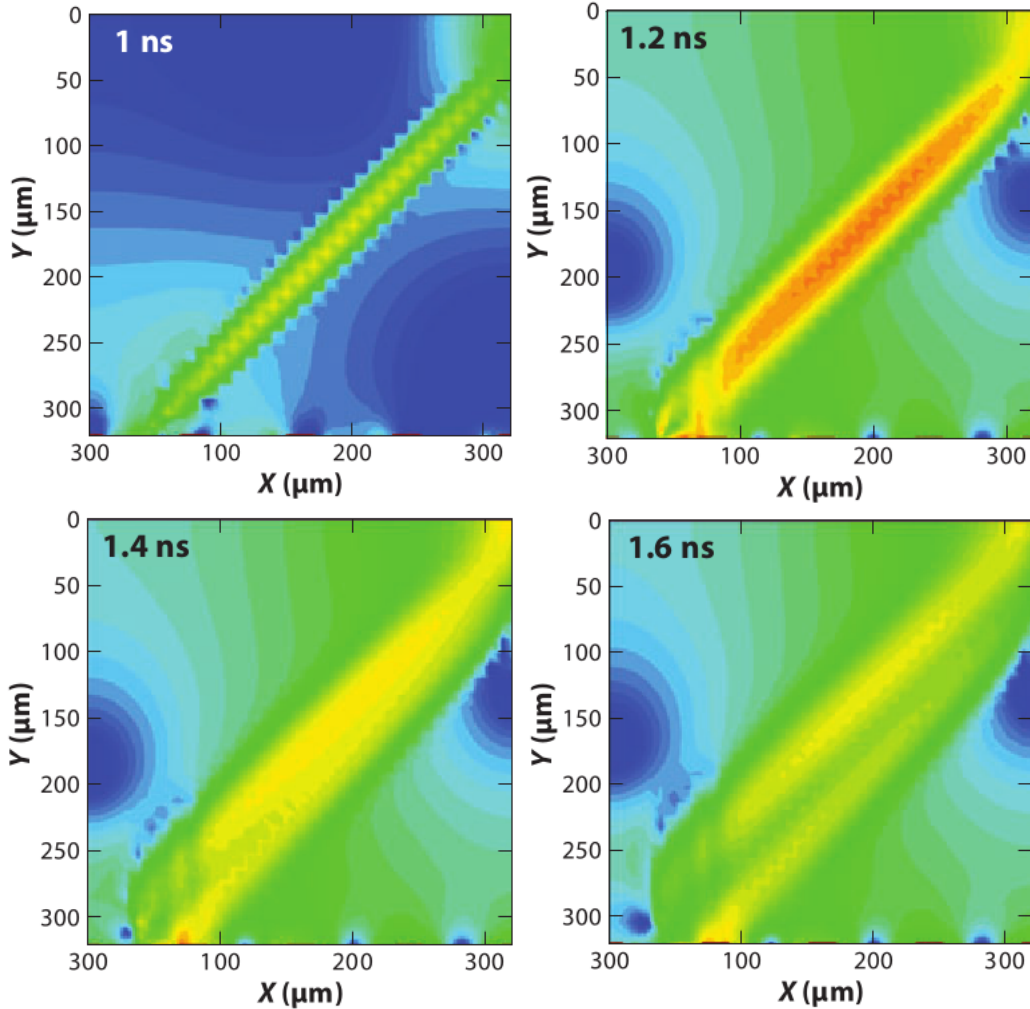
Figure 3.2: An example TCAD simulation [48], part 1. A MIP-like particle traverses the strip sensor from top right to bottom left. The particle creates electron-hole pairs along its path. The charge densities are depicted for various points in time between 1.0 ns and 1.6 ns. A high density of charge carriers is shown in red, a low concentration in blue.

Besides visualisations of properties over the mesh points, plots of electrical quantities at certain nodes can be created. For the same example, the collected charge at each strip is shown in figure 3.4. Furthermore, the electric field configurations both over the sensor volume and through the sensor bulk are depicted, followed by the extracted mobilities for both charge carriers.

From this, an immediate advantage of TCAD simulations can be seen — a multitude of physical properties can easily be accessed and quantified at any point
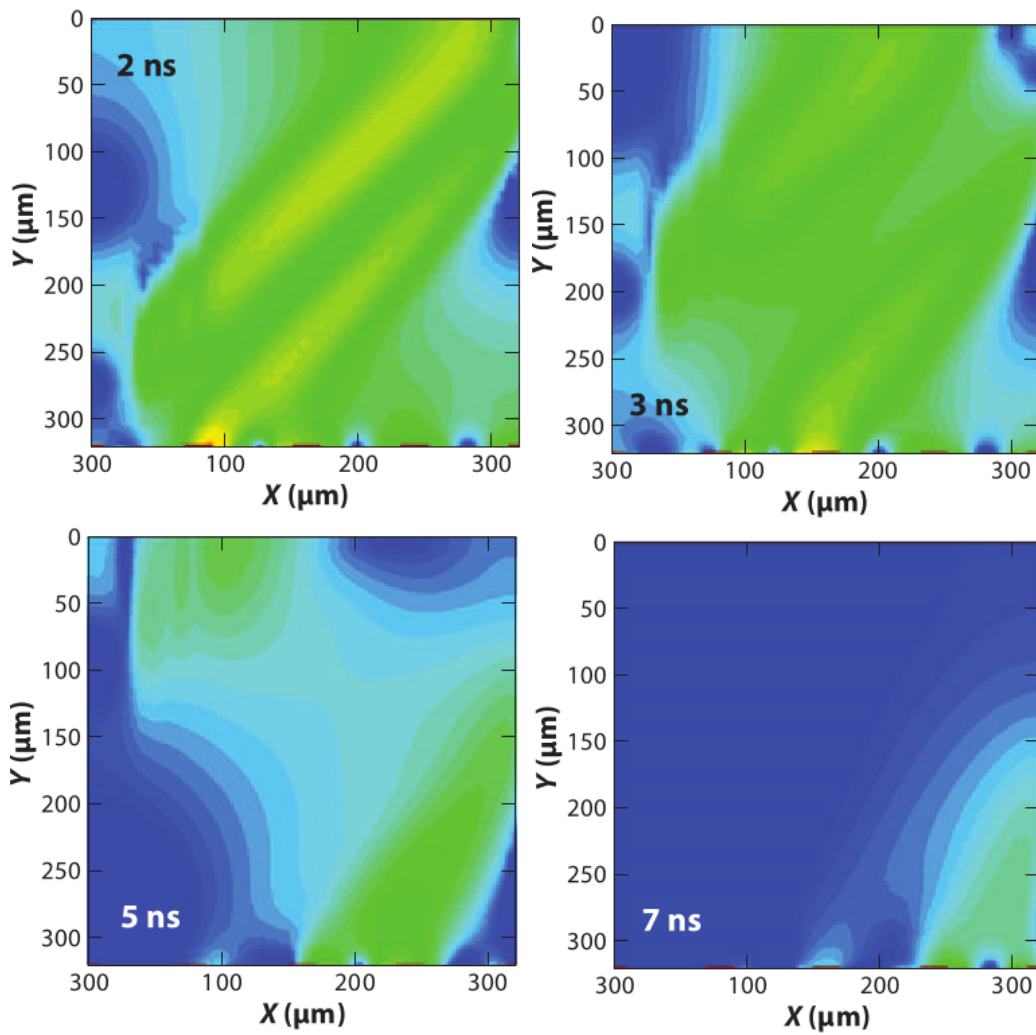
Figure 3.3: An example TCAD simulation [48], part 2. A MIP-like particle traverses the strip sensor from top right to bottom left. The particle creates electron-hole pairs along its path. The charge densities are depicted for various points in time between 2 ns and 7 ns.
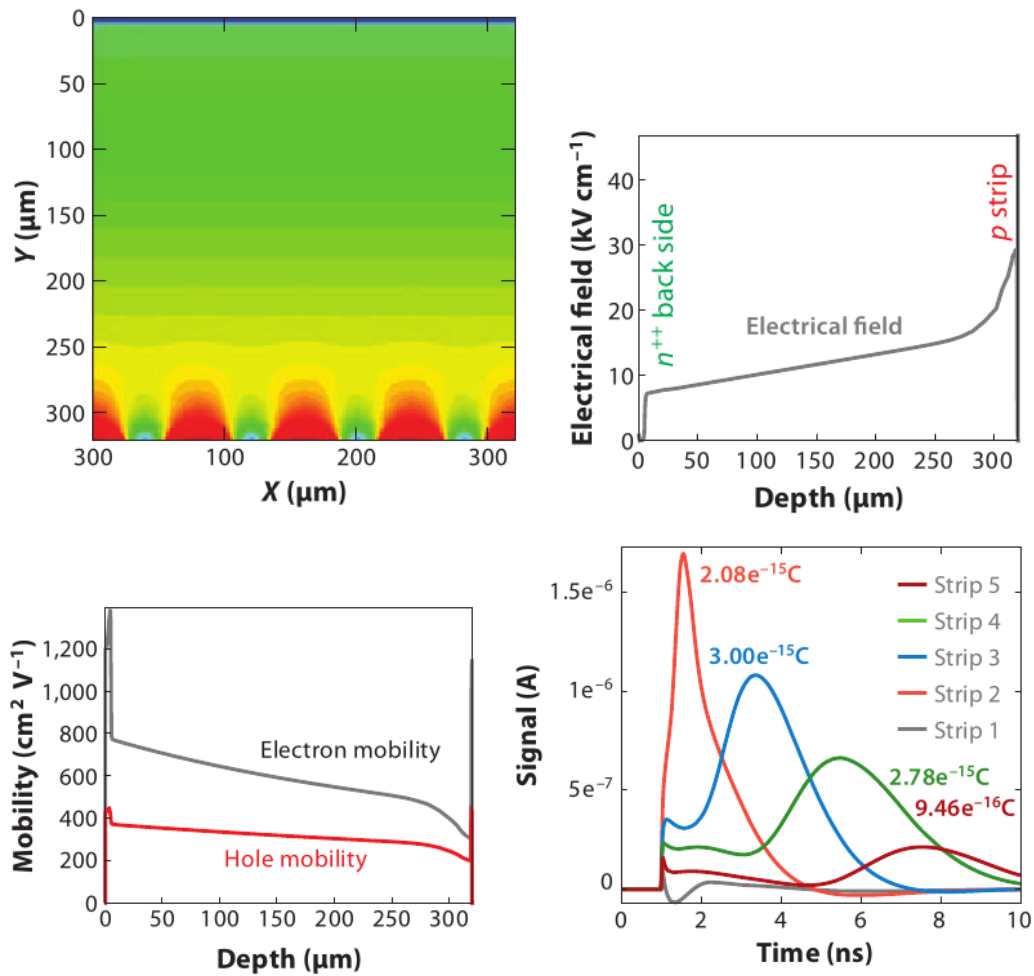
Figure 3.4: Top row: Corresponding electric field over the sensor volume (left) and through the sensor bulk between backplane and strip (right). Bottom row: The carrier mobility (left) for electrons and holes, respectively. Right: the collected signals at the strips over time [48].

within a sensor. This is not necessarily the case for laboratory measurements.

3.2 THE DESY-II TEST BEAM

The DESY-II test beam facility at DESY in Hamburg delivers positron or electron test beams to three beam lines in four areas. Test beams are sometimes referred to as the *gold standard* of particle physics detector development, as they offer several advantages in the testing of detectors, compared to other experimental methods, such as radioactive sources or cosmic particles. Some of these advantages are:

- Fixed particle energy and type
  In a test beam, the beam composition is known to the user. The DESY-II test beam uses electrons and positrons. Other examples are protons and pi-

ons at the CERN test beams or pions at PSI². The particle momentum is also known within limits and can be changed by the user. If the particle's momentum is known, then the exact amount of energy deposited by each particle in a detector can be calculated. This is a large advantage compared to measurements with radioactive sources.

- Triggering and timing
  Test beams can pass through triggering and timing setups before entering a detector, so that detectors can be tested with their own *data acquisition* (DAQ) systems. Especially for larger and complex systems, this is a major advantage. Furthermore, combinations of several detector systems can be tested in a single test beam setup.

- Particle rate
  The particle rates obtainable in test beams are considerably higher than those of, for example, cosmic rays. In some cases this also allows testing of the intended experimental design rates.

Evaluating a detector's performance in a test beam can be considered the final test for the detector, as it is the measurement setup closest to the real experiment.

Beam Generation and Properties

The DESY-II synchrotron is mainly used as a pre-accelerator for the PETRA-III ring at DESY. Its circumference is 292.8 m and it itself is fed by the LINAC-II linear accelerator and the PIA storage ring. Injection from LINAC-II is possible every 80 ms with a particle momentum of 450 MeV/c. The particle beam is accelerated and decelerated in a sinusoidal mode with a frequency of one fourth of the 50 Hz power grid frequency, about 12.5 Hz. The revolution frequency is 1 MHz [41].

Typical PETRA-III operations require a top-up from DESY-II every 60 to 120 s. This injection takes 12 s, after which DESY-II may have to be refilled again. Until the next injection into PETRA-III, the DESY-II beam can be used for test beam generation [10].

A bremsstrahlung beam is generated by insertion of a carbon fibre into the electron/positron beam of the DESY-II synchrotron. A metal converter target converts the resulting bremsstrahlung photons into electron/positron pairs. A dipole magnet spreads the beam and allows a momentum selection between 1 and 6 GeV/c. Two collimators, before and after the beam shutter, enable changes to the final beam size. The deliverable rate to user experiments is in the order of several kilohertz, depending on momentum selection. A schematic drawing of the beam generation can be seen in figure 3.5.

---

2 Paul Scherrer Institut, Villigen, Switzerland.
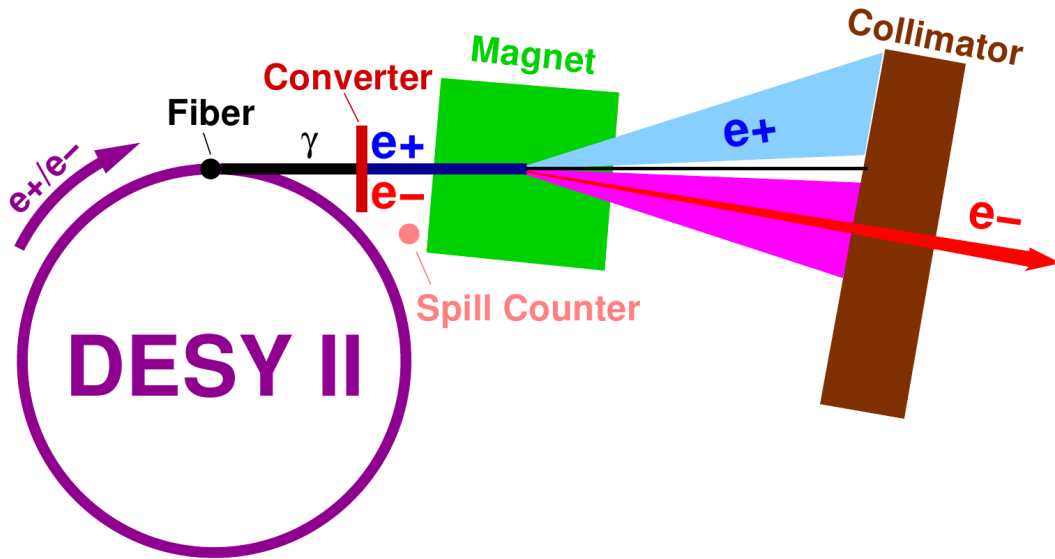
Figure 3.5: Schematics of the DESY-II test beam generation [41].

3.3 PIXEL BEAM TELESCOPES

So-called *pixel beam telescopes* are some of the most used instruments in a test beam environment, especially for detector development and research. A beam telescope allows a precise reconstruction and tracking of the particles generated by a test beam. With this information it is then possible to assess the properties of a *device under test* (DUT) with the tracking information obtained from the beam telescope. The timing and spatial information of the particle tracks traversing the DUT, gained from the telescope, can be checked against the data delivered from the DUT.

Beam telescopes utilise several sensor planes to measure the particle tracks. In most cases, the sensor technology is based on semiconducting silicon sensors. Telescopes exist both with strip sensor planes as well as with pixel sensor planes. Examples using the former technology are the ZEUS MVD telescope [8] or the CMS SiBT telescope [51]. Pixel beam telescope examples are the Timepix telescope [3] and the DATURA telescope, which is explained in detail in 3.3.1. The obvious disadvantage in using strip sensors is the lack of two sensitive sensor coordinates in each plane.

The figure of merit for a beam telescope is its resolution — both in time and in space — as this defines the precision with which each particle trajectory can be measured. The timing resolution is largely dependent on the readout speed of the used sensors, their buffer sizes and the data acquisition system. Spatial resolution depends on the individual intrinsic sensor resolution, the number of telescope measurements in each reconstructed track and their position, as well as the multiple scattering of the beam particles. The expression

$$\sigma_{meas}^2 = \sigma_{DUT}^2 + \sigma_{Tel}^2 + \sigma_{MS}^2 \tag{3.4}$$

shows the contributing terms that have to be considered for the overall resolution [18]. The measured residual width on a DUT sensor plane is expressed by σ_{meas}, σ_{DUT} is the actual achievable resolution on the DUT plane, σ_{Tel} is the resolution of the telescope and σ_{MS} represents the contribution from multiple scattering. In the following, all terms are discussed.

The resolution of a telescope σ_{Tel} can be expressed by

$$\sigma_{\text{Tel}}^2 = k \cdot \sigma_{\text{Intrinsic}}^2 \, , \tag{3.5}$$

with the geometric scaling factor k defined as

$$k = \frac{\sum_i^N z_i^2}{N \cdot \sum_i^N z_i^2 - \left(\sum_i^N z_i\right)^2} \, , \tag{3.6}$$

assuming all N telescope planes have the same intrinsic resolution $\sigma_{\text{Intrinsic}}$ [18]. The distance of the i-th telescope plane to the DUT positioned at $z = 0$ is then z_i.

Multiple scattering is the term used to describe the deflection of a charged particle traversing any medium. It depends on the particle energy, particle type and the radiation length of the matter traversed [68]. The angular scattering distributions are centred around 0, their width can be expressed by

$$\Delta\theta_0 = \frac{13.6\,\text{MeV}}{\beta cp} \cdot z\sqrt{x/X_0} \cdot \left(1 + 0.038\ln\left(x/X_0\right)\right) \tag{3.7}$$

according to [100], with the particle velocity βc, momentum p and charge number z. The expression x/X_0 defines the thickness of the scattering medium in radiation lengths, with values of $X_0 = 21.82\,\text{g/cm}^2$ for silicon and $X_0 = 36.62\,\text{g/cm}^2$ for dry air, according to [133].

Equation 3.7 shows that the angular distortion due to multiple scattering increases with the material budget and the inverse energy. Therefore, at low-energy beams, such as the 6 GeV DESY-II test beam, it is advantageous to have very thin telescope sensors. As the beam particles also interact with the atoms in the air, a contribution to the amount of multiple scattering depending on the distance between sensor planes has to be considered. At high-energy hadron beams, which for example are available at the SPS facility at CERN, the contribution from multiple scattering can be neglected.

3.3.1 *The DATURA Telescope*

The *DATURA* telescope (DESY Advanced Telescope Using Readout Acceleration) is a copy of the original EUDET telescope [116] permanently installed in the DESY-II test beam area 21. It provides a flexible and portable infrastructure with two

telescope lever arms, equipped with three sensors each, mounted on rails. The sensors are mounted in aluminium jigs to provide mechanical protection and an exact positioning. The jigs have a coolant in- and outlet to provide water cooling to the sensors. A Huber cooling device controls the sensor temperature. During operations it is set to 14 °C, to ensure stable conditions.

The position of each sensor along the beam axis can be changed to create different geometries, the smallest spacing between sensors being 20 mm, the largest 150 mm. Between the front three upstream planes and the back three downstream planes, a DUT of up to 50 cm size along the beam axis can be positioned. A 3D movable stage can be used to change the DUT position relative to the telescope with micrometre precision. A picture of the DATURA telescope installed in the DESY-II test beam area 21 is depicted in figure 3.6.
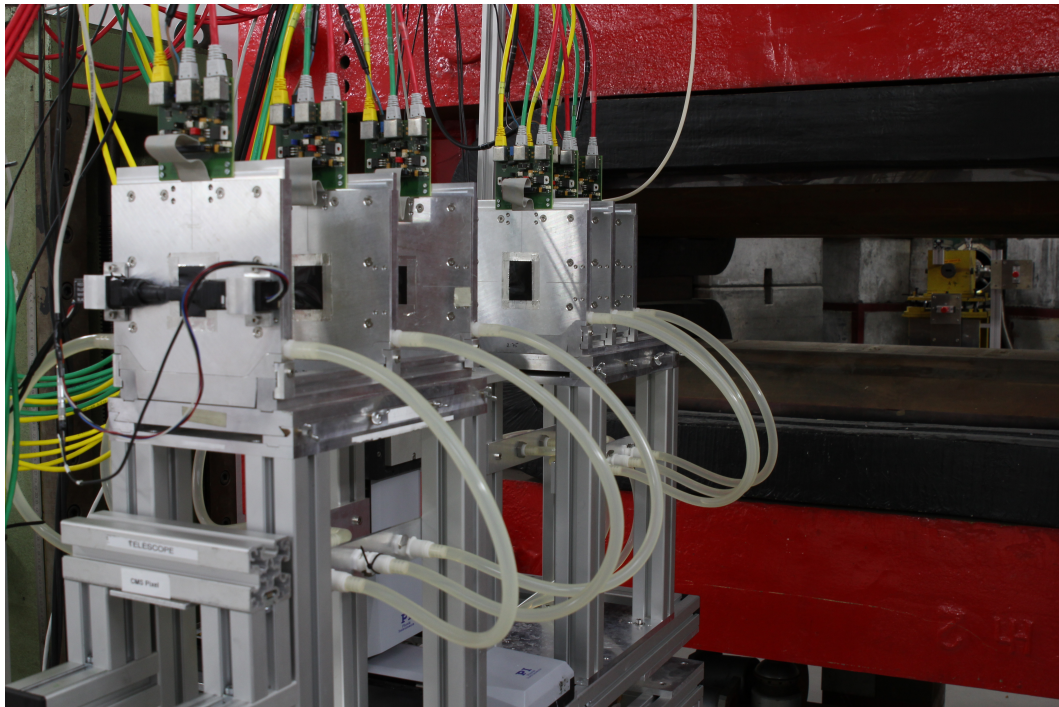
Figure 3.6: The DATURA telescope installed in the DESY-II test beam area 21 [120]. The beam is brought into the beam area from the right. It is collimated by a lead collimator and can be deflected by the red dipole magnet. The beam then enters the telescope from the side nearest to the magnet, traversing all six sensor planes, which are numbered from 0 to 5. Coolant water is pumped in and out of each jig through the transparent coolant tubes. Auxiliary boards provide power, data, configuration, and clock connections to the sensors. The black PMTs, of which two more are mounted in front of the telescope, provide trigger signals to the *Trigger Logic Unit* (TLU).

The telescope design and architecture used for the DATURA telescope has been proven successful, so that additional telescope copies have been produced for other test beam facilities all over the world. At the DESY-II test beam facility, the DATURA telescope is installed in beam area 21. One of the copies, the *ATLAS*

Copy of National Instruments based Telescope (ACONITE) was installed in beam area 22 and used for some measurements, which are presented in chapter 5.

3.3.2 *Telescope Sensors*

The sensors used in the DATURA telescope are MIMOSA 26 monolithic active pixel sensors, fabricated in CMOS technology [7] and designed and developed by IPHC[3]. They have square pixels with a size of $18.4\,\mu m \times 18.4\,\mu m$, arranged in 1152 columns and 576 rows. This results in a sensitive area of $21.2\,mm \times 10.6\,mm$. The sensors are thinned down from the back side to an overall thickness of $50\,\mu m$. Each sensor is read out in a rolling shutter mode, row by row, with 16 cycles of an 80 MHz clock used per row. This results in a readout time of $115.2\,\mu s$ per frame. Zero suppression, correlated double sampling and digitisation of the signals are performed on the chip, leading to a very low readout noise. Discriminator signal-to-noise ratio (SNR) thresholds can be set for groups of 288 columns for each sensor. The sensors are biased through an AGILENT E3644A power supply, which delivers 8 V to the sensors. A schematic of the MIMOSA 26 sensor is shown in figure 3.7.
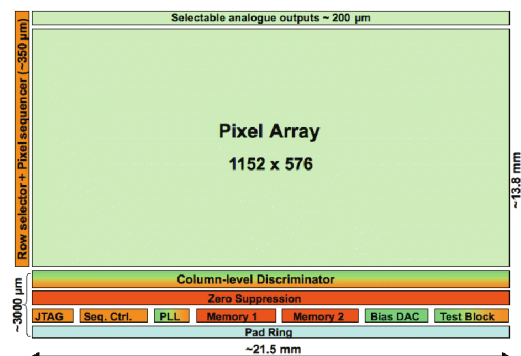
Figure 3.7: The MIMOSA 26 sensor used in the DATURA telescope. Image from [7].

Bias voltage, clock, JTAG[4] programming configuration and data connections to each sensor are provided via auxiliary boards mounted on top of each sensor jig.

3.3.3 *Data Acquisition and Readout*

The JTAG programming of each sensor is done by a special software installed on a National Instruments NI-PXIe-1082 crate. The crate also receives and handles the data acquisition of the telescope. The DAQ software, EUDAQ, is designed to be as lightweight and modular as possible [105]. A central *Run Control* process creates a graphical user interface to control other *producers*. Each of these producers is

---

3 Institut pluridisciplinaire Hubert Curien, Strasbourg, France.
4 Joint Test Action Group, IEEE Std. 1149.1-1990.

responsible for a single task: writing telescope or DUT data to disk, logging messages, distributing triggers, or monitoring the data. Figure 3.8 illustrates the data acquisition scheme.
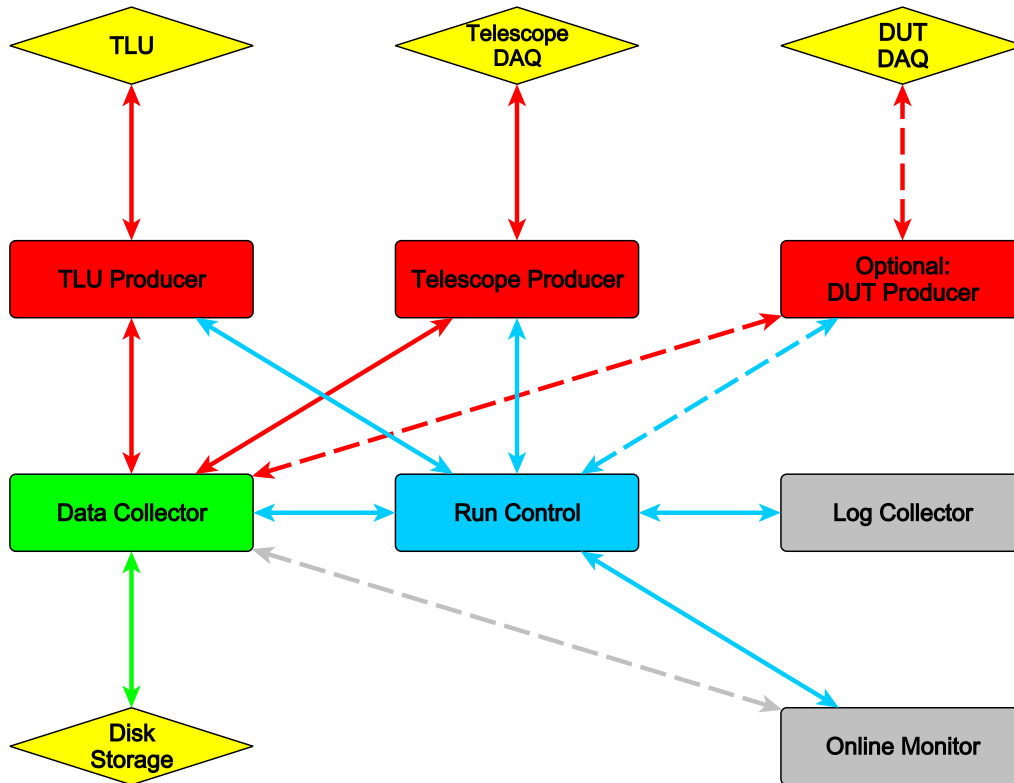
Figure 3.8: EUDAQ schematic. The central Run Control configures the producers, which then interact with the hardware. The producers send their raw data packets to the Data Collector producer, which writes them to disk.

One of the major advantages of the EUDAQ software is the possibility to include an external DUT into the DAQ by writing a separate producer for this device [35]. This allows the DUT to be controlled by the Run Control and to be synchronised with the telescope.

3.3.3.1   *Trigger Logic Unit*

The *Trigger Logic Unit* (TLU) is responsible for distributing a common trigger signal between all connected devices [37]. It is configured by the TLU producer and receives trigger input signals from four *photomultiplier tubes* (PMTs). Two PMTs are mounted in front of the first telescope plane and two behind the last plane. Depending on the settings passed by the TLU producer, the TLU can issue a trigger signal on receiving a PMT signal, or on coincidence of two or more PMTs. In practice, however, a coincidence of all four PMTs is used to ensure only particles traversing the entire telescope result in a trigger signal. A TLU is depicted in figure 3.9, with a telescope and a DUT connected. The TLU itself is based on

the commercially available ZestSC1 FPGA [101] and besides the interfaces to the PMTs, can be connected to the telescope and any DUT by RJ45 and LEMO connectors. Depending on configuration, two handshake modes can be selected for trigger distribution, with a different mode selectable for each connected device. The first mode requires the acknowledging of each issued trigger by all connected devices. Following that, the timestamp of the trigger and its ID is sent out to the devices. The second, simpler mode only requires a device to acknowledge a trigger by sending back a *busy* signal. While a busy signal is being sent, no further triggers are sent to any device.
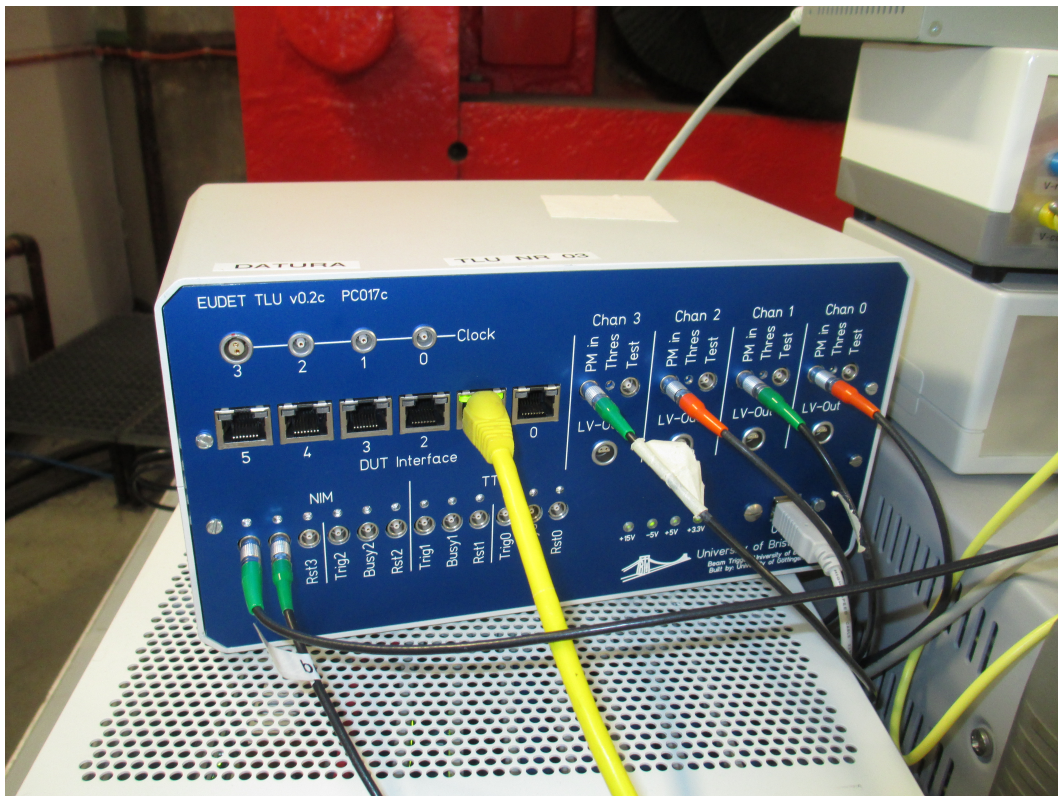
Figure 3.9: The Trigger Logic Unit (TLU) used in the DATURA telescope. The four PMTs providing the trigger input are connected by LEMO connectors on the right. The telescope is connected by the yellow RJ45 cable. A DUT is connected via LEMO connectors on the bottom left. The readout computer is connected over the grey USB cable, over which the TLU producer's configurations are sent.

3.4 THE EUTELESCOPE SOFTWARE FRAMEWORK

The EUTelescope software framework [54] is a set of Marlin processors (cf. section 3.4.4) utilising the ILCSoft framework. EUTelescope was first designed for usage as an analysis software with the EUDET telescope project. With EUTelescope, raw detector data can be converted into higher level objects, such as clusters. These themselves can then be transformed into hits in a three-dimensional space. Following that, alignment can be performed and tracks traversing the detectors

can be searched. The found tracks can then for example be used to characterise the detectors. EUTelescope offers many advantages in the analysis of test beam data. It is very flexible and modular, so that adaptations to individual setups are comparatively easy.

3.4.1 *ILCSoft*

The ILCSoft framework was originally developed for Monte Carlo simulations of the future *International Linear Collider* (ILC) [6]. ILCSoft has been extended for use in the test beam analysis with EUTelescope in the EUDET telescope project [59]. ILCSoft provides the software tools and framework to combine, among others, the LCIO event data model, the GEAR geometry API and the Marlin application framework. Other packages included in ILCSoft are for example Mokka, a Geant4-based detector simulation framework, the test beam reconstruction software MarlinTPC or the CED graphical event display.

3.4.2 *LCIO*

LCIO (*Linear Collider I/O*) is a persistency framework for the International Linear Collider [60] and is used as the data format for the EUTelescope software framework. One of the great advantages of LCIO is the fact that it is an event-based data format. All data corresponding to an individual trigger decision and readout of the detectors is stored together and can be accessed by the event number.

Each event is composed of an event header and the data collections. Timestamp information, detector information and run numbers are stored in the header. The data collection types are specific for a certain step of the reconstruction chain. Some prominent examples are `TrackerData`, which contains processed detector data, or `TrackerHit`, in which reconstructed hits are saved. Each collection has certain specific fields in which the relevant data is stored. These fields can then be cross-referenced by other collections. A track in the `Track` collection can reference the hits it is created from, which in turn reference the clusters they are calculated from. Each cluster can furthermore reference the detector charge that created it. This eases the analysis of high-level objects.

3.4.3 *GEAR*

GEAR (*Geometry API for Reconstruction*) is the geometry description markup language used within ILCSoft for event reconstruction. An abstract interface to accommodate variable detector configurations is available. The detector geometry specified within GEAR is nevertheless simplified to some extent, as for example the material description does not need to be as detailed for reconstruction purposes as for simulations. Within EUTelescope, GEAR is used to position and rotate telescope and DUT sensors in the global coordinate system. The internal

sensor geometry is also included, that is the number of pixels in each dimension, their pitch and the sensor's active and passive thickness, with according radiation lengths. EUTelescope processors can obtain the needed geometrical information for their task directly from the GEAR file. Switching between different setups and geometries can then be easily performed by loading another GEAR file.

Within the GEAR file itself, XML markups are used to describe the detector and DUT planes. The XML markups contain global parameters, such as any magnetic field. Hierarchical classes are included for various detector types, such as calorimeters, TPC chambers, and silicon sensor planes.

3.4.4   *Marlin*

Marlin (*Modular analysis and reconstruction for the Linear Collider*) is an application framework for software based on the LCIO data format. As its name suggests, its main purpose is to keep analysis and reconstruction code as modular as possible and to help with distributed development. Each computing task is implemented as a separate Marlin processor. A Marlin processor gives the user a set of callbacks to be used and via steering files the possibility to activate and pass parameters to the processor. The processors are called for every event in an LCIO file, with `LCCollections` as input and output containers.

Steering files for Marlin processors are given in XML format and define the execution order of processors. They can also contain global parameters, such as the LCIO files to write, and parameters for individual subprocessors. A detailed description of the most commonly used processors is given in section 5.3.

3.4.5   *The `datura-noDUT` Example Processors*

Within EUTelescope, an example set of processors and configurations was created as an introduction for new users to EUTelescope. Two GEAR files are provided, for different telescope geometries. As the name suggests, no external device under test is used, only the six MIMOSA 26 telescope planes are included. The goal of the `datura-noDUT` example is to get from raw detector data to unbiased track residuals of each telescope plane. A definition of the unbiased residual distribution is given in section 3.5. In the `datura-noDUT` directory, there are several subdirectories and configuration files:

- `output/`
  This folder contains all output from EUTelescope. The LCIO files are stored here, along with log output, ROOT histograms [129] and alignment constants.

- `steering-files/`
  The steering files are located in this folder. Each step used within the example has its own steering file containing Marlin processors.

- `config.cfg`
  In this file all configuration settings are stored. Global settings, such as the path to the raw data, as well as optional parameters for the processor steering files are located here.

- `runlist.csv`
  The run list contains the run numbers of the raw data and can include parameters for each run, such as the geometry used, or the applied threshold. The parameters are passed to the Marlin processor.

The `datura-noDUT` example is constructed such, that a certain sequence of Marlin processors are called with steering files. After all steps have been applied to a run, the unbiased residuals for this run should have been successfully calculated. An overview of the steps is shown in figure 3.10.
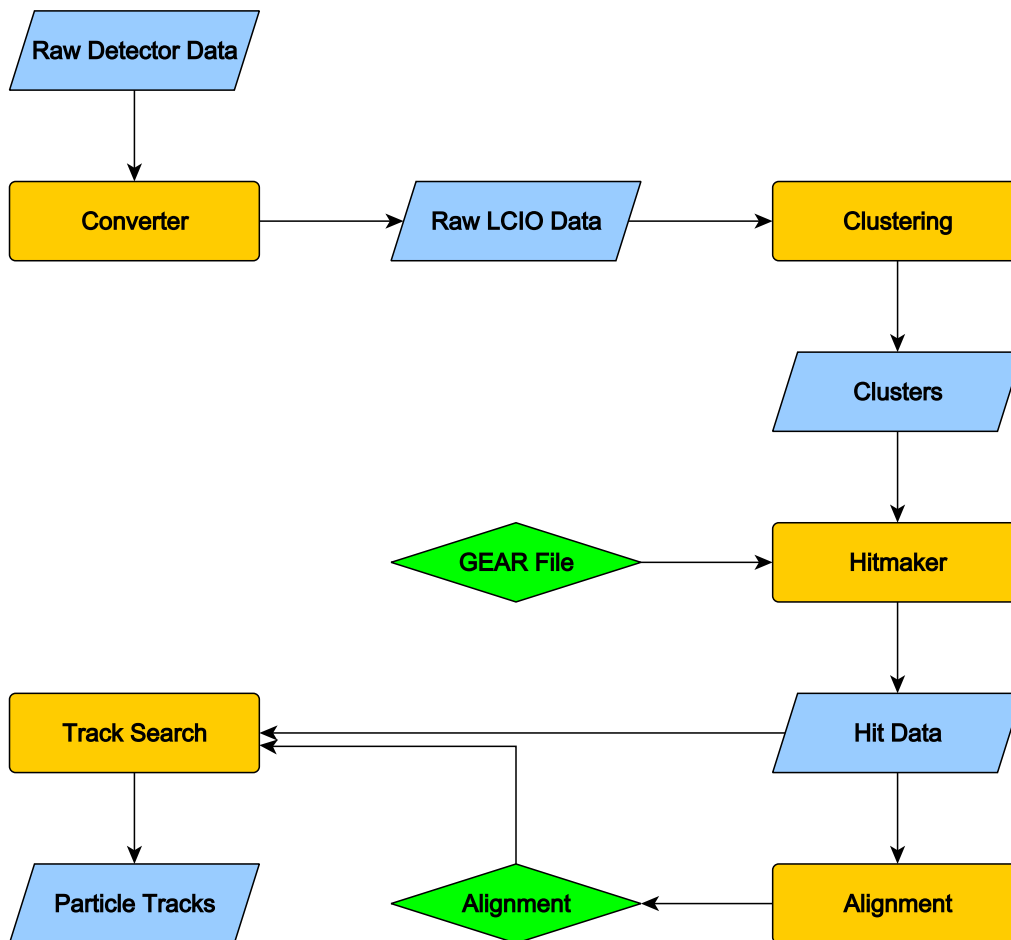
Figure 3.10: Sequence of the steps performed in the `datura-noDUT` example. Data states are indicated blue, external files green. The individual steps are coloured yellow.

The first steering file called is the converter. Its goal is to convert the raw MI-MOSA 26 detector data into the LCIO format and remove any noisy pixels. For this, it calls two Marlin processors: the `EUTelNativeReader` and the `EUTelAutoPede-stalNoiseProcessor`.

Following the converter, a clustering of adjacent pixel hits is performed. The processor used for this is `EUTelClusteringProcessor`. Clusters are searched on each telescope plane and written to an LCIO collection. A preliminary correlation is calculated and can be used for debugging and cross-check purposes.

The `EUTelHitMaker` processor called in the hitmaker step transforms the clusters from two-dimensional local coordinates on a telescope plane into hits in a global three-dimensional frame of reference. Rough pre-alignment shifts are calculated and stored in a database.

For alignment two separate methods are available — either a simple straight line tracking with `EUTelMille` or an implementation of the deterministic annealing filter (DAF) fitter [62] `EUTelDafFitter`. In both cases, the pre-alignment is loaded and applied to the hit data. Tracks are searched and passed to `MillepedeII` [17] to determine the alignment constants. These constants are then stored in another database file.

The final fitter step calculates the unbiased residual distribution for each telescope plane with the `EUTelDUTHistograms` processor, using all other planes for the reference track fit. The pre-alignment and alignment are loaded and applied to the hit collections. Once again, tracks are searched, but with one telescope plane considered passive, thus not contributing to the track fit. Instead, the track is extrapolated to this plane, and the residual distance to this plane's hits is calculated. This is repeated for each telescope plane, with histograms written to ROOT files.

3.5 TELESCOPE PERFORMANCE

To verify the performance of the DATURA telescope, measurements of the achievable resolutions were performed in 2012, for different settings of beam momentum, sensor SNR threshold and sensor spacing. In the following, the analysis is outlined and the performance results are presented. The quoted errors in this section stem from statistical uncertainties, systematic errors are not included. A source of systematic errors could for example be a possibly uncorrected remaining misalignment of sensor planes.

3.5.1 *Measuring Unbiased Residuals*

With the `datura-noDUT` example included in the EUTelescope framework, which is described in detail in section 3.4.5, tracks with hits in all six telescope planes are

sought. From these tracks, the unbiased residual distribution of each sensor plane has been calculated. To calculate this distribution, each of the six telescope planes is iteratively considered as a DUT. Within each iteration, tracks are calculated from the hits of the five non-DUT planes. The unbiased residual distribution is then filled by the distance between the hit position and the track extrapolation in the DUT plane. By using each telescope plane as a DUT, equation 3.4 is modified under the assumption that $\sigma_{\text{Intrinsic}} = \sigma_{\text{DUT}} = \sigma_{\text{M26}}$, leading to

$$\sigma_{\text{meas}}^2 = \sigma_{\text{M26}}^2 \cdot (1 + k) + \sigma_{\text{MS}}^2 \,. \tag{3.8}$$

Figure 3.11 shows an example of unbiased residual distributions for a telescope sensor spacing of 20 mm, a beam momentum of 5 GeV/c and a sensor SNR threshold setting of 6. The residual widths for the outer planes 0 and 5 are larger than the widths obtained from the inner sensors. This is expected due to the fact that the track extrapolation to the inner sensors is done from both sides, hence is comparatively more precise than for the outer sensors, where the extrapolation can only be performed from one direction. Furthermore, multiple scattering increases the uncertainty on a reconstructed track. This is especially pronounced for the residuals of the outer planes due to the comparatively larger distances of the measurement points used for the track reconstruction. In all cases, the distributions are fitted with a Gaussian. The Gaussian fit is then repeated with the range restricted to $[-2\sigma, 2\sigma]$. From this fit the residual width σ_{meas} is determined, for each plane and dimension.

3.5.2   *Intrinsic Telescope Sensor Resolution*

By using a χ^2 minimisation method, as shown in [136], which in turn is based on [86], the intrinsic resolution of the MIMOSA 26 telescope sensors is calculated from the unbiased residual widths. For each telescope sensor dimension, the individual contribution $\Delta\chi_i^2$ from plane i is defined as:

$$\Delta\chi_i^2 = \left(\frac{y_i - p_i}{\sigma_i}\right)^2 \Bigg|_{i \neq i_{\text{DUT}}} + \left(\frac{\theta_i - \theta_{i-1}}{\Delta\theta_i}\right)^2 \Bigg|_{i \neq 0, N-1} \,, \tag{3.9}$$

with the telescope plane numbering beginning at 0. The measured hit position is denoted by y_i, the position extrapolated from the track by p_i. θ_{i-1} and θ_i are the angles between the nominal beam direction and the track direction. The former is the track angle entering plane i, the latter the angle of the outbound track segment. σ_i is the intrinsic resolution of sensor plane i. In the following, it is assumed that σ_i does not differ between planes and is also equal for both measurement dimensions. $\Delta\theta_i$ is the width of the multiple scattering distribution, according to equation 3.7. If the beam axis is denoted by z, then θ_i can be expressed as:

$$\theta_i = \frac{p_{i+1} - p_i}{z_{i+1} - z_i} \,. \tag{3.10}$$
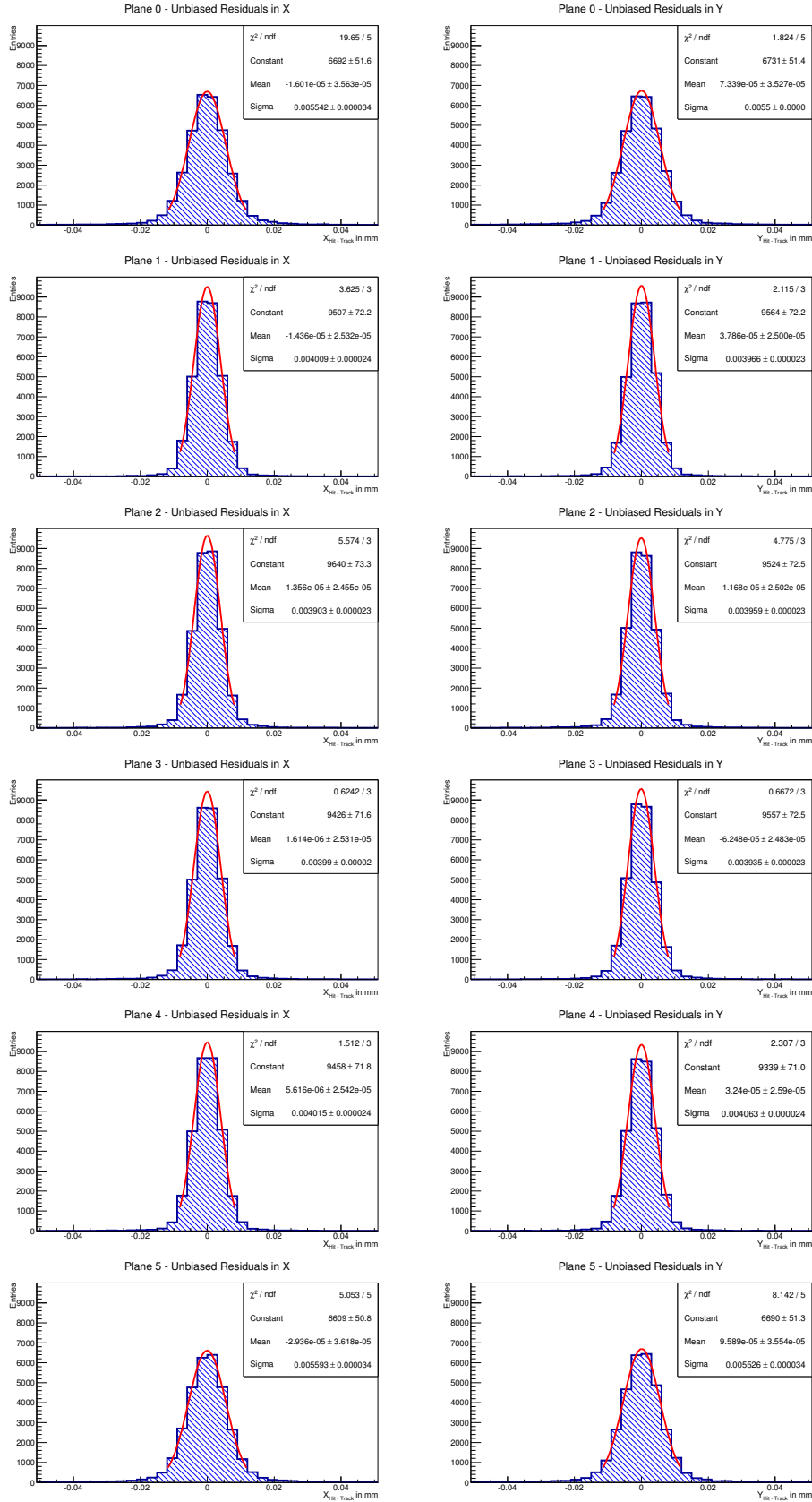
Figure 3.11: Unbiased residual distributions to determine the DATURA telescope's resolution. From top to bottom: The measured residuals σ_{meas} for planes 0, 1, 2, 3, 4 and 5, left for the x direction, right for the y direction. Each sensor plane is considered as a passive layer during the track reconstruction. The distributions are fitted with Gaussian functions twice, first with unlimited fit range, then with the fit range restricted to $[-2\sigma, 2\sigma]$.

In equation 3.9 the first term, resulting from the hit measurement, is not included in the χ^2 calculation if the plane concerned is the DUT. Similar, for the first and last planes the second term in equation 3.9 is omitted, since the scattering angle can not be determined. This results in the global χ^2 expression:

$$\chi^2 = \sum_{i=0}^{N} \alpha_i \left(y_i - p_i\right)^2 + \sum_{i=1}^{N-1} \left(\frac{p_{i+1}\beta_i + p_{i-1}\beta_{i-1} - p_i\left(\beta_i + \beta_{i-1}\right)}{\Delta\theta_i}\right)^2 , \quad (3.11)$$

with coefficients α_i and β_i defined as [136]:

$$\alpha_i = \begin{cases} \sigma_i^{-2} & \text{for } i \neq i_{\text{DUT}} \\ 0 & \text{for } i = i_{\text{DUT}} \end{cases}$$

$$\beta_i = \frac{1}{z_{i+1} - z_i} . \quad (3.12)$$

The minimum of equation 3.11 is then calculated to find the intrinsic sensor resolution $\sigma_i = \sigma_{\text{Intrinsic}}$. The results for both a tighter plane spacing of 20 mm and a wider spacing of 150 mm are shown in figures 3.12a and 3.12b, respectively.

In both cases, an error of 2.5 mm on the plane distance Δ_z is assumed. The calculated intrinsic resolution $\sigma_{\text{M26}} = \sigma_{\text{Intrinsic}}$ of the MIMOSA 26 sensors is (3.42 ± 0.03) μm for a plane spacing of $\Delta_z = 20$ mm and (3.44 ± 0.03) μm for $\Delta_z = 150$ mm. For both geometries, the expected resolution of ≈ 3.5 μm, according to [7], can be confirmed. The underlying assumptions in the method presented here are:

- The intrinsic resolution $\sigma_{\text{Intrinsic}}$ of all sensor planes is assumed to be equal. As the discriminator SNR thresholds are set for subframes of each plane individually, however, this is not necessarily true. Figure 3.13 shows the dependence of $\sigma_{\text{Intrinsic}}$ on the applied SNR threshold.

- The multiple scattering terms are calculated considering the nominal sensor thicknesses, the air between sensor planes, and a 25 μm thick Kapton foil on either side of each sensor. The particle momentum initially assumed prior to minimisation is the nominal beam momentum.

Figure 3.13 shows the measured intrinsic telescope sensor resolution for different beam energies, plane distances and applied sensor SNR thresholds. The minimum of the MIMOSA 26 sensors' intrinsic resolution is reached for a SNR threshold setting of 6. While the measured residual width for wider sensor spacings or lower beam momenta is higher, as can be seen in figures 3.12a and 3.12b, these effects are accounted for in equation 3.4 by the terms σ_{Tel}^2 and σ_{MS}^2. If the measurable telescope *track pointing resolution* is defined as

$$\sigma_{\text{Point}} = \sqrt{\sigma_{\text{meas}}^2 - \sigma_{\text{DUT}}^2} = \sqrt{\sigma_{\text{Tel}}^2 + \sigma_{\text{MS}}^2} , \quad (3.13)$$

(a) Intrinsic telescope sensor resolution at 20 mm plane spacing.

(b) Intrinsic telescope sensor resolution at 150 mm plane spacing.
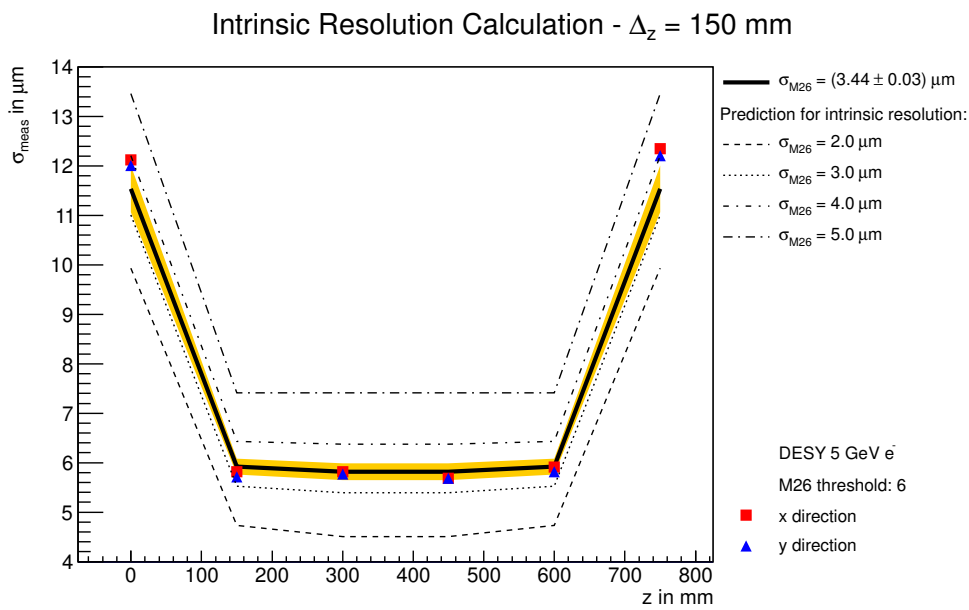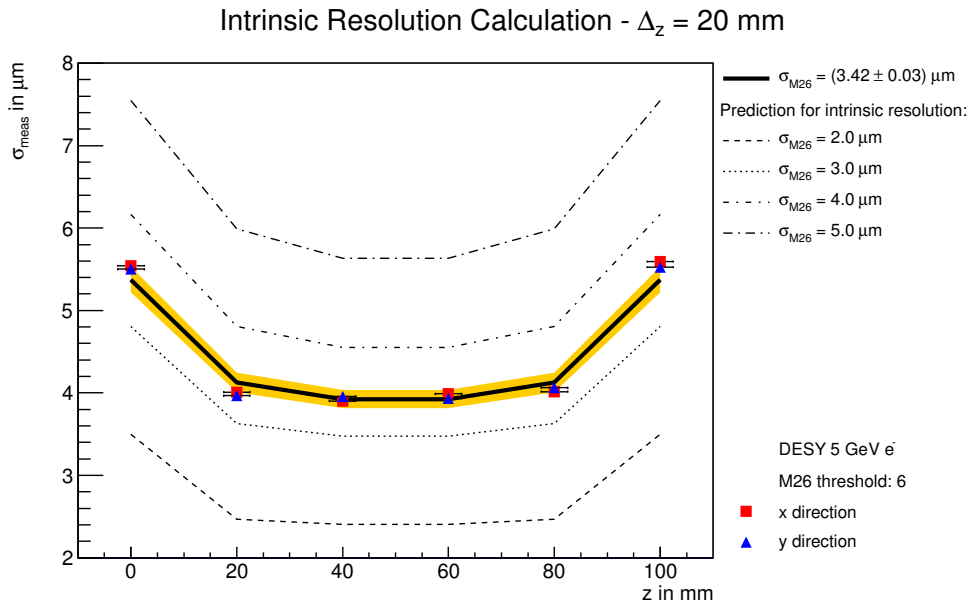
Figure 3.12: Intrinsic telescope sensor resolution at 20 mm (top) and 150 mm (bottom) plane spacing. The measured residual widths of each telescope plane are shown, for both the x and y direction. Dotted and dashed lines indicate the predicted measurements, if a different intrinsic resolution is assumed. The black line shows the calculated intrinsic telescope sensor resolution, the yellow band the measurement variance. For both telescope geometries, data was taken at a sensor SNR threshold setting of 6 and with 5 GeV electrons at DESY-II.
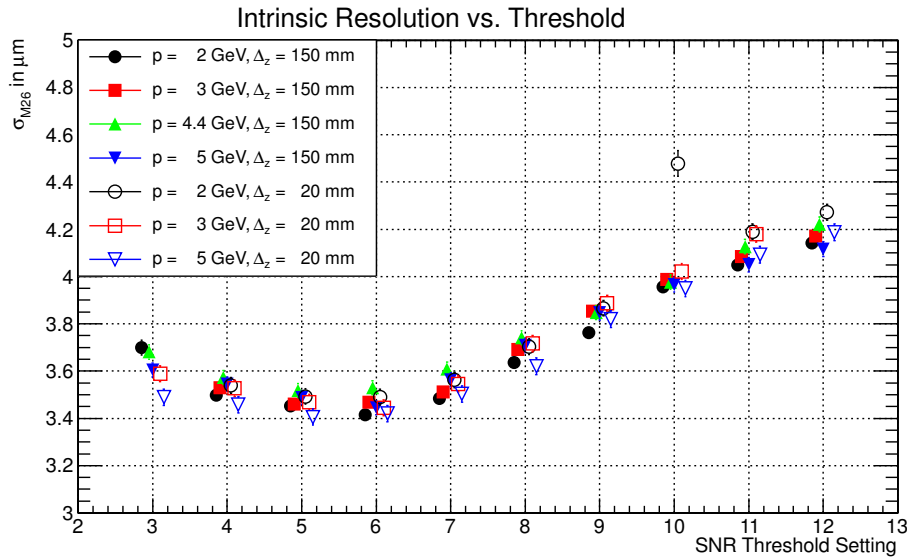
Figure 3.13: The measured intrinsic resolution of the DATURA telescope's MIMOSA 26 sensors σ_{M26} for different beam energies p, sensor spacing Δ_z and applied sensor SNR threshold. Some values are shifted on the x axis for improved legibility.

a track pointing resolution of $\sigma_{Point} = (1.94 \pm 0.08)$ µm on the inner telescope planes (i.e. on plane 2 or on plane 3) can be achieved at the DESY-II test beam facility, with 5 GeV electrons, SNR threshold 6 and 20 µm telescope plane spacing. Extrapolation of the measured pointing resolution to a DUT located at the telescope centre yields a possible track pointing resolution of $\sigma_{Centre} = (1.77 \pm 0.09)$ µm. The achievable pointing resolution at plane 3 is shown in figure 3.14 for varying energy and telescope plane spacing. The measured pointing resolutions are in good agreement with theoretical calculations performed with *General Broken Lines* (GBL) [72, 78], for which the same geometrical telescope configuration is used. For the GBL calculations, an intrinsic telescope sensor resolution between 3.3 µm and 3.5 µm is assumed.

Two measurements with 12.5 GeV electrons and 120 GeV protons are also shown. Data for these points was measured by Rubinskiy [114] with the ACONITE telescope at SLAC[5] and at the CERN SPS[6], respectively. As the discriminator settings for the ACONITE telescope sensors can possibly differ from the configuration settings used for the DATURA sensors, the resulting measured intrinsic resolution can differ between telescopes for a certain threshold. For comparability, the ACONITE data points in figure 3.14 are taken with a SNR threshold setting of 8. For this setting, $\sigma_{intrinsic}$ has been measured to be (3.31 ± 0.04) µm for data taken at the CERN SPS and (3.33 ± 0.03) µm for measurements performed at SLAC, thus similar to the DATURA values measured at DESY-II.

---

5 Stanford Linear Accelerator Center, Menlo Park, USA.
6 Super Proton Synchrotron, cf. section 1.2.1.

Track Pointing Resolution on Plane 3
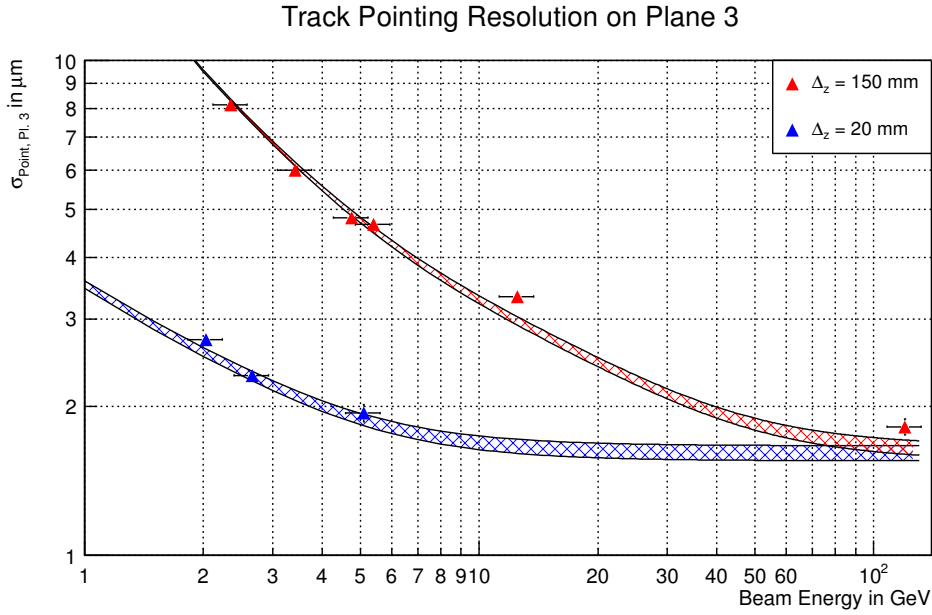
Figure 3.14: Double-logarithmic plot showing the achievable pointing resolution on plane 3 for varying beam energies and telescope plane distances. An error of 10 % on the energy is assumed, the value of which is taken from the χ^2 minimisation. Filled bands indicate expected results from GBL calculations, in which a range of the intrinsic telescope sensor resolution σ_{M26} between 3.3 μm and 3.5 μm is used. Data at 12.5 GeV and 120 GeV was taken with the ACONITE telescope [114] at SLAC and at the CERN SPS, respectively.

Measurements of the intrinsic sensor resolution by Behr [11], taken at high SNR thresholds > 10 show comparable results of $\sigma_{M26} = (4.35 \pm 0.10)$ μm. Extrapolating to infinite energies, as suggested in [34] and [96] by a fit over the inverse square energy, to measure the intrinsic telescope sensor resolution without multiple scattering effects, was not entirely successful. This is in parts due to the uncertainty of the beam energy, caused by deviations in the dipole magnet current, as shown in [117].

3.5.3 *Telescope Sensor Efficiency*

The signal-to-noise threshold applied to each telescope sensor is a critical parameter for a telescope's performance. A higher SNR threshold cuts into the signal, thus reducing the amount of clusters found on each plane and therefore reducing the amount of reconstructible tracks, which reduces the sensor efficiency. A lower SNR threshold allows an increasing amount of noise signals to be wrongly identified as clusters. This again leads to a broadening of the residual distributions. Figure 3.15 shows the efficiency distribution over a sensor plane. The efficiency in a telescope sensor plane is defined as the ratio of traversing tracks, with an associated hit measured in the plane, to the overall number of tracks. 100 μm is considered as maximum distance to associate a hit to a track. A noisy pixel column at x ≈ −8 mm can be observed. This column is masked during the converter step

in the `datura-noDUT` example and subsequently is not used during the analysis. Disregarding this area, an overall average efficiency over 98 % is observed.
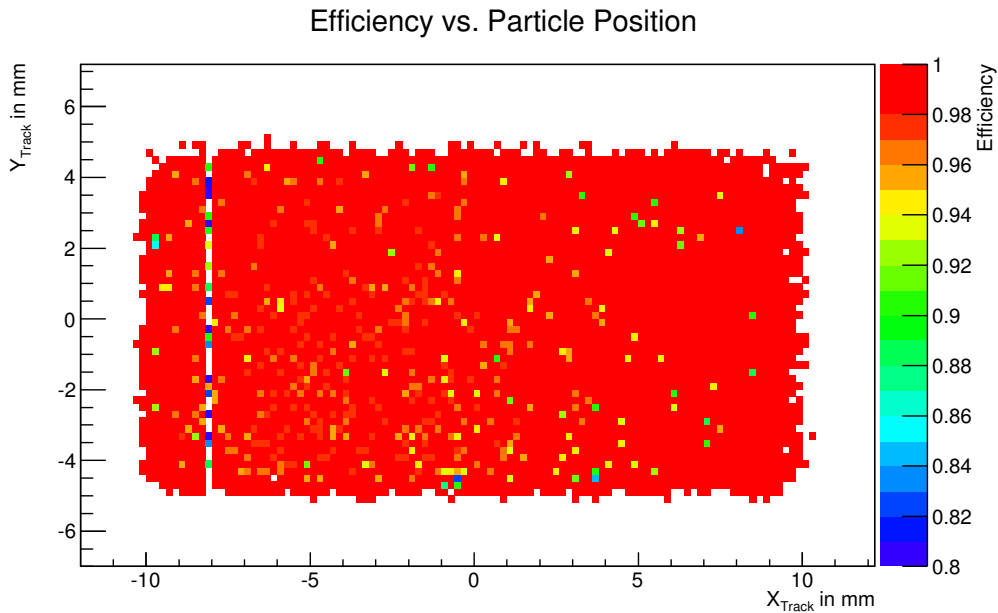
Figure 3.15: Efficiency of telescope sensor plane 3 at a SNR threshold of 6 and 5 GeV/c beam momentum. The noisy pixel column at $x \approx -8$ mm is masked in the data analysis.

In figure 3.16, the efficiency dependence on the sensor SNR threshold is shown, for various beam energies and sensor spacings. Efficiencies are averaged for all six sensor planes. In all cases, the efficiency is $\geqslant 97$ % up to a SNR threshold setting of 7. With increasing SNR threshold, the efficiency declines, until an efficiency of 86 % for SNR threshold 12 is reached. The difference between beam energies and plane spacings can be attributed to misalignment of sensor planes and a reduced track resolution due to multiple scattering.

3.5.4 *Summarising the Telescope Performance*

In this section the performance of the DATURA telescope in the DESY-II test beam facility has been investigated. The intrinsic telescope sensor resolution has been calculated from measurements taken with varying telescope settings and configurations. For the DATURA telescope, the lowest possible intrinsic resolution at DESY-II of $\sigma_{intrinsic} = (3.42 \pm 0.03)$ μm is obtained for a SNR threshold setting of 6, with a beam energy of 5 GeV and a telescope plane spacing of 20 mm. The average efficiency at this threshold is above 98 %.

The telescope track pointing resolution has been calculated from the measured residual widths and the intrinsic telescope sensor resolution. With 5 GeV electrons at DESY-II, a track pointing resolution at the third telescope plane of (1.94 ± 0.08)
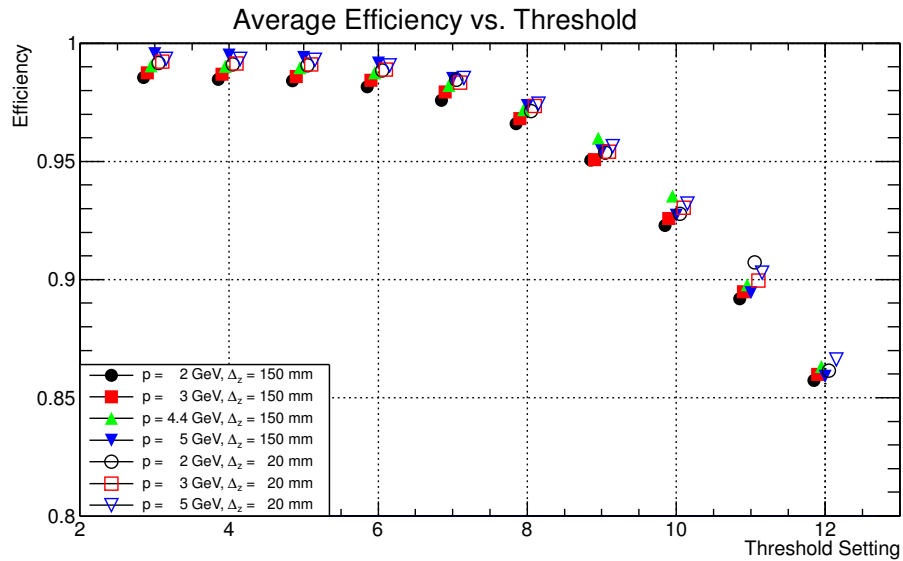
Figure 3.16: Average efficiency of all telescope sensors in both dimensions for different beam energies and sensor spacing vs. applied SNR threshold. An efficiency decline with increasing SNR threshold can be observed. Some values are shifted on the x axis for improved legibility. Statistical errors are included.

µm can be achieved. The measured results are in excellent agreement with calculations performed with GBL.

In the analysis presented here, a telescope sensor plane is used as device under test (DUT), resulting in five telescope planes being used for tracking. For an external DUT, six telescope planes can be used, thus further improving the pointing resolution. While the results presented suggest a small telescope plane spacing of 20 µm to be advantageous, this is actually due to the small distance between telescope plane and (telescope) DUT, as this minimises the extrapolation error. If an external DUT is used, it can be beneficial to use a telescope configuration in which the inner telescope planes 2 and 3 are positioned as close as possible to the DUT, whereas the outer planes are positioned at larger distances, to increase the telescope lever arm.

3.6   THE ALIBAVA READOUT SYSTEM

The *ALiBaVa* (A Liverpool Barcelona Valencia) readout system is a portable setup for the analysis of microstrip sensors [90]. It is compartmentalised into two parts: the motherboard to digitise signals, process triggers and to communicate with the readout computer, and the daughterboard with two readout chips and the sensor connection. The included software runs on all major operating systems and allows several operation modes — for example for calibration or for pedestal measurement.

The readout chips used in this setup are *Beetle* chips from the LHCb *Vertex Locator* (VELO) detector [85]. Analogue front-end signals are sampled into the pipeline with the Beetle chip clock frequency of 40 MHz. The parameters of the pulse shaper and the preamplifier can be changed by the user, to accommodate different load capacitances. These capacitances differ, depending among other parameters, on the used sensor. A block diagram of the Beetle chip is shown in figure 3.17.
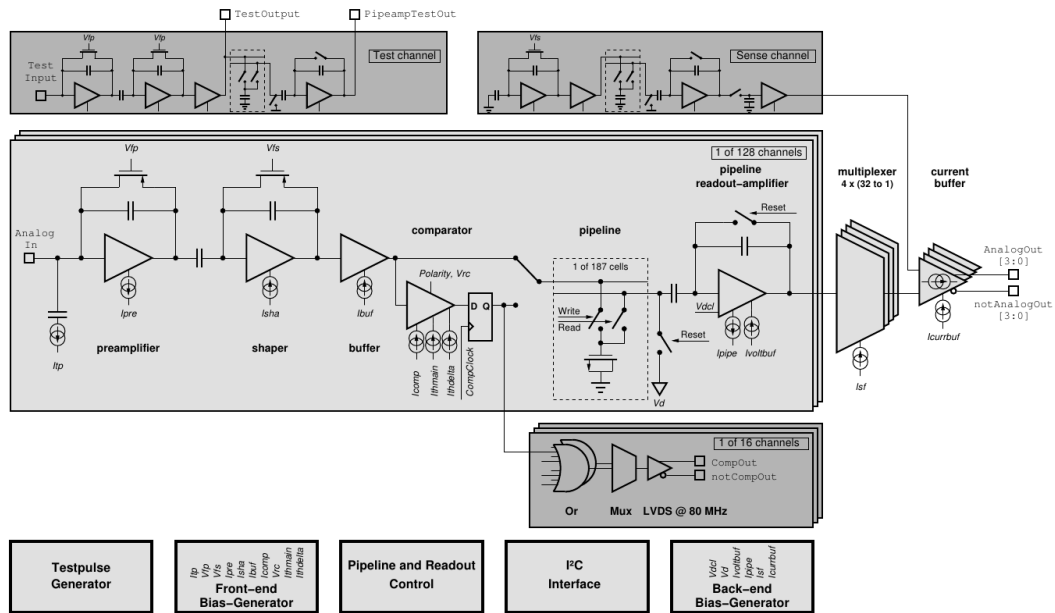
Figure 3.17: Block diagram of the Beetle chip. Image from [85].

3.6.1 *Calibration*

To compare measured signals from the ALiBaVa system with other measurements, a conversion of ADCs to electrons must be performed. For this, the gain of the readout chip must be determined. The ALiBaVa readout software has a special calibration mode to measure the gain of a sensor. The gain of the Beetle chip is not constant, but rather varies depending on several parameters. The most important ones are the settings of the chip and its temperature. The Beetle chip's gain also varies depending on the sensor that is bonded to it.

In the software's calibration mode, a predefined amount of charge is injected into the input of the Beetle chip and the resulting signal is measured. This procedure is repeated for all channels and both polarities with increasing amounts of charge. An example calibration can be seen in figure 3.18. The mean signal and the RMS of each channel and the injected charge are filled into a profile plot. Linear fits are then performed between ± 10000 and ± 50000 electrons. The slopes then give the gain of the measured sensor at a certain temperature for both polarities.
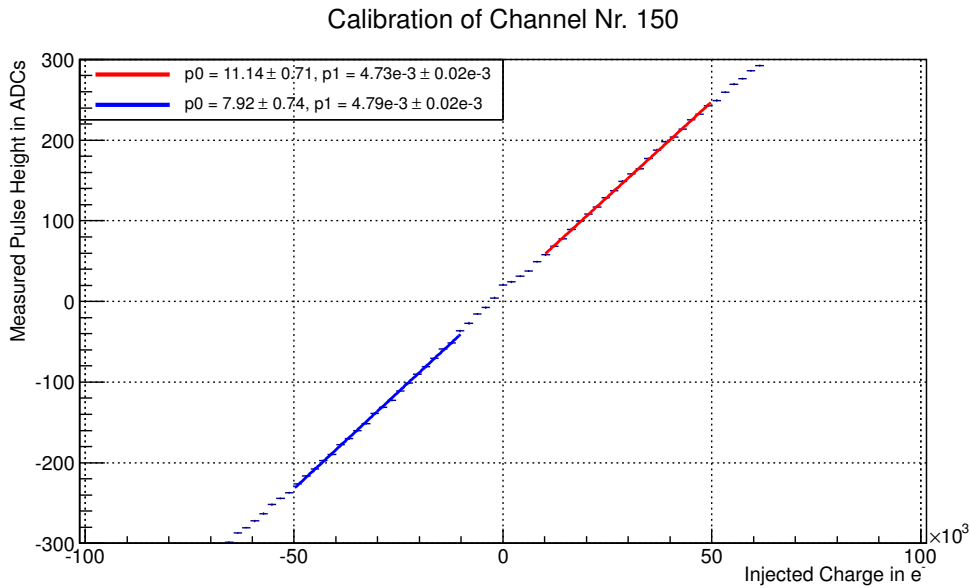
Figure 3.18: Calibration of the ALiBaVa system. The signal response to the injection of a fixed charge is shown. Values are shown for one of the used channels. A 200 μm thick Magnetic Czochralski p-bulk sensor was connected and measured at $-39.8\,°C$ temperature. Data from [22].

3.6.2 *Pedestal Analysis*

The base signal level recorded for any given channel is called the pedestal and has to be subtracted from the actual sensor signal in any subsequent analysis. To effectively determine this background, the ALiBaVa software can operate in a *Pedestal Mode*. In this mode, a user-defined number of random triggers are generated, and each channel's background signal is recorded. From these distributions, each channel's pedestal value can be calculated. Chapter 5.3.3 explains this in detail, along with further reconstruction steps, such as the subtraction of common mode noise.

3.6.3 *Data Analysis*

After pedestals have been recorded, an *RS Run* can be performed. In this mode, an external trigger signal has to be fed into the system to trigger the readout of data. To accommodate for the latency of the trigger signal, the ALiBaVa system stores four clock cycles of 25 ns in a buffer. Figure 3.19 shows the front-end pulse shape of a signal obtained from the Beetle chip. The peak voltage of the front-end pulse signal is proportional to the collected charge at the detector channel. The peaking time t_p, at which the voltage peaks, is fixed to the Beetle clock.

For the ALiBaVa system to measure the entire signal associated with a trigger pulse, the signal maximum must coincide with the sampling point at the peaking time t_p. To assess this, a *time-to-digital converter* (TDC) measures the time between the Beetle chip clock and the incoming trigger signal. In a later analysis, events
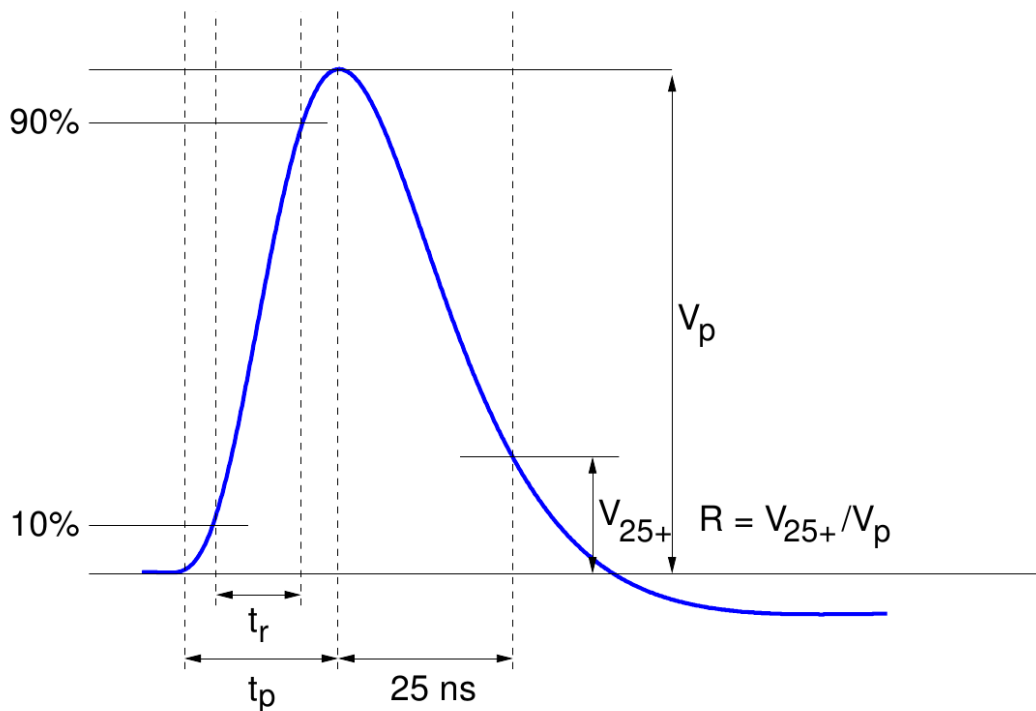
Figure 3.19: Pulse shape of the Beetle chip. Image from [85]. The signal height V_p strongly depends on the sampling time t_p.

outside a tight window of TDC values are cut. The TDC window is selected such that the measured signal is maximised.

The signal registered at the sampling point is digitised by an *analogue-to-digital converter* (ADC) and then stored in a binary format on the readout computer and can be analysed by the user. Some online monitoring features are provided by the software, showing preliminary signal and noise distributions. The analysis of data taken with the ALiBaVa system in a test beam environment is presented in chapter 5.

3.7   SENSOR IRRADIATIONS

An important aspect of evaluating a silicon sensor's suitability for a future CMS tracker is its radiation hardness. To assess this, samples must be irradiated to fluence levels expected after the full HL-LHC run time. The fluence levels expected for the Phase-II CMS tracker are shown in figure 1.6.

Several irradiation facilities exist around the world that can perform the necessary irradiations and are briefly listed in the following. In general, sensor samples are exposed to the primary or secondary particle beam available at the facility. During irradiation, various forms of dosimetry are performed to measure the samples' sustained fluence. When the desired fluence level has been reached, samples are

removed from the irradiation area and are shipped for measuring when the induced activity has decayed.

3.7.1   *CERN PS*

Most sensors investigated within this thesis were irradiated at the *Proton Synchrotron* (PS) at CERN. Proton spills with an energy of 23 GeV from the primary PS beam are delivered to the irradiation area, with a maximum beam intensity of 2×10^{11} protons per spill [63]. The proton flux is monitored online and an additional measurement of the activation of aluminium foils can be performed, to give a more precise fluence value.

3.7.2   *Los Alamos LANSCE*

Several sensors were irradiated at the *Los Alamos Neutron Science Center* (LANSCE) with 800 MeV protons [84]. Macropulses were delivered at a rate of 1 Hz to the irradiation area in the *Blue Room*, with each macropulse containing 697 micropulses. The dosimetry was performed with a PIN-diode array, which consisted of 7×7 diodes on a PCB and was mounted in front of the sensor samples. A constant current was supplied to all 49 diodes, with the drawn voltage measured by a readout computer. With the increase in voltage known to be proportional to the irradiation fluence, an average flux of $\approx 4.8 \times 10^8 \, \mathrm{p/cm^2}$ per micropulse was calculated. Figure 3.20 shows the fluence distribution obtained from 340 macropulses on the PIN-diode array, resulting in a fluence of $\approx 1 \times 10^{14} \, \mathrm{n_{eq}/cm^2}$ on the sensor.
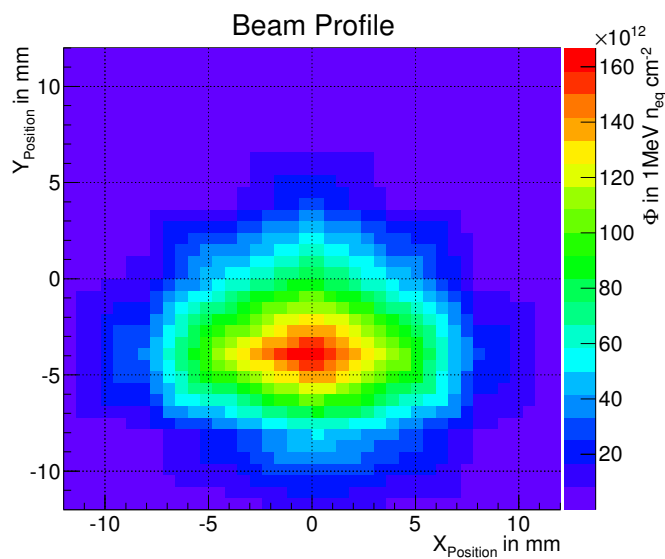
Figure 3.20: Fluence measurement by a PIN-diode of irradiations performed at LANSCE with 800 MeV protons.

3.7.3 *Other Irradiation Centres*

Besides the aforementioned irradiation centres, two other irradiation facilities are used within the HPK campaign described in chapter 1.4.4. Since no sensors used in this thesis were irradiated there, they are only listed for completeness.

3.7.3.1 *Karlsruhe Zyklotron AG*

The cyclotron in Karlsruhe provides a beam of $\approx 23\,\text{MeV}$ protons, with nickel foils used for dosimetry. The very small beam spot of $\approx 7\,\text{mm}$ requires samples to be scanned with an XY-stage [42].

3.7.3.2 *Ljubljana Reactor*

The TRIGA Mark II reactor in Ljubljana serves as a neutron irradiation facility. Sensor samples can be inserted into the reactor core, with the fluence determined by the reactor's power and the irradiation time [119].

4

SIMULATING A STRIP SENSOR

The future high luminosity upgrade of the LHC will create a more intense radiation environment than the present CMS tracking system was designed for. To maintain the excellent performance of the CMS tracker, new radiation hard sensors are necessary. Equipped with such sensors, the tracker will be refurbished during the Phase-II upgrade. To identify the technological baseline for future sensors, a dedicated campaign has been started by the CMS Tracker Collaboration, as described in chapter 1.4.4. Within this campaign, a simulation working group has been created to streamline simulation efforts and coordinate tasks. The group aims to provide insight into the understanding of radiation hard silicon sensors. With simulations, cross-checks of measured electrical properties can be performed. Furthermore, models have been developed to include radiation damage in simulations. By including radiation damage, simulations can gain predictive power and can help in the decision on future sensors.

The simulation group has recently published an internal CMS detector note [14] encompassing a wide range of simulation results. Contributions towards the aforementioned note in form of simulations of the interstrip capacitance of strip sensors are presented here. Some results have also been shown in [49] and [50]. The measurement data used for comparison in this chapter is taken from the CMS upgrade database [45].

4.1 SIMULATION FRAMEWORK

The simulation software package used, *Synopsys Sentaurus*, has already been introduced in 3.1. Here, the general settings and configuration details used in the device simulations are listed. Complete command files can be found in the appendix A.1.

4.1.1 *Carrier Mobility*

The mobility μ of a charge carrier defines the relation between its drift velocity $\vec{v}_d$ and the electric field $\vec{E}$:

$$\vec{v}_d = \mu \vec{E} \, . \tag{4.1}$$

As the mobility is not constant throughout the sensor, its value can be adjusted by including several mobility models in the simulation. Mobility contributions by the different models μ_1, μ_2, etc. are combined by Matthiessen's rule:

$$\frac{1}{\mu} = \frac{1}{\mu_1} + \frac{1}{\mu_1} + \dots .$$ (4.2)

The models are given as parameter options to the `Mobility` statement in the `Physics` section of the command file:

```
   Physics
   {
     Mobility
     (
5      DopingDependence
       eHighFieldSaturation
       hHighFieldSaturation
       CarrierCarrierScattering
       (
10       ConwellWeisskopf
       )
     )
   }
```

A reduction of mobility due to the scattering of charge carriers at the dopant atoms is considered in the simulation by the `DopingDependence` statement, which in silicon uses the *Masetti* model [91]:

$$\mu_{dop} = \mu_{min,1} \cdot \exp\left(-\frac{P_c}{N_{A,o} + N_{D,o}}\right) + \frac{\mu_{const} - \mu_{min,2}}{1 + ((N_{A,o} + N_{D,o})/C_r)^\alpha}$$
$$- \frac{\mu_1}{1 + (C_s/(N_{A,o} + N_{D,o}))^\beta} .$$ (4.3)

$N_{A,o}$ and $N_{D,o}$ are the active acceptor and donor concentrations. The default parameters and coefficients used here are listed in the simulation manual [126] and can also be found in the appendix A.1.1.

The saturation of the carrier mobility at high electric fields F is an important feature needed in the sensor simulations, especially for operations at high voltages after irradiation. It is activated by the commands `eHighFieldSaturation` and `hHighFieldSaturation` for both electrons and holes. The default model used is the *Canali* model [21]:

$$\mu(F) = \frac{(\alpha + 1) \cdot \mu_{low}}{\alpha + \left[1 + \left(\frac{\alpha + 1 \cdot \mu_{low} F_h}{v_{sat}}\right)^\beta\right]^{1/\beta}} ,$$ (4.4)

which expresses the temperature dependence by

$$\beta = \beta_0 \cdot \left(\frac{T}{300\,\text{K}}\right)^{\beta_{exp}} .$$ (4.5)

The default values of the parameters α, β_0 and β_{exp} are given in the simulation manual [126] and are listed in appendix A.1.1, together with the saturation velocity

$$v_{sat} = v_{sat,0} \cdot \left(\frac{300\,\text{K}}{T} \right)^{v_{sat,exp}} . \tag{4.6}$$

A further contribution to the mobility is the scattering of carriers with other carriers. The model is activated with the command `CarrierCarrierScattering ( ConwellWeisskopf )` and adds the term

$$\mu_{eh} = \frac{D \left(\frac{T}{300\,\text{K}} \right)^{3/2}}{\sqrt{np}} \cdot \left[\ln \left(1 + F \left(\frac{T}{300\,\text{K}} \right)^2 (np)^{-1/3} \right) \right]^{-1} \tag{4.7}$$

to the mobility. The parameters D and F are set to $1.04 \times 10^{21}\,\text{cm}^{-1}\text{V}^{-1}\text{s}^{-1}$ and $7.452 \times 10^{13}\,\text{cm}^{-2}$, respectively.

4.1.2 Recombination Models

The exchange of charge carriers between conduction and valence band and their generation and recombination are controlled in simulations by the `Recombination` statement in the `Physics` section:

```
Physics
{
  Recombination
  (
    SRH
    (
      DopingDependence
      TempDependence
      ElectricField
      (
        LifeTime = Hurkx
      )
    )
    Auger
    eAvalanche
    (
      vanOverstraeten
      Eparallel
    )
    hAvalanche
    (
      vanOverstraeten
      Eparallel
    )
    CDL
  )
}
```

In Synopsys Sentaurus, the Shockley-Read-Hall net recombination rate when using Fermi statistics (cf. the `Fermi` parameter further on) is given by

$$R_{net}^{SRH} = \frac{np - \gamma_n \gamma_p n_{i,eff}^2}{\tau_p \left(n + \gamma_n n_1 \right) + \tau_n \left(p + \gamma_p p_1 \right)} , \tag{4.8}$$

with

$$\gamma_n = \frac{n}{N_C} \exp\left(-\frac{E_{F,n} - E_C}{k_B T}\right) \tag{4.9}$$

and

$$\gamma_p = \frac{p}{N_V} \exp\left(-\frac{E_V - E_{F,p}}{k_B T}\right) . \tag{4.10}$$

Here, n and p specify the electron and hole densities. N_C and N_V are the occupation numbers of the conduction and valence bands, with E_C and E_V representing their energies. $E_{F,n}$ and $E_{F,p}$ are the Fermi levels for electrons and holes. $n_{i,eff}$ is the effective doping concentration and n_1 and p_1 are expressed by

$$n_1 = n_{i,eff} \cdot \exp\left(\frac{E_{Trap}}{k_B T}\right) \qquad \text{and} \qquad p_1 = n_{i,eff} \cdot \exp\left(\frac{-E_{Trap}}{k_B T}\right) . \tag{4.11}$$

Shockley-Read-Hall recombination is activated by the command `SRH` and given the arguments (`DopingDependence TempDependence`). With these arguments, a dependence of the carrier lifetimes τ_n and τ_p on the doping concentration and the temperature is introduced. The former is governed by the *Scharfetter relation*, the latter by a power law. Both implementations are described in the simulation manual [126]. Passing the argument `ElectricField ( LifeTime = Hurkx )` to the `SRH` command introduces a dependency on the electric field to the SRH lifetimes. This is especially important in regions of electric fields greater 3×10^5 V/cm [126]. The *Hurkx* model of trap-assisted tunnelling has been found to work best.

Auger recombination is a model typically important only at high carrier densities over $\approx 5 \times 10^{18}$ cm^{-3} [112]. In this model, a conduction band electron recombines with a valence band hole, with the energy used to excite a third carrier. This third carrier then loses its excess energy to thermal vibrations. This recombination model is activated by the `Auger` command.

At high electric fields, charge carriers can create avalanches if their drift velocity is very high. The generation rate of avalanches G^{ii} is given by

$$G^{ii} = \alpha_n n \nu_n + \alpha_p p \nu_p . \tag{4.12}$$

The ionisation coefficients $\alpha_{n,p}$ are the reciprocals of the mean free path lengths for electrons and holes and are calculated by the *van Overstraeten–de Man* model. The driving force for impact ionisation is computed from the electric field component in the direction of the current. The command `eAvalanche ( vanOverstraeten Eparallel )` activates these models for electrons, `hAvalanche` with the same arguments likewise for holes.

A coupling of defect levels can be activated by usage of the `CDL` statement. If this model is activated, energy levels in the band gap, created by radiation damage, can exchange carriers with each other. Without this model, levels can only interact with the conduction and valence bands. This model is crucial especially for the simulation of irradiated sensors.

4.1.3 *Other Physics Settings*

Besides mobility and recombination models, general physics settings are passed to the simulator in the `Physics` section of the command file:

```
Physics
{
  Temperature = @SimulationTemperature@
  Fermi
  EffectiveIntrinsicDensity
  (
    Slotboom
  )
}
```

The `Temperature` command specifies the sensor temperature in kelvin. The statement `Fermi` results in the electron and hole densities being calculated according to Fermi–Dirac statistics rather than the default Boltzmann statistics. Different band gap models can be selected in the simulation. They are selected by the command `EffectiveIntrinsicDensity`. The keyword `Slotboom` activates the Slotboom model, in which the band gap ΔE_g^0 at $0\,\mathrm{K}$ is determined to be [126]:

$$\Delta E_g^0 = E_{\mathrm{ref}} \cdot \left[\ln\left(\frac{N_{\mathrm{tot}}}{N_{\mathrm{ref}}}\right) + \sqrt{\left(\ln\left(\frac{N_{\mathrm{tot}}}{N_{\mathrm{ref}}}\right)\right)^2 + 0.5} \right] . \tag{4.13}$$

E_{ref} and N_{ref} are parameters which, in the Slotboom model are set to $6.92 \times 10^{-3}\,\mathrm{eV}$ and $1.3 \times 10^{17}\,\mathrm{cm}^{-3}$ in silicon, respectively. N_{tot} is the total doping concentration. Further additions to the `Physics` section of the simulation command file concerning radiation damage are described later in this chapter.

4.2 MSSD SENSORS

Prior to the simulation of an irradiated sensor, it must be ensured that simulations without radiation damage agree with measurements. Only through these cross-checks a later sensor simulation including radiation damage can gain some predictive power. These comparisons allow a validation of the simulation process. Within the aforementioned HPK campaign, measurements performed on *multi-geometry silicon strip detector* (MSSD) sensors were used as a comparison. The MSSD sensors are fabricated with several strip pitch sizes and strip implant widths to investigate

the interstrip capacitance C_{int}. This property is very important for the future performance of a strip sensor, as it is one of the main contributors to the strip noise (cf. chapter 2.1.2.4).

4.2.1   *Sensor Specifications*

When simulating a MSSD sensor structure, the issue arises that not all sensor design parameters needed for simulations are known or have even been released by the manufacturer. Knowledge of these parameters is nevertheless vital for a comparison of simulation results with measurements. As a first step, the simulated structure must therefore be approximated to the actual sensor geometry.

The MSSD sensors are divided into twelve distinct regions with four different strip pitches (70 µm, 80 µm, 120 µm, and 240 µm). By using different strip implant widths, three width-to-pitch ratios w/p are available. The sensors have an active thickness of either 120 µm, 200 µm or 320 µm and are produced both with p-bulk and n-bulk material. For p-bulk material, both p-stop and p-spray strip isolations are available. Each sensor has 32 strips. Table 4.1 lists the twelve MSSD regions with their corresponding pitch and implant widths.

Table 4.1: Geometrical MSSD sensor properties from the wafer submission.

Region	Strip pitch in µm	Implant width in µm	Aluminium width in µm	w/p ratio
1	120	18	26	0.15
2	240	36	44	0.15
3	80	12	20	0.15
4	70	10.5	18.5	0.15
5	120	30	38	0.25
6	240	60	68	0.25
7	80	20	28	0.25
8	70	17.5	25.5	0.25
9	120	42	50	0.35
10	240	84	92	0.35
11	80	28	36	0.35
12	70	24.5	32.5	0.35

A close up, simplified image of one of the MSSD sensors from the submission layout can be seen in figure 4.1. The sensor strips run from left to right and are surrounded on the outside by the bias and guard rings. The implantation borders of the rings and the strips are shown in blue, the extent of the aluminium covers in red. The p-stop isolation position for p-bulk sensors using this technology is indicated in green. Each strip has two AC pads on the left neighboured by a DC pad on the right. The pads are staggered to allow easier wire bonding or needle

probing for measurements.
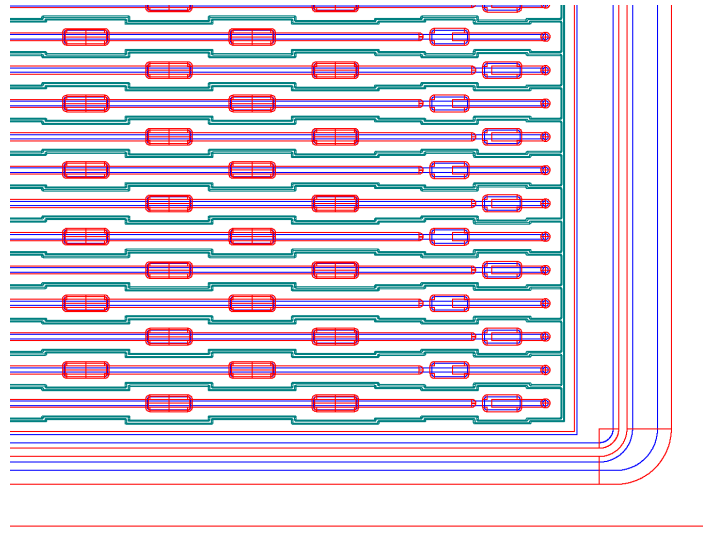
Figure 4.1: Close up of the layout of one of the MSSD sensors from the wafer submission. Implantations are depicted in blue, aluminium in red and possible p-stop positions are shown in green. Each strip has two AC readout pads and one DC pad.

4.2.2 *Simulated Geometry*

To reproduce measurements with simulations, the simulated geometry follows the sensor submission structure as closely as possible. However, to reduce simulation processing time, a two-dimensional structure is simulated[1]. The simulation structure represents a cut through the sensor bulk perpendicular to the strip orientation. Results are then scaled to the actual sensor strip length of 3.04 cm. Likewise, only five strips are simulated instead of the 32 present in the sensor. The simulated structure is shown in figure 4.2.

Geometrical sizes and doping profiles follow the patterns measured by Treberspurg in [131]. The silicon dioxide on top of the bulk is assumed to be 1 μm thick, above the implant this thickness goes down to 230 nm. A 50 nm thick layer of silicon nitride is included between SiO_2 and the aluminium electrode and extends 5 μm beyond the electrode on both sides. The aluminium width is given by the wafer submission specifications. Additionally, a diagonal element is included to model the etching process. The strip implant has a depth of 1.5 μm. It is assumed that the implantation profile follows a Gaussian function and has a peak concentration of 1×10^{19} cm^{-3}, well above any impurity or radiation induced defect concentration. The lateral diffusion of the strip implant was varied between 0.2 μm and 0.8 μm, with no significant difference in sensor performance observed, both with and without radiation damage included in the simulation.

---

1 The simulator assumes a structure thickness of 1 μm in the third dimension.
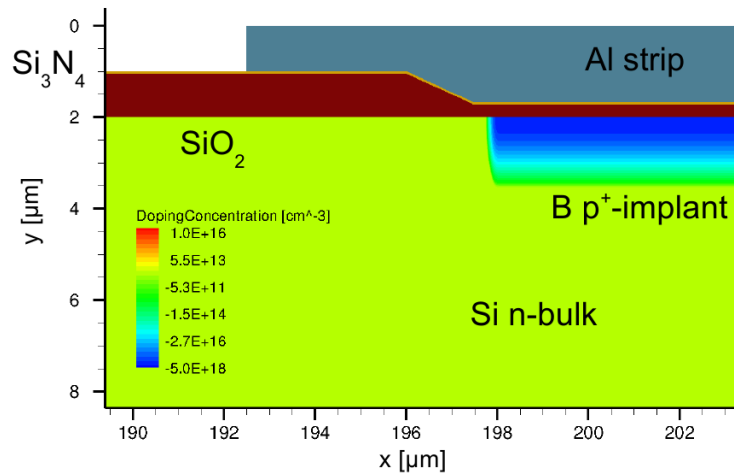
Figure 4.2: Close up of the simulated MSSD sensor geometry. The top aluminium electrode is displayed in grey with an additional diagonal element to model the etching process. The n-type silicon bulk is shown in green and the silicon dioxide in brown. The boron strip implant has a blue colour, depending on the doping concentration. A silicon nitride layer, shown in yellow, is placed between the SiO_2 and the aluminium electrode.

In the case of p-bulk material, both p-stop and p-spray sensors were simulated. For p-stop isolation, two $4\,\mu m$ wide implants are placed centrally between strips, with a spacing of $6\,\mu m$ between p-stop implants. The p-stop implant concentration is $1 \times 10^{16}\,cm^{-3}$, in the case of p-spray isolation the concentration is slightly lower at $5 \times 10^{15}\,cm^{-3}$ [46]. For implant depths, $1\,\mu m$ is used for p-stop and $0.2\,\mu m$ for p-spray isolation [131].

The values of the bulk doping concentration N_B range from $1.5 \times 10^{12}\,cm^{-3}$ to $4.5 \times 10^{12}\,cm^{-3}$ and were found by comparison of CV curves from measurements and simulations [46]. These values can be confirmed by simulations of the interstrip capacitance, which are shown in section 4.3.1. As previously stated, the MSSD sensors come with three different active thicknesses. The manufacturer achieves this by deep diffusion of the wafer, resulting in a shallow increase of the doping concentration towards the backplane [74]. For simulations this process is modelled by using an error function doping profile of the backplane implant. Length and inflection point of the error function are set in a way that the backplane doping concentration is at the bulk doping concentration level at the depth corresponding to the active thickness [46]. A summary of the structure parameters is given in table 4.2.

4.3   INTERSTRIP CAPACITANCE

The interstrip capacitance C_{int} is an important sensor property, as it is a major contributor to the strip noise. In the simulation process, at each voltage step of a bias voltage ramp, an AC signal is sent to the central electrode. The capacitance

Table 4.2: Geometrical MSSD sensor properties used for simulations

Property	FZ320N	FZ200N	FZ120N	FZ320P/Y	FZ200P/Y	FZ120P/Y
SiO$_2$ thickness between strips in µm			1.0			
SiO$_2$ thickness above the strip implant in µm			0.23			
Si$_3$N$_4$ thickness in µm			0.05			
Strip implant concentration in 10^{19} cm^{-3}			1.0			
Bulk doping concentration in 10^{12} cm^{-3}	3.0	3.0	4.5	3.4	3.0	1.5
p-stop concentration in 10^{15} cm^{-3}				10.0	10.0	10.0
p-spray concentration in 10^{15} cm^{-3}				5.0	5.0	5.0
Backplane error function depth in µm	31	115	198	33	125	215

is evaluated by measuring the resulting signal at the two neighbouring strips. As detailed in [30], several capacitances contribute to C_{int} between two strips i and j:

$$C_{int} = C_{AC_{i,j}} + C_{DC_{i,j}} + C_{DC_iAC_j} + C_{AC_iDC_j} \, . \qquad (4.14)$$

Here, $C_{AC_{i,j}}$ denotes the capacitance between the two AC electrodes, $C_{DC_{i,j}}$ the capacitance between two DC electrodes. $C_{DC_iAC_j}$ and $C_{AC_iDC_j}$ represent the capacitance between a DC electrode and an AC electrode and vice versa. Figure 4.3 shows a schematic representation of the capacitance network. The coupling capacitances $C_{CC_{i,j}}$ are several orders of magnitude larger and can be neglected in the calculation of the interstrip capacitance. In both experiment and simulation the capacitance is measured at a frequency of 1 MHz.
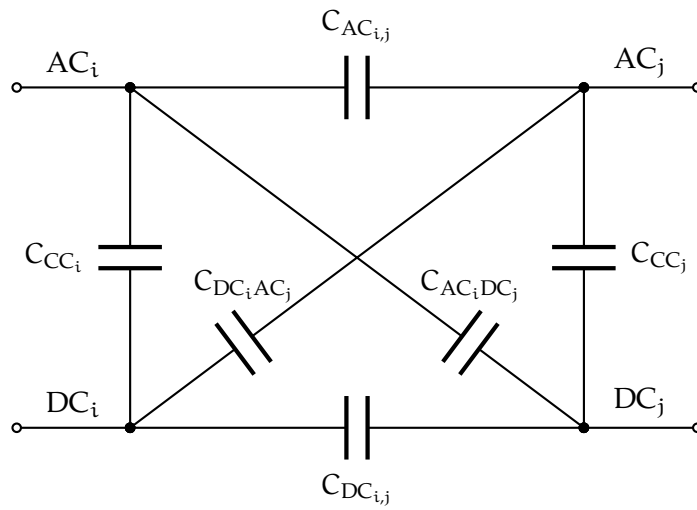

Figure 4.3: Interstrip capacitance simulation scheme. AC$_i$ and AC$_j$ are the contacts at the AC pads of strips i and j, respectively. The DC pad contacts are DC$_i$ and DC$_j$.

4.3.1   *Cross-Check of the Bulk Doping*

With equation 4.14, the interstrip capacitance of a MSSD sensor can be calculated. C_{int} can also be used to cross-check parameters and values of the sensor structure. An example of this can be seen in figure 4.4. Here, simulations with different values of the bulk doping concentration N_B are compared against the measured values. The sensor has an active thickness of 320 μm and uses n-bulk material. The extremely large pitch of 240 μm (region 2) results in a very low measured capacitance value for bias voltages below $\approx$ 140 V. C_{int} then rises and reaches a value of $\approx$ 1.1 pF at 400 V bias. The measurement values are approximated best by a simulated doping concentration of 3×10^{12} cm^{-3}, shown in green. Lower doping concentrations cause an increase of C_{int} at lower voltages than measured. Likewise, a higher value of N_B results in a delayed increase. For voltages greater 400 V, similar values for C_{int} are obtained for all doping concentrations.
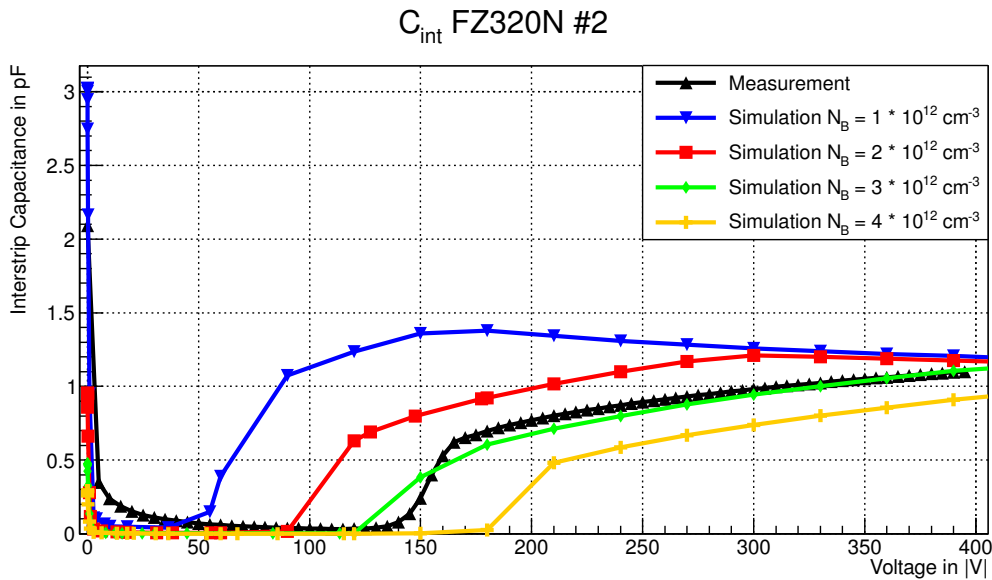
Figure 4.4: Interstrip capacitance of a 320 μm thick n-bulk MSSD sensor from region 2 for different values of the bulk doping concentration N_B. The measured data, indicated in black, is best reproduced for a bulk doping concentration of $N_B = 3 \times 10^{12}$ cm^{-3}.

4.3.2   *Cross-Check of the Interface Charge*

A further sensor property with great influence on a MSSD sensor's performance is the interface charge Q_f. As stated in previously in 2.3.2, interface charges can be introduced to the silicon - silicon dioxide interface by radiation damage. Through processing steps, some initial defects can be created in the oxide layer, creating charges at the interface even without any irradiation of the sensor. Simulations of C_{int} for different values of Q_f can be seen in figure 4.5. A 320 μm thick n-bulk sensor has been simulated with varying values of the strip pitch, representing MSSD

regions 9 to 12. All four configurations have a width-to-pitch ratio w/p of 0.35. Furthermore, w/p values of 0.25 and 0.15 are included for the $80\,\mu m$ pitch MSSD sensor. This corresponds to the regions 7 and 3, respectively.
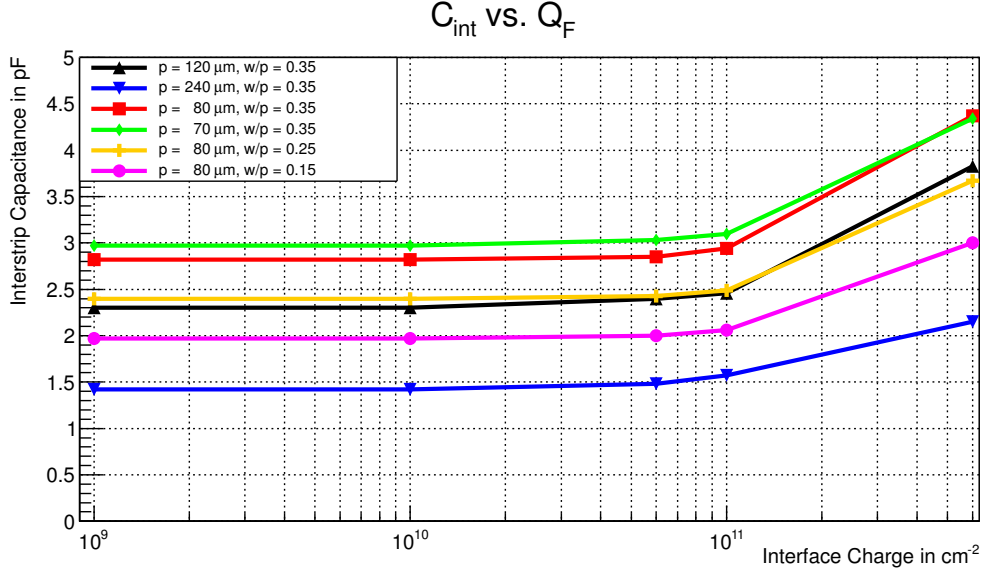
Figure 4.5: Interstrip capacitances of $320\,\mu m$ thick n-bulk MSSD sensors from different MSSD regions for several values of the interface charge Q_f. An increase in C_{int} is seen with rising interface charge. C_{int} values are taken at 1.2 times the depletion voltage V_{depl}.

Values of the interstrip capacitance are taken at 1.2 times the depletion voltage V_{depl} of each sensor. For all sensor configurations, C_{int} increases for Q_f values greater $6 \times 10^{11}\,cm^{-2}$. An increase in C_{int} with decreasing pitch size can also be observed, as is expected. In the simple assumption that the region between two strips behaves as a parallel plate capacitor of the form

$$C = \epsilon_0 \epsilon_r \frac{A}{d}, \tag{4.15}$$

decreasing the electrode distance acts as a reduction of plate distance d. C_{int} also decreases for smaller ratios of w/p. From a comparison with measured C_{int} values it has been determined that using an interface charge of $Q_f = 1 \times 10^{11}cm^{-2}$ in simulations reproduces measurements best.

4.3.3 The Interstrip Capacitance of MSSD Sensors

With values of N_B and Q_f found, C_{int} curves of all MSSD regions for all sensors were simulated and compared against measured data. Examples can be seen in figures 4.6, 4.7 and 4.8. In all cases, the simulations can reproduce the measured behaviour. The scattering of the measurement values gives an indication of the

measurement precision. In figure 4.8, the C_{int} behaviour simulated with an alternative simulation package, Silvaco ATLAS, is shown in addition. While using the same parameter settings, both simulators agree with each other and the measured data.
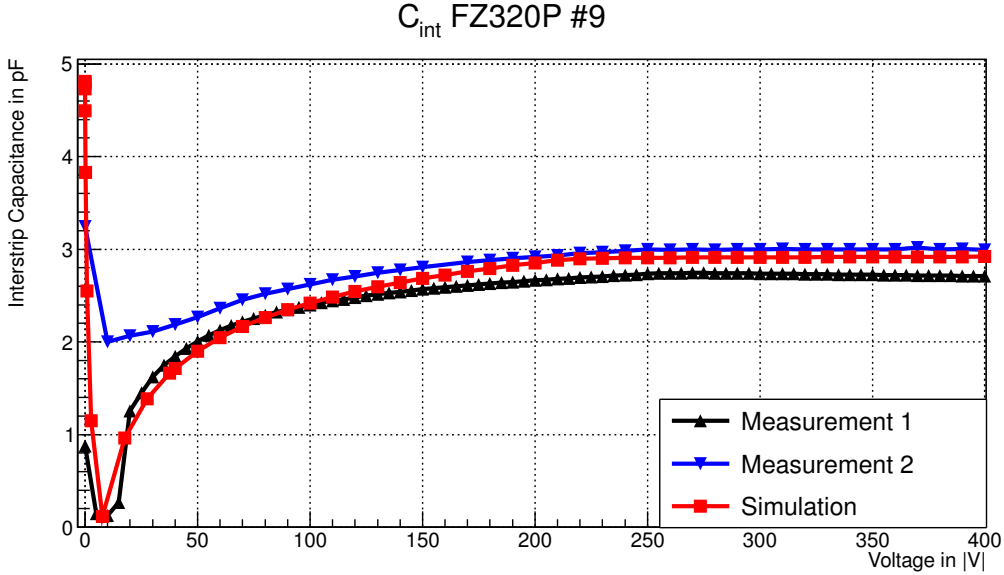
Figure 4.6: Simulated interstrip capacitance of a FZ320P sensor from MSSD region 9.

4.4   MODELLING RADIATION DAMAGE

With the validity of the simulation models and structures established for non-irradiated scenarios, the incorporation of radiation damage is now discussed. Within Synopsys TCAD, radiation damage effects can be included into simulations with two basic concepts [126]. The first method is by including fixed charges. These charges can be placed in the different materials (e.g. in the silicon dioxide), in certain regions (e.g. in the vicinity of the surface) or at material or region interfaces. The charge concentration and sign can be specified. The second method allows the creation of traps in the band gap. Again, the traps can be placed in a certain region, in a material or at a given interface with a user-specified concentration. In most cases, the concentration is parametrised by an introduction rate η, which relates the concentration of a trap c to the equivalent fluence Φ_{eq}:

$$c = \Phi_{eq} \cdot \eta \, . \tag{4.16}$$

Furthermore, a trap is characterised by two cross sections σ_e and σ_h for interactions with electrons and holes, and an energy level in the band gap. It can also be decided if the trap should act as an acceptor or a donor trap.

Figure 4.7: Simulated interstrip capacitance of a FZ120Y sensor from MSSD region 4.
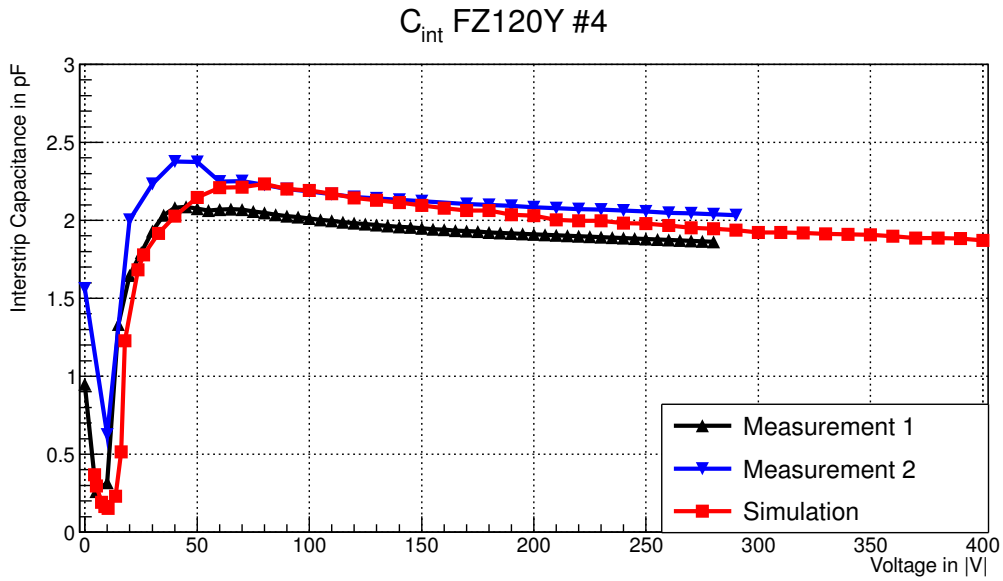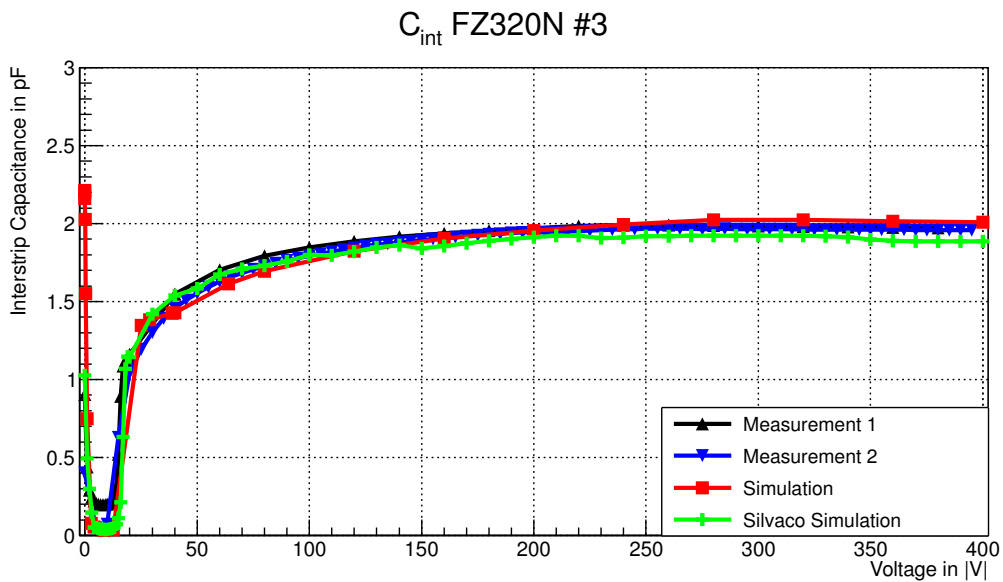

Figure 4.8: Simulated interstrip capacitance of a FZ320N sensor from MSSD region 3. A simulation performed with the same parameter settings using Silvaco ATLAS [110] is shown in green.

4.4.1   Bulk Damage

Radiation damage to the silicon sensor bulk is included to simulations by specifying traps. Two main approaches can be distinguished: either modelling the actual physical defects with their properties obtained from defect measurements, or rather implementing an effective trap model. The former obviously not only necessitates exact measurements, but also a knowledge of all defect states in a sensor. Especially in the presence of cluster defects, this can become increasingly complicated. Within the silicon sensor simulation community, the approach of finding an effective model is therefore preferred. In the last years, a multitude of models have been proposed. In the following, a selection is presented and discussed.

4.4.1.1   The EVL Model

The *EVL model* was proposed by Eremin, Verbitskaya, and Li and originated in the description of the double peak observed in the electric field of irradiated sensors [52]. The model was not designed for TCAD simulations as such, but rather for analytical calculations. It contains three trap levels, two deep levels to create the additional space charge resulting in the measured electric field shape. A third trap level in the middle of the band gap is merely used to create the increase in leakage current observed in measurements. As a defect level contributing exclusively to the current can not be implemented in the TCAD simulation packages, the model has been slightly modified, with parameters listed in table 4.3.

Table 4.3: Modified EVL radiation damage model parameters [49].

Defect	Energy in eV	σ_e in cm^2	σ_h in cm^2	η in cm^{-1}
Acceptor	$E_c - 0.525$	4×10^{-14}	4×10^{-14}	0.8
Donor	$E_v + 0.48$	4×10^{-14}	4×10^{-14}	0.8

4.4.1.2   Further Radiation Damage Models

Further radiation damage models have been developed by Petasecca et al. [106] for p-type sensors, and Moscatelli et al. [97] for n-type sensors. Both models account for a multitude of effects, such as leakage current, depletion voltage and charge collection efficiency. They use three or four defect levels each, but require an additional parametrisation to reproduce measurement data at the high fluence levels expected at the High Luminosity LHC. Chiochia et al. [32] and Swartz et al. [124] have developed models to reproduce measurements obtained with irradiated pixel sensors in test beams. These models are also based on the defect levels found in the EVL model. The EVL model has therefore been used as a basis to find a damage model for the investigated HPK sensors.

4.4.1.3 *Proton Model by Eber*

In [46] a radiation damage model is developed for HPK diodes irradiated to fluences over $1 \times 10^{14}\,\mathrm{n_{eq}/cm^2}$. The damage levels are based on those present in the EVL model with parameters tuned by current-voltage, capacitance-voltage and transient current technique measurements. The model is given for proton or neutron irradiation and is validated for measurement temperatures of 253 K. The proton model, listed in table 4.4, is used as a basis in the following simulations.

Table 4.4: Proton radiation damage model by Eber [46].

Defect	Energy in eV	σ_e in cm^2	σ_h in cm^2	Concentration
Acceptor	$E_c - 0.525$	1×10^{-14}	1×10^{-14}	$1.189\,\mathrm{cm}^{-1} \cdot \Phi_{eq} + 6.454 \times 10^{13}\,\mathrm{cm}^{-3}$
Donor	$E_v + 0.48$	4×10^{-14}	4×10^{-14}	$5.598\,\mathrm{cm}^{-1} \cdot \Phi_{eq} - 3.949 \times 10^{14}\,\mathrm{cm}^{-3}$

4.4.2 *Surface Damage*

The radiation damage sustained by the silicon dioxide in irradiated sensors is especially critical to strip sensors. The bulk damage models used in simulations are mainly developed from measurement data obtained from diodes, which do not suffer as much from surface damage as do segmented sensors. As previously described, surface damage can be included into simulations in form of oxide charges, interface charges, and interface traps. Oxide charges have a diminutive effect on the interstrip capacitance in simulations and are therefore disregarded. Charges placed at the interface however are, as shown in figure 4.5, of great importance in the simulation of C_{int}.

An expected increase of interface charge Q_f at high irradiation fluences however can not reproduce measured charge collection efficiencies, interstrip resistances and interstrip capacitances due to a shortening of the strips [103]. Peltola proposes to include the increased surface damage as a defect level instead [102]. In this approach, an additional shallow acceptor level in the silicon bulk is introduced, but only in the bulk area immediately beneath the silicon dioxide. Defect parameters are listed in table 4.5.

Table 4.5: Surface damage defect level [102], augmenting the proton model in table 4.4.

Defect	Energy in eV	σ_e in cm^2	σ_h in cm^2	η in cm^{-1}
Shallow acceptor	$E_c - 0.40$	8×10^{-15}	2×10^{-14}	40

For simulations performed with Silvaco ATLAS, a similar approach was chosen by Dalal et al. [39]. Using this simulation framework it was also not possible to reproduce experimental measurements of C_{int} and R_{int} for higher values of the interface charge [40]. The damage model used here is extended to five defect levels,

listed in table 4.6.

Table 4.6: Radiation damage model used in Silvaco ATLAS encompassing surface damage [39].

Defect	Energy in eV	σ_e in cm^2	σ_h in cm^2	η in cm^{-1}
Acceptor	$E_c - 0.525$	1×10^{-14}	1.4×10^{-14}	3
Acceptor	$E_c - 0.45$	8×10^{-15}	2×10^{-14}	40
Acceptor	$E_c - 0.40$	8×10^{-15}	2×10^{-14}	40
Donor	$E_v + 0.50$	4×10^{-15}	4×10^{-15}	0.6
Donor	$E_v + 0.45$	4×10^{-15}	4×10^{-15}	20

4.5 INTERSTRIP CAPACITANCE AFTER IRRADIATION

For simulations of the interstrip capacitance in irradiated sensors the question arises, in which way both bulk and surface damage are to be implemented. Figure 4.9 shows a comparison between the two-level proton model on the one hand, and its augmented version with an additional shallow trap on the other hand. Simulations of C_{int} in a HPK campaign MSSD sensor are shown for various values of the interface charge Q_f at an irradiation fluence of $5 \times 10^{14}\,n_{eq}/cm^2$.

In the comparison of both models it can be seen, that with the two-trap model even the initial interface charge of $Q_f = 1 \times 10^{11}\,cm^{-2}$ causes a spike in C_{int} at low voltages below $50\,|V|$. If Q_f is further increased, assuming an accumulation of surface damage with irradiation, C_{int} rises to unrealistically high values. The three-trap model on the other hand shows only a gradual increase of C_{int} with increasing Q_f. Hence from an interstrip capacitance perspective, the three-trap model is preferred.

With the interface charge Q_f remaining at $1 \times 10^{11}\,cm^{-2}$ and utilising the three-trap model to include further surface damage, simulations of sensors irradiated to a fluence of $5 \times 10^{14}\,n_{eq}/cm^2$ can be compared to measured data. This is shown in figures 4.10 and 4.11 for both n-bulk and p-bulk sensors of different thicknesses.

For both p- and n-bulk material, a flat interstrip capacitance over the voltage domain is observed. This behaviour is well reproduced by simulations, again for all sensor materials and thicknesses, as well as all MSSD regions.

4.6 SUMMARY

In this chapter, simulations of the interstrip capacitance C_{int} of strip sensors have been shown. The largely unknown exact geometry and parameters of the MSSD sensors have been reconstructed by simulations. With these settings, the behaviour of C_{int} can be reproduced for all materials, sensor thicknesses and regions prior
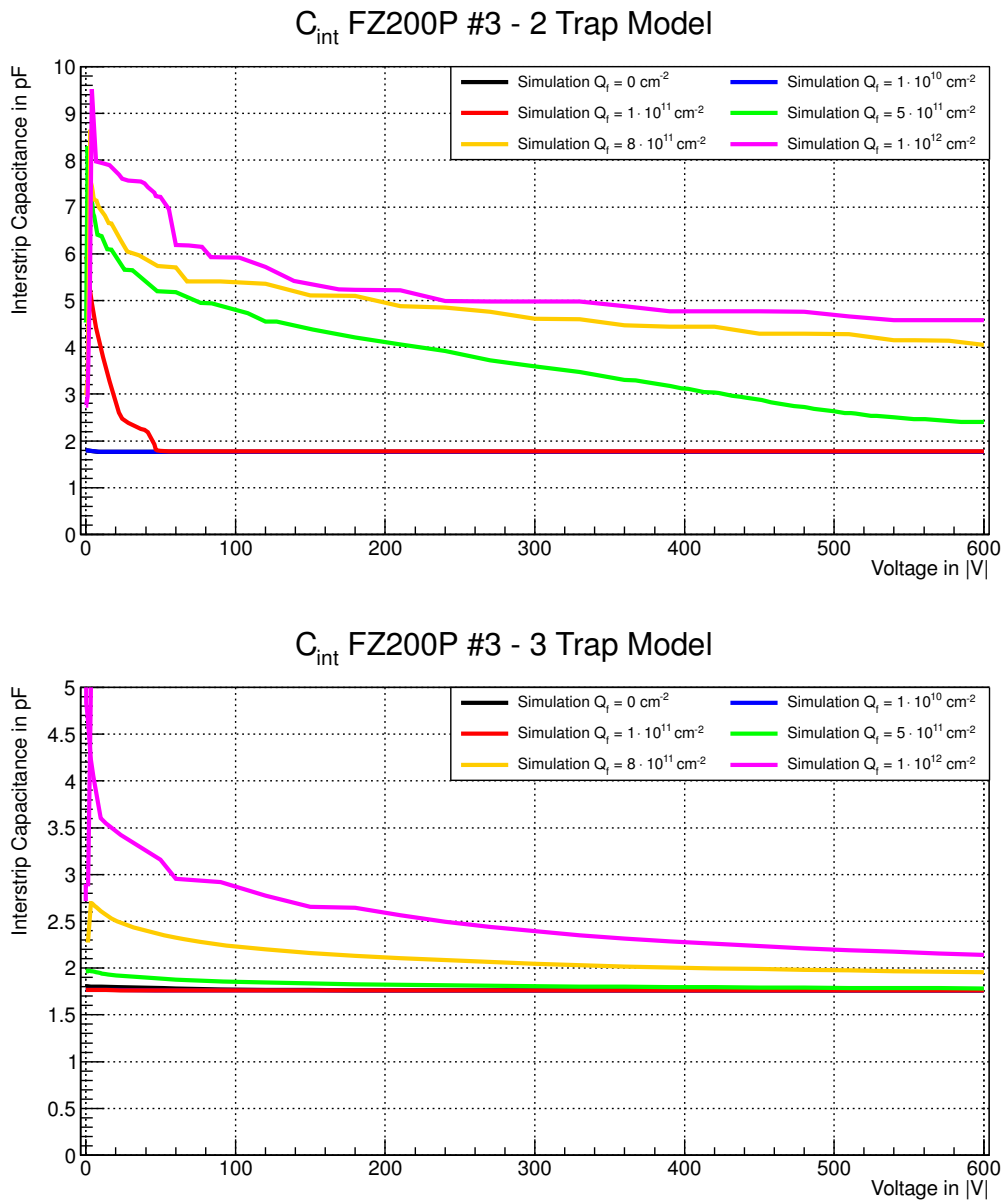
Figure 4.9: Simulations of C_{int} after irradiation using a two-trap model (top) and a three-trap model (bottom). In both cases the HPK campaign MSSD sensor FZ200P from region 3 is simulated.
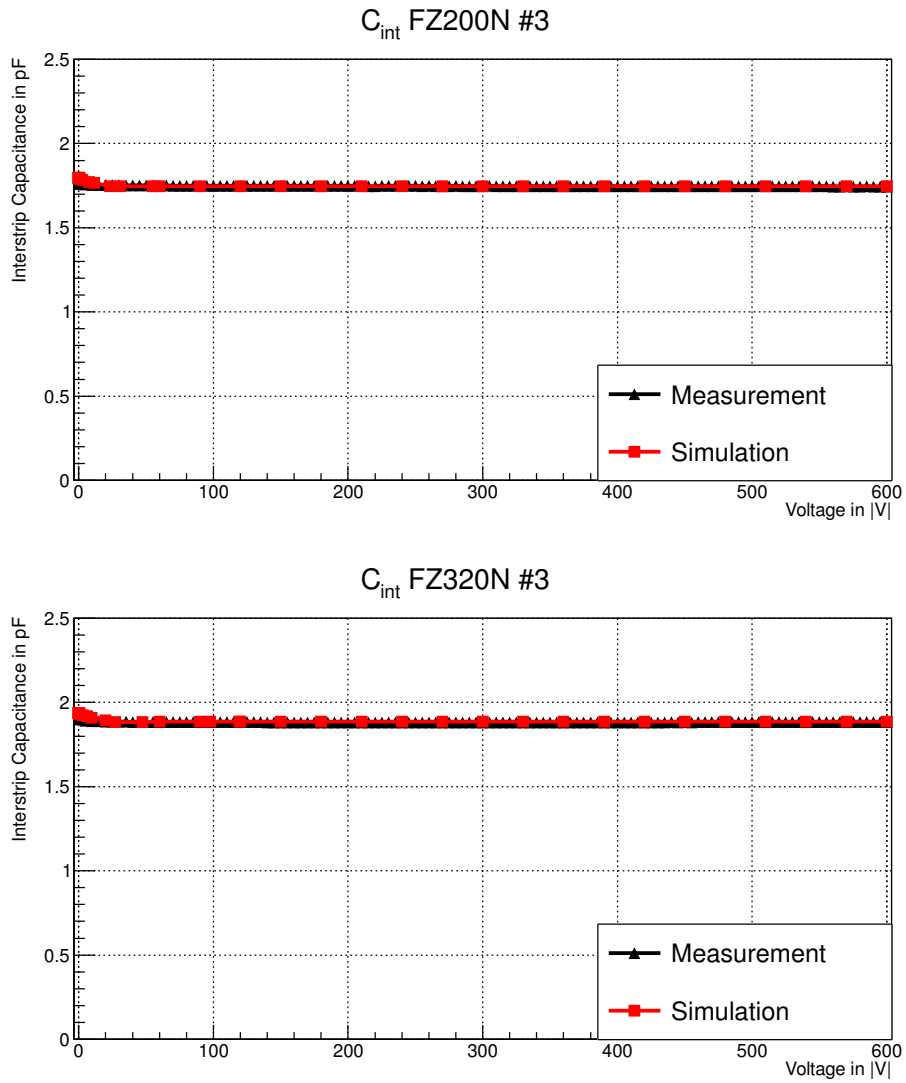
Figure 4.10: Comparison of simulated C_{int} ramps of n-bulk sensors after irradiation with measurement data. For both $200\,\mu m$ and $320\,\mu m$ active sensor thickness the measurement values can be reproduced. In both cases, the strip pitch is $80\,\mu m$.
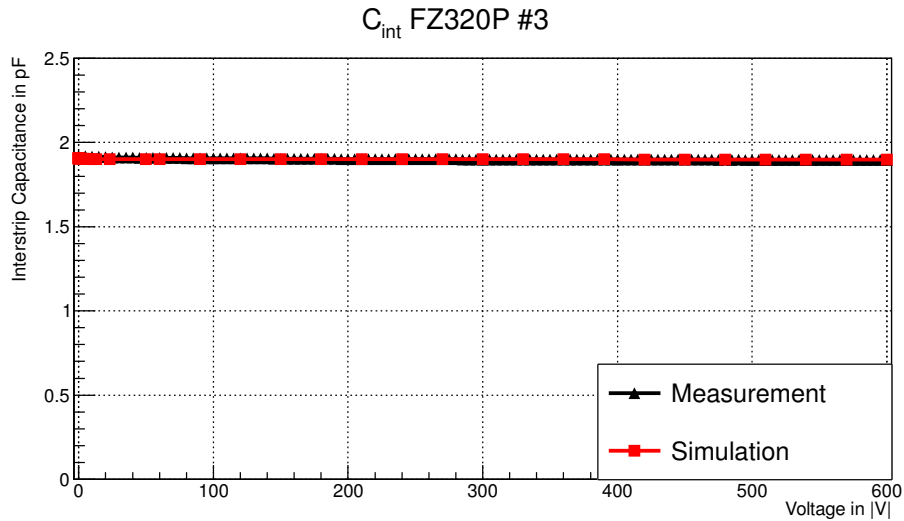
Figure 4.11: Comparison of a simulated C_{int} ramp of a p-bulk sensor after irradiation with measurement data.

to irradiation. With a simulation structure established, several models to include radiation damage have been discussed. With a model consisting of two effective traps throughout the silicon bulk and an additional trap level near the Si-SiO$_2$ interface, measurements of the interstrip capacitance after irradiation can also be reproduced in simulations.

The CMS Collaboration has decided to focus on p-bulk sensors as a baseline for the future Phase-II outer tracker sensors [47]. While no significant difference between n-bulk and p-bulk material can be determined from capacitance simulations of irradiated sensors, this changes if the electric field behaviour is considered [14]. Extremely high electric fields at the strip edges in n-bulk sensors could be the cause of non-Gaussian noise discharges in this material. Examples of occurrences of this effect are presented in the next chapter.

EPITAXIAL SILICON — A RADIATION HARD SENSOR MATERIAL

With the future High Luminosity LHC, an irradiation fluence of over 1×10^{16} n_{eq}/cm^2 for the innermost layers of the CMS pixel detector is expected (cf. section 1.4). A new material and a new design for the pixel sensors of the CMS experiment are required to withstand this unprecedented amount of radiation. A possible sensor material is thin, epitaxial silicon. Thin sensors have the advantage that they can be operated at a lower bias voltage and have less leakage current than thicker sensors. Because of this, their power dissipation is also lower, leading to reduced requirements for cooling, in turn reducing the overall material budget. The disadvantage of thin sensors is that since the signal generation in silicon sensors prior to irradiation is proportional to their thickness, thin sensors initially have a lower signal than thicker sensors.
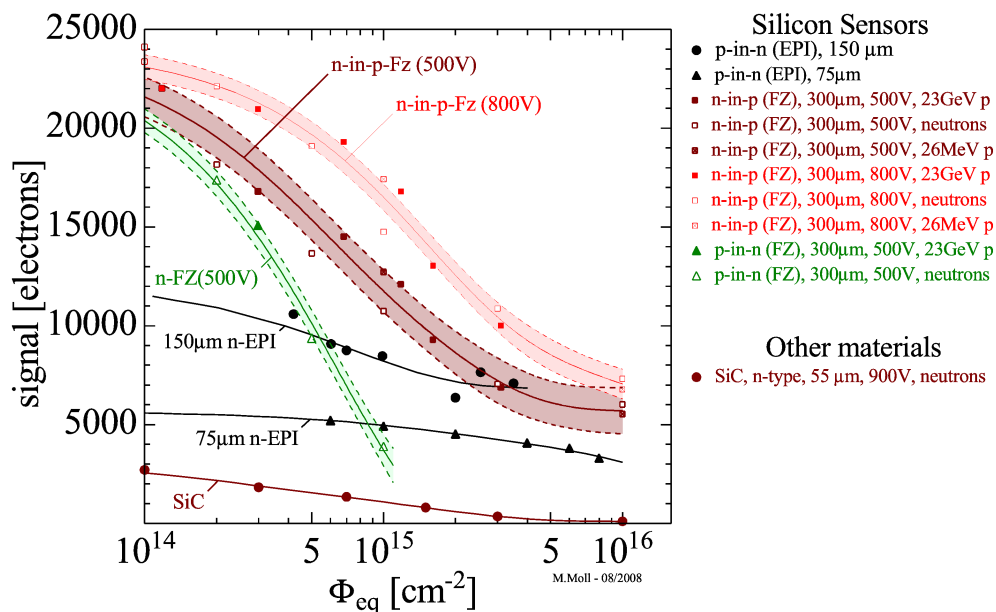
Figure 5.1: Comparison of signals from different silicon materials. Image from [111].

Epitaxial silicon sensors have the drawback that they can not necessarily be procured from every vendor. Furthermore, they can often only be produced in six-inch wafer technology, resulting in a higher unit price. Nevertheless, compared for example to novel *3D sensors*, the amount of processing steps required is similar to that needed for conventional planar sensor technology.

A clear advantage of epitaxial sensors is that with increasing fluence, they show a smaller signal degradation than thicker ones, as can be seen in figure 5.1. A sen-

sor signal height which remains at the same level throughout the High Luminosity LHC's run time would also be beneficial for the readout electronics. This would make thin, epitaxial silicon a candidate material for the Phase-II CMS tracker sensors. Furthermore, charge multiplication effects have been observed in epitaxial silicon [80]. Charge multiplication can be beneficial in irradiated sensors, as it can be a solution to overcome the signal degradation caused by radiation damage.

In this chapter, an investigation of epitaxial silicon sensors, irradiated to highest fluences of $1.3 \times 10^{16}\,n_{eq}/cm^2$ is presented. The fluence limits for the applicability of epitaxial material are examined and a comparison with thicker, non-epitaxial sensor materials is drawn.

5.1   MEASUREMENT PROGRAMME AND SENSORS

To assess the properties and the performance of highly irradiated epitaxial sensors, a test beam campaign comprising several sensors and irradiations was created. The sensors used were small standard strip sensors from the CMS HPK campaign (cf. chapter 1.4.4). A schematic cut view of the sensors is shown in figure 5.2, a top view is depicted in figure 5.3.
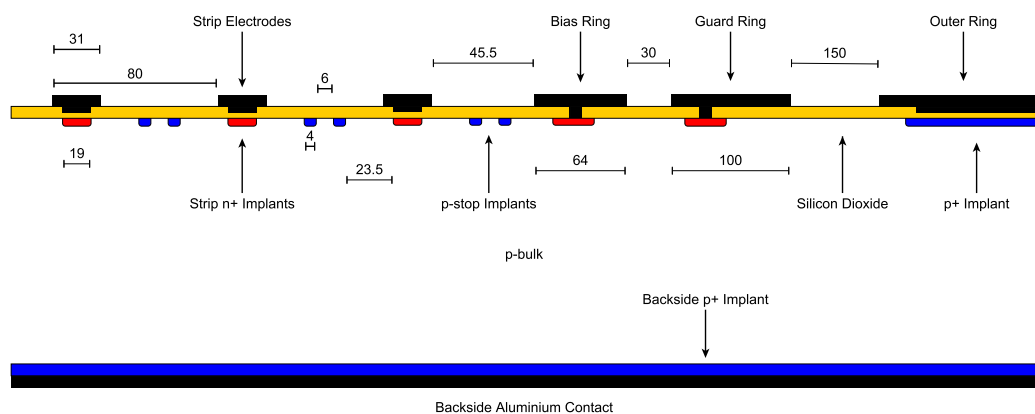
Figure 5.2: Schematic cut view of the layout of the investigated sensors, here for p-stop material. The outer three strips are shown, together with the surrounding periphery. The image is not to scale, with all sizes given in μm.

An advantage of using strip sensors is that the bare sensors can be irradiated without their readout electronics. This is usually not possible for pixel sensors, where sensors are bump bonded to the readout chip prior to irradiation. The process of bump bonding is heat-intensive, which especially after high irradiations would lead to annealing effects in the sensor. The technique of bump bonding at colder temperatures has not yet been established within the semiconductor industry. By using strip sensors, any radiation effects measured can therefore be attributed to the sensor alone.

A disadvantage is that the noise in a strip sensor is higher than it would be for a pixel sensor. This is due to a multitude of effects, for instance the higher leakage current and sensor capacitance due to the increased sensor size. Also, pixel sensors are, contrary to strip sensors, not AC-coupled. In summary, by investigating strip sensors, no conclusion on sensor properties related to the future readout scheme can be given. Instead, a direct access to the properties of examined materials is possible.

Figure 5.3: Top view of the investigated sensors' layout. Altogether, each sensor is 5.12 mm wide and 25 mm long.
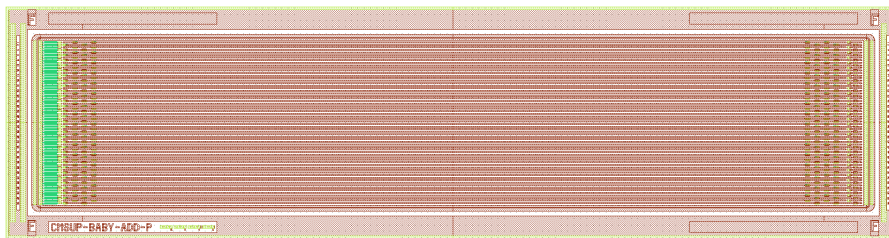
Table 5.1 lists the sensor materials which were measured in the test beam and their irradiations. The materials were produced as strip sensors for the CMS HPK campaign (cf. section 1.4.4). Both n- and p-type silicon are available, with the latter divided into p-stop and p-spray isolated strips. The sensors have a physical thickness of 320 μm, of which the top 100 μm are active. Some sensors with different active thicknesses of 70 μm have been measured as a reference. The overall physical thickness here remains at 320 μm. The Fth200Y and the MCz200N, MCz200P, and MCz200Y sensors are thinned down to a physical and active thickness of 200 μm. The sensor strip pitch is 80 μm and irradiations with fluences of up to $1.3 \times 10^{16} \, n_{eq}/cm^2$ by 800 MeV and 23 GeV protons were performed.

Each sensor was measured at multiple voltage steps, preferably above depletion, to explore charge collection efficiency and signals. By rotating the sensor, a change in beam incidence angle can be created. This allows for an additional investigation of charge sharing. Furthermore, due to the 3.8 T magnetic field within CMS, the future tracker sensors will also encounter inclined tracks. Sensor behaviour under non-perpendicular incidence is also critical for the future tracker module design (cf. section 1.4.3.2). In the higher η regions of a HL-LHC CMS barrel pixel detector, very large cluster sizes due to shallow incidence are to be expected, as are for the ATLAS barrel pixel detector [88]. This effect can be partially reduced by using very thin sensors, giving further motivation to the investigation of thin, epitaxial sensors for varying beam incidence angles. Table 5.2 gives an overview of the measured rotations.

With the tracking capabilities of the test beam telescopes, presented in section 3.5, a sub-pitch track resolution can be achieved. The results presented in this chapter are from the first ever test beam measurements of highly irradiated epitaxial silicon sensors.

Table 5.1: List of sensors measured in the test beam. Unmarked irradiations were not available for the sensor material. An explanation of the sensor abbreviations is given in section 1.4.4.

Irradiation	Epi100P	Epi100Y	Epi70N	Epi100N	MCz200P	Fth200Y	MCz200Y	MCz200N
non-irradiated	✓	✓	✓					
$\Phi = 1 \times 10^{15}\,\mathrm{n_{eq}/cm^2}$ 800 MeV Los Alamos	✓	✓	✓	✓				
$\Phi = 1.5 \times 10^{15}\,\mathrm{n_{eq}/cm^2}$ 23 GeV CERN	✓	✓		✓				
$\Phi = 3 \times 10^{15}\,\mathrm{n_{eq}/cm^2}$ 23 GeV CERN	✓			✓				
$\Phi = 1.3 \times 10^{16}\,\mathrm{n_{eq}/cm^2}$ 23 GeV CERN	✓	✓		✓	✓	✓	✓	✓

Table 5.2: List of measured sensor rotations in the test beam. Additionally, the Epi100P sensor irradiated to $\Phi = 1.5 \times 10^{15}\,\mathrm{n_{eq}/cm^2}$ was measured at 38.7° incidence. The angle is measured between the sensor strip surface and the vertical axis.

Beam incidence angle	70 μm epitaxial	100 μm epitaxial	200 μm non-epitaxial
0°	✓	✓	✓
25°	✓	✓	✓
31.7°			✓
41.2°	✓		
51.3°		✓	

5.2 TEST BEAM SETUP

In the following pages, the measurement setup is described. The data was taken in five test beam runs at DESY-II, three with the DATURA telescope in area 21, two with the ACONITE telescope in area 22. For each week-long run, the setup was reassembled with the same specifications.

5.2.1 Device Under Test

The sensors were fixed to a copper plate, which in turn was connected to an ALiBaVa daughterboard (cf. chapter 3.6). The copper plate provides the bias contact to the sensor's backplane and the cooling contact. The strip sensor was then wire bonded to the fan-in of the Beetle chip. A picture of the complete module is

shown in figure 5.4.

With a support plate, the daughterboard and strip sensor were mounted in an aluminium cold box. To reduce multiple scattering of the beam particles, windows were cut into the box and covered with Kapton foil.
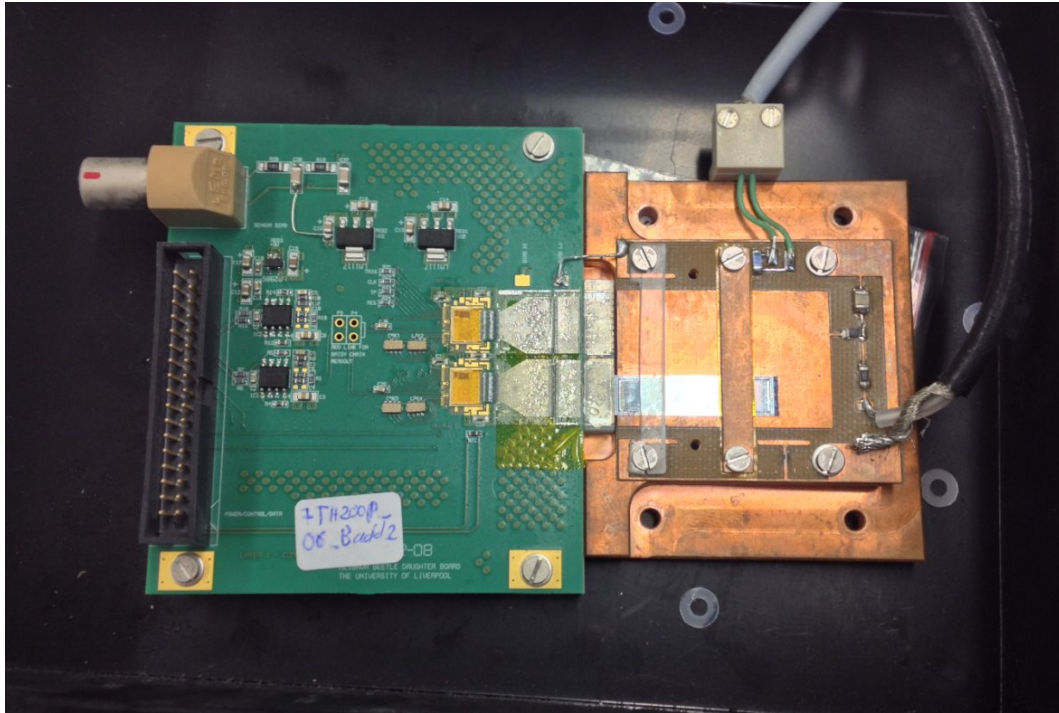

Figure 5.4: A strip sensor wire bonded to an ALiBaVa daughterboard. A Pt-100 resistor for measuring the temperature is affixed at the top. High voltage is brought in via a bias filter on the right.

The ALiBaVa daughterboard was connected by a 3 m ribbon cable to the ALiBaVa motherboard. The cable was wrapped in aluminium foil to provide some minimal shielding from noise pickup. Since the ALiBaVa system has to be reset from time to time after an error or a misconfiguration, its reset switch was connected to an Arduino microcontroller, which in turn was controlled by the readout computer. This eliminated the need for human access to the beam area to reset the motherboard. Temperature readings from the Pt-100 resistor were also monitored by the readout computer. For beam operation, 5 GeV electrons were selected. A few runs were taken with 3 GeV electrons, as other experimental groups were the main test beam users at that particular time.

5.2.2   Powering and Cooling

To reduce the leakage current in the irradiated sensors (cf. equation 2.21), these were cooled down to temperatures of below $-20\,°C$. The leakage current in sensors irradiated to $1.3 \times 10^{16}\,n_{eq}/cm^2$ was at such a height that the temperature had to be reduced even further to below $-25\,°C$. Condensation was prevented by

flushing the sensor box with nitrogen. The sensor support plate was connected to a suitable chiller, with the piping and the sensor box covered in insulating Armaflex foam. Table 5.3 lists the required sensor temperatures for each irradiation level.

Table 5.3: Maximum sensor temperatures for different irradiation levels.

Irradiation level in n_{eq}/cm^2	0	1×10^{15}	1.5×10^{15}	3×10^{15}	1.3×10^{16}
Maximum sensor temperature in °C	≈ 20	< -20	< -20	< -20	< -25

Bias voltage was supplied from a Keithley power supply located in the control room and connected via high-voltage cables and SHV connectors. For safety reasons, no remote operation of the voltage supply was considered.

5.2.3   Telescope Integration

The sensor box was mounted onto a rotation stage, which was in turn attached to a moveable XY stage. The stage was then fixed to the telescope support frame between the two lever arms. To accommodate rotations of the sensor box, the distance between the last upstream telescope plane and the first downstream telescope plane (planes 2 and 3) had to be set to 300 mm. The distance between the telescope planes on each lever arm was fixed to 60 mm. This setup configuration was repeated for each test beam run. Figure 5.5 shows the setup in the DATURA telescope in test beam area 21. The XY stage was connected to the telescope DAQ computer and was set up to be remote controllable, again minimising human access to the test beam area. The MIMOSA 26 sensor thresholds were set to a signal-to-noise ratio of 6 for all planes. The telescope coolant temperature was kept at 14 °C.

5.2.4   DAQ Synchronisation

The combination of two different data acquisition systems proved to be quite difficult. The MIMOSA 26 telescope sensors require 115 μs for the readout of an event. Within this time the event data is written to disk, so no time is lost due to buffer and memory constraints. With a sampling time of 25 ns, the ALiBaVa's Beetle chip however is much faster. As the ALiBaVa's buffer is limited, it can only store 1000 events. To ensure synchronous readout of both systems, a custom gate generator and FPGA solution [134] was implemented. The schematics of the setup can be seen in figure 5.6.

Hits from the telescope's four photomultipliers (PMTs) are sent to the telescope Trigger Logic Unit (TLU, cf. section 3.3.3.1). On coincidence of all four PMTs, a
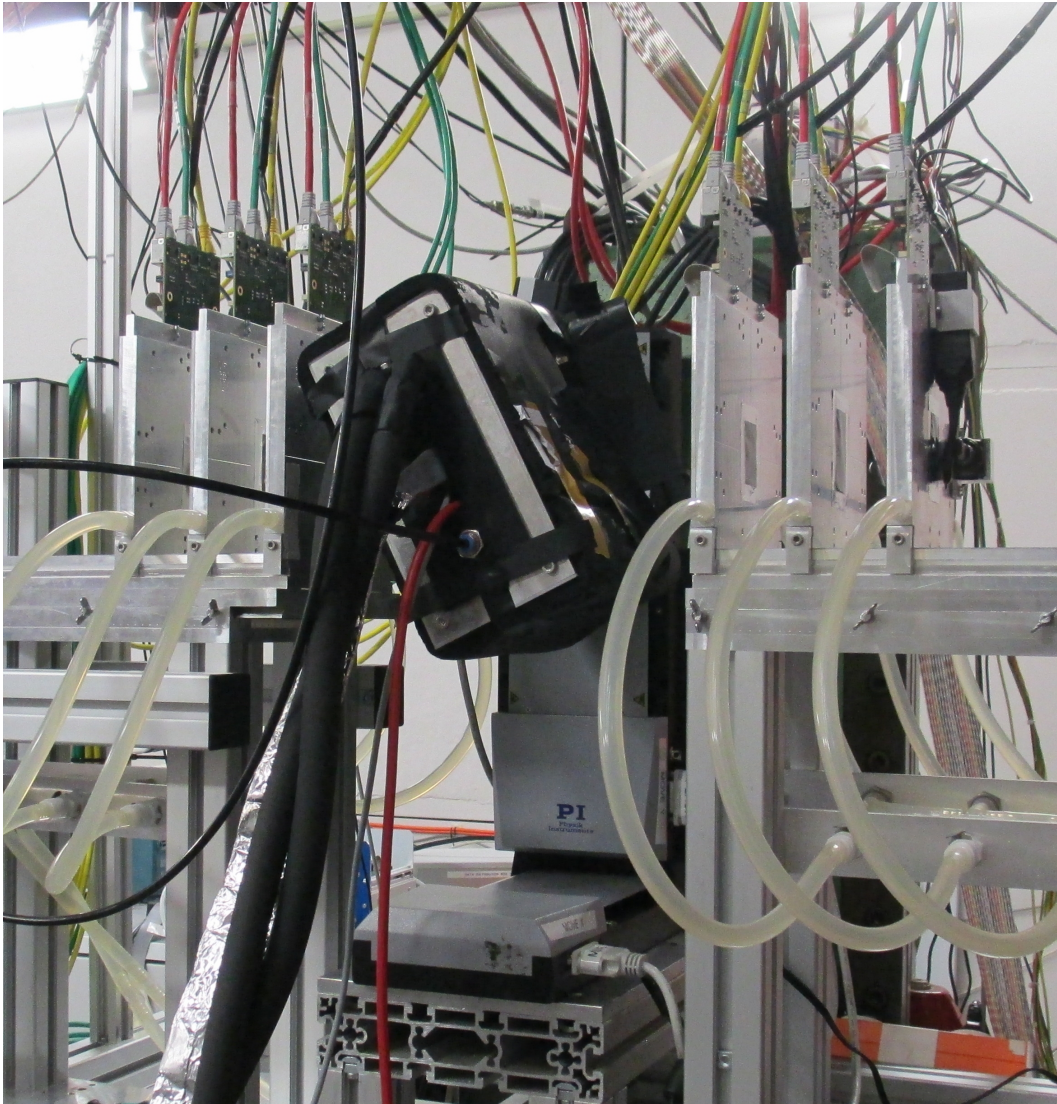
Figure 5.5: The sensor box housing the ALiBaVa DUT mounted in the DATURA telescope in test beam area 21. The sensor box has been isolated with Armaflex foam and is rotated to 25 °. High voltage and data cables along with N_2 and coolant pipes are connected to the box.
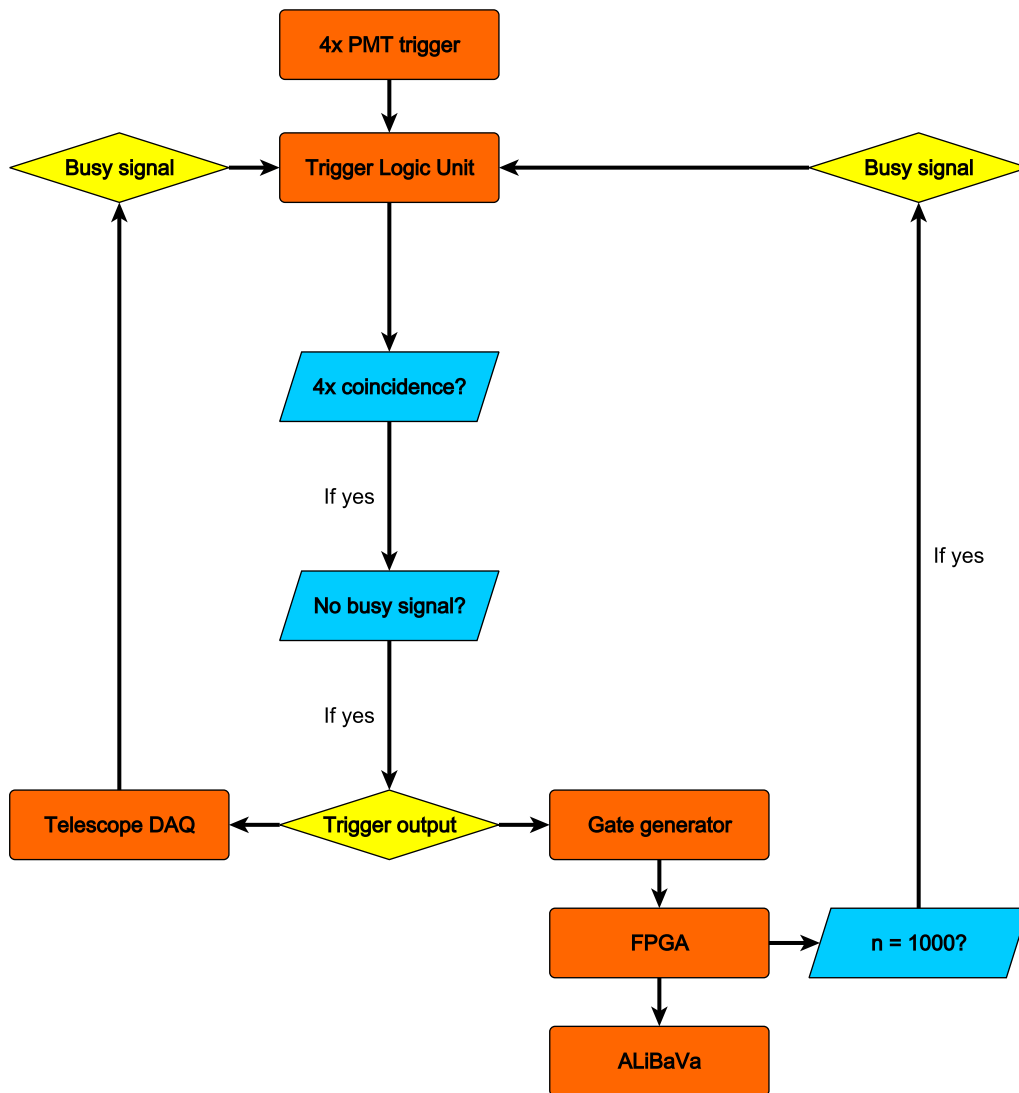
Figure 5.6: Schematic of the setup used to combine ALiBaVa and telescope DAQs.

trigger signal is issued to the telescope DAQ and the gate generator simultane-ously. The telescope acknowledges the trigger and issues a busy signal to the TLU, so that no other triggers are sent during its readout. The gate generator shapes the trigger signal, damping any spikes on the trigger line. The gate generator's output line is sent to an FPGA. The FPGA counts triggers and sends incoming triggers out to the ALiBaVa's trigger input. If the FPGA count reaches 1000, it issues a 2.5 s long busy signal back to the TLU. This time is sufficient for the ALiBaVa to write out its buffer to disk and prepare for the next trigger.

With this method, there is no need for a global clock, as both DAQ systems are synchronous on an event-by-event basis. Both data streams can then be matched offline. A disadvantage is the resulting event rate, which on average is only 125 Hz.

5.3 ANALYSIS CHAIN

The strategy behind the analysis chain in EUTelescope, as introduced in section 3.4, is aimed at transforming discrete charge depositions in the individual pixel beam telescope planes and the strip sensor DUT into higher level objects, such as tracks in a global coordinate system, with which the properties of the DUT can then be assessed. The combination of a strip sensor, read out by an ALiBaVa system, with the pixel telescope planes in EUTelescope necessitates a major redesign of the EUTelescope analysis chain. New processors are introduced and existing ones modified. An overview of the analysis steps and the corresponding EUTelescope processors is given in figure 5.7. They are described in detail in the following chapters.

In order to be able to reconstruct these tracks, all six telescope planes and the DUT must be correctly aligned. Emphasis is placed on the fact that the final sensor analysis presented in section 5.4 does not use the DUT clusters and hits obtained from EUTelescope processors, as these are only used for the alignment and the subsequent tracking.

5.3.1   *Data Conversion and Concatenation*

As a first step, both the ALiBaVa and MIMOSA 26 raw data files are converted to the LCIO data format, which is described in section 3.4.2. Wide TDC time cuts (cf. section 3.6) are placed on the ALiBaVa data to ensure only good hits are used for alignment. Events with a TDC time below 35 ns or above 55 ns are flagged for later removal. The raw ADC values for all 128 channels of the two chips in the ALiBaVa system are written out for each event. At this stage, a cut on the Beetle chip's temperature is possible.

On the telescope side, hot pixels are removed from the zero suppressed, binary telescope data. A pixel is considered hot if it fires in more than 0.1 % of events.
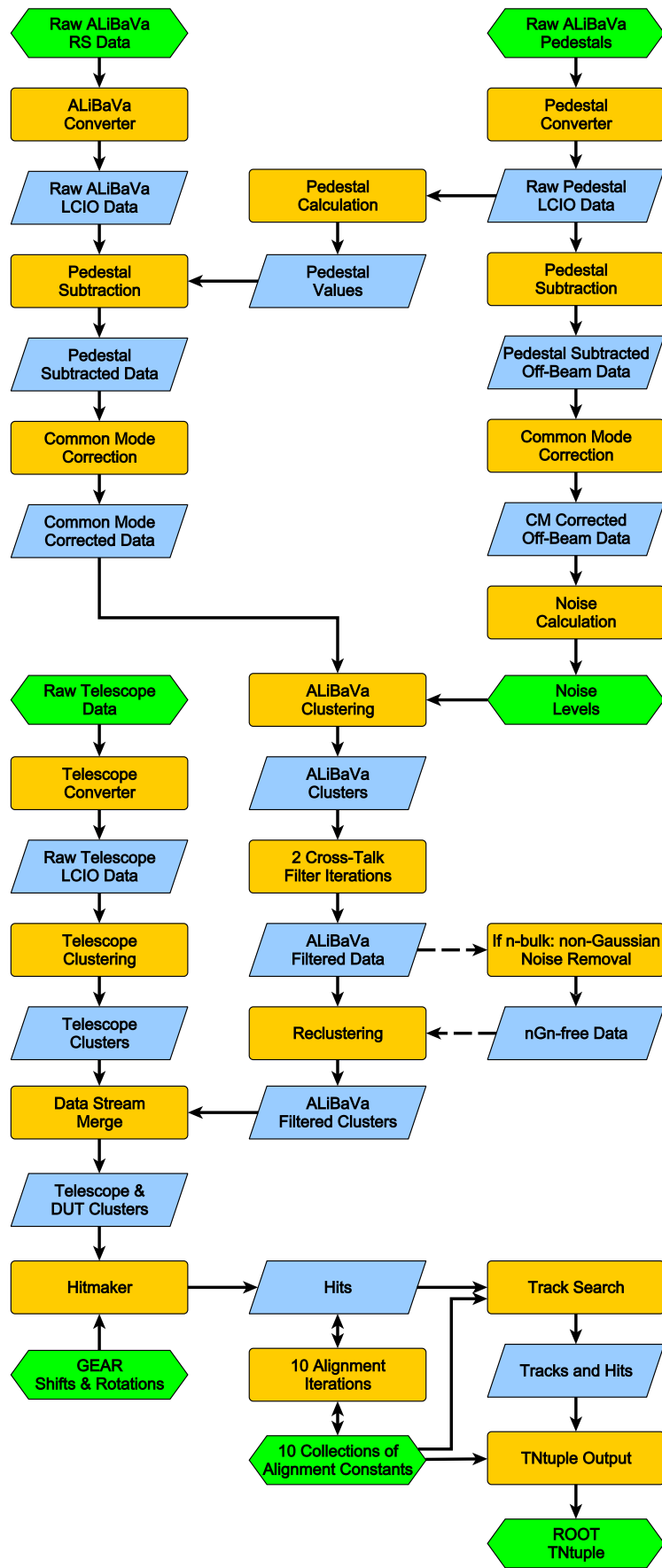
Figure 5.7: Schematic of the analysis chain implemented in EUTelescope. Data states are indicated blue, processors yellow. External files are shown in green.

Depending on beam telescope (DATURA or ACONITE) and plane, up to about 100 pixels of the $1152 \times 576 = 663552$ pixels are removed. For each telescope plane and event, the x and y coordinates of fired pixels are written out. For simplicity, the LCIO data of ALiBaVa and telescope are still in separate files.

Several runs in test beam area 22 with the ACONITE telescope were taken with other experimental groups as the primary beam users. This sometimes resulted in long accesses to the beam area, in which no data was recorded. Nevertheless, the DAQ systems were left running. Because of this, it occurred in some cases that the telescope raw file reached a file size limit, so that two or more files were written to disk. After the conversion of each raw file to the LCIO data format, these runs are immediately concatenated into one LCIO file.

5.3.2 *Telescope Clusters*

In the following step, cluster patterns of fired pixels are searched on the telescope data. Two searchable cluster shapes are included in EUTelescope: a fixed frame of $N \times N$ fired pixels or a sparsified group of neighbouring pixels. To ensure optimal clustering performance, the latter algorithm was used [115]. An example of cluster shapes can be seen in figure 5.8. The geometrical centre of gravity is then calculated for each cluster, with all individual pixel charges equal to 1 ADC.
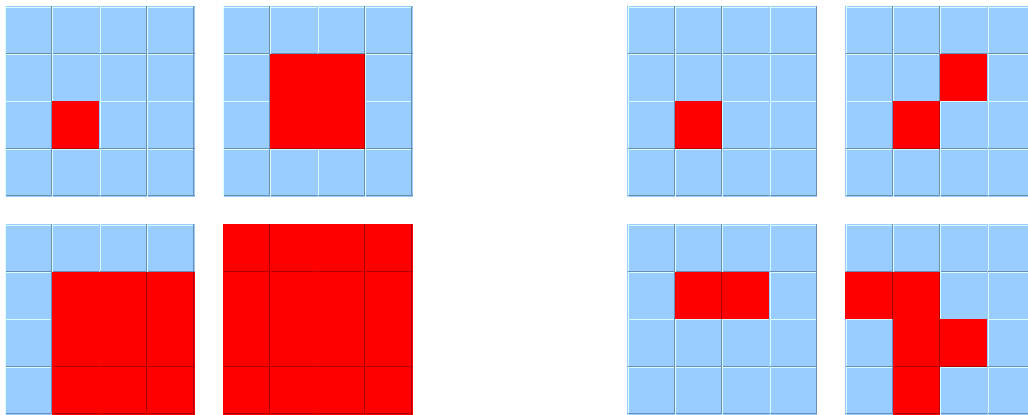
Figure 5.8: Examples of telescope cluster shapes. Hit pixels are coloured red. Left: Fixed frame algorithm, with $N = 1, 2, 3$ and 4. Right: Some example cluster shapes found with the sparse cluster algorithm.

5.3.3 *Pedestal Analysis and Data Reconstruction*

The pedestal analysis for the ALiBaVa data was written into LCIO processors and performed on specific off-beam pedestal runs. For each channel, the raw ADC values are filled into a histogram over all events and fitted with a Gaussian function. An example is shown in figure 5.9. The mean of this fit gives the channel's

pedestal value, the width the preliminary noise. Channels with noise outliers and their neighbours are masked from here on. This can be seen in figure 5.10. The pedestals for each channel are written out and then subsequently subtracted from the raw ADC counts in a separate EUTelescope processor.
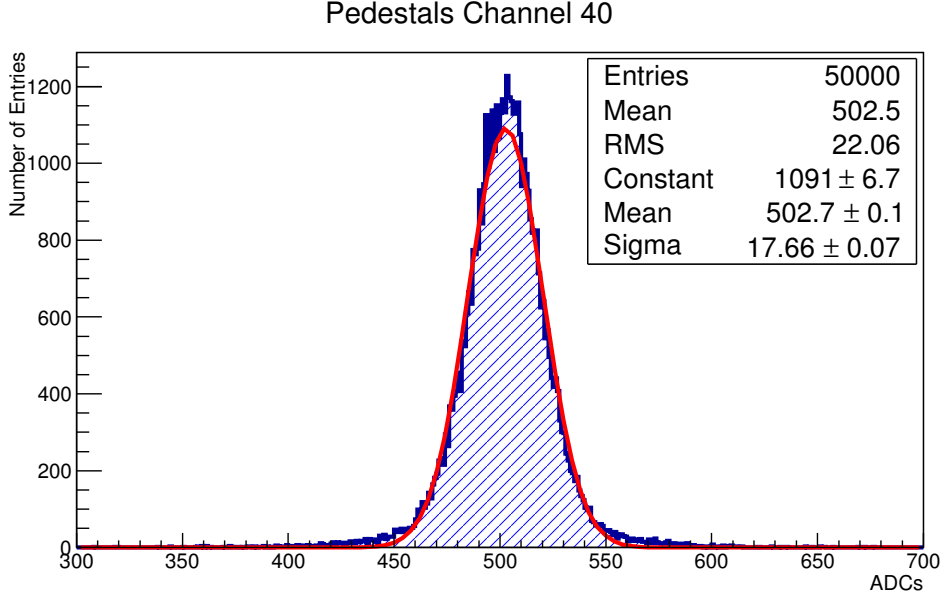

Figure 5.9: Pedestal distribution of channel 40, taken from a non-irradiated epitaxial sensor with p-stop isolation technology at $-300\,\mathrm{V}$ bias. The pedestal value for this channel is (502.7 ± 0.1) ADCs.

After the pedestals have been subtracted, the common mode value for each event is calculated. In a first step, the mean signal of all unmasked channels in an event is calculated. In two subsequent iterations, any signals outside of 2.5 times the standard deviation are excluded from the calculation of the mean. The common mode of an event is then assumed to be sloped over the channel domain, with the common mode value c_i for a channel i expressed by

$$c_i = a + b \cdot i \tag{5.1}$$

with parameters

$$a = \frac{\sum_i i^2 \cdot \sum_i s_i - \sum_i (i \cdot s_i)}{\Delta}, \tag{5.2}$$

$$b = \frac{N \cdot \sum_i (i \cdot s_i) - \sum_i i \cdot \sum_i s_i}{\Delta}, \tag{5.3}$$

and

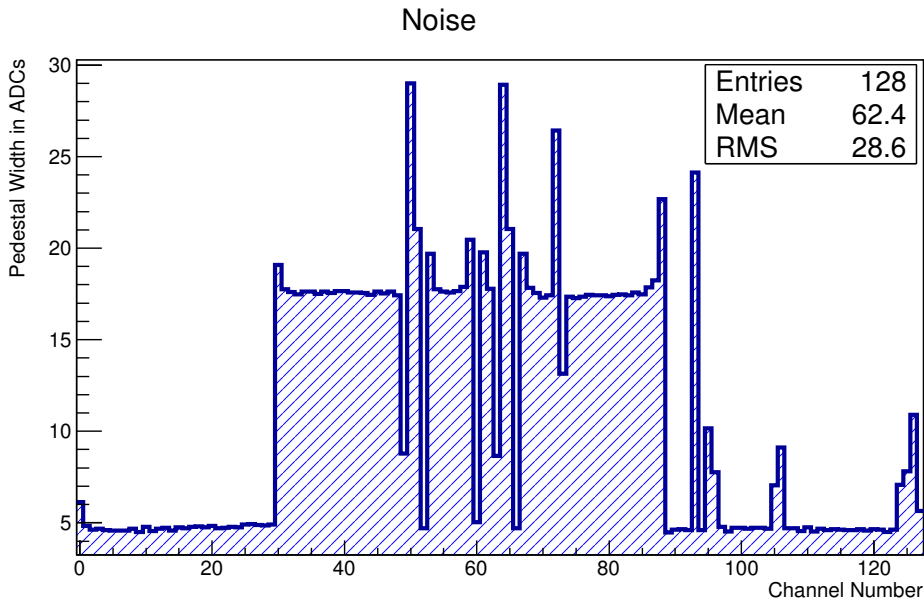$$\Delta = N \cdot \sum_i i^2 - \sum_i i \cdot \sum_i i, \tag{5.4}$$

Figure 5.10: The preliminary channel noise of a non-irradiated epitaxial sensor with p-stop isolation technology at $-300\,\text{V}$ bias. Outliers, such as the channels between 49 and 53, stem from broken channels or misplaced bond wires. Channels below channel 31 and above channel 87 have no sensor strip bonded to them. They all are masked for the following analysis.

s_i representing the pedestal corrected signal of channel i in this event and N the number of channels. An example event can be seen in figure 5.11. The individual common mode values are then subtracted from the signal.

The sum of all corrections to a channel in an event is calculated and subtracted from the off-beam pedestal run. The result is filled into a histogram, after which a Gaussian fit is performed. The width of these Gaussians is now considered the channel's noise value and is used in the subsequent clustering steps. An example is shown in figure 5.12.

With the pedestal values and common mode correction algorithm described above, the on-beam data is now corrected. Pedestals are subtracted from each channel and the common mode is calculated for each channel and event before subtraction. Each step writes its own LCIO file and LCIO collection.

5.3.4 *Clustering*

As done with the telescope data, clusters are searched on the now corrected ALiBaVa DUT data with a specially written EUTelescope processor. However, there are great differences between these steps, as a telescope plane is a digitally read out pixel sensor, whereas the ALiBaVa DUT is strip sensor with analogue readout.
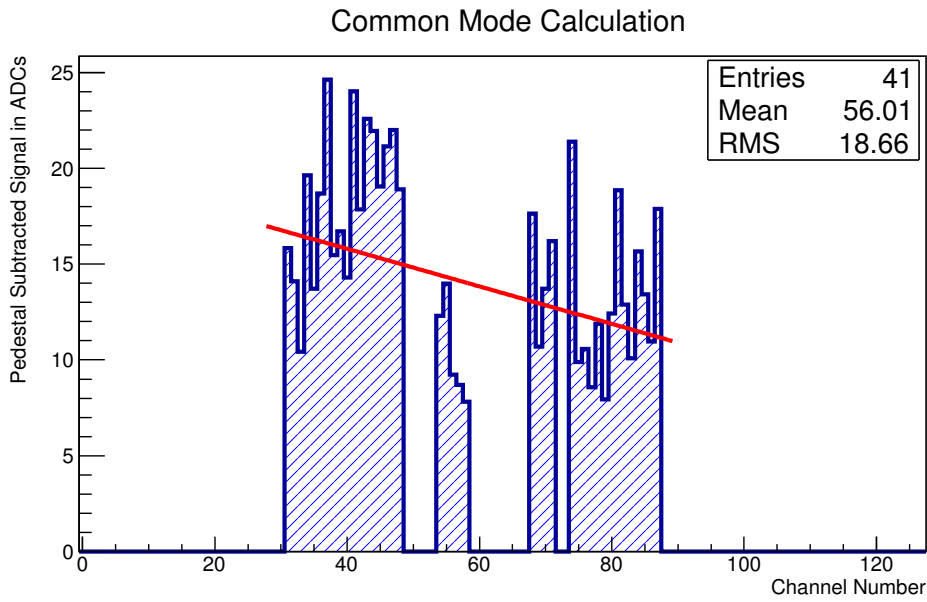
Figure 5.11: Calculation of an event's common mode after each channel's pedestals have been subtracted. The signal in masked channels has been set to 0 ADCs for this plot. A common mode value for each channel in every event is calculated and subsequently subtracted.
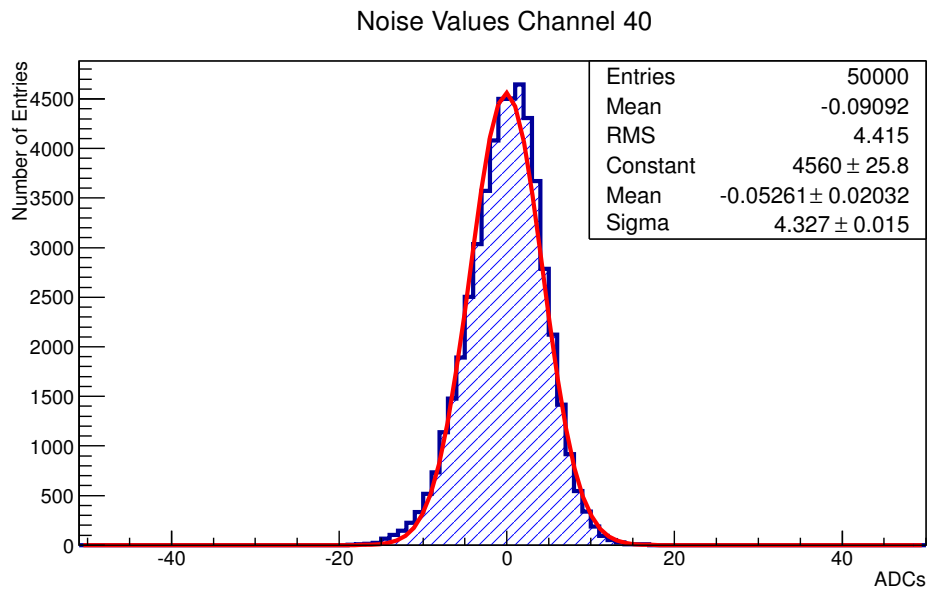
Figure 5.12: Noise distribution of channel 40, taken from a non-irradiated epitaxial sensor with p-stop isolation technology at -300 V bias. Pedestal values and common mode noise have been subtracted from the off-beam pedestal run. From the Gaussian fit, this channel's noise is determined to be 4.3 ADCs.

In each event, the processor searches for a channel with a corrected signal larger than five times this channel's noise value. The channel must not be masked and must not border a masked channel on either side. Channels fulfilling these requirements are considered seeds of a cluster.

Non-masked channels, neighbouring a seed, can be added to the cluster if they have a signal higher than 2.5 times their noise. If a *neighbour* channel has a higher signal-to-noise ratio than its *seed*, their roles are swapped. If a neighbour channel is found between two seeds, two clusters are created and the neighbour is assigned to the seed with the higher signal-to-noise ratio. In the highly unlikely case that two channels passing the neighbour cut are found between two seed channels, they are split into two clusters. Some cluster control plots are shown in figure 5.13.

5.3.5 *Filtering*

After clustering, the η-distribution (cf. section 2.1.2.9) is calculated for each run. It has been found that all runs show a distinct asymmetry, as can be seen in figure 5.14. With η defined as

$$\eta = \frac{Q_L}{Q_L + Q_R} \, ,$$ (5.5)

it can be concluded that the right neighbour channels of seed strips have comparatively more charge than the left neighbour channels. This is due to the way the η-distribution is calculated. The charges of the two channels neighbouring the seed are compared. If the channel on the left has a higher charge than the channel on the right, it is assigned to Q_L and the seed channel to Q_R. If the charge in the right neighbour channel is larger than that on the left, it is assigned to Q_R and the seed to Q_L. As the seed charge is larger than the neighbouring charge, the latter case must happen more often for a resulting η-distribution with an asymmetry towards 1.

A comparison of the neighbour channel's charges relative to the seed strip gives the distributions in figure 5.15. The data, which is taken from a non-irradiated epitaxial sensor with p-stop isolation technology at $-300\,\text{V}$ bias, shows the mean charge of a channel located to the left of a seed to be 2.6 % the seed's charge. On the right side of the seed, this value rises to 6.4 %, explaining the asymmetry in the η-distribution shown in figure 5.14.

Data taken by Yildirim in a separate test beam setup [134] with a different ALiBaVa system and sensors show similar cross-talk effects. This is shown in figure 5.16.

A possible explanation for this effect could be the serial readout mode of the Beetle chip [85] used by the ALiBaVa system: in each event, channels are read out serially, starting with channel zero. A signal distortion in the readout cable could
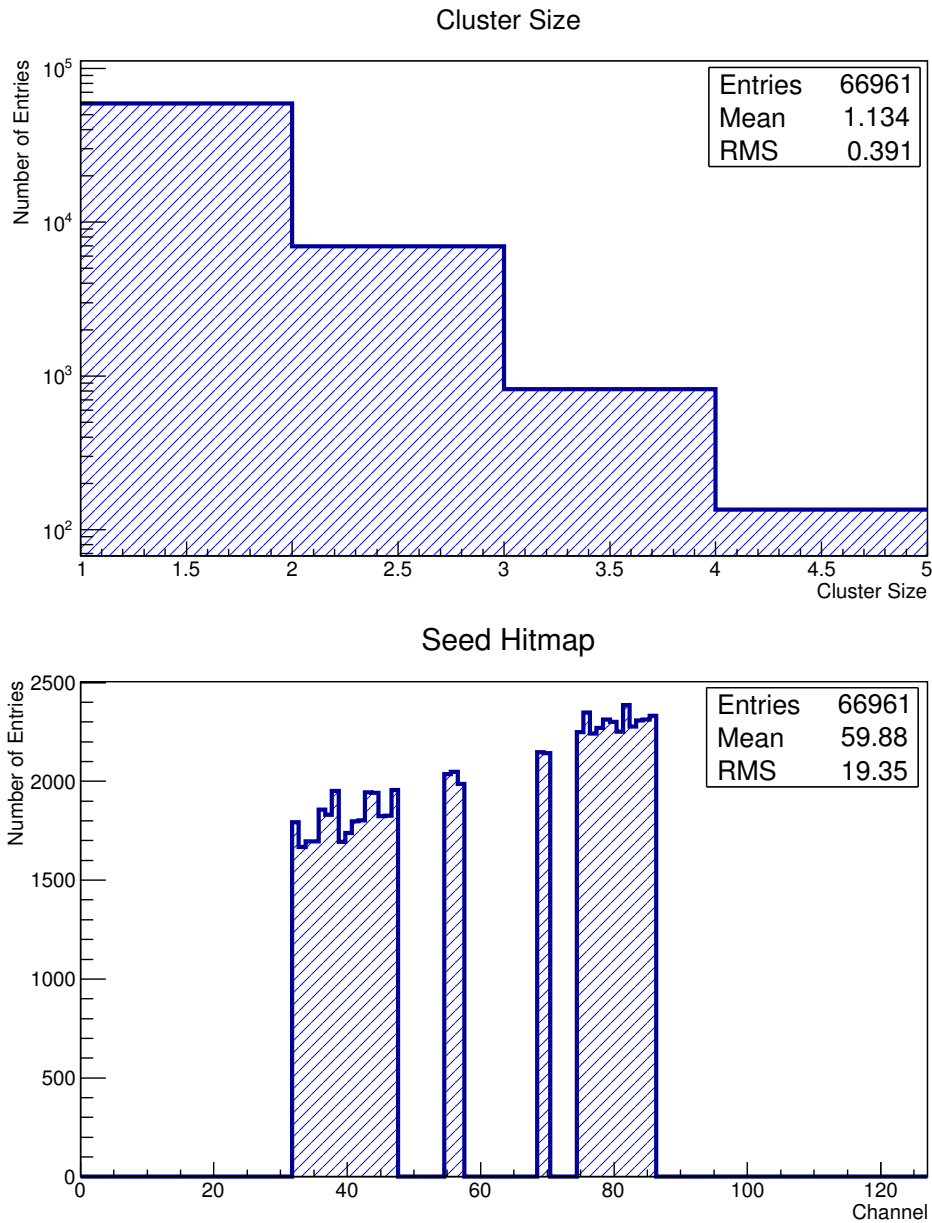
Figure 5.13: Cluster control plots. Top: Cluster size distribution in logarithmic scale, showing a mean cluster size of 1.1 with an RMS value of 0.4. Bottom: Distribution of found seeds during the clustering process over the channel domain. Due to the positioning relative to the beam during this particular run, more seeds are found on channels with a higher number. Both plots are from a non-irradiated epitaxial sensor with p-stop isolation technology at $-300\,\text{V}$ bias.

Figure 5.14: An asymmetric η-distribution as observed after clustering. The two Gaussian fits are merely to guide the eye.

Figure 5.15: Charge distributions of the channels neighbouring the seed. The top row shows the channels neighbouring the seed to the left and to the right. The bottom row shows the next but one neighbours on the left and right, respectively.
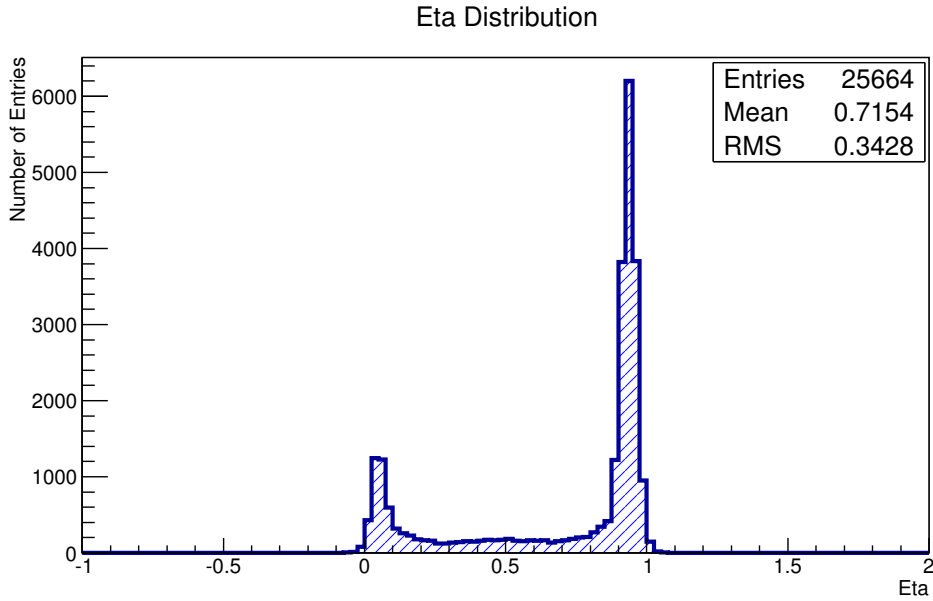
Figure 5.16: An asymmetric η-distribution can also be observed in data taken by an independent setup, here from Yildirim [134].

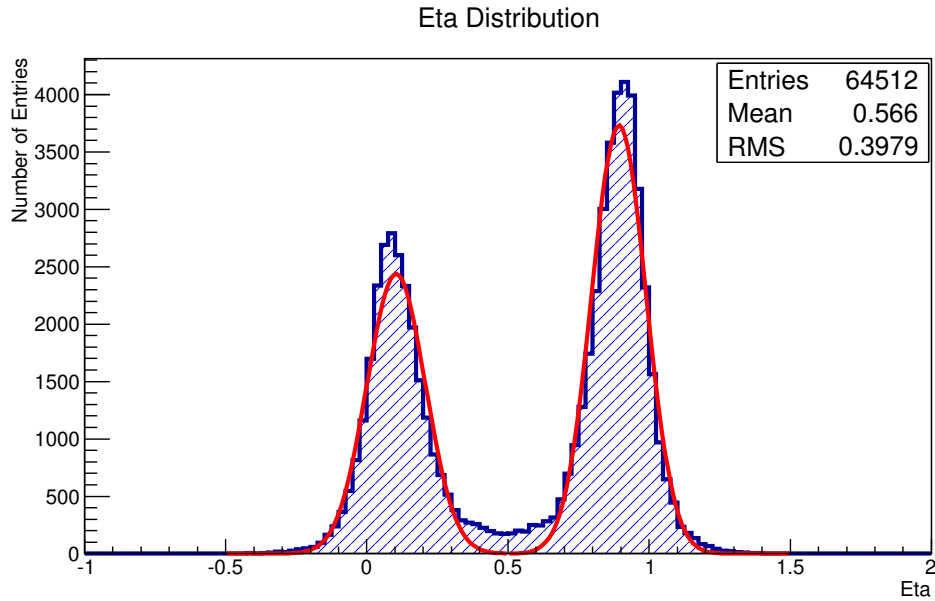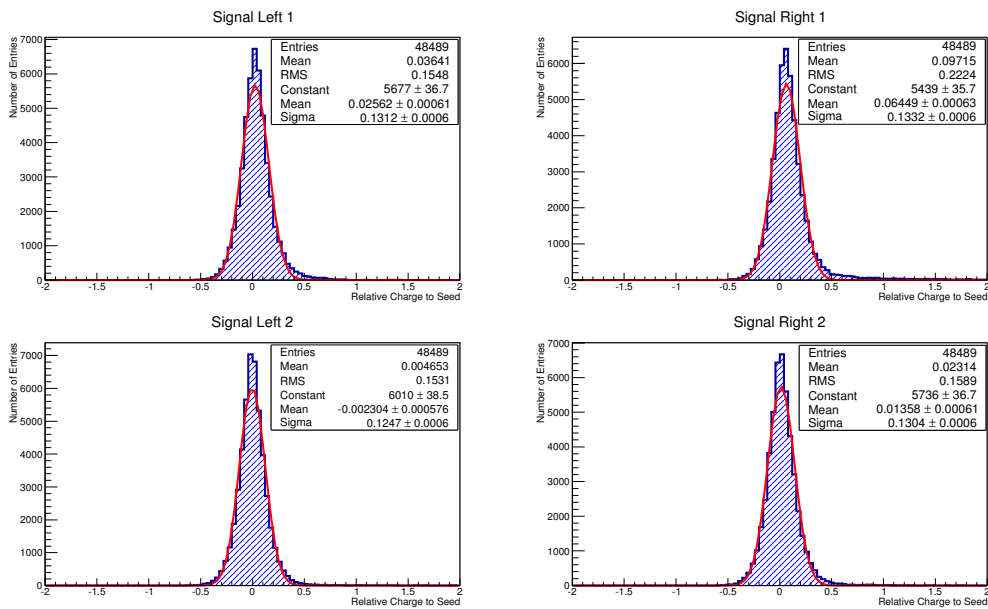lead to charge from earlier channels being added to later channels. A bias toward higher channel numbers could be the cause of the asymmetric cross-talk observed in the η-distributions.

It should be noted that other laboratory analyses using the ALiBaVa setup by Erfle [53] found a similar asymmetry in charge distribution. The asymmetry was corrected by shortening and shielding the ribbon cable between ALiBaVa motherboard and daughterboard. The LHCb experiment's VELO Detector, which also uses the Beetle chip observes similar cross-talk. This cross-talk is corrected by implementation of a FIR[1] filter, as described in [2] and [128]. Butz [19] also observes cross-talk in strip sensor data, read out by a different chip, and shows it can be corrected by implementing a FIR filter.

5.3.5.1 *Filter Implementation*

In a general FIR filter of the order N, each output value y is computed as a weighted sum of the previous N input values x:

$$
\begin{aligned}
y[n] &= b_0 \cdot x[n] + b_1 \cdot x[n-1] + \ldots + b_N \cdot x[x-N] \\
&= \sum_{i=0}^{N} b_i \cdot x[n-i] \,.
\end{aligned}
\tag{5.6}
$$

---

1 Finite Impulse Response.

Since no cross-talk beyond two channels is observed, a filter order of $N = 2$ is sufficient. This is also consistent with observations from the Beetle header cross-talk, which are shown further on. Equation 5.6 can then be written as:

$$y[n] = 1 \cdot x[n] - b_1 \cdot x[n-1] - b_2 \cdot x[n-2] \,, \tag{5.7}$$

with b_1 and b_2 both $\geqslant 0$. The above algorithm is modified such, that the cross-talking charge components subtracted from channel n, $b_1 \cdot x[n-1]$ and $b_2 \cdot x[n-1]$, are added back to the channels $n-1$ and $n-2$ they originated from, respectively. This ensures conservation of charge:

$$\sum_n Q_{\text{prefilter}} = \sum_n Q_{\text{postfilter}} \,. \tag{5.8}$$

The values of b_1 and b_2 are determined by the means of the neighbour and next but one neighbour charge-to-seed ratios, shown in figure 5.15.

$$\begin{aligned} b_1 &= \sum_n \frac{Q_{\text{left}}}{Q_{\text{seed}}} - \sum_n \frac{Q_{\text{right}}}{Q_{\text{seed}}} \\ b_2 &= \sum_n \frac{Q_{\text{left but one}}}{Q_{\text{seed}}} - \sum_n \frac{Q_{\text{right but one}}}{Q_{\text{seed}}} \,. \end{aligned} \tag{5.9}$$

Moving from the rightmost to the leftmost available channel, the reconstructed DUT data is filtered in two iterations. After each iteration, the data is reclustered to calculate the charge-to-seed ratios. Then b_1 and b_2 are recalculated accordingly.

5.3.5.2 *Comparison with Header Cross-Talk*

During the readout of an event, the Beetle chip sends out 16 binary headers prior to sending the channel data, as shown in figure 5.17. These headers contain information such as the chip status and parity bits and are not used for this analysis, but can nevertheless be accessed. These headers should also cross-talk, both onto themselves as well as onto the first channels. Since no sensor is bonded to these channels, sensor effects can be excluded.

An EUTelescope processor has been written to access the headers and calculate and subtract the pedestal of each header. Figure 5.18 shows the correlations between the first channel and the last two headers. After pedestal subtraction, a binary header produces a signal of approximately ± 109 ADCs. The last header (header channel 15) changes the signal in the first data channel by ± 3.9 ADCs. The last but one header (header channel 14) has an influence of about ± 1.5 ADCs. Filter coefficients calculated from these ratios are very similar to those calculated by the method described above, as can be seen in table 5.4.
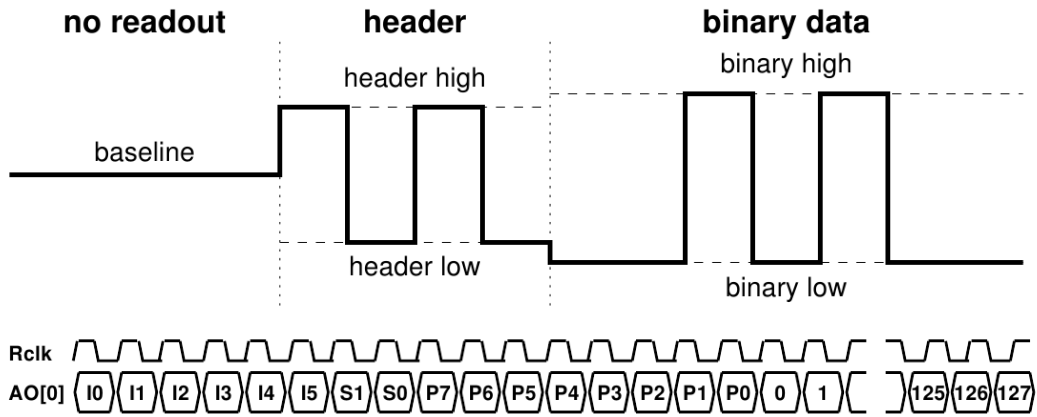
Figure 5.17: Top: Schematic of the pulse heights for reading out binary headers or binary data. Bottom: The readout sequence of the Beetle chip. 16 binary headers I0, ..., S1, ..., P0 and the 128 analogue channels are multiplexed onto the output port $A0[0]$ with the clock speed of 40 MHz. Both figures taken from [85].
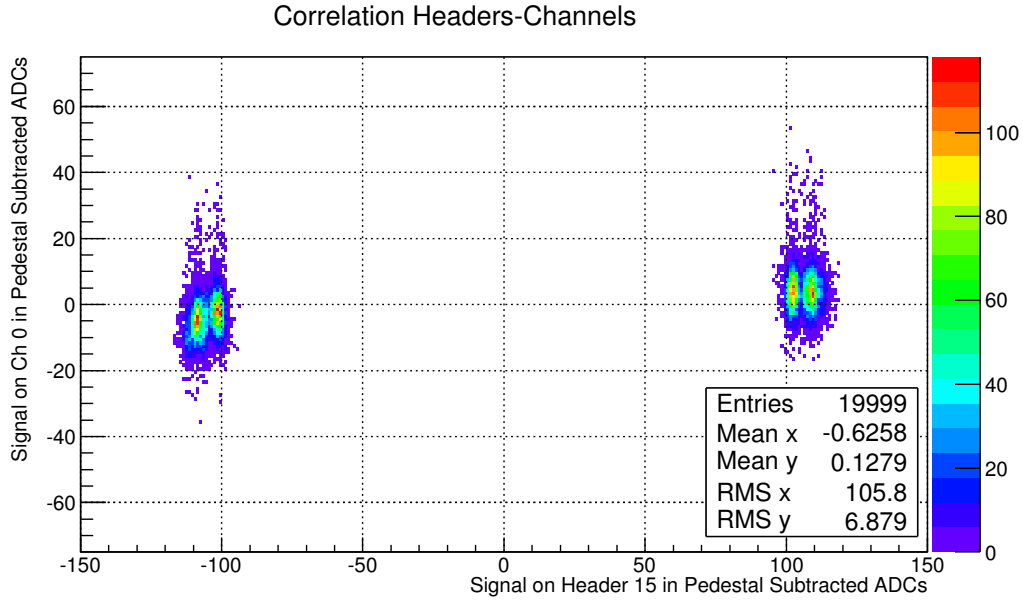
Figure 5.18: Cross-talk between the last headers and the first channel. The signal height in the first channel (channel 0) depends on the signal height (binary high or low) of the last header (header 15). Within each header signal peak, one can distinguish two sub-peaks from the last but one header (header 14). The colour scale denotes entry counts.

Table 5.4: FIR filter coefficients b_1 and b_2, as obtained from the sensors' η-distributions and coefficients c_1 and c_2, as obtained from the Beetle chip's header. Values are averaged over all $0°$ beam incidence runs.

Coefficient	p-stop sensors	p-spray sensors	n-bulk sensors
b_1	3.4 %	3.4 %	3.6 %
b_2	1.4 %	1.5 %	1.3 %
c_1	3.2 %	3.3 %	3.3 %
c_2	1.3 %	1.4 %	1.3 %

### 5.3.5.3 *Reclustering*

Following the filtering of the DUT data, clustering is once more performed as described in section 5.3.4. This is due to the fact that the filtering steps might have changed cluster positions, with the ADC counts of individual channels now above or below the thresholds. The overall cluster count or cluster size distribution is not changed significantly. Finally, the η-distribution is recomputed as a control plot, no longer showing an asymmetry, as can be seen in figure 5.19.
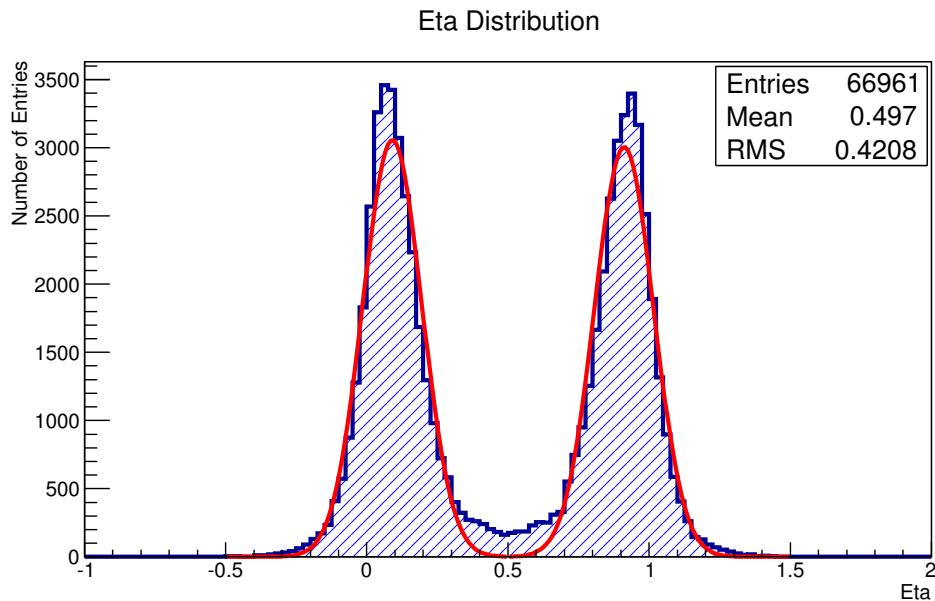
Figure 5.19: The η-distribution after two filtering iterations and reclustering has been performed. The asymmetry previously observed has been removed, the Gaussian fits again are solely to guide the eye.

Since the filtering process has changed the ADC values of each channel, the channel's signal distribution, the pedestal, common mode and noise levels can also change. With the filter coefficients obtained from the clustered data, the off-beam pedestal runs can be filtered and the noise values recalculated. The recalculated noise distribution for an example channel is shown in figure 5.20. Compared with the distribution without filtering from figure 5.12, the difference is about 0.2 ADCs. This change, amounting to $\approx 5\,\%$ of the noise levels, is small, especially compared

with the differences between channels. Therefore the pedestal data is not filtered and the beam data not recorrected.

Figure 5.20: Noise distribution of channel 40, taken from a non-irradiated epitaxial sensor with p-stop isolation technology at $-300\,\text{V}$ bias after filtering. Pedestals and common mode have been subtracted from the filtered raw data. From the Gaussian fit, this channel's noise is determined to be 4.6 ADCs.
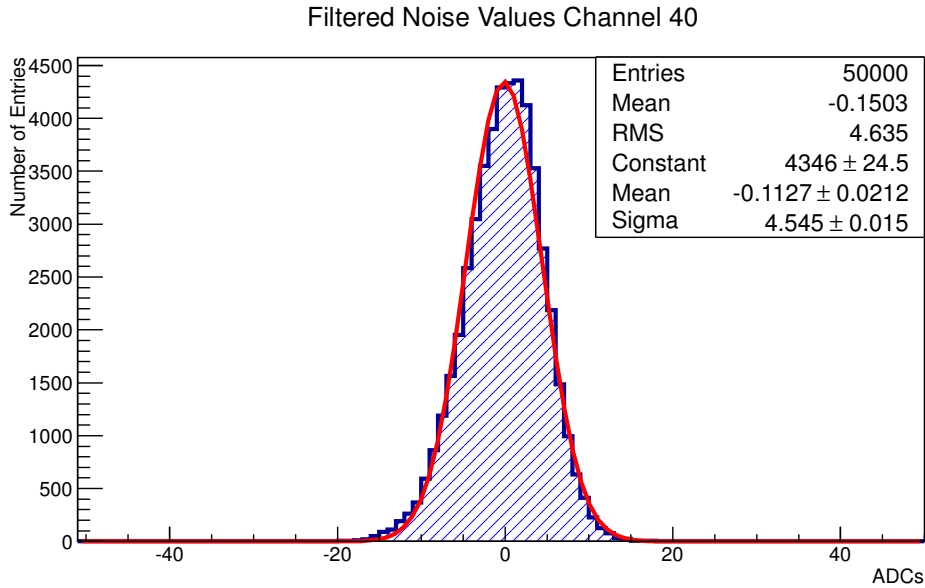
5.3.5.4 *Non-Gaussian Noise*

Previous works by Erfle [53] and Nürnberg [99] discovered increased noise in n-bulk sensors from the HPK campaign. This effect was found to depend on bias voltage, sensor thickness, sensor annealing state and irradiation. The increased noise consists of two main contributions: a broadened Gaussian noise distribution and non-Gaussian discharges. Within this test beam campaign, the effect was also observed. An example off-beam noise distribution illustrating this effect is shown in figure 5.21. Each channel's signal is filled into a histogram in events where no track is traversing the DUT sensor. A Gaussian is fitted to the distribution, in this case returning a noise value of 7.1 ADCs. Entries outside $[-5\sigma, 5\sigma]$, i.e. the tails of the distribution, are considered non-Gaussian noise discharges.

Especially the non-Gaussian noise contributions are problematic for a sensor operating as a tracking detector, as high signal discharges could be wrongly identified as a particle hit. At this point in the analysis, fake hits can lead to a misalignment of the DUT relative to the telescope planes. To combat this effect, the following corrections were applied to all n-bulk sensors with a non-Gaussian noise ratio of over 1 %, in an attempt to salvage some of the data:
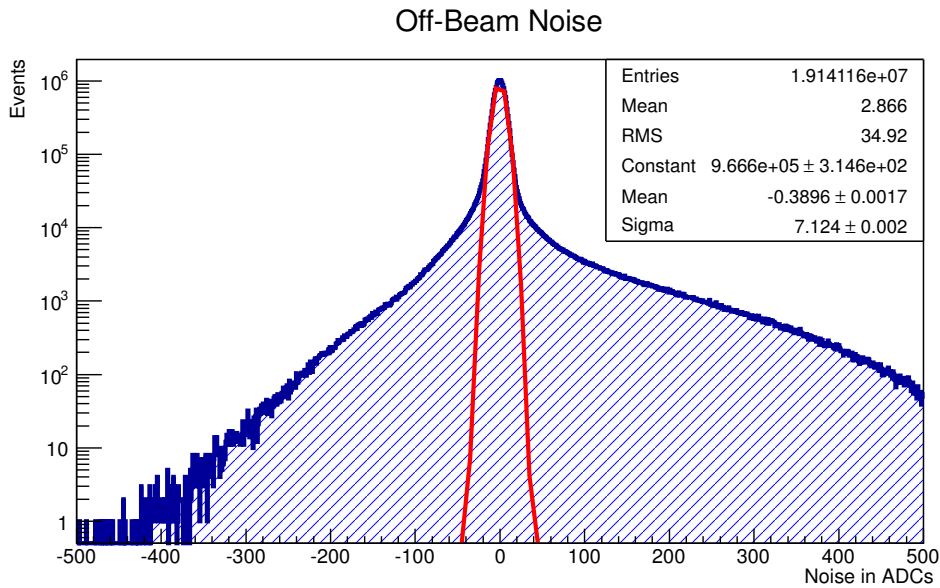
Figure 5.21: Noise distribution in log scale of an n-bulk sensor, biased to $400\,V$ and irradiated to $1 \times 10^{15}\, n_{eq}/cm^2$. Besides the already wide Gaussian distribution centred around 0 ADCs, non-Gaussian tails to both sides can be seen.

- All signals over 150 ADCs are considered to be noise discharges. An event with any channel over this limit is discarded from clustering.

- As can be seen from p-bulk data, events with more than one DUT cluster per event are rather unlikely. Events with multiple clusters are therefore also removed for clustering.

- Figure 5.22 shows a typical event with a noise discharge. Some discharges passing the seed cut can be identified as noise by looking at their neighbour channels. Should a seed candidate have a neighbouring channel with signal of twice the negative channel noise, the event is discarded for clustering.

With the cuts and selections described above, non-Gaussian noise discharges can be omitted in some of the n-bulk runs. With these signals discarded for the clustering process, the alignment steps described in the following produce a functioning set of alignment constants. The majority of n-bulk runs however, especially at high fluences and bias voltages, cannot be salvaged. Noise levels here are too high and the amount of non-Gaussian entries exceeds 5 %. For these runs, it is also questionable if the pedestal and common mode subtraction techniques described above work.

For the following analysis, only those n-bulk sensors are considered which can be corrected by this method and their results are shown for comparison.
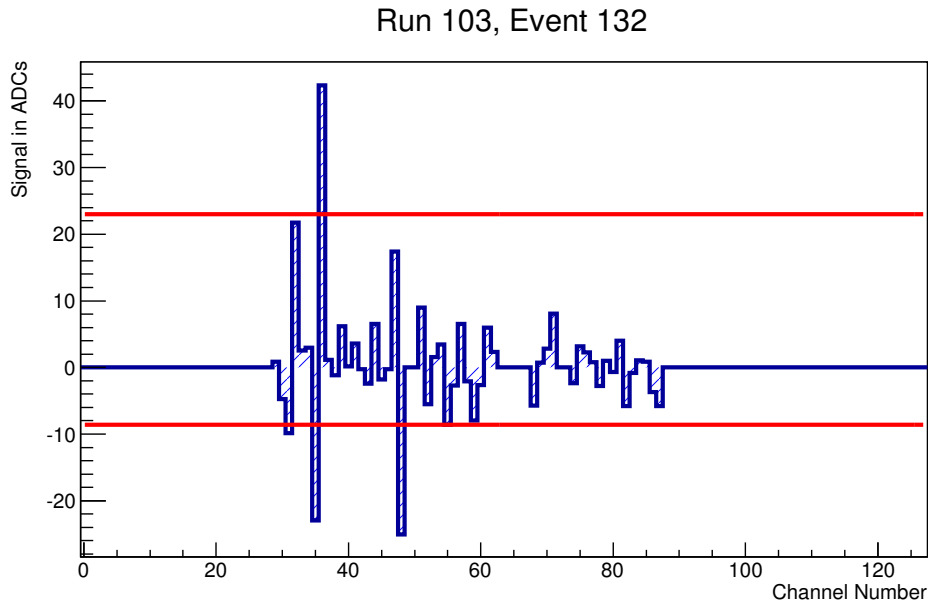
Figure 5.22: An event with a noise discharge. Shown are the signals of each channel with a line indicating the seed cut (top) and twice the negative noise value (bottom). Channel 36 passes the seed cut, but as it has a neighbour channel (35) with a signal twice as high as the negative noise, it is not considered for clustering. The event is taken from a 100 μm thick epitaxial n-bulk sensor, biased to 300 V and irradiated to 1.5×10^{15} n_{eq}/cm^2.

5.3.6   *Merging the Data Streams*

Before merging the two-dimensional telescope clusters with the one-dimensional DUT clusters, the DUT clusters have to be transformed into the telescope LCIO cluster data structure, which means assigning a second spatial coordinate to each cluster, even though the strip sensor only has one sensitive dimension. To achieve this, the relative position of each ALiBaVa cluster on the DUT is calculated in its sensitive dimension. Following that, the telescope cluster nearest this relative position in the DUT's sensitive dimension on the preceding telescope plane is searched. This cluster's coordinate in the DUT's unsensitive dimension is then assigned to the DUT cluster. Should there be no telescope cluster in this event on the preceding plane, the plane further upstream is used.

After transformation of the DUT clusters into two-dimensional clusters, both telescope and DUT cluster collections can be merged. This process is eased by the fact that LCIO collections are event-based and both LCIO cluster collections now have the same structure. Control plots, showing the difference Δy between relative cluster position in a telescope plane and in the DUT are written and can be seen in figure 5.23. The relative distance Δy is calculated from the centre of gravity of the telescope and DUT clusters $CoG_{Tel,y}$ and CoG_{DUT} respectively, and the total

number of pixels $N_{\text{Pixels,y}}$ available in the telescope plane and number channels N_{Channels} in the DUT:

$$\Delta y = \frac{\text{CoG}_{\text{Tel,y}}}{N_{\text{Pixels,y}}} - \frac{\text{CoG}_{\text{DUT}}}{N_{\text{Channels}}}. \tag{5.10}$$

A loss of synchronisation during data taking can now be visualised. A correlation between the DUT seed channel and the seed position on the corresponding axis of the telescope plane 2 also indicates a successful merge of streams. An example is shown in figure 5.24.
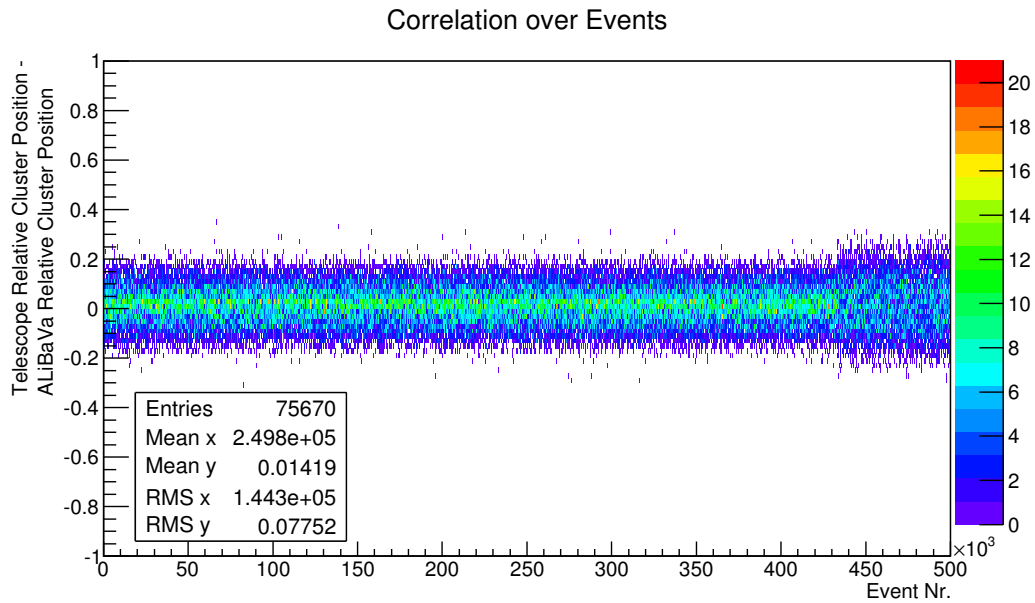
Figure 5.23: Control plot for merging the telescope and DUT data streams. The difference Δy (cf. equation 5.10) between relative cluster positions on DUT and preceding telescope plane is plotted over events. A sudden widening of the distribution, as can be seen from event 430000 onwards, indicates loss of synchronisation.

If a synchronisation loss has been detected, individual events in either telescope or DUT data stream can be skipped in order to regain synchronisation.

5.3.7 *Hit Creation and Coordinate Systems*

With both data streams merged into one collection and file, the cluster centre of gravity positions are now transformed into hits in a global three-dimensional coordinate system. A separate GEAR file (cf. section 3.4.3) for all different measurement setups was created and instructs the hit making processor on how to position and rotate each telescope and DUT plane.

Figure 5.24: Seed correlation between telescope plane 2 and the ALiBaVa DUT. The colour scale shows the entry count of a bin. The diagonal, which can be seen from bottom left to top right, indicates a correlation between telescope and DUT.

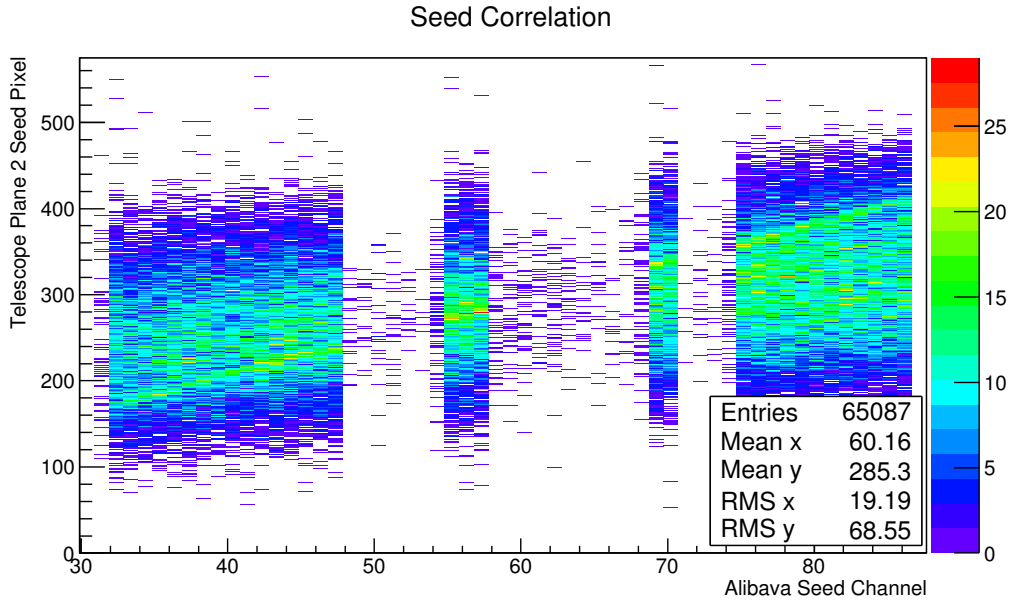The default EUTelescope orientation has been used: in the test beam areas 21 and 22 the positive x direction points South, the positive y direction towards the floor and the positive z direction along the beam axis. This also defines the rotations of the DUT, which in this measurement programme were in a negative α direction. For reference, a diagram of the coordinate system is depicted in figure 5.25.

The translation between local sensor coordinates and global xyz coordinates is done by

$$x,y_{\text{global}} = \left(-\text{Cluster}_{\text{CoG } x,y} + \frac{N_{\text{channels } x,y}}{2} - 0.5 \right) \cdot \text{Pitch}_{x,y} , \qquad (5.11)$$

with z_{global} set by the plane position from the GEAR file. x_{global}, y_{global} and z_{global} are the coordinates of each hit in the global coordinate system. $\text{Cluster}_{\text{CoG } x,y}$ is the position of each cluster centre of gravity in local channel units. $N_{\text{channels } x,y}$ is the total amount of channels in the particular plane and dimension. $\text{Pitch}_{x,y}$ is the corresponding pitch. Equation 5.11 positions the centre of each sensor plane at the origin of the global coordinate system in the xy plane. If a hit results from a binary cluster, it is placed in the centre of the according channel.

5.3.8 *Alignment and Tracking*

The objective of alignment is to find the actual positions of each telescope and DUT plane, relative to their nominal input positions, by shifts and rotations in all

(a) Global coordinate system

1152 pixels

576 pixels

576

0

1152

0
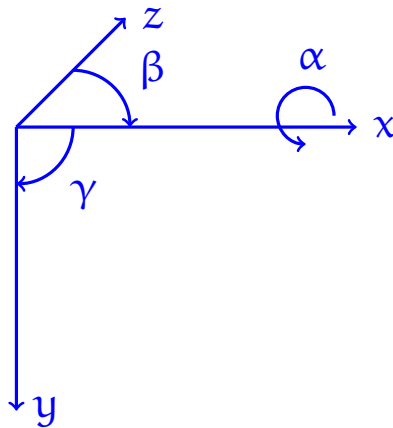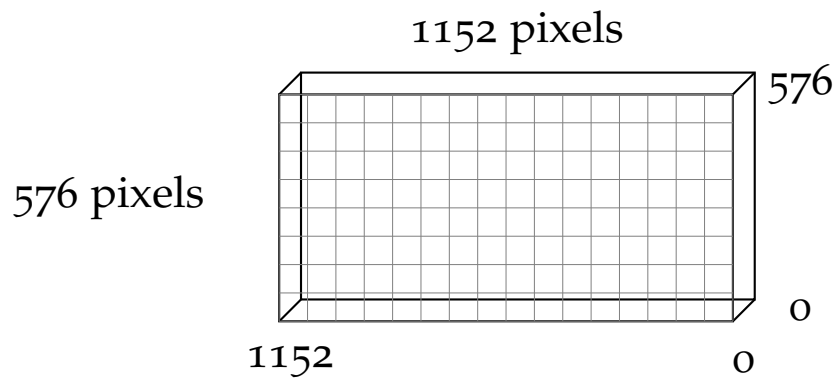
(b) Schematic of a telescope plane

128 channels

128

0
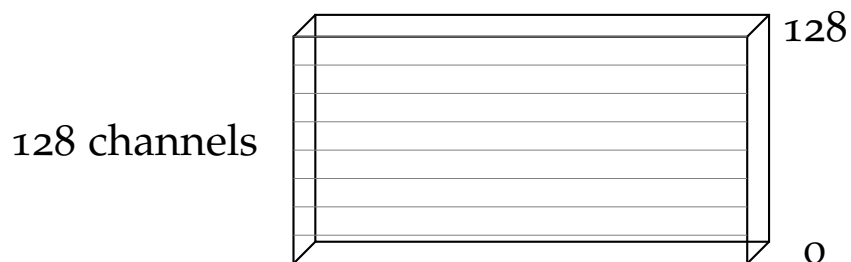
(c) Schematic of the ALiBaVa DUT

Figure 5.25: a) The coordinate system used within EUTelescope at the DESY-II test beam. The positive z axis is in the direction of the beam, the y axis points to the ground and the x axis points South.
b) and c) The pixel and strip orientation for the telescope planes and the ALiBaVa DUT.

six dimensions. In EUTelescope, a tracking processor searches for tracks traversing the telescope and the DUT. These tracks, along with the associated hits, are then passed to `MillepedeII` [17], which performs a least squares fit to determine the alignment constants.

5.3.8.1 *Pre-Alignment*

With all clusters now transformed into hits in a global coordinate system, the telescope and DUT planes can now be aligned. As a preliminary first step, all global hit x and y coordinates are folded back onto the first telescope plane. From the peaks of these distributions, a very rough shift of each plane relative to the first telescope plane can be determined. These shifts are then written out as alignment constants and applied to the hits.

5.3.8.2 *Alignment Iterations*

In EUTelescope, the main tracking processor is the *deterministic annealing filter* (DAF) fitter [62]. DAF is an iterated filter, predicting the track positions in each sensor layer, using information gained from previous tracks [58]. Based on the predictions, weights are assigned to individual hits. Assignment probabilities of hits to a track can be calculated, and the filtering process is repeated with updated information. Implementations of other fitters, such as a fitter based on GBL² [78] exist, but are not yet entirely usable. Over the course of five iterations, an instance of DAF fitter searches for tracks through the telescope and DUT planes and passes the track fit points with their errors to `MillepedeII`, which returns the alignment constants of this iteration. The shifts and rotations from the alignment constants are then applied to the hits. The input parameters are listed in table 5.5 with the coordinates and planes fixed listed in table 5.6. A track is required to have at least one hit in each of the six telescope planes and one in the DUT. The tracks are discarded after an iteration as to not introduce a bias.

Table 5.5: The input parameters for the first alignment iterations. The telescope xy residual cut is denoted by $R_{T\,US}$ for the upstream telescope planes, by $R_{T\,DS}$ for the downstream telescope planes. $\sigma_{T\,xy}$ represents the telescope resolution in both x and y passed to `MillepedeII`, $\sigma_{DUT\,x}$ and $\sigma_{DUT\,y}$ the resolution of the DUT in x and y respectively. All values are given in µm.

Iteration	$R_{T\,US}$	R_{DUT}	$R_{T\,DS}$	$\sigma_{T\,xy}$	$\sigma_{DUT\,x}$	$\sigma_{DUT\,y}$
1	±1000	±2000	±1000	10	55	35
2	±300	±800	±500	8	50	30
3	±300	±800	±400	5	45	25
4	±300	±800	±300	5	35	25
5	±300	±800	±300	5	35	25

---

2 General Broken Lines, cf. also section 3.5.2.

Table 5.6: The fixing of telescope and DUT planes and their coordinates for the first align-
ment iterations. An entry means this coordinate of the plane is fixed. A denotes
a plane that has all coordinates $(x, y, z, \alpha, \beta, \gamma)$ fixed.

Iteration	Plane 0	Plane 1	Plane 2	DUT	Plane 3	Plane 4	Plane 5
1	A	z	z	z	z	z	A
2	A	z	z	z	z	z	A
3	A	z	z	z	z	z	A
4	A	z	z	z	z	z	A
5	A	A	A	x,y,z, α, β	A	A	A

As can be seen in table 5.6, the first and last telescope plane are fixed in their
position during all alignment iterations. This is done to avoid weak modes during
the alignment. The fifth alignment iteration is used solely to remove a DUT mis-
alignment in γ. As this angle represents a rotation around the z axis, the lack of
a sensitive x measurement on the DUT is extremely critical. To further improve
the DUT alignment, a sixth alignment iteration is performed. Here tracks are only
searched in the three upstream telescope planes (0, 1, 2) to exclude any effects
of multiple scattering at the DUT. These tracks are then extrapolated to the DUT
position by means of plane and vector intersection. Following that, the unbiased
residuals (cf. section 2.1.2.10) of the DUT hits with the track extrapolations are
calculated. The residuals are plotted against the x coordinate of the extrapolated
track impact position and a linear fit is applied (see figure 5.26). The slope of this
fit is subsequently considered as an alignment constant for the DUT in γ and ap-
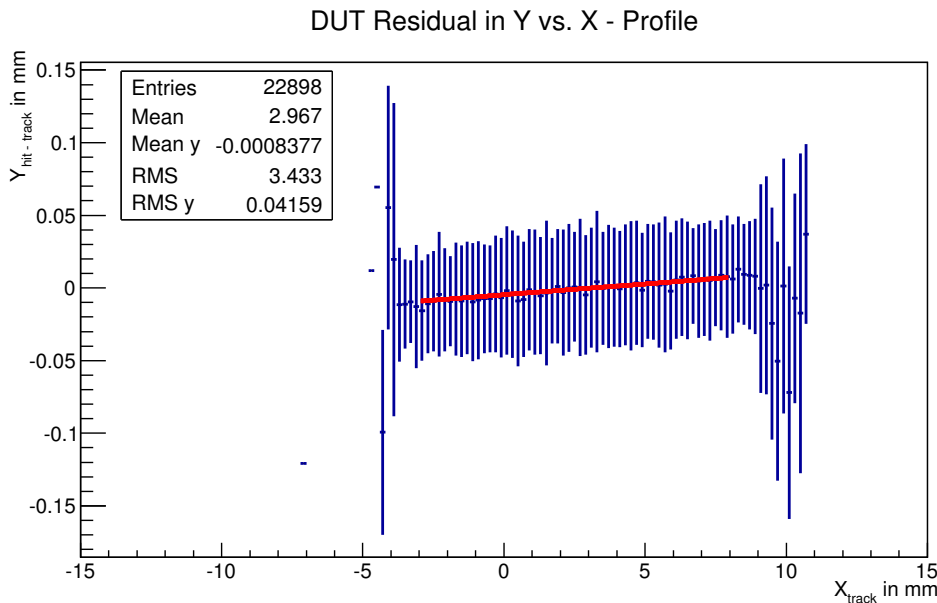plied to the hit collection.

Figure 5.26: Alignment of the DUT by the width of its residuals. The slope of the fit sug-
gests an additional rotation of 1.5 mrad around γ.

Since the rotation in γ obtained by this sixth alignment step is not necessarily around the z axis, applying this rotation might have introduced a DUT shift in x and y. This is then corrected by a subsequent seventh alignment iteration. Any remaining misalignment in γ is corrected by repeating iterations 6 and 7. A tenth iteration fixes all telescope planes and leaves only the DUT z coordinate free. A z resolution of 1 mm is assumed. The alignment parameters for iterations six to ten are summarised in table 5.7.

Table 5.7: The fixing of telescope and DUT planes and their coordinates for the latter alignment iterations. An entry means this coordinate of the plane is fixed. An A denotes a plane that has all coordinates (x, y, z, α, β, γ) fixed. For iterations 6 and 8 tracks are searched only in planes 0, 1 and 2, and then extrapolated to the DUT. Residual cuts and assumed resolutions are as noted in table 5.5 for iteration 5.

Iteration	Plane 0	Plane 1	Plane 2	DUT	Plane 3	Plane 4	Plane 5
6	A	A	A	x,y,z, α, β	A	A	A
7	A	A	A	z, α, β, γ	A	A	A
8	A	A	A	x,y,z, α, β	A	A	A
9	A	A	A	z, α, β, γ	A	A	A
10	A	A	A	$x,y, \alpha, \beta, \gamma$	A	A	A

5.3.9 *Tracks on the DUT*

After ten alignment iterations a final track search is performed. Again, only hits in the upstream telescope planes are considered to exclude multiple scattering effects, and the tracks then extrapolated to the DUT. In order to not introduce a bias from hit positions, all alignment constants are applied to the DUT plane. With the plane correctly positioned in the global coordinate system, its intersection with the track vectors can be calculated. An example is shown in figure 5.27. The hit and track information together with the DUT data is then written to a ROOT `TNtuple` for analysis.

Figure 5.28 shows the final event visualisation within EUTelescope. The DUT and the six telescope sensor planes are shown in grey, with the former rotated to achieve a beam incidence angle of 51.3°. The beam enters the telescope from the right, where hits in the three upstream telescope planes are measured. A track is reconstructed and extrapolated to the DUT and the three downstream planes. Hits measured here do not contribute to the track reconstruction used for the final analysis.

5.3.10 *Using Tracks to Investigate Sensors*

Prior to the analysis of the DUT sensor data, cuts are applied to the track sample stored in the `TNtuple`. A schematic overview is shown in figure 5.29 with a de-
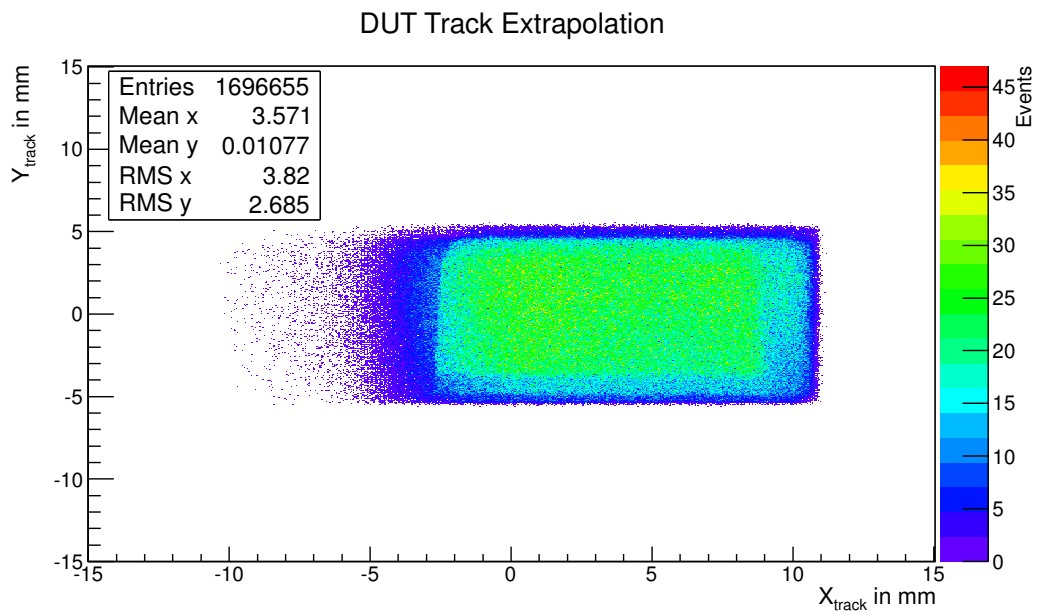
Figure 5.27: Hitmap of tracks extrapolated to the DUT, in this case an Epi100P sensor irradiated to $1.3 \times 10^{16}\,\mathrm{n_{eq}/cm^2}$, operated at 800V under $0\,^\circ$ beam incidence. Shadows of the telescope PMTs are visible.
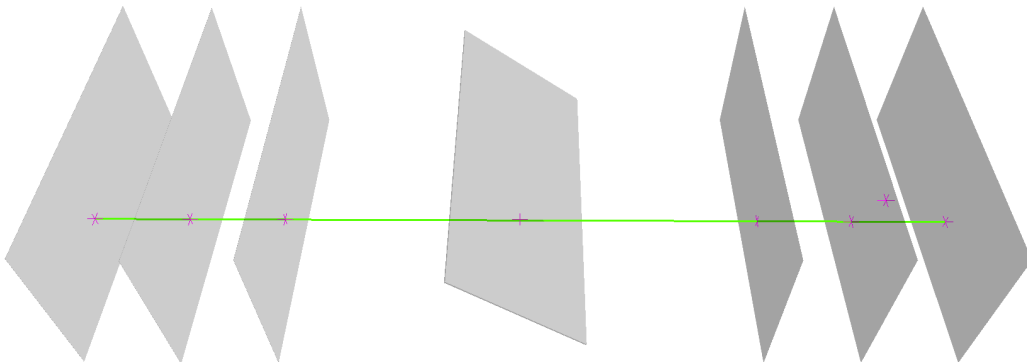

Figure 5.28: Event visualisation within EUTelescope. The telescope sensors and the DUT are shown in grey, with distances between planes not to scale. Hits are measured on all six telescope planes and the rotated DUT sensor. A reconstructed track and its extrapolation to the DUT and the downstream planes is shown in green.

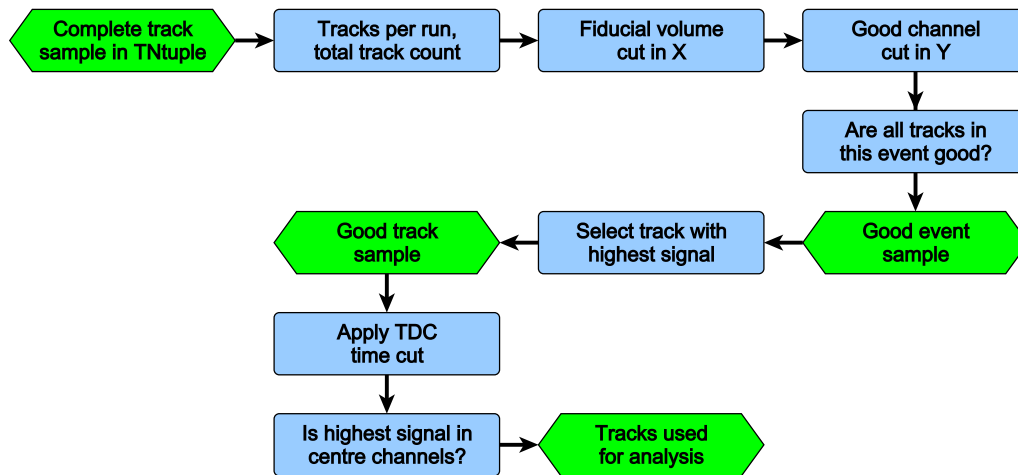scription of the cuts and their motivation given in the following:

Figure 5.29: Schematic of the cuts placed on reconstructed tracks.

- Tracks per run: This first cut can be applied to reduce the number of tracks analysed or to ensure similar sample sizes for runs.

- Fiducial volume cut in x: The tracks are then cut depending on their extrapolated track impact position on the DUT in x. Since the track sample contains tracks without a hit requirement in the downstream telescope planes, this cut increases the probability that the track traversed the entire telescope. Furthermore, although the sensors measured have a length in x of 25 mm, parts of them were covered from the beam spot by mounting brackets. The fiducial cut in x therefore also increases the probability of the track inducing charge in the DUT. Depending on each sensor's individual position in the telescope, the accepted range of track x values is varied. Tracks with an x value at the DUT outside this range are discarded.

- Good channel cut in y: The remaining track sample is then cut on the extrapolated track impact position on the DUT in y. Here a track is required to have passed through a non-masked (cf. section 5.3.3) channel. This again increases the chance of the DUT measuring the track.

- Good event cut: Following the volume cuts, a cut on the events is placed. As an event can contain several tracks, those events are selected that only consist of good tracks passing the fiducial cuts. Multiple hits in a telescope plane in an event can result in several tracks being reconstructed, even if the event contained only one actual particle track. Should the correct track be rejected in the fiducial cuts, a fake track would remain in the sample, biasing results. The events remaining are deemed *good events*.

- Highest signal track cut: Further cuts can now be placed on the extant tracks in the good events. A motivation for further cuts is the different readout

speeds of the devices concerned. Whereas the fixed frame readout of the MIMOSA 26 telescope sensors takes about 115 µs, the ALiBaVa's Beetle chip is much faster at 25 ns. It is therefore likely that in an event the telescope records more tracks than the ALiBaVa system. Not cutting the tracks would introduce a bias towards the noise levels in the signal distributions registered by the ALiBaVa, since it is blind to charge deposited outside of its readout time frame. Since limiting the event sample to events containing only a single track greatly limits statistics, an approach similar to the method shown in [89] is chosen: A region of 5 channels, centred on the extrapolated channel from each track impact point is defined. The signals of the channels in the region are summed and compared with other tracks from this event. Only the track inducing the highest charge in the sensor is left remaining, others from this event are cut.

- ALiBaVa TDC time cut: This *good track* selection is now further cut, depending on the event's TDC time. As explained in section 3.6, the registered pulse height depends on the sampling time. For each run, a 10 ns window in the TDC time range with the highest Landau MPV is selected. Events outside this window are cut from the selection.

- Centre channel cut: A final cut is applied to remove ambiguities from insufficient track extrapolation. Out of each track's selected 5 channel window, the channel with the highest individual pulse hight is determined. Tracks where the channel with the highest pulse height is not one of the centre three are cut, this being indicative of a possible fault in tracking. The remaining tracks are used for the sensor analysis.

5.4 RESULTS

After application of all cuts on the found tracks, an analysis of all the measured DUT sensors can be performed. The tracks are extrapolated to the sensor surface and the corresponding pointed-to channel is calculated by undoing the aforementioned hit making and alignment steps. In the following pages, the obtained results are presented and discussed.

5.4.1 *Resolution*

To assess the quality of the track extrapolation and the underlying alignment, the unbiased residual distribution of the DUT sensor for each run is calculated. The width of this distribution allows to extract the resolution which can be achieved on the sensor. Residuals are calculated for each track from the extrapolated track point and the registered hit.

A sensor's resolution is dependent to some extent on the cluster size its hits are calculated from. For example, a cluster's centre of gravity can be computed more precisely for a two-strip cluster than for a single-strip cluster. For a beam

incidence angle of $0°$, the average cluster size is slightly greater than 1 for all runs, as exemplified in figure 5.13. The achievable resolution for $0°$ beam incidence is therefore slightly smaller than the binary resolution, as derived in section 2.1.2.10:

$$\sigma_{binary} = \sqrt{\left(\frac{pitch}{\sqrt{12}}\right)^2 - \sigma_{point}^2 - \sigma_{MS_{DUT}}^2} \, . \tag{5.12}$$

Assuming an effective telescope pointing resolution of

$$\sigma_{eff} = \sqrt{\sigma_{point}^2 + \sigma_{MS_{DUT}}^2} \approx 5\,\mu m \, , \tag{5.13}$$

with the multiple scattering effects of the DUT $\sigma_{MS_{DUT}}$ included, the expected binary resolution σ_{binary} can be calculated (cf. chapter 3.5). With a sensor pitch of $80\,\mu m$, σ_{binary} equates to $22.6\,\mu m$. The measured resolution on the DUT sensor σ_{res} can be calculated from the measured residual width σ_{meas} via

$$\sigma_{res} = \sqrt{\sigma_{meas}^2 - \sigma_{point}^2 - \sigma_{MS_{DUT}}^2} \, . \tag{5.14}$$

Figure 5.30 shows a measured sensor residual width of $22.2\,\mu m$. Again assuming an effective telescope resolution of $5\,\mu m$ including multiple scattering, this leads to a measured sensor resolution of $21.6\,\mu m$, improving on the binary value.

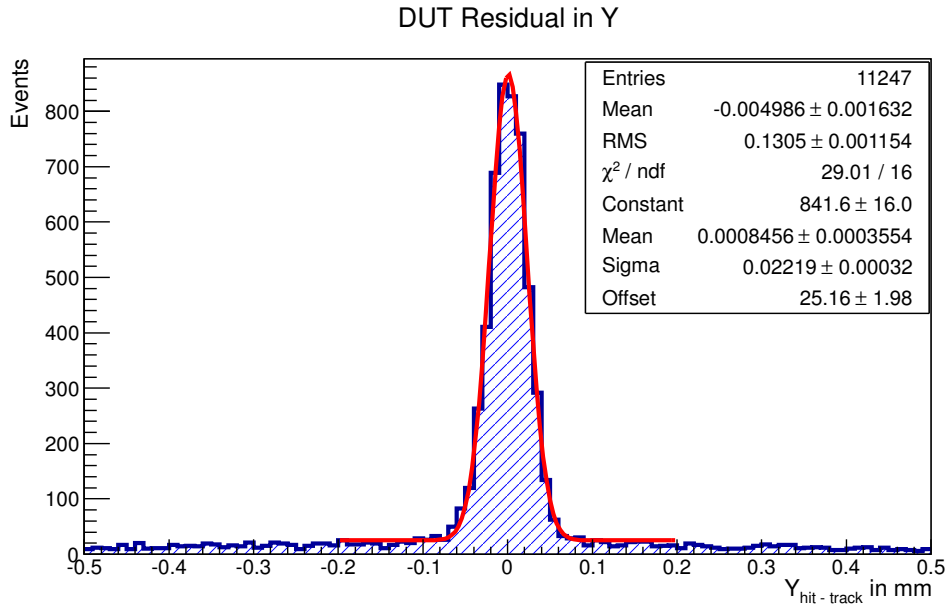DUT Residual in Y

Entries	11247
Mean	-0.004986 ± 0.001632
RMS	0.1305 ± 0.001154
χ^2 / ndf	29.01 / 16
Constant	841.6 ± 16.0
Mean	0.0008456 ± 0.0003554
Sigma	0.02219 ± 0.00032
Offset	25.16 ± 1.98

Figure 5.30: Measured residual of an Epi100P sensor, irradiated to $1.5 \times 10^{15}\,n_{eq}/cm^2$ and measured at $0°$ beam incidence and at $-300\,V$ applied bias voltage.

For most sensors, however, a larger residual is measured, leading to a sensor resolution worse than expected from the binary resolution. Figures 5.31, 5.32 and 5.33 give an overview of the residuals of all measured sensors. The red line in each figure shows the expected binary residual, if a telescope resolution of $5\,\mu m$ including

multiple scattering is assumed. For legibility, some points are shifted on the x axis. Here one sees that the resolution measured in most sensors at $0\,^\circ$ incidence angle is larger than the binary expectation. A notable exception are the p-stop sensors irradiated to 1 and $1.5 \times 10^{15}\,\mathrm{n_{eq}/cm^2}$, when measured below $-500\,\mathrm{V}$ bias voltage. At higher voltages, the MCz200Y sensor, irradiated to $1.3 \times 10^{16}\,\mathrm{n_{eq}/cm^2}$ has a resolution below the binary expectation.

For $25\,^\circ$ beam incidence, the measured residuals are much closer to the binary expectation and many more sensors improve on this than compared to $0\,^\circ$ incidence. This can be attributed to the increased cluster size. Similar considerations apply for runs taken at higher beam incidence angles, such as $51.3\,^\circ$. The smallest sensor resolution measured is $21.0\,\mathrm{\mu m}$ for a $1.5 \times 10^{15}\,\mathrm{n_{eq}/cm^2}$ p-stop sensor at $-800\,\mathrm{V}$ and $38.6\,^\circ$ incidence. In the following, possible impacts and considerations on the resolution are discussed:
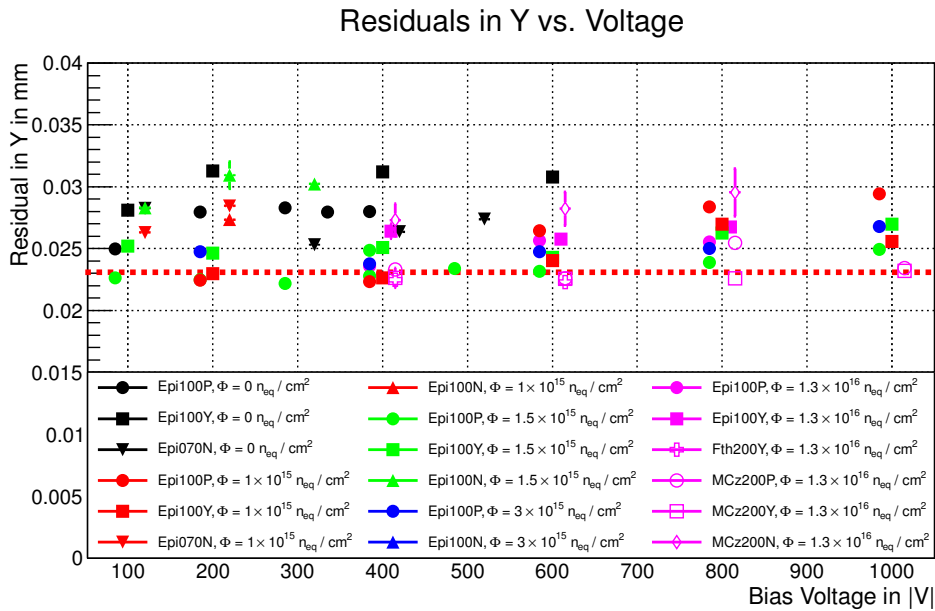

Figure 5.31: Measured sensor residuals for $0\,^\circ$ beam incidence. Most residuals widths are slightly larger than the binary expectation.

- The devising of the sensor x coordinate: As previously detailed, the strip sensor is unsensitive to this coordinate, which is estimated from the preceding telescope planes. This might introduce a small bias, especially concerning rotations in β and γ. Test runs, in which this coordinate was always defaulted to 0 (resulting in only *one channel in* x), with alignment parameters adjusted accordingly, yielded no improvement.

- The predominant cluster size of 1: Due to the cuts introduced in the clustering process, a charge below a certain threshold is disregarded in the positioning of a hit, leading to inaccuracies. Using only cluster sizes larger than 1 for alignment is not always possible due to a lack of statistics. An increase in charge shared between strips, for example at higher beam incidence angles,
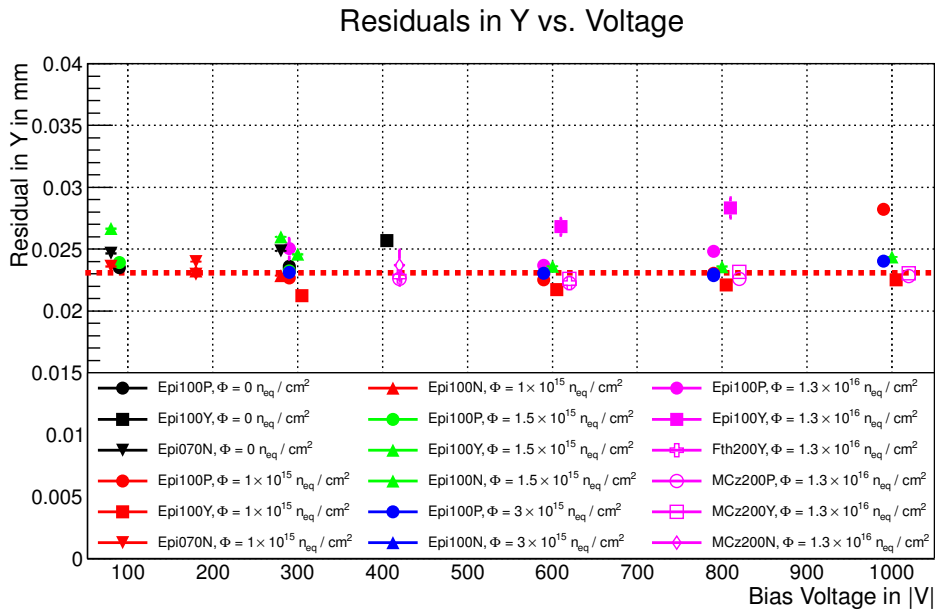
Figure 5.32: Measured sensor residuals for 25° beam incidence. The residual widths are much closer to the binary expectation, which can be due to the slightly increased cluster size at this incidence angle.
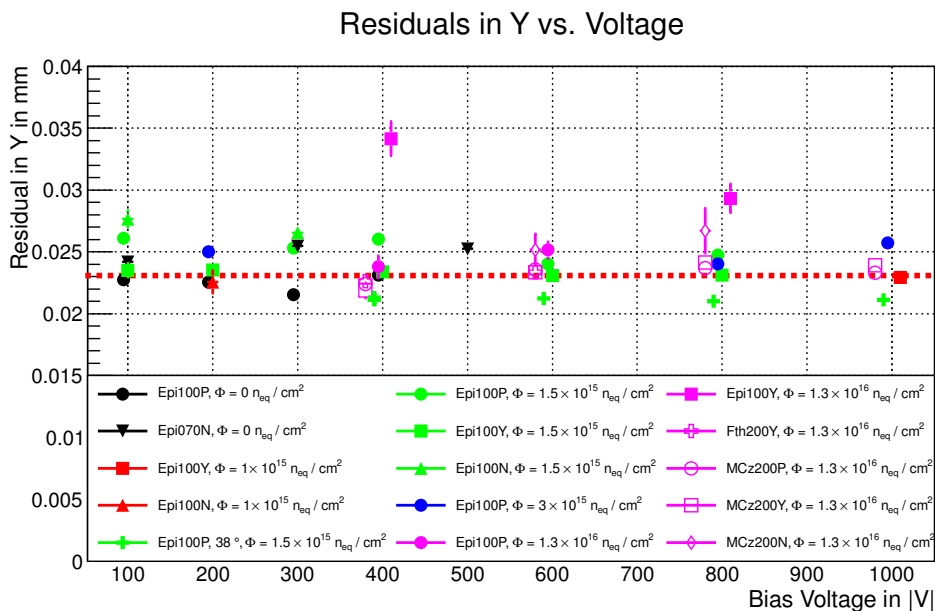

Figure 5.33: Measured sensor residuals for higher beam incidence angles. In 100 μm thick sensors, this angle is 51.3°. The 70 μm thick Epi70N sensors were measured at 41.2°, the 200 μm thick MCz and Fth sensors at 31.7° beam incidence.

does not necessarily improve the resolution. Charge sharing is discussed in detail in section 5.4.5.

- Software errors and systematic flaws: These can be ruled out to a certain extent, as all runs were processed with the same parameter settings and code. Sensors with a sub-binary resolution show that the analysis methodology can yield the expected results.

- Sensor noise: As described in 5.3.5.4, some of the n-bulk sensors show non-Gaussian noise discharges. Despite the filtering processes, it cannot be entirely ensured that all non-Gaussian noise is removed. Some noise may exceed clustering thresholds and thus bias the alignment process, resulting in a larger residual.

5.4.2 *Sensor Noise*

To put the obtained sensor signals into perspective, it is necessary to first look at each sensor's noise. Figure 5.34 shows a comparison of the noise values of each sensor. The noise value is averaged over the individual channel noise of all good channels. For non-irradiated and low to moderate irradiations of up to $\Phi = 1.5 \times 10^{15} \, n_{eq}/cm^2$, the sensor noise value is between 4 and 4.5 ADCs for p-spray and p-stop sensors. Unirradiated sensors were measured at room temperature, irradiated sensors at $-20\,°C$. For fluences of $\Phi = 1.5 \times 10^{15} \, n_{eq}/cm^2$ and greater, the noise values are increased at highest voltages. The Epi100P sensor irradiated to $3 \times 10^{15} \, n_{eq}/cm^2$ has a slightly higher noise value, which goes up to 5.5 ADCs at the highest bias voltage of $-1000\,V$. The Epi100P and Epi100Y sensors irradiated to $1.3 \times 10^{16} \, n_{eq}/cm^2$ show a higher noise, which at $-800\,V$ bias amounts to over 7 ADCs. At the same irradiation level, the thicker sensors MCz200P, MCz200Y and Fth200Y show a much lower noise level of 4.8 ADCs, rising to 5.4 ADCs at $-1000\,V$ bias. The sensors irradiated to a fluence of $\Phi = 1.3 \times 10^{16} \, n_{eq}/cm^2$ were measured at temperatures below $-25\,°C$.

Concerning n-bulk sensors, only very few runs can be salvaged from the non-Gaussian noise described earlier. All epitaxial sensors irradiated to a fluence of $1.5 \times 10^{15} \, n_{eq}/cm^2$ can only be aligned up to a bias voltage of $300\,V$ before the non-Gaussian noise makes alignment impossible. At $3 \times 10^{15} \, n_{eq}/cm^2$ this voltage drops to $100\,V$. As can be seen in figure 5.34, for higher voltages, the noise levels in these sensors are vastly increased. Epitaxial n-bulk sensors irradiated to $1.3 \times 10^{16} \, n_{eq}/cm^2$ cannot be used at all. The $200\,\mu m$ thick Magnetic Czochralski sensor however can be filtered and aligned at voltages of up to $800\,V$. Nevertheless, at this voltage, the average channel noise is greater than 17 ADCs, over 3 times as much as a similar p-bulk sensor.
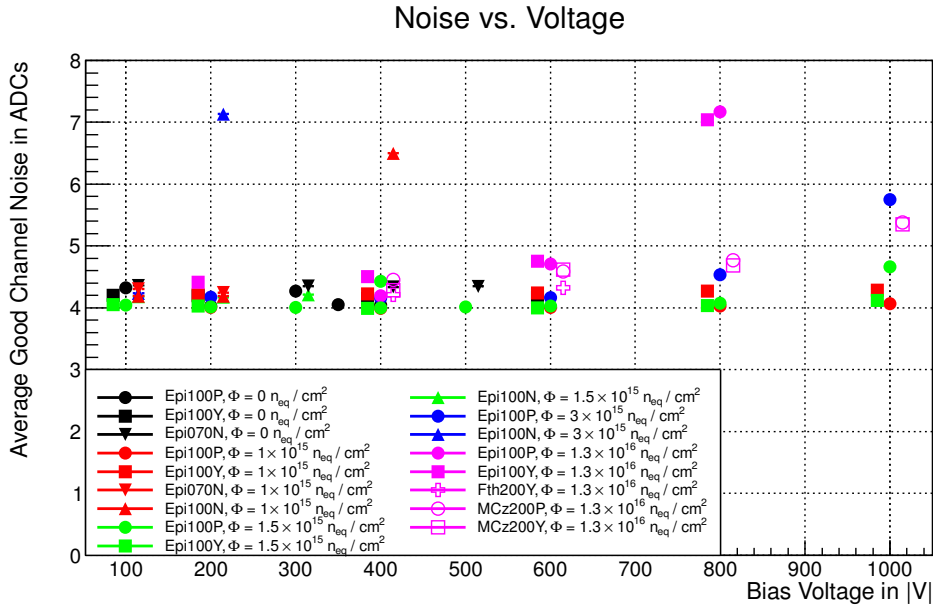
Figure 5.34: Comparison of sensor noise. For each sensor and voltage step, the average noise value of all good channels is calculated. Since the noise values are independent of the beam incidence angle, only values taken at $0°$ rotation are shown. The errors from the individual channel noise distributions are averaged and included. Some points are shifted on the x axis for legibility.

5.4.3   *Charge Collection Efficiency*

The charge collection efficiency and its performance after irradiation is an important sensor property. It presents a quantification of a detector's ability to correctly track and identify traversing particles. To assess this characteristic, the following method is used for all sensor runs:

From each run's analysis track sample, the pedestal and common mode corrected signals in the five channels surrounding each track impact point are added, and the sum filled into a histogram. This is then fitted by the sum of a Gaussian and a Landau function convolved with a separate Gaussian function [24]:

$$f(x) = g_1(x) + (l(x) * g_2(x)) . \tag{5.15}$$

The mean and width of $g_1(x)$ were obtained from a separate fit over the sum of the off-beam noise in five channels. In the signal fit, $g_1(x)$ is constrained to these values, with only the multiplicative constant left free, as are the parameters of the convolved Landau/Gaussian function $l(x) * g_2(x)$. Thus $g_1(x)$ can accommodate for the remaining sensor noise in the distribution and $g_2(x)$ represents the Gaussian smearing of the Landau distribution $l(x)$. Figure 5.35 shows the signal distribution of a sensor and the corresponding fit.

Using the most probable value (MPV) of the Landau function as the definition of a sensor's measured signal, a comparison of sensors can be performed. The
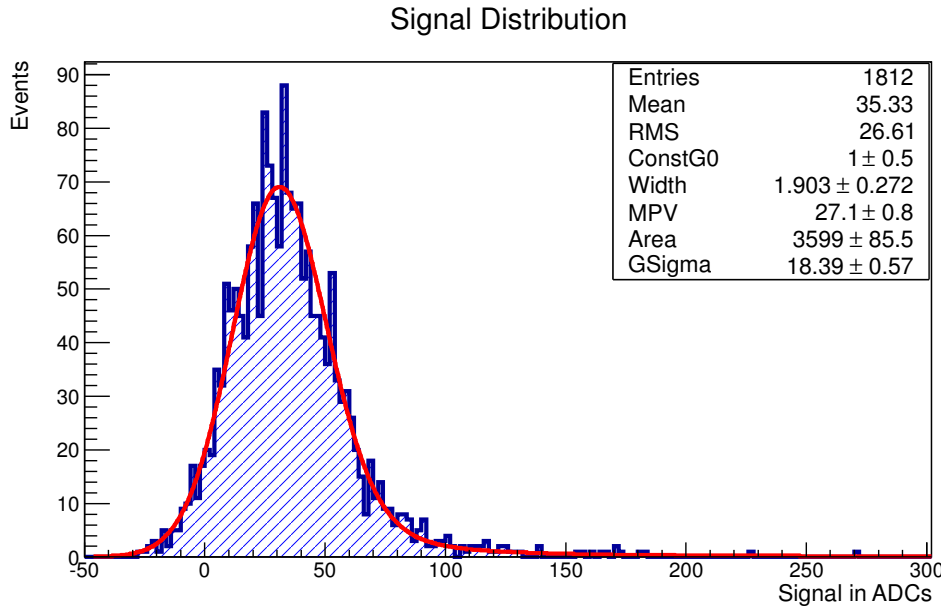
Figure 5.35: Signal distribution of a sensor, here a $100\,\mu$m thick epitaxial p-bulk sensor with p-spray isolation. The sensor is biased to $-800\,$V and irradiated to a fluence of $1.3 \times 10^{16}\,n_{eq}/cm^2$. The most probable value of the Landau function is (27.1 ± 0.8) ADCs.

signals collected from each sensor are shown in figures 5.36 to 5.42, with the error on the Landau MPV included. Figures encompassing all measurements can be found in appendix A.2.1. Prior to irradiation, at $-400\,$V bias and $0\,°$ beam incidence, signals from the p-stop and p-spray sensors amount to (40.1 ± 0.6) ADCs and (40.1 ± 1.2) ADCs, respectively. A signal of (31.0 ± 0.6) ADCs is measured in the non-irradiated $70\,\mu$m thick n-bulk sensor at $400\,$V bias. If scaled to the p-bulk sensor thickness of $100\,\mu$m, the signal height is similar to that obtained from the p-bulk sensors.

For all sensors, signals generally increase with voltage, the exception being the non-irradiated n-bulk sensor at $0\,°$ and $25\,°$ beam incidence, where the signals remain almost constant or slightly drop with increasing voltage. At the highest bias voltages of $-1000\,$V, p-bulk sensors irradiated to up to $3 \times 10^{15}\,n_{eq}/cm^2$ can deliver signals of (34.4 ± 0.5) ADCs, which is over $80\,\%$ of the signal measured in the sensor before irradiation. For the highest irradiations of $1.3 \times 10^{16}\,n_{eq}/cm^2$, the recouped signal in epitaxial sensors drops to (27.1 ± 0.8) ADCs at a bias voltage of $800\,$V, which is over $65\,\%$ of the non-irradiated signal. Signals measured in the thicker, non-epitaxial p-bulk Magnetic Czochralski and thinned Float-Zone sensors are smaller than those measured in epitaxial sensors at the same bias voltages and fluence levels.

For n-bulk sensors, the situation is different. As described above, most irradiated sensors show non-Gaussian noise discharges, preventing alignment, tracking and any subsequent analysis. For low irradiations and bias voltages, these can be corrected to some extent. The resulting signals are shown in figure 5.42. However, as
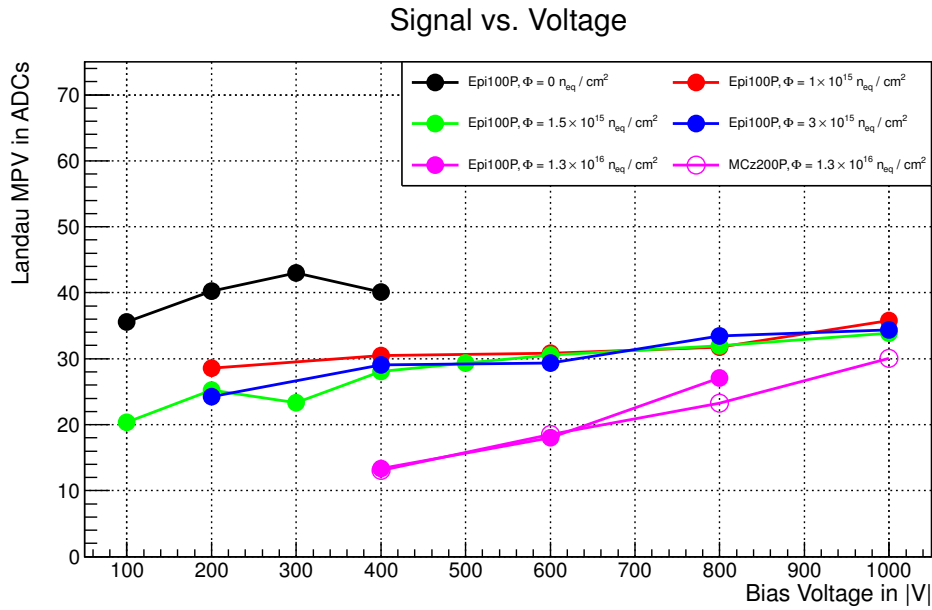
Figure 5.36: The charges collected for p-stop sensors at $0°$ beam incidence. At $-1000\,\text{V}$ bias, the signal in the sensor irradiated to $3 \times 10^{15}\,\text{n}_{\text{eq}}/\text{cm}^2$ amounts to over $80\,\%$ of the signal prior to irradiation.
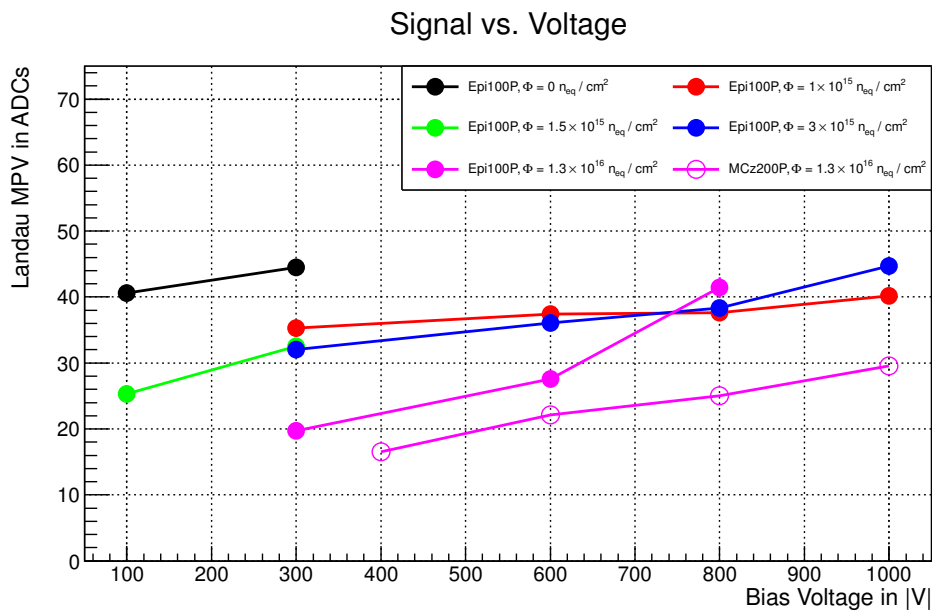
Figure 5.37: The charges collected for p-stop sensors at $25°$ beam incidence. At $-1000\,\text{V}$ bias, the signal measured in the sensor irradiated to $3 \times 10^{15}\,\text{n}_{\text{eq}}/\text{cm}^2$ surpasses that measured before irradiation. At $-800\,\text{V}$ bias, the signal measured at a fluence of $1.3 \times 10^{16}\,\text{n}_{\text{eq}}/\text{cm}^2$ is vastly increased, suggesting an onset of charge multiplication.

Figure 5.38: The charges collected for p-stop sensors at higher beam incidence angles. Signal levels are increased due to the higher incidence angle, which is $38.6\,°$ and $51.3\,°$ for the $100\,\mu m$ thick epitaxial sensors and $31.7\,°$ for the $200\,\mu m$ thick MCz200P sensor. Again, for an irradiation fluence of $3 \times 10^{15}\,\mathrm{n_{eq}/cm^2}$ at $-1000\,V$ bias, the signal measured almost amounts to that measured in the sensor without irradiation.

Figure 5.39: The charges collected for p-spray sensors at $0\,°$ beam incidence. At a fluence of $1.5 \times 10^{15}\,\mathrm{n_{eq}/cm^2}$ at $-1000\,V$ bias, over $85\,\%$ of the pre-irradiation signal is measured.
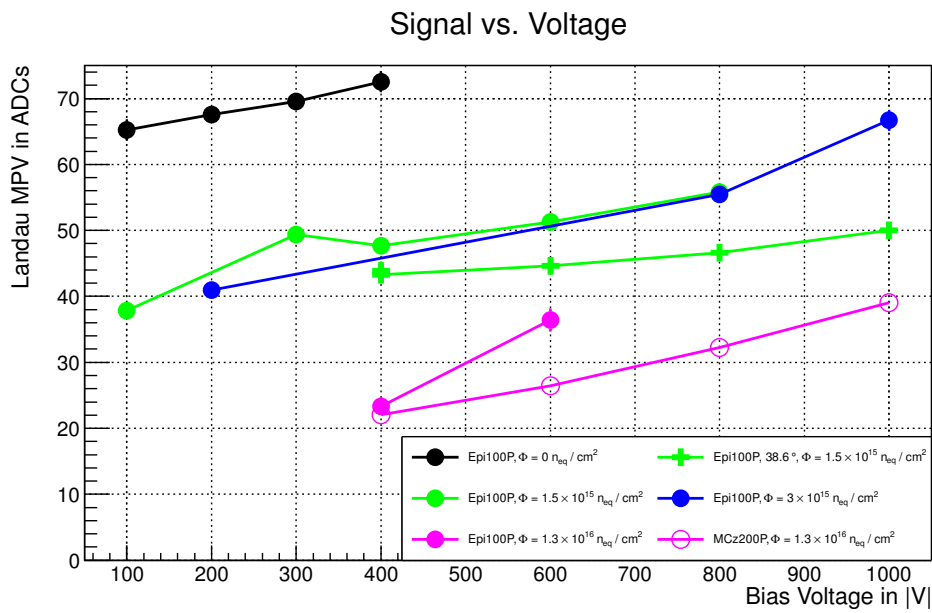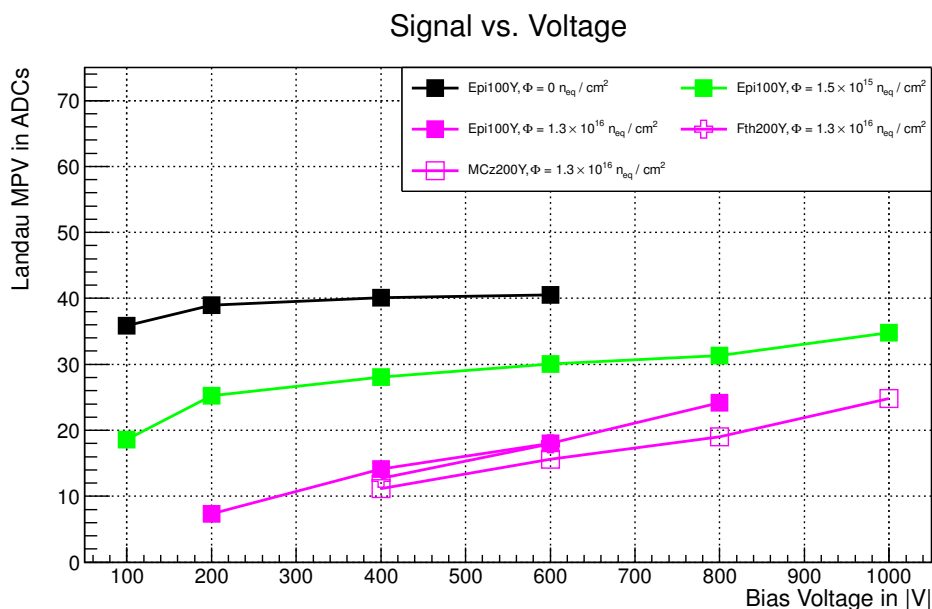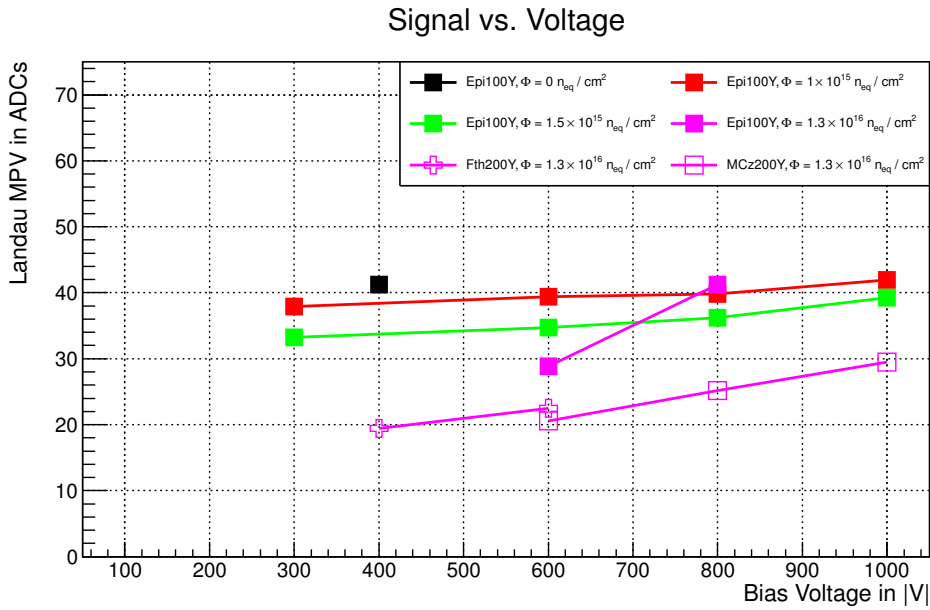
Figure 5.40: The charges collected for p-spray sensors at 25° beam incidence. At the highest bias voltage, signals in the epitaxial sensor irradiated to $1.3 \times 10^{16}\,\mathrm{n_{eq}/cm^2}$ are at the same level as those in the non-irradiated sensor.

Figure 5.41: The charges collected for p-spray sensors at higher beam incidence angles. At $-800\,\mathrm{V}$ bias, the signal measured after an irradiation of $1.3 \times 10^{16}\,\mathrm{n_{eq}/cm^2}$ is higher than that measured for the sensor irradiated to $1.5 \times 10^{15}\,\mathrm{n_{eq}/cm^2}$. Incidence angles are $51.3°$ for the epitaxial sensors and $31.7°$ for the $200\,\mathrm{\mu m}$ thick sensors.

Figure 5.42: The charges collected for all n-bulk sensors. Due to non-Gaussian noise effects, the number of analysable runs is limited.

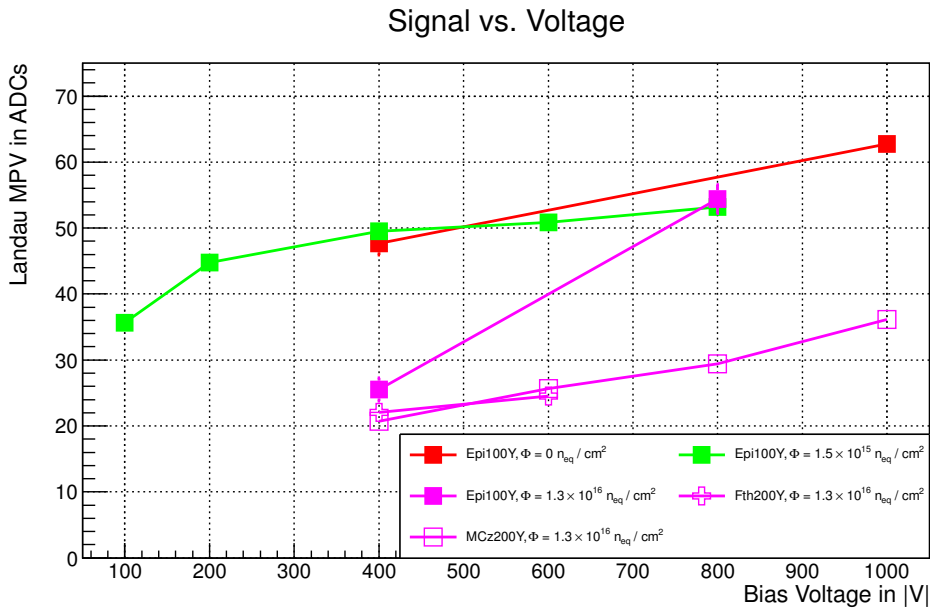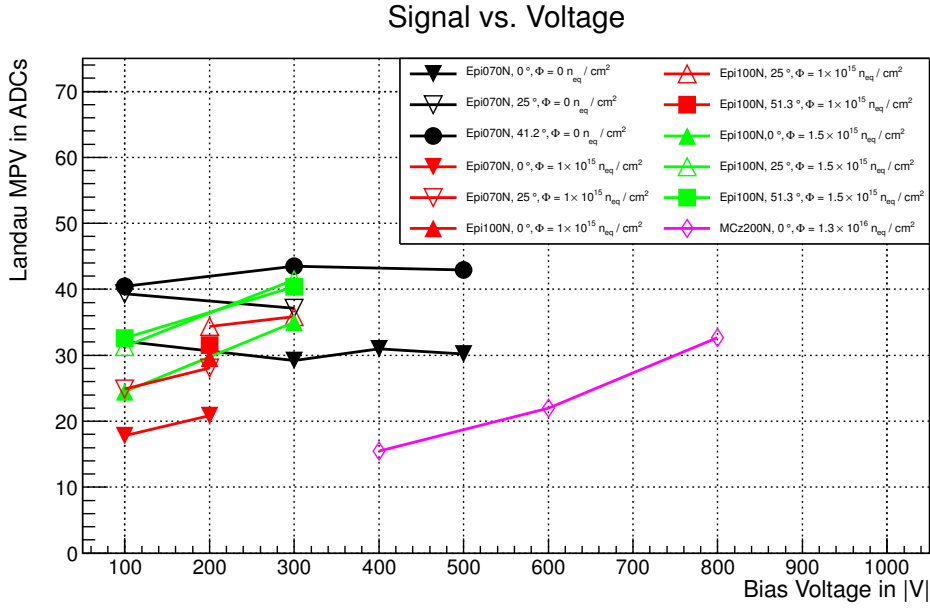these processes can diminish parts of the signal, an absolute comparison to other sensors is not always possible. A notable exception is the 200 μm thick MCz200N sensor irradiated to $1.3 \times 10^{16} \, n_{eq}/cm^2$, from which a signal can successfully be extracted. A caveat here is that this sensor shows a very high noise level, which is discussed later on.

All sensors show an increase of signal with rising beam incidence angle. As a rotation of the sensor by an angle α enlarges its effective thickness traversed by the beam by a factor of $1/\cos\alpha$, this effect is to be expected. Especially for higher irradiations, the increase of signal with incidence angle is larger than would be expected from geometrical considerations. This is suggestive of a non-linear electric field within the sensor bulk. Figure 5.43 shows the charges collected for example sensors at various beam incidence angles.

As an example, a signal of (24.2 ± 0.6) ADCs is collected at $-800\,\mathrm{V}$ bias voltage from the epitaxial p-spray sensor irradiated to $1.3 \times 10^{16} \, n_{eq}/cm^2$ at $0\,°$ incidence. At $25\,°$ incidence, an increase to

$$\frac{(24.2 \pm 0.6) \, \mathrm{ADCs}}{\cos{(25\,°)}} \approx 26.7 \, \mathrm{ADCs} \tag{5.16}$$

would be expected. The actually measured signal however is (41.2 ± 1.1) ADCs. A similar effect is observed for $51.3\,°$ incidence, where the expected signal of ≈ 38.7 ADCs is surpassed by the measured one of (54.4 ± 2.2) ADCs.

While charge multiplication at fluences over $4 \times 10^{15} \, n_{eq}/cm^2$, as measured with an infrared laser in a TCT setup for epitaxial diodes by Lange in [80], could not be observed directly from the measured signals, the increased signal at high incidence
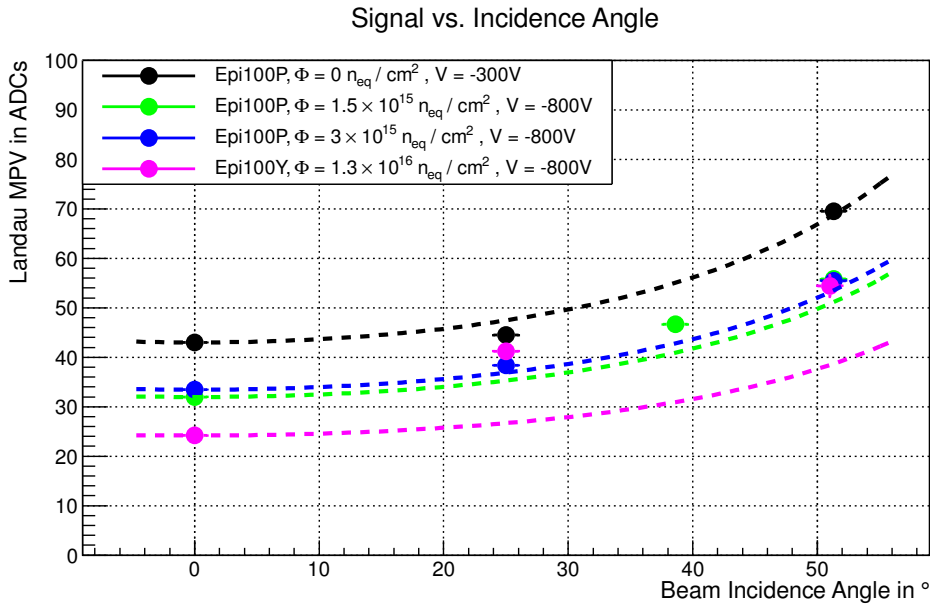
Figure 5.43: The charges collected for select sensors at various beam incidence angles. The dotted line indicates the geometrical expectation from equation 5.16. While the signals in non-irradiated sensors and sensors irradiated up to $3 \times 10^{15}\,n_{eq}/cm^2$ show an increase proportional to the inverse cosine of the incidence angle, the measured signals at the highest fluence of $1.3 \times 10^{16}\,n_{eq}/cm^2$ are vastly increased.

angles can nevertheless be indicative of charge multiplication effects. Furthermore, for inclined tracks, the measured signals in thin, epitaxial sensors irradiated to the highest fluence of $1.3 \times 10^{16}\,n_{eq}/cm^2$ are larger than those in thicker, non-epitaxial sensors at the same fluence. This suggests that the charge multiplication effects could possibly be more dominant in epitaxial material.

Summarising, a reduction of charge collection efficiency with irradiation is measured. Nevertheless, for an irradiation fluence of $3 \times 10^{15}\,n_{eq}/cm^2$, over 80 % of the signal prior to irradiation can be recovered. This fluence corresponds to the charged hadron fluence, expected over the entire High Luminosity LHC runtime, for a sensor in the third barrel layer of the future CMS pixel detector (cf. table 1.2). At $\Phi = 1.5 \times 10^{15}\,n_{eq}/cm^2$, corresponding to the expected fluence on the innermost layer of a future outer strip tracker, over 85 % of the pre-irradiation signal is measured. The signal distributions measured at higher beam incidence angles differ from expectations and are discussed further in the following sections.

5.4.4 Signal-To-Noise

Figures 5.44 through 5.50 show the signal-to-noise ratios (SNR) obtained from the test beam measurements. Since the noise levels are not changed with rotation of the DUT sensor, an increase with beam incidence angle is observable, as is for the signals described above. For the 100 µm thick non-irradiated p-bulk sensors, the

signal-to-noise ratio is 9.8 at $|400|$ V bias for $0\,^{\circ}$ incidence. At the same voltage and angle, the 70 μm thick, non-irradiated n-bulk sensors have a signal-to-noise ratio of 7.1.
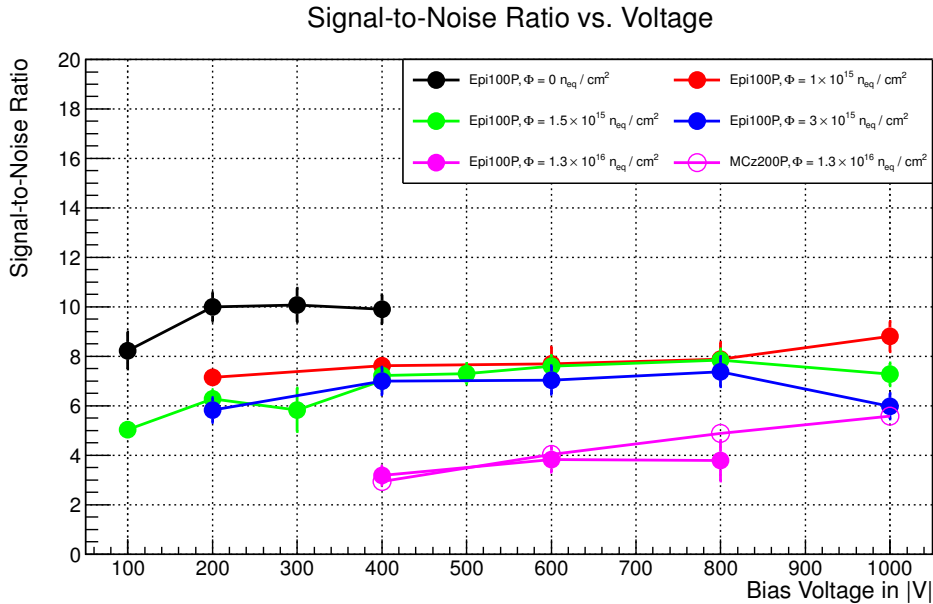

Figure 5.44: The signal-to-noise ratios measured for p-stop sensors at $0\,^{\circ}$ beam incidence. While the SNRs for sensors irradiated to fluences between $1 \times 10^{15}\,n_{eq}/cm^2$ and $3 \times 10^{15}\,n_{eq}/cm^2$ are similar in value, at -1000 V bias, the difference in SNR is about 2.5. This might be due to the possible onset of charge multiplication effects.

For both p-stop and p-spray sensors, a gradual increase of the SNR over the voltage range can be seen. As for the signals, a decrease with irradiation is measured. While the signal-to-noise ratio of a 100 μm thick p-stop sensor still is 7.4 at -800 V bias for an irradiation fluence of $3 \times 10^{15}\,n_{eq}/cm^2$, this drops to 3.8 at $1.3 \times 10^{16}\,n_{eq}/cm^2$. At the same bias voltage and fluence, the thicker, non-epitaxial sensors MCz200P, Fth200Y and MCz200Y give a SNR of 4.8, 4.2 and 4.1 respectively. While signals in these sensors are smaller than in epitaxial material of same irradiation, this is also true for their noise, as shown in figure 5.34, resulting in the slightly higher SNR for these sensors.

While the few analysable n-bulk sensor runs at low fluences and voltages show a similar behaviour to their corresponding p-bulk sensors, the very low SNR of 2.0 for the highly irradiated MCz200N sensor shows the drawback of this sensor. Although signal levels similar to those in p-bulk material can be achieved, this effect comes at the expense of very high noise rates due to surface discharges, leading to this diminutive SNR. Nevertheless, changes to the sensor surface design might mitigate this effect.

Up to now the signals obtained from the sensors are given in ADC units, as written out by the ALiBaVa system. For a real-world comparison, a calibration
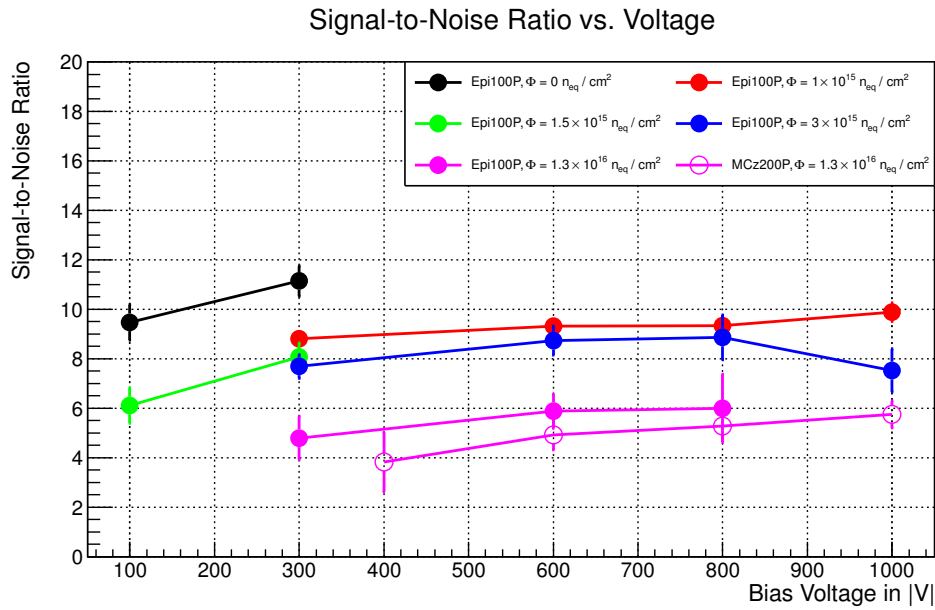
Figure 5.45: The signal-to-noise ratios measured for p-stop sensors at $25\,°$ beam incidence. Values are increased compared to $0\,°$ incidence due to elevated signals. At $25\,°$ incidence the SNR of the epitaxial sensor irradiated to $1.3 \times 10^{16}\,\mathrm{n_{eq}/cm^2}$ is higher than that of the MCz200P sensor irradiated to the same fluence, suggestive of an onset of charge multiplication as shown in figure 5.37.
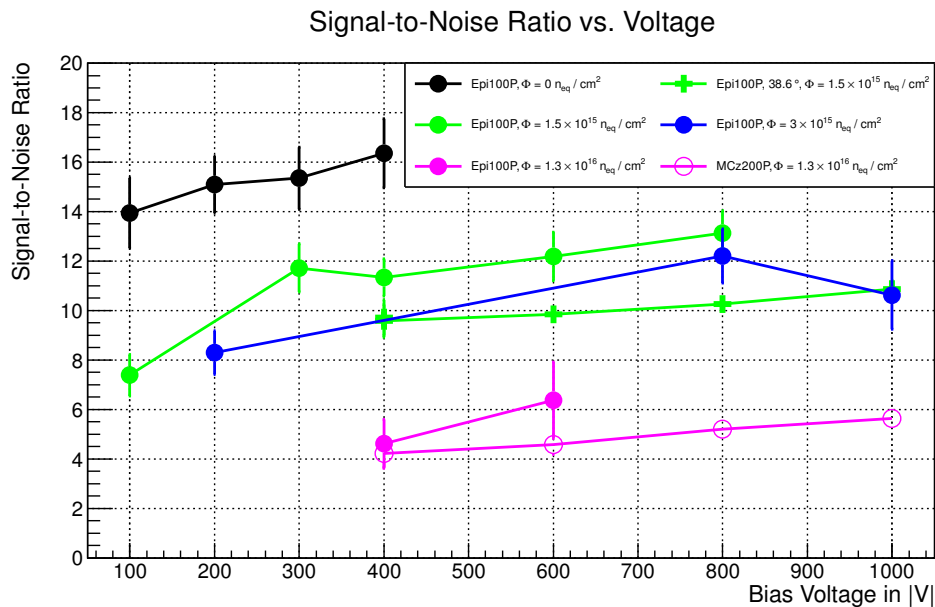
Figure 5.46: The signal-to-noise ratios measured for p-stop sensors at higher beam incidence angles: $38.6\,°$ and $51.3\,°$ for the $100\,\mu m$ thick epitaxial sensors, $31.7\,°$ for the $200\,\mu m$ thick MCz200P sensor.
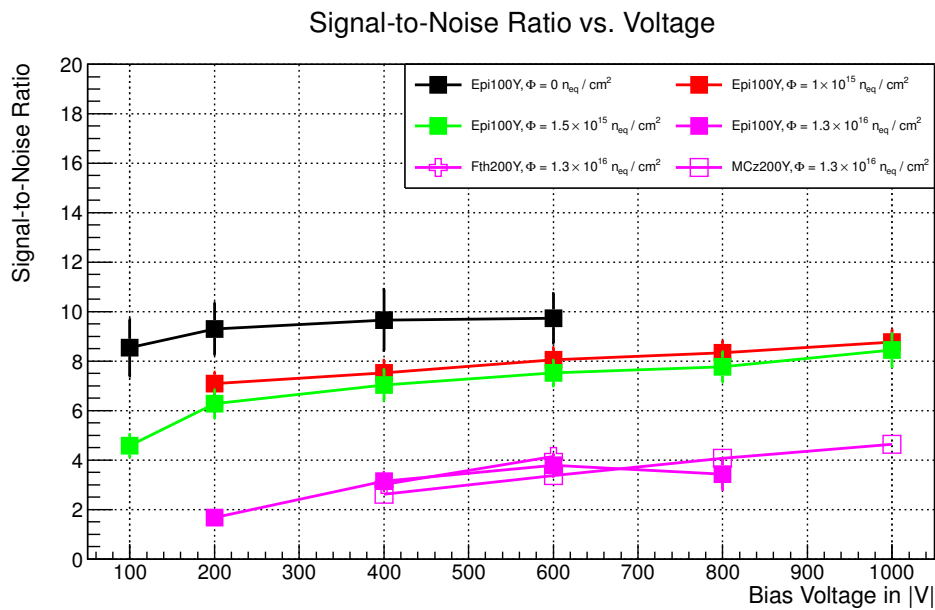
Figure 5.47: The signal-to-noise ratios measured for p-spray sensors at $0\,°$ beam incidence. A similar behaviour as for the p-stop sensors at $0\,°$ incidence is observed, with little difference measured between the SNRs of sensors irradiated to $1 \times 10^{15}\,n_{eq}/cm^2$ an $1.5 \times 10^{15}\,n_{eq}/cm^2$.
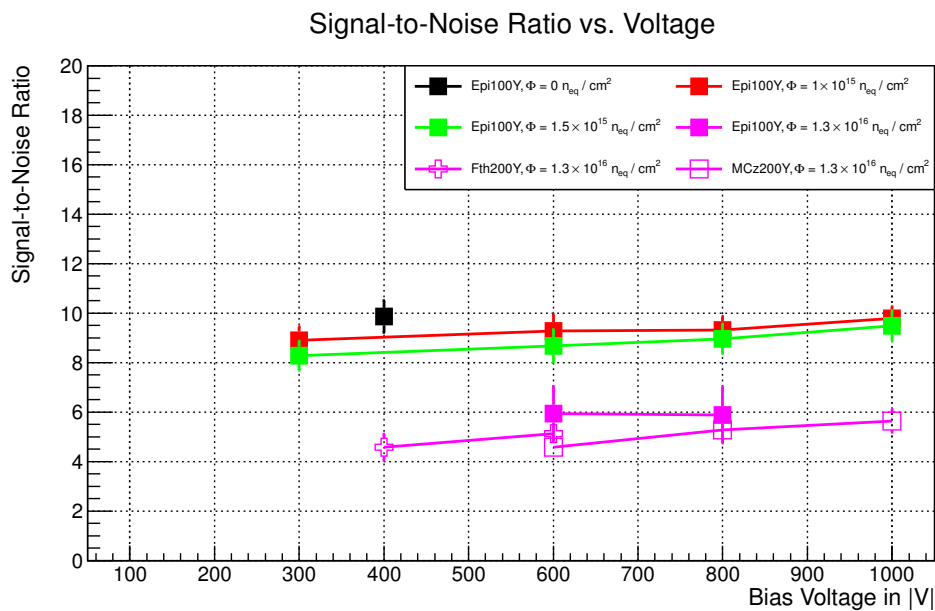
Figure 5.48: The signal-to-noise ratios measured for p-spray sensors at $25\,°$ beam incidence. Again, similar conclusions can be drawn as for the p-stop sensors, shown in figure 5.45.
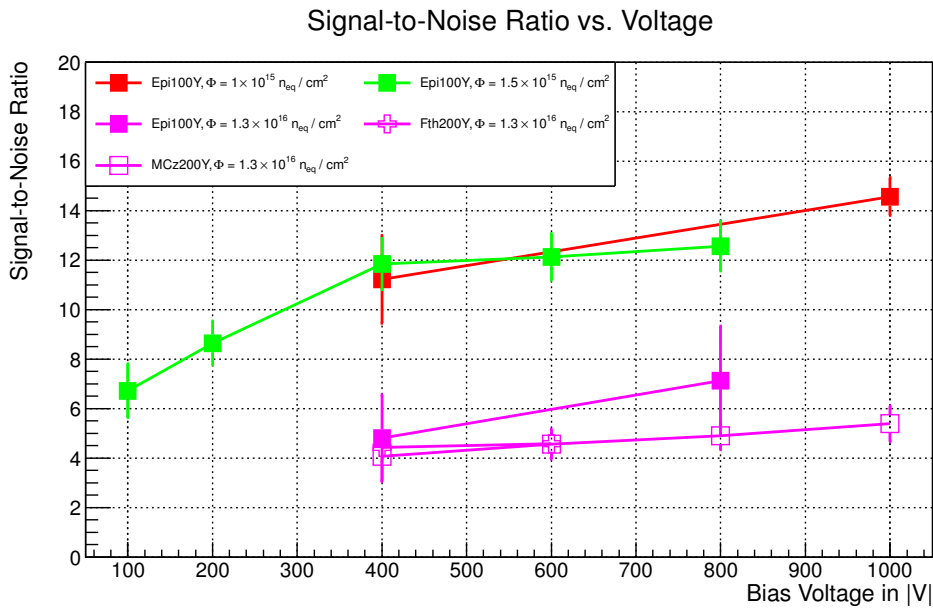
Figure 5.49: The signal-to-noise ratios measured for p-spray sensors at higher beam incidence angles, $51.3\,^\circ$ for the $100\,\mu m$ thick epitaxial sensors, $31.7\,^\circ$ for the $200\,\mu m$ thick sensors.
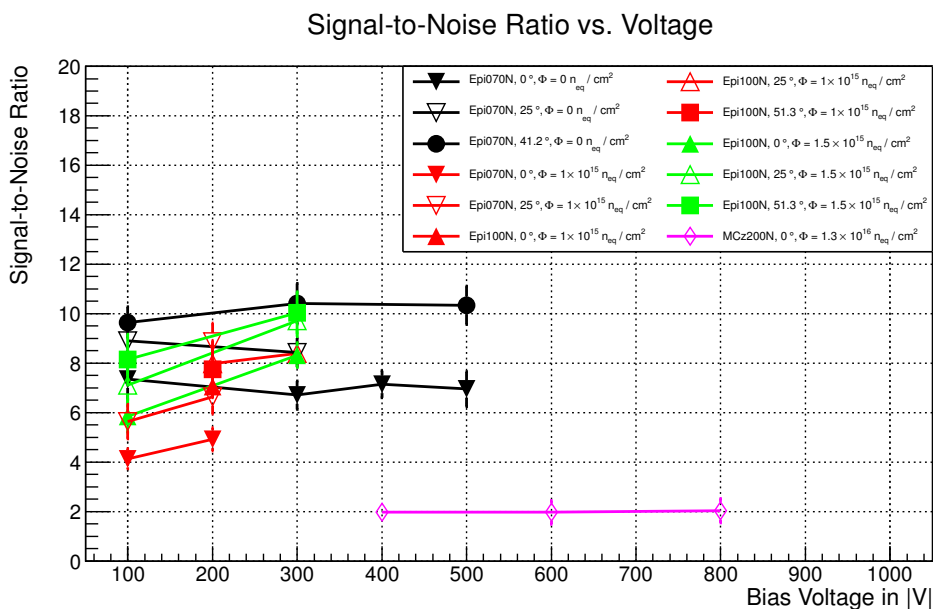
Figure 5.50: The signal-to-noise ratios measured for n-bulk sensors. The thin epitaxial sensors, irradiated to lower fluences show SNR figures similar to those found in the corresponding p-bulk sensors. The SNR of the MCz200N sensor irradiated to $1.3 \times 10^{16}\,n_{eq}/cm^2$ is only ~ 2.

and a conversion of signals to a universal unit — electrons (e$^-$) — is necessary, as described previously in section 3.6. A detailed analysis of the calibrations of the used sensors will be presented in [23].

From the calibration of a non-irradiated 100 µm thick epitaxial p-stop sensor, a conversion factor of roughly 2040 e$^-$ per 10 ADCs can be calculated. This puts the signals obtained from an epitaxial sensor before irradiation at $\approx$ 8100 e$^-$. After irradiation with a fluence of 1.3×10^{16} n$_{eq}$/cm^2, the signal drops to $\approx$ 5700 e$^-$, with the sensor noise level here at 1400 e$^-$.

A future tracker detector in the CMS experiment will need a new generation of readout chips. For the strip tracker, the CBC (CMS binary chip) will be used [56]. For the CBC, the noise threshold is expected to be between 4000 e$^-$ and 6000 e$^-$, with signals of 8000 e$^-$ considered acceptable [9]. The chip which will be used for the pixel detector has not been decided on yet. Signals of 3000 e$^-$, with accordingly low noise levels, could be sufficient for the future pixel detector, if a chip performance comparable to the present chip is to be expected [75].

Summarising, with the signal-to-noise levels presented here a direct assessment of the feasibility of a certain sensor technology can not be performed. The strip sensors measured have an AC-coupled readout and a larger area, thus a larger capacitance than expected for a future pixel detector sensor. Nevertheless, a relative comparison of the materials and sensor thicknesses is possible. From the measured SNR values, the onset of charge multiplication effects at high fluences, as described earlier, can be confirmed. High noise levels in irradiated n-bulk sensors result in a low SNR for this material.

5.4.5 *Charge Sharing*

As already described in earlier chapters, a sensor's charge sharing abilities are an important characteristic. If an amount of charge carriers, which are generated in the vicinity of a cell boundary of a segmented sensor, are measured in the neighbouring cell, this amount of charge is considered *shared*. In any segmented sensor, a sharing of induced charge between cells is beneficial to some extent, as it allows a more precise reconstruction of the traversing particle which is to be detected. Depending on the sensor technology, sharing charge between too many cells can have a negative effect on resolution and efficiency, as amounts of charge can be cut off by thresholds or specific effects of the used clustering algorithms.

An approach to quantify the amount of charge shared in a sensor is to look at the η-distribution, introduced in chapter 2.1.2.9. Without any tracking information, the distribution is filled depending on the ratios of seed neighbours, as shown in section 5.3.5 for the filtering step performed during reconstruction to remove crosstalk. By utilising tracks however, an alternative method can be used:

For each track in a sensor's analysis sample (cf. section 5.3.9), the charge ratio of the channels left and right of the track impact point is calculated and filled into a histogram. An example η-distribution is shown in figure 5.51. Entries between 0.2 and 0.8 are considered as tracks sharing charge. These entries are counted and divided by the overall entry count to determine a sensor's charge sharing ratio.
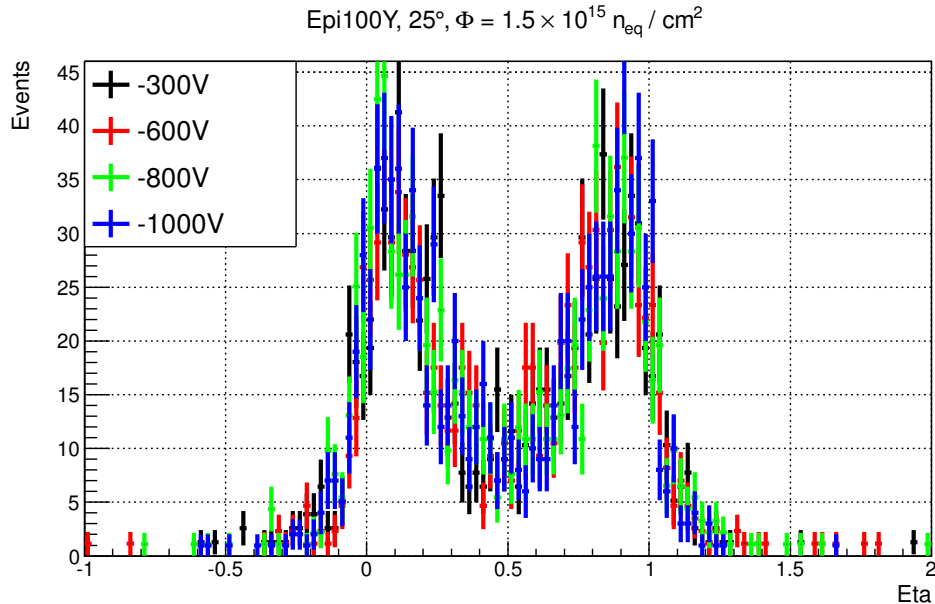

Figure 5.51: Examples of track-based η-distributions to determine charge sharing. The used sensor is a 100 μm thick p-spray isolated sensor, irradiated to a fluence of $1.5 \times 10^{15} \, n_{eq}/cm^2$. The sensor was rotated to achieve a beam incidence angle of 25°, with colours denoting the bias voltage applied. Entries outside the interval [0, 1] stem from opposite-sign noise entries.

This method results in the plots shown in figures 5.52 to 5.58. For all sensors, a gradual decline in charge sharing with increasing voltage can be observed. This can be attributed to the elevated electric field within the sensor bulk. The decline is less pronounced for higher irradiation fluences, up to the highest fluence of $1.3 \times 10^{16} \, n_{eq}/cm^2$, where there is no decline observable throughout the voltage domain.

Intermediate rotations of 25° show an unexpected effect. At this rotation angle, all irradiated sensors share a similar amount of charge to their unrotated counterparts, contrary as to what would be expected from geometrical considerations. For highest fluences the amount of charge shared is even less. An explanation for this could be an unsensitive sensor area between the sensor strips. The charge of tracks impacting the sensor here would not be collected on either the left or the right strip for 0° incidence. In this case the η-distribution is filled with the noise levels of the neighbouring channels. As channel noise levels are very similar in height, this would lead to entries in the centre of the η-distribution, which would wrongly be considered as charge shared. For an inclination angle of 25° however, these tracks would leave the *unsensitive area* at some point in the sensor bulk. In

Figure 5.52: The amount of charge sharing for p-stop sensors at $0°$ incidence, calculated from the η-distribution. The amount of charge shared between strips gradually declines, except at highest fluences. In the non-irradiated sensor very little charge is shared between neighbouring strips.
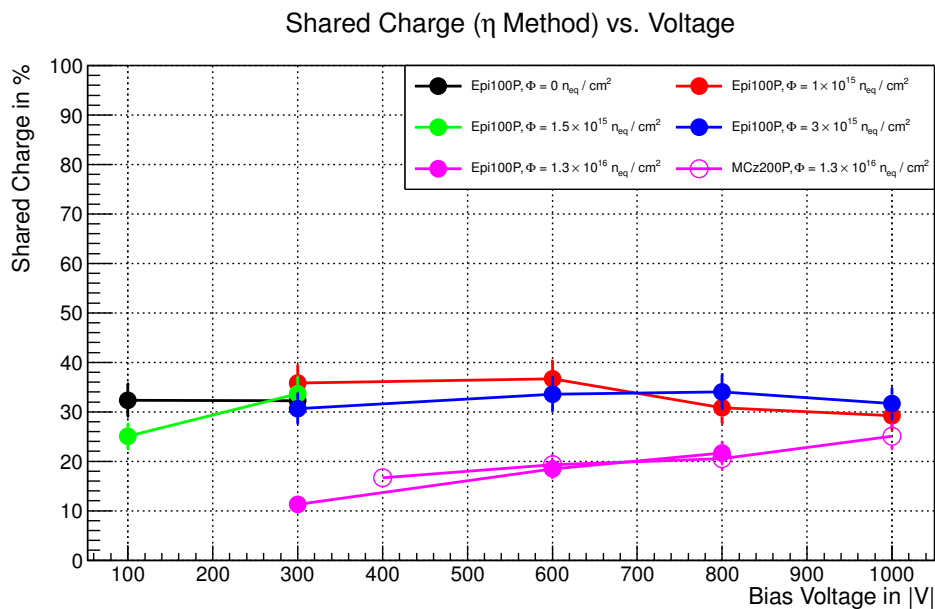
Figure 5.53: The amount of charge sharing for p-stop sensors at $25°$ incidence, calculated from the η-distribution. The amount of charge shared for moderately irradiated sensors is at the same level as for $0°$ incidence, at highest fluences however less charge is shared. Solely from geometrical considerations an increase, as seen for the non-irradiated sensor, would be expected.
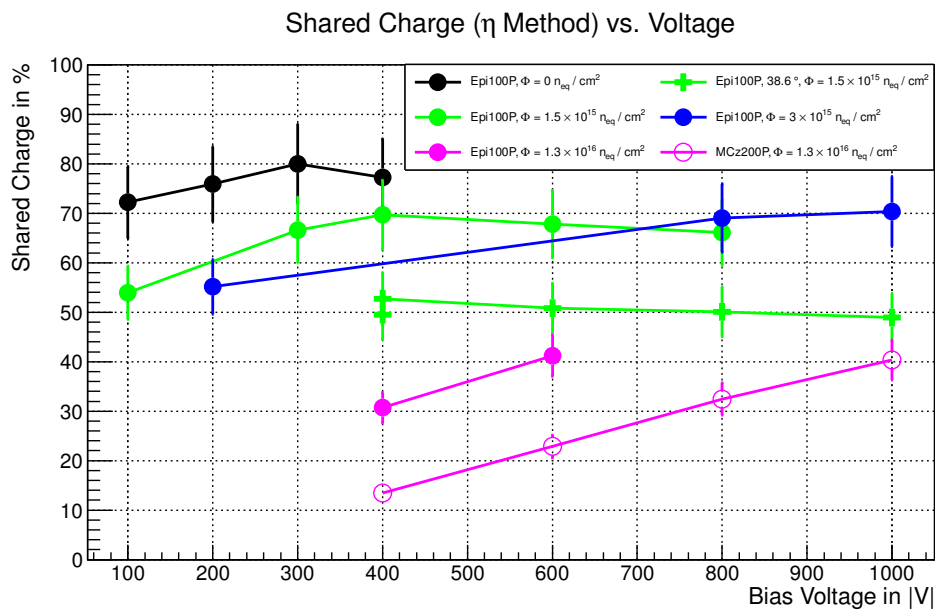
Figure 5.54: The amount of charge sharing for p-stop sensors at higher incidence angles (38.6 ° and 51.3 ° for epitaxial, 31.7 ° for non-epitaxial sensors), calculated from the η-distribution. With increasing bias voltage, more charge is shared than for 0 ° and 25 ° beam incidence.
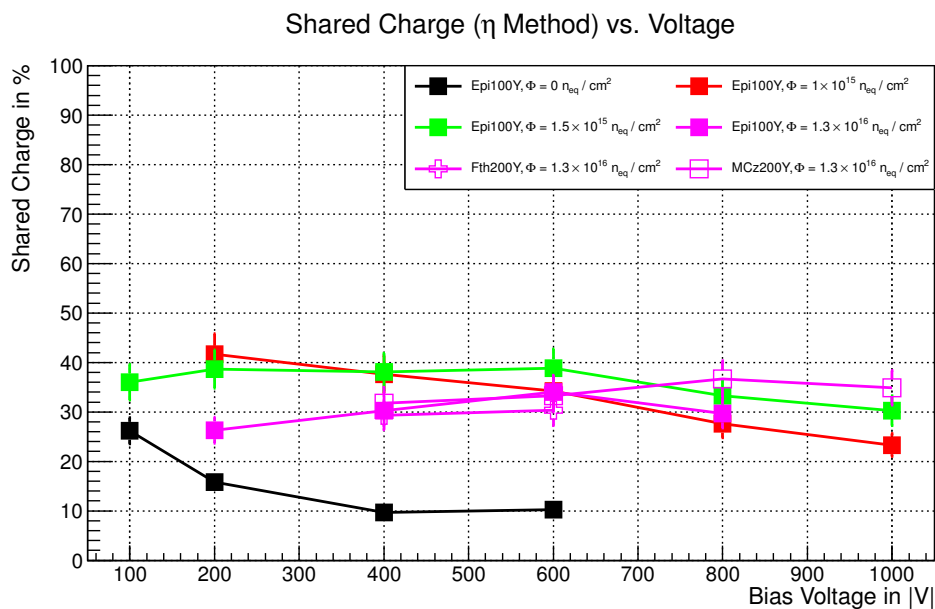
Figure 5.55: The amount of charge sharing for p-spray sensors at 0 ° incidence, if the η-distribution of each run is integrated. η values between 0.2 and 0.8 are considered as shared. A similar behaviour as for the p-stop sensors shown in figure 5.52 is observed.
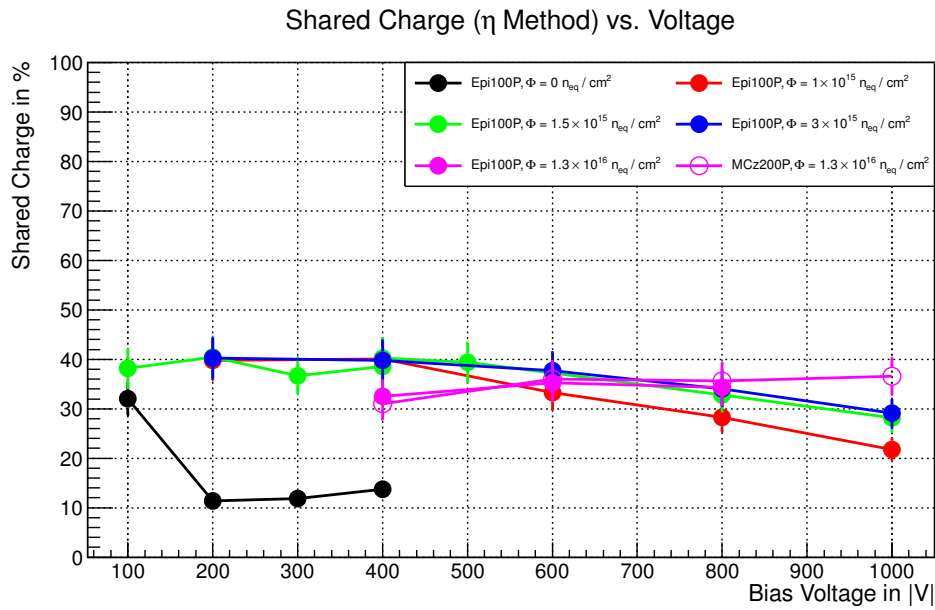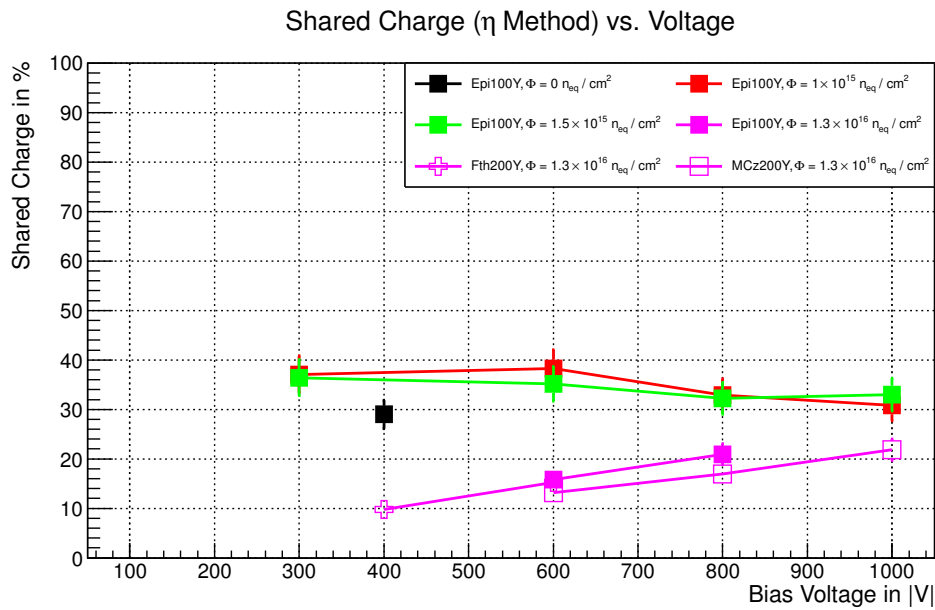
Figure 5.56: The amount of charge sharing for p-spray sensors at $25°$ incidence, calculated from the η-distribution. The amount of charge shared for sensors irradiated to 1 and $1.5 \times 10^{15}\,n_{eq}/cm^2$ is slightly higher than for $0°$ incidence. At $1.3 \times 10^{16}\,n_{eq}/cm^2$ much less charge is shared than at $0°$ incidence.
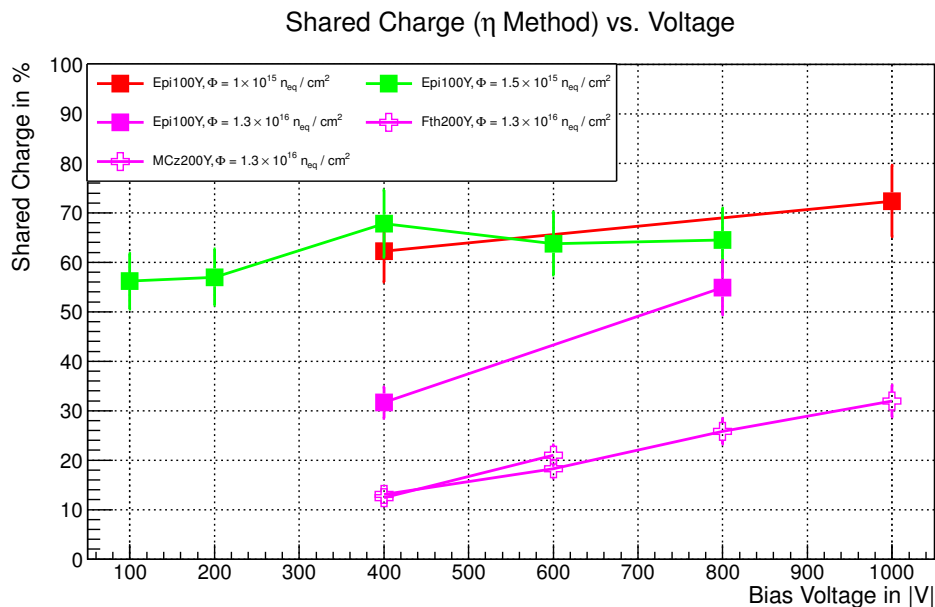
Figure 5.57: The amount of charge sharing for p-spray sensors at higher incidence angles ($51.3°$ for epitaxial, $31.7°$ for non-epitaxial sensors), calculated from the η-distribution. With increasing bias voltage, more charge is shared than for $0°$ and $25°$ beam incidence, even for fluences of $1.3 \times 10^{16}\,n_{eq}/cm^2$. A similar behaviour is seen in p-stop sensors. The $200\,\mu m$ thick MCz and Fth sensors do not share more charge than at $0°$ incidence.
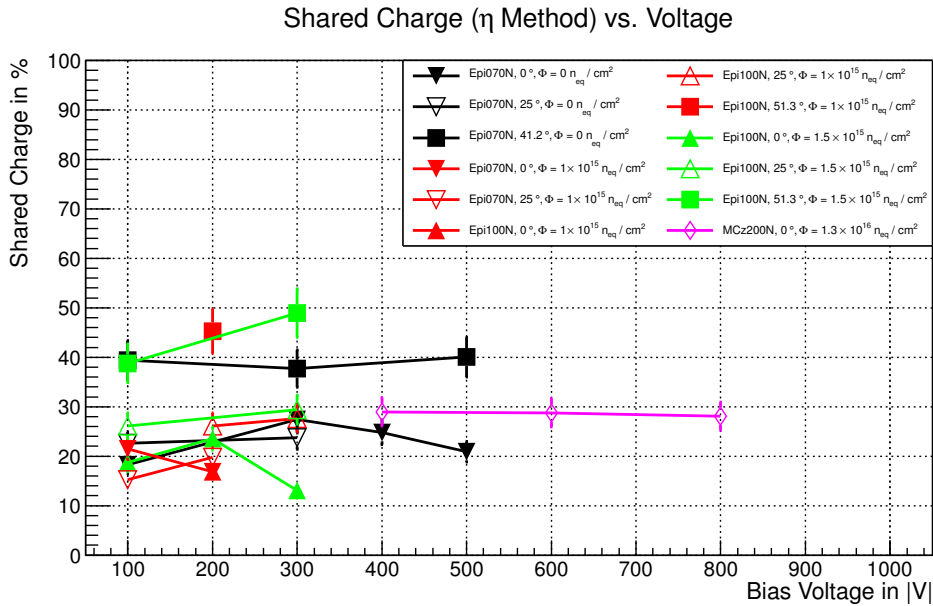
Figure 5.58: The amount of charge sharing for n-bulk sensors, if the η-distribution of each run is integrated. η values between 0.2 and 0.8 are considered as shared. In general, an increase in charge sharing is observed for all sensors with increasing incidence angle. Lacking analysable data at higher voltages, other effects seen in p-bulk sensors can not be confirmed.

this case a remaining signal would be registered by only one of the neighbouring channels, filling the η-distribution around either 0 or 1.

A very simple toy Monte Carlo simulation illustrates this point. In this simulation, 10000 tracks are randomly distributed between two strips with a pitch of 80 μm, with a track inclination of either 0° or 25°. The bulk is then divided into two sensitive areas left and right, and a central unsensitive area. Each track generates a signal proportional to its path length in each sensitive area. This signal is then collected by the corresponding strip. Each strip also registers a noise charge, which is taken from a randomly generated Gaussian distribution centred around 0 with a width of 5. From these generated signals, the resulting η-distribution is calculated, for varying widths of the central unsensitive area. Figure 5.59 shows two scenarios for 25° track inclination. The resulting η-distributions can be seen in figure 5.60. If the entire sensor bulk is considered sensitive, then the resulting η-distribution shows a clear picture: For 0° incidence, the only charge sharing contributions in this simple model stem from the noise of the other strip, whereas there is far more charge sharing for 25°. If the unsensitive area is widened, both distributions begin to converge. For unsensitive areas greater 35 μm, the 0° distribution indicates more charge sharing than for 25°.

For this simulation model, an unsensitive area encompassing the entire sensor thickness is used. In reality, it is highly improbable that the entire depth of the bulk is unsensitive. Charges deposited beneath this unsensitive area, would however not reach the strips within the readout time, thus the sensor bulk here can

Figure 5.59: Toy Monte Carlo schematic for 25° track inclination. A sensor bulk between two strips is shown. In the left picture, signals are created throughout the entire path of the track and are collected either on the left or the right strip. The right picture sh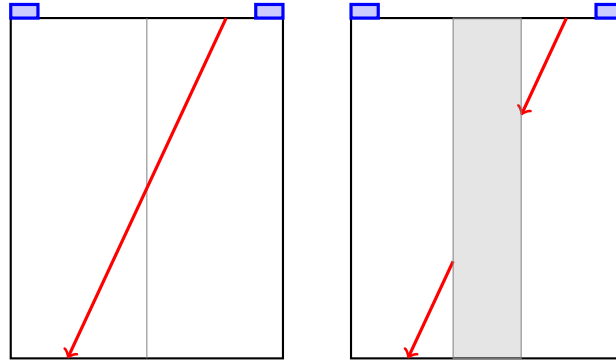ows the same track, if a 20 μm wide central unsensitive area is assumed. The area in which a signal is generated is reduced.

be regarded as an *effectively inefficient bulk*. In an actual p-bulk sensor, the electric field lines point vertically from the sensor strips at the surface towards the sensor backplane, with a curvature in the strip area due to the electric field in this region. Negative charge carriers generated centrally between strips are therefore drawn towards the strips where they are then read out, positive charges are collected at the backplane. Field lines not originating from the strips, but from the sensor surface, would however result in those charges not being collected, but being lost. Charge loss effects between strips in other HPK sensors were reported for example by Erfle, Klanner and Pöhlsen in [53], [77] and [108], respectively.

The measured amount of charge shared between strips is increased for larger beam incidence angles $\geqslant 38.6°$. This is due to geometrical considerations: an inclined track's lateral distance x in a sensor of thickness d is given by $x = d \cdot \tan \alpha$. Should x increase beyond the sensor strip pitch of 80 μm, the track deposits charge in more than one unit cell. This is still the case even if there is an unsensitive area between strips.

For the highest irradiations of $1.3 \times 10^{16} \, n_{eq}/cm^2$ however, at the highest incidence angles (51.3° for 100 μm thick sensors, 31.8° for 200 μm thick ones) this is no longer the case. This is due to the electric field configuration within the sensor. At this irradiation fluence, the entire sensor bulk is not necessarily depleted, thus reducing the effective thickness of the sensor. Inclined tracks therefore traverse a depleted bulk region only below a single strip, filling the η-distribution in turn with entries either around 0 or 1. This can explain the reduced charge sharing in this case.

An alternative method to determine the amount of charge shared within a sensor can be done by a form of clustering process. For each extrapolated track impact point on the DUT sensor, the signals in adjacent strips are compared against a certain threshold. Should the signals exceed this cut, the charge deposited by the
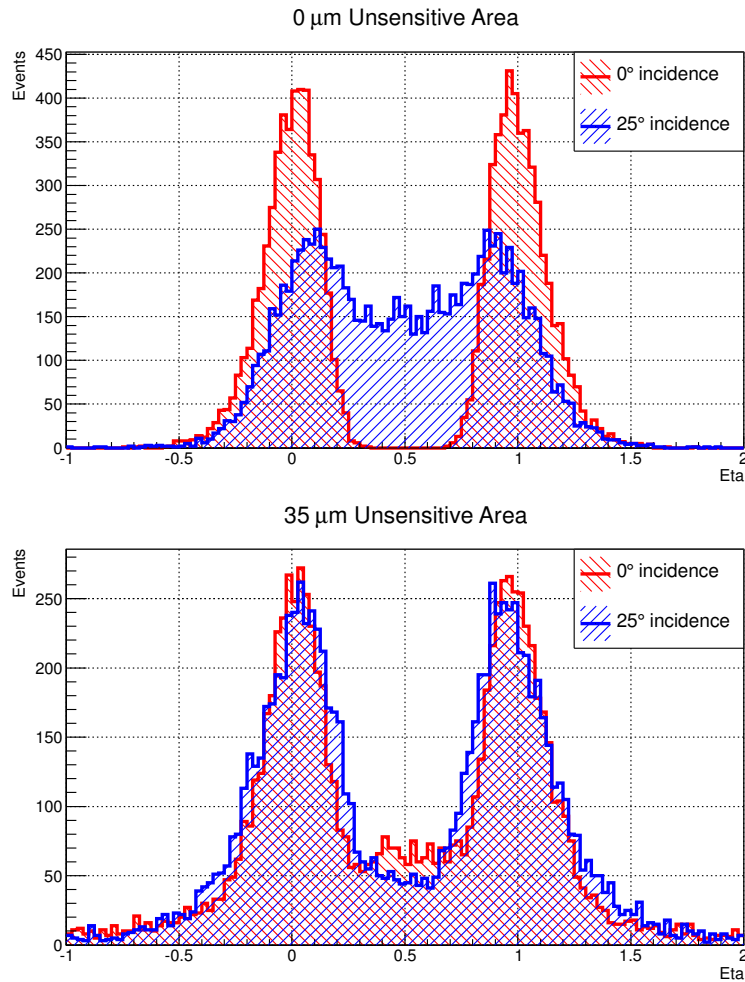
Figure 5.60: The η-distributions obtained from toy Monte Carlo simulations. The distributions from 0 ° tracks are displayed in red, the 25 ° distributions in blue. In the upper figure, no unsensitive area is assumed. An unsensitive area of 35 µm results in the bottom figure. If charge sharing is defined as the ratio of entries between η = 0.2 and η = 0.8 to those entries outside, in this scenario tracks with an inclination of 25 ° share less charge than perpendicular ones.

track in the sensor can be considered shared between the strips in question.

The obvious deficit of this method is that by the introduction of a cut, small signals are not considered. This can be problematic especially in those cases where the signal-to-noise ratio is low, for example at highest irradiations. Also, the amount of shared charge (in %) determined from this method differs from the previously introduced one, so that absolute values can not directly be compared.

Figures 5.61 through 5.67 show the amount of charge sharing for different sensor bulk materials, if a cut of 1.5 times the channel noise is considered as a threshold. This value has been found to be the best compromise between cutting off small charges on the one hand and including noise charges on the other hand.

Figure 5.61: The amount of charge sharing for p-stop sensors at $0°$ incidence, if a threshold cut of 1.5 times the individual channel noise is considered. As in the previously shown η-distribution method, the amount of shared charge increases with irradiation and declines with rising bias voltage, except for the fluence of $1.3 \times 10^{16}\,n_{eq}/cm^2$, where the highest amount of charge shared is measured at $-1000\,V$.
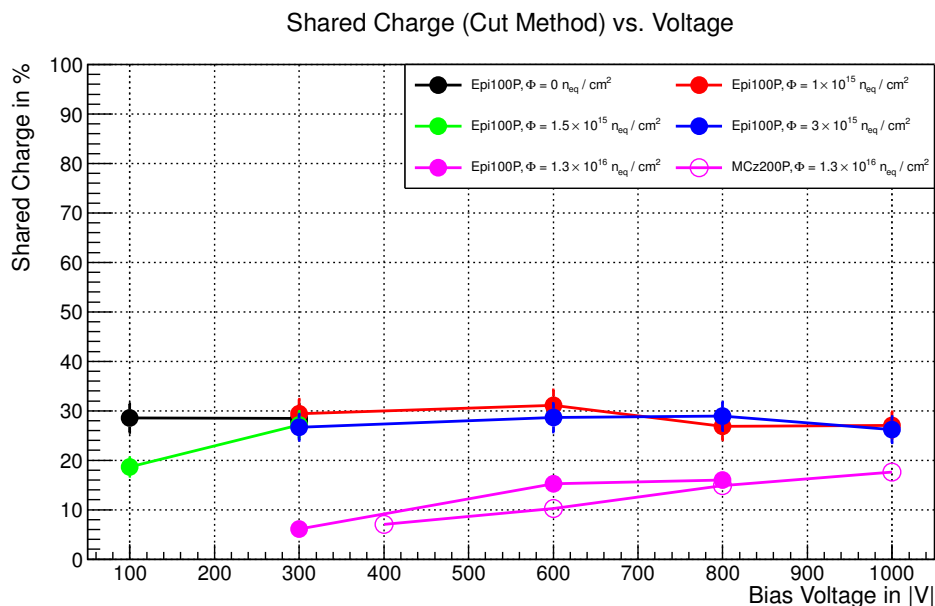
Figure 5.62: The amount of charge sharing for p-stop sensors at $25°$ incidence, calculated by the threshold cut method. Similar levels of charge sharing are measured as for $0°$ incidence, for all sensors and fluence steps.
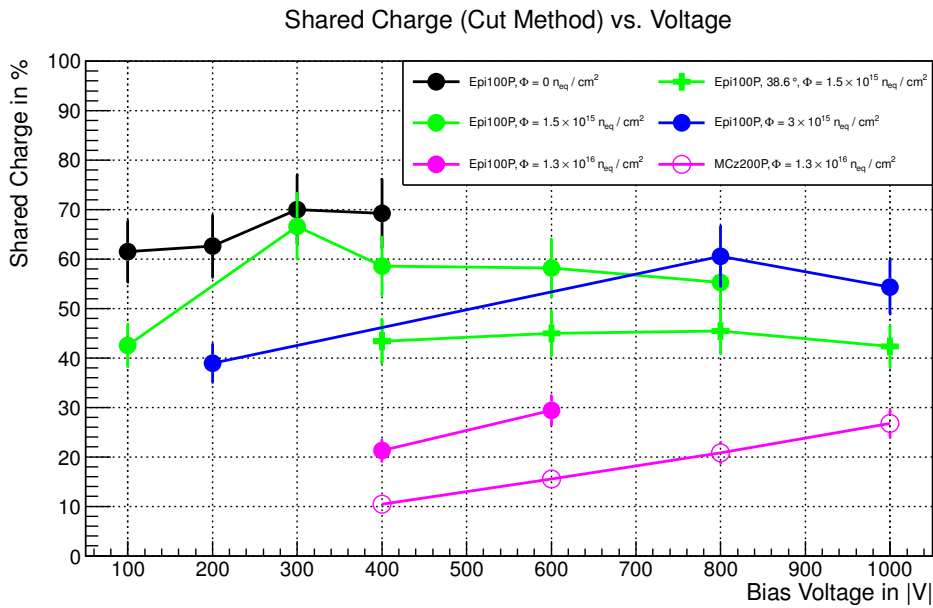
Figure 5.63: The amount of charge sharing for p-stop sensors at higher incidence angles, 38.6° and 51.3° for epitaxial sensors, 31.7° for non-epitaxial sensors, if a threshold cut is considered. Whilst absolute levels of charge sharing are different, a similar charge sharing behaviour as obtained by the η-distribution method is found. For all sensors, an increase of charge shared with incidence angle can be observed.
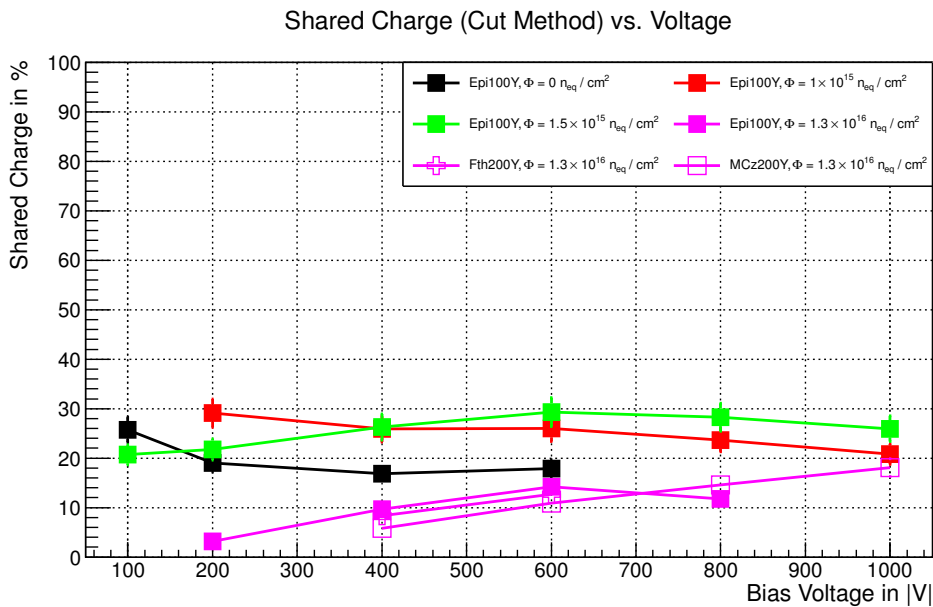
Figure 5.64: The amount of charge sharing for p-spray sensors at 0° incidence, if a threshold cut is considered. Again, absolute values are smaller than those obtained from the η-distribution, but nevertheless a similar behaviour can be observed. The exception to this is the non-irradiated sensor, where values are larger.
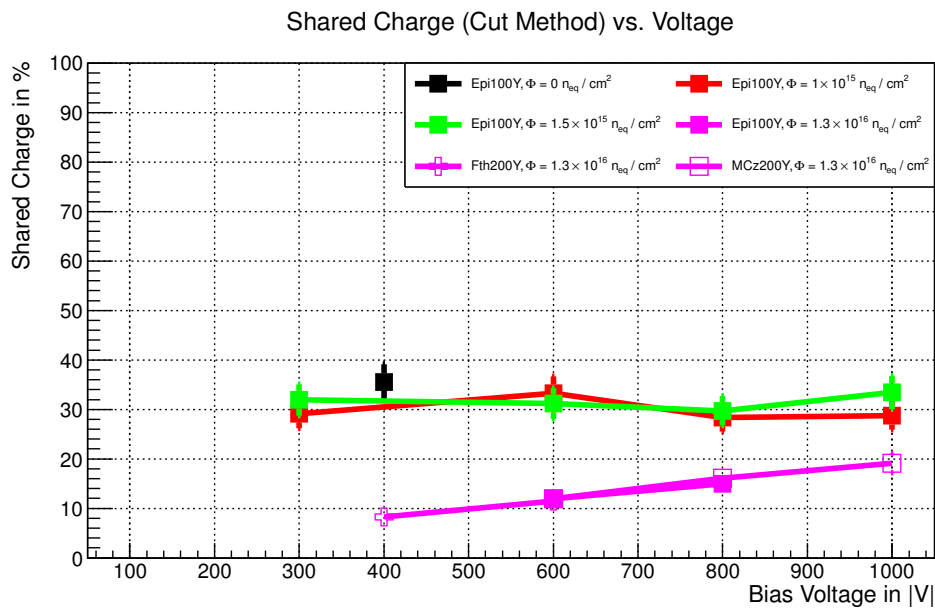
Figure 5.65: The amount of charge sharing for p-spray sensors at 25° incidence, using a threshold cut. As seen in figure 5.62, the drop in charge shared for sensors irradiated to $1.3 \times 10^{16}\,\mathrm{n_{eq}/cm^2}$ between 0° and 25° incidence, as shown when using the η-distribution, is no longer observed when using this method. This leads to the conclusion that the reduction in charge sharing may be due to the methodology.
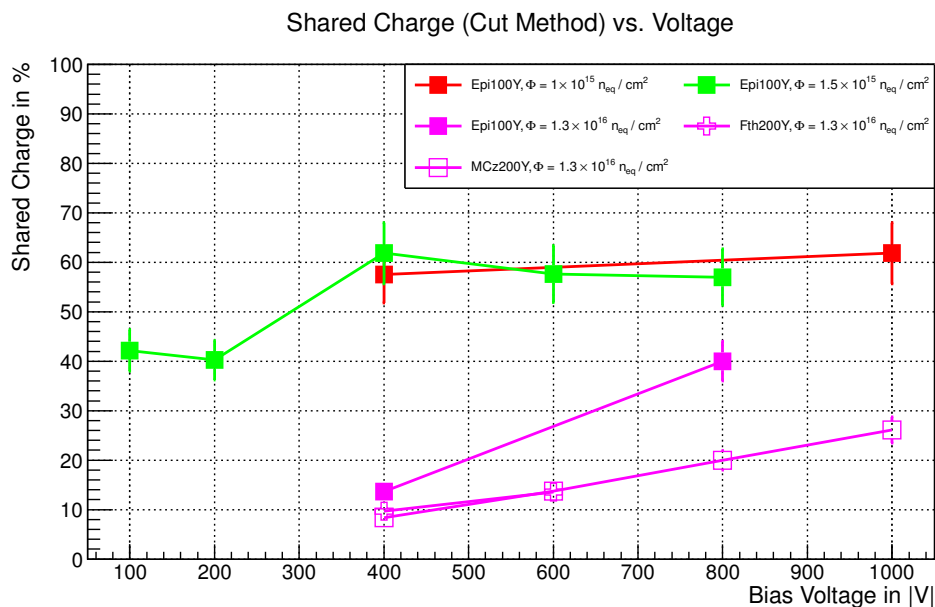
Figure 5.66: The amount of charge sharing for p-spray sensors at higher incidence angles, 51.3° for epitaxial sensors, 31.7° for non-epitaxial sensors, if a threshold cut is considered. As is to be expected, all sensors share more charge than for smaller incidence angles.
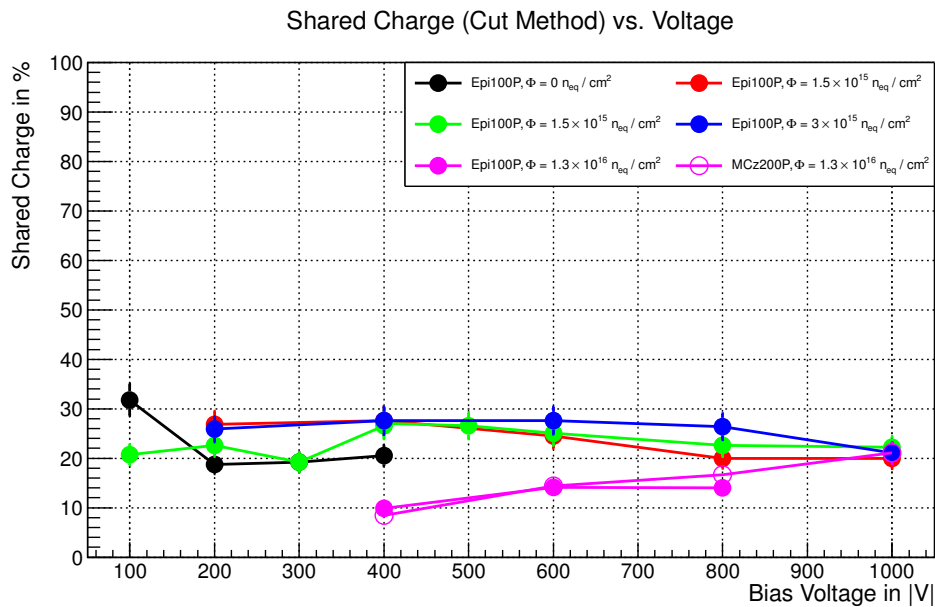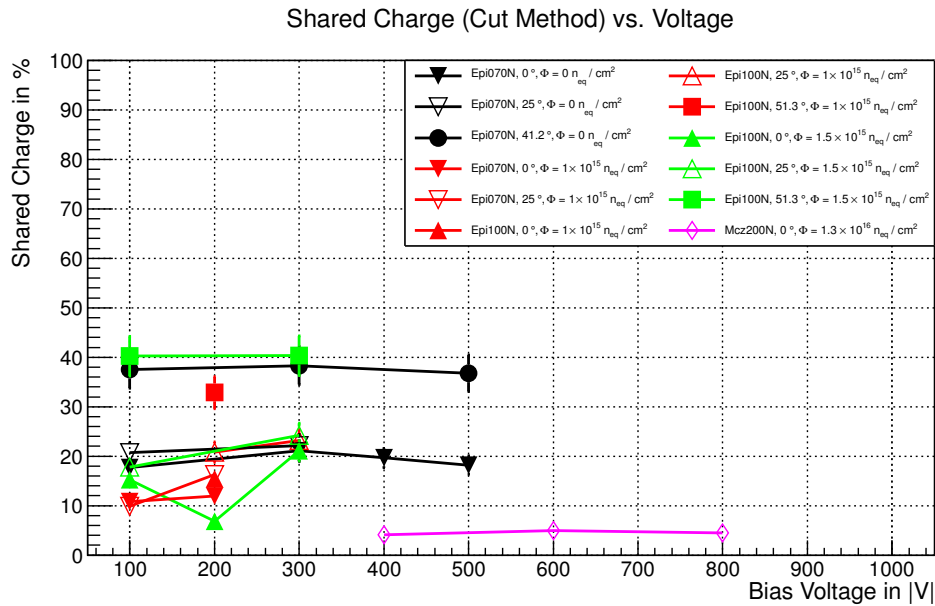
Figure 5.67: The amount of charge sharing for n-bulk sensors, if a threshold cut of 1.5 times the individual channel noise is considered. Similar results are obtained with the η-distribution method.

Compared with the amount of charge shared obtained from the integration of the η-distribution, this threshold method shows some similarities. The amount of charge shared generally increases with beam incidence angle and with irradiation. A decline with increasing bias voltage is also observed. The main difference lies in the behaviour of the sensors irradiated to 1.3×10^{16} n_{eq}/cm^2. Here the amount of charge shared is considerably less than seen from the η-distribution, which can be explained by the signal-to-noise levels in these sensors.

Both methods have their advantages and drawbacks. Extracting the amount of charge shared from the η-distribution does not require a cut on the charge, which is beneficial for high irradiations. On the other hand, other sensor effects such as non-depleted or unsensitive areas of the bulk influence the filling of the distribution. This is avoided by the clustering method. Both methods can be susceptible to the high noise levels found in the sensors investigated in this work.

In summary, the charge sharing results obtained by two different methods show similar results. Charge sharing increases with irradiation and incidence angle. For highest fluences of 1.3×10^{16} n_{eq}/cm^2, the amount of charge shared rises with applied bias voltage. For lower fluences a gradual decrease with voltage is observed. Furthermore, an inactive layer at the sensor surface in highly irradiated sensors can describe the charge sharing distributions presented for different incidence angles.

5.4.6 *Sensor Currents*

During the data taking in the test beams, the current drawn by each sensor from the Keithley power supply was noted into the operations log. While this is no substitution for a laboratory IV measurement of sensors, it nevertheless gives an indication of the sensors' leakage current behaviour and can provide further information on sensor properties. Figure 5.68 shows the drawn current during the test beams. The values are averaged over the rotation steps of each sensor and voltage. Since the current was only noted at the start of each run and might have changed unknowingly during operation, a 10 % error is assumed. Furthermore, the exact sensor temperature is not known, which can also account for inaccuracies.
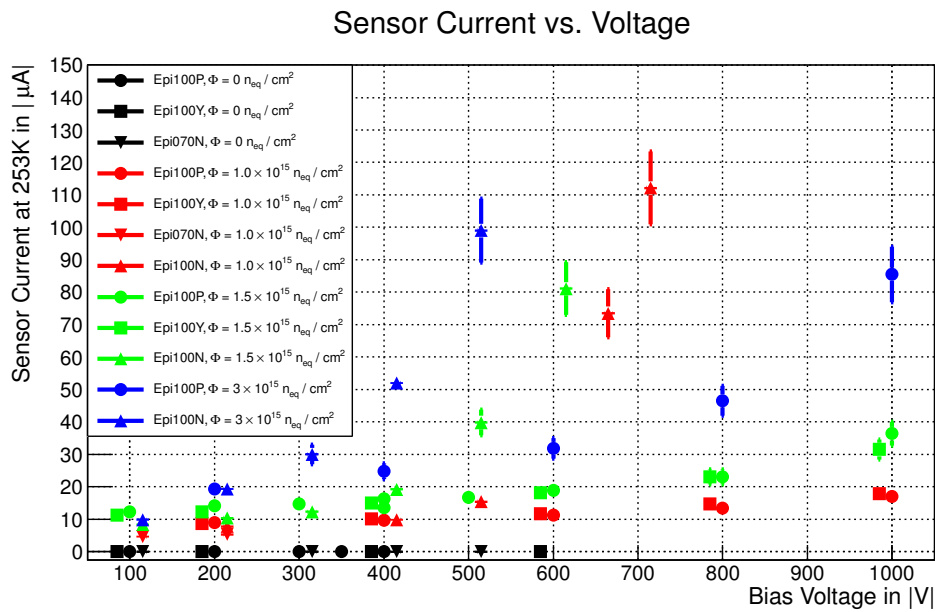
Figure 5.68: Measured sensor currents during the test beams, for sensors irradiated to fluences of $3 \times 10^{15}\,\mathrm{n_{eq}/cm^2}$ and below. An error of 10 % on the current is assumed, some points are shifted on the x axis for legibility.

For comparison, all currents were scaled to 253 K with equation 2.21, as described in chapter 2.1.1.4. For irradiations of up to $3 \times 10^{15}\,\mathrm{n_{eq}/cm^2}$, the drawn current does not exceed 100 µA for p-bulk sensors, with a possible onset of soft breakdown observable. With increasing voltage, the irradiated n-bulk sensors draw a much higher current than comparable p-bulk sensors, which can be due to the micro discharges at the sensor surface, explained earlier.

In figure 5.69, the currents measured for sensors irradiated to fluences of $1.3 \times 10^{16}\,\mathrm{n_{eq}/cm^2}$ are compared to currents measured on diodes of equal material, irradiated to the same fluence. All measurements are scaled to the surface area of the device concerned and to a temperature of 253 K. Horizontal lines indicate the expected leakage current at depletion voltage for both 100 µm and 200 µm device thickness, if the parametrisation from [94] is used (cf. equation 2.46). With no annealing, $\alpha\,(-20\,^\circ\mathrm{C}) = (8.5 \pm 0.2) \times 10^{-19}\,\mathrm{A/cm^3}$ is assumed. For most materials,

Currents in Diodes and Sensors
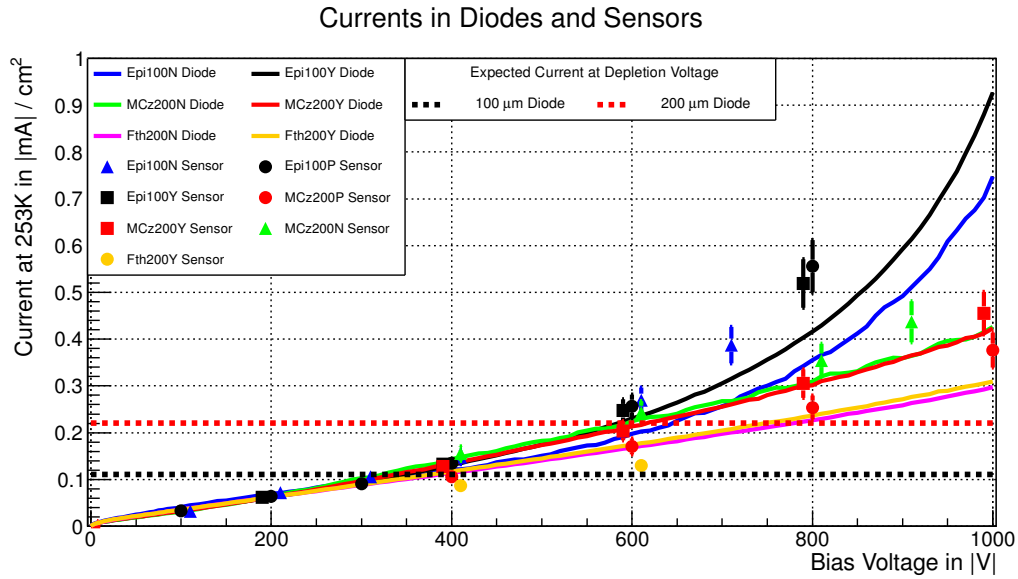
Figure 5.69: Comparison of the currents measured in the strip sensors with currents measured on diodes of the same material. All diodes and sensors were irradiated to a fluence of $1.3 \times 10^{16}\,n_{eq}/cm^2$. Measurements are scaled to the device surface area and to $253\,K$. For legibility, some strip sensor points are shifted on the x axis, with an assumed $10\,\%$ error on the currents measured in the test beam. Diode data from [73].

the current per surface area observed in the strip sensors is higher than in the corresponding diodes. This behaviour is also observed in other strip sensors in the HPK campaign [43] and can result from additional surface currents. Nevertheless, strip sensors and diodes show a similar general behaviour: The thicker MCz and Fth materials show a linear current increase over the voltage domain, whilst the current measured in both epitaxial strip sensors and diodes shows an exponential rise toward higher voltages, again suggestive of charge multiplication.

5.5 summary

In this chapter, test beam measurements of silicon strip sensors with pixel beam telescopes in the DESY-II test beam have been presented. These measurements were the first ever of irradiated epitaxial sensors in a test beam. The sensors were irradiated to different fluences, with the highest one representing the life-time charged hadron fluence expected for the innermost layer of the CMS Phase-II pixel detector (cf. section 1.4.3.1). After a description of the setup and the data acquisition systems, the analysis steps undertaken have been explained.

The strip sensors were read out with the ALiBaVa system and integrated into the pixel beam telescopes and their software analysis framework, *EUTelescope*. All necessary reconstruction steps were implemented into this framework, so that ultimately the strip sensor DUT could be aligned with respect to the pixel telescope.

Filtering steps to remove cross-talk effects and non-Gaussian noise from n-bulk sensors have been implemented. Two different methods to measure the amount of cross-talk and to calculate correction values have been presented, both yielding similar results. With the tracks measured in the telescope extrapolated to the strip sensor, an analysis of the strip sensor properties has been performed and results have been presented.

The measured resolution of the strip sensors is at the binary level. For some runs this could be improved on, for others the resolution is not as good as expected. No systematic could be found. The lowest measured resolution was 21.6 µm. The channel noise measured in the epitaxial sensors amounted to less than 6 ADCs for moderate irradiations and increased to 7 for highest irradiation levels of $1.3 \times 10^{16}\, \mathrm{n_{eq}/cm^2}$.

The charge collected for p-bulk sensors irradiated to a fluence of 3×10^{15} $\mathrm{n_{eq}/cm^2}$ amounted to over 80 % of the pre-irradiation levels. For highest irradiations, the collected charge dropped to over 65 %. The signals increase with bias voltage and beam incidence angle. Especially for high fluences, the increase in signal for rotated sensors is larger than would be expected from geometrical considerations alone. This suggests a non-linear electric field within these sensors at high fluences and can also be indicative of charge multiplication. The resulting signal-to-noise ratios from these signal measurements are 7.4 for moderate and 3.8 for highest fluences. Prior to irradiations, these levels were at 9.9.

Two methods to determine charge sharing between sensor strips have been explained. Both show a consistent behaviour, with charge sharing decreasing with bias voltage and increasing with fluence. Neither method can be considered optimal, as both have some drawbacks. Introducing cuts to measure charge sharing underestimates the amount of charge shared at highest irradiations. However, if charge sharing is calculated from η-distributions, an overestimation of sharing for perpendicular beam incidence can occur due to unsensitive regions between strips. A very simple simulation shows that an unsensitive area, with electric field lines not terminating at the strips, would result in similar η-distributions. The exact configuration of the electric field within the sensor bulk however, can only be determined by other measurement techniques, for example by Edge-TCT measurements [79].

The currents measured during test beam operation are also comparable with measurements on diodes of the same material. An exponential rise in current at a fluence of $1.3 \times 10^{16}\, \mathrm{n_{eq}/cm^2}$ towards higher bias voltages in the epitaxial strip sensors can be indicative of charge multiplication. A similar rise in current is measured on epitaxial diodes, on which charge multiplication has been observed [81].

These test beam results show that thin, n-bulk epitaxial silicon is not a viable option for a radiation hard tracking detector, if a design similar to the one used on the investigated strip sensors is used. Despite showing similar noise, signal and charge sharing levels prior to irradiation as p-bulk sensors, non-Gaussian noise

discharges, as observed previously by others, render this material and design useless after irradiation. Correction methods were applied to nevertheless be able to compare against p-bulk sensors, but this was only possible for low bias voltages and fluences. Higher bias voltages, which would be necessary for the depletion of the entire sensor after irradiations, result in an uncorrectable amount of non-Gaussian noise. It was possible to successfully align the $200\,\mu m$ thick Magnetic Czochralski n-bulk sensor in the telescope, although it was irradiated to a fluence of $1.3 \times 10^{16}\,n_{eq}/cm^2$. The resulting signal-to-noise ratio, however is only 2, due to the high overall noise level. The absence of non-Gaussian noise could be due to the more homogeneous electric field in this material, but this does not improve the sensor's performance. Nevertheless, n-bulk material can not generally be excluded for a future tracker sensor material. However, more efforts are needed to sufficiently reduce the non-Gaussian noise discharges, which can result from high electric fields at the sensor surface, caused by an interplay between surface and bulk damage [14]. Because of the time constraints due to the foreseen upgrade schedule, the CMS experiment has focussed on p-bulk material [47]. The signals, noise levels and also the annealing behaviour measured within the HPK campaign also show no compelling advantage of n-bulk material over p-bulk material, which could necessitate these efforts [123].

No significant difference between p-spray and p-stop isolated p-bulk material could be observed. The measured resolutions, signals, noise values and the amount of charge shared between strips are equal within the errors for both isolation techniques.

The results presented in this chapter were obtained from the first ever measurements of highly irradiated, thin epitaxial silicon sensors in a test beam. From them it can be concluded that p-bulk epitaxial silicon could be successfully used as a radiation hard sensor material for tracking detectors in a future High Luminosity LHC. Further measurements of epitaxial silicon should be performed to investigate the charge collection efficiency at intermediate fluences between $3 \times 10^{15}\,n_{eq}/cm^2$ and $1.3 \times 10^{16}\,n_{eq}/cm^2$. With this, the applicability as a sensor material for the CMS pixel and tracker detectors could be further established. These test beam measurements have used strip sensors to investigate material properties, as the exact readout specifications of the future CMS tracker at the HL-LHC have not yet been entirely finalised. An analysis of sensors adhering to these requirements could then be used to perform detailed signal and noise level measurements.

The ALiBaVa system used as strip sensor data acquisition system in this work has proven to be a versatile system. As it is also used in several laboratory setups using radioactive sources, a comparison of test beam data to these results could be performed. Nevertheless, due to the precise tracking information provided by the pixel beam telescopes, test beam measurements offer unique measurement possibilities and prospects. The use of an additional reference plane located downstream from the pixel telescope could provide finer timing information. This in

turn could be used to investigate and analyse sensor efficiencies.

SUMMARY AND OUTLOOK

The future upgrade of the Large Hadron Collider at CERN to a *High Luminosity LHC* promises exciting times for particle physics. An increased luminosity will however present the tracking detectors of the LHC's experiments with an unprecedented particle fluence, leading to an increased occupancy and radiation damage of the silicon sensors.

The CMS experiment will replace its entire tracker detector to combat these effects and maintain the excellent tracking performance the current detector delivers. A new tracker detector will need new, even more radiation hard, silicon sensors. A dedicated campaign to find the technological baseline of a future sensor has been undertaken by CMS, in the course of which, simulations and test beam measurements, presented in this thesis, have been performed.

TCAD (*technology computer-aided design*) simulations can be a valuable tool in the development of semiconductor sensors, especially concerning their radiation hardness. A working group within the CMS Tracker Collaboration has been formed to streamline simulation tasks. To establish the predictive power of simulations, these have to be compared against measurement data, both before and after irradiation. For this comparison, a reconstruction of the exact sensor geometry is crucial. Simulations of the interstrip capacitance of strip sensors of various geometries have been presented in this thesis, well in agreement with measurement data. With the inclusion of an effective radiation damage model, simulated capacitance values correspond to those measured on irradiated strip sensors. Ongoing and future simulation work will concern the performance of irradiated pixel sensors and the interplay between bulk and surface defects in silicon.

The test beam measurements have made use of the high-precision pixel telescopes available at the DESY-II test beam facility. The excellent performance of the telescopes has been proven in several measurements and the intrinsic resolution of the telescope sensors has been measured. Under optimal conditions, a track pointing resolution at the *device under test* (DUT) of under 2 μm can be achieved at DESY-II test beam facility.

Test beam measurements with high-precision pixel beam telescopes have proven to be a versatile tool for a wide range of semiconductor sensor studies. A continuous development is ongoing to upgrade and enhance the data acquisition systems and the analysis frameworks. This process is driven by the large and diverse user community, which extends to all areas of detector development.

Epitaxial silicon is a promising candidate material for future radiation hard sensors for the High Luminosity LHC. Strip sensors of this material have been irra-

diated to various fluences of up to $1.3 \times 10^{16}\,n_{eq}/cm^2$, which corresponds to the lifetime charged hadron irradiation expected for the innermost layers of the CMS pixel detector at the HL-LHC. Sensors were wire bonded to an *ALiBaVa* readout system and measured with aforementioned pixel telescopes in the DESY-II test beam facility, with the goal of assessing the radiation hardness of epitaxial silicon.

The epitaxial strip sensor data was included into the pixel telescope reconstruction software, allowing the alignment of the sensors relative to the pixel telescope planes. Reconstruction and filtering steps were implemented to remove signal cross-talk and, for n-bulk sensors, non-Gaussian noise effects from the epitaxial sensors. With particle tracking information from the telescope, a wide range of the epitaxial strip sensors' properties has been investigated. The achievable resolution on the DUT sensors is at a binary level, which corresponds to the measured cluster size. At irradiation levels of $3 \times 10^{15}\,n_{eq}/cm^2$, the charged hadron fluence expected for the third pixel barrel layer of the CMS detector at the HL-LHC, the charge collected in p-bulk epitaxial silicon amounts to over 80 % of the pre-irradiation levels. For highest fluences of $1.3 \times 10^{16}\,n_{eq}/cm^2$, the collected charge drops to over 65 %. These charge collection efficiency values result in signal-to-noise levels of 7.4 for the former, and 3.8 for the latter fluence.

The charge sharing behaviour of epitaxial sensors has also been investigated, with two different evaluation methods presented. Indications of possible charge losses at the sensor surface have been found. Analysis of data taken with varying beam incidence angles shows signs of charge multiplication for highly irradiated epitaxial sensors. Charge multiplication could partially avert the losses in charge collection efficiency at highest irradiations. The measured leakage current behaviour supports this hypothesis and is consistent with measurement data obtained from epitaxial diodes. These were irradiated to the same fluence and have shown charge multiplication effects in laboratory measurements. Epitaxial sensors produced with an n-type bulk show non-Gaussian noise discharges after irradiation, a behaviour which is also seen in n-bulk sensors of other materials, produced by the same vendor. While this is partially correctable for certain scenarios in measured test beam data, this is not applicable for an actual tracking detector in the CMS experiment. Altogether, with the results presented in this thesis, it has been shown that p-bulk epitaxial silicon is a promising candidate material for use as a radiation hard sensor material for tracking detectors in a future High Luminosity LHC.

Future work in this area could further investigate the charge multiplication effects at highest irradiations. For this, more test beam measurements seem feasible, especially including measurements of inclined sensors and using intermediate irradiation steps. While this evaluation of the radiation hardness of epitaxial silicon has been performed on strip sensors, measurements of pixelated epitaxial sensors, adhering to the future CMS readout specifications, could further prove the suitability of this material for use as a HL-LHC pixel sensor material.

APPENDIX

A.1 SYNOPSYS TCAD SETTINGS AND SOURCE CODE

For comparison and reproducibility of results, some of the settings and source code used for the simulations in this thesis are listed in this section. For a complete overview of the parameters, settings and an explanation of the used commands, the interested reader is referred to the simulation manual [126].

A.1.1 *Parameters and Settings*

A.1.1.1 *Masetti Model for Doping-Dependent Mobility*

The used default values in equation 4.3 for the Masetti model are:

Table A.1: Default coefficients of the Masetti model, as stated in [126].

Symbol	Unit	Electrons	Holes
$\mu_{min,1}$	cm^2/Vs	52.2	44.9
$\mu_{min,2}$	cm^2/Vs	52.2	0
μ_1	cm^2/Vs	43.4	29.0
P_c	cm^{-3}	0	9.23×10^{16}
C_r	cm^{-3}	9.68×10^{16}	2.23×10^{17}
C_s	cm^{-3}	3.43×10^{20}	6.10×10^{20}
α	1	0.680	0.719
β	1	2.0	2.0

A.1.1.2 *Canali Model for Field-Saturated Mobility*

The used default values in equations 4.4 and 4.5 for the Canali model are:

Table A.2: Default coefficients of the Canali model, as stated in [126].

Symbol	Unit	Electrons	Holes
β_0	1	1.109	1.213
β_{exp}	1	0.66	0.17
α	1	0	0
$v_{sat,0}$	cm/s	1.07×10^7	8.37×10^6
$v_{sat,exp}$	1	0.87	0.52

A.1.2 *Structure Generation*

The following `Tcl` script is used to generate the two-dimensional strip sensor structures used for simulations. The workbench tool of Synopsys TCAD, `swb`, allows the user to keep track of all simulation parameters and variables. Depending on the individual setup selected, `swb` passes these to the script, which in turn generates an input device file for the meshing process. While the `z` coordinate is set to zero, in the subsequent device simulation, results can be scaled to larger devices with the `areafactor` command. `Tcl` uses *Polish notation*, possibly unnecessary brackets are included for legibility.

First, some shortcuts, the dopants and the doping profiles are defined:

```
0   # Shortcuts
    (define sens_w(* pitch(- stripcount 1)))
    (define tot_t(+ str_t(+ ox_t(+ sens_t backp_t))))
    (define bulkstpos(+ str_t ox_t))

5   # Define dopants according to sensor type, default n-type
    (define dop_bulk "PhosphorusActiveConcentration")
    (define dop_back "PhosphorusActiveConcentration")
    (define dop_str "BoronActiveConcentration")
    (if(string=? sensortype "p")||(string=? sensortype "y")
10    (begin
        (set! dop_bulk "BoronActiveConcentration")
        (set! dop_back "BoronActiveConcentration")
        (set! dop_str "PhosphorusActiveConcentration")
      )
15  )

    # Doping profiles
    (sdedr:define-gaussian-profile "Str_dop" dop_str "PeakPos" str_p "PeakVal" imp_dop "ValueAtDepth"
      bulk_dop "Depth" implantthickness "Erf" "Factor" str_er)
    (sdedr:define-erf-profile "Dop_Def_Backp" dop_back "SymPos" sympos "MaxVal" backp_dop "ValueAtDepth"
      bulk_dop "Depth" backp_imp_t "Erf" "Factor" backp_er)
20  (sdedr:define-gaussian-profile "Iso_dop" "BoronActiveConcentration" "PeakPos" isol_p "PeakVal" ido_dose
      "ValueAtDepth" bulk_dop "Depth" iso_t "Erf" "Factor" isol_er)
    (sdedr:define-constant-profile "Dop_Bulk" dop_bulk bulk_dop)
```

Then, the first and last strips are created, together with the bulk structure. A guard ring and a bias ring are added. To model the HPK wafer structures, strips and rings have an additional layer of silicon nitride:

```
    # Main structures: backplane
25  (sdegeo:create-rectangle(position(-(-(-(-(- 0(/ str_w 2))bias_s)bias_w)guard_s)guard_w)(- tot_t
      backp_t)0)(position sens_w tot_t 0)"Aluminum" "Backplane")
    (sdedr:define-refeval-window "Dop_Backp" "Line"(position(-(-(-(-(- 0(/ str_w
      2))bias_s)bias_w)guard_s)guard_w)(- tot_t backp_t)0)(position sens_w(- tot_t backp_t)0))

    # Bulk, oxide
    (sdegeo:create-rectangle(position(-(-(-(-(- 0(/ str_w 2))bias_s)bias_w)guard_s)guard_w)bulkstpos
      0)(position sens_w(- tot_t backp_t)0)"Silicon" "Bulk")
30  (sdegeo:create-rectangle(position(-(-(-(-(- 0(/ str_w 2))bias_s)bias_w)guard_s)guard_w)str_t
      0)(position sens_w bulkstpos 0)"SiO2" "Oxide")

    # Strip 1
    (sdegeo:create-rectangle(position(- 0(/ str_w 2))0 0)(position(/ str_w 2)str_t 0)"Aluminum"
      "Strip_Top_1")
    (sdegeo:create-rectangle(position(-(- 0(/ imp_w 2))overlay_w)str_t 0)(position(+ overlay_w(/ imp_w
      2))(+ str_t impvia)0)"Aluminum" "Strip_Bottom_1")
35  (sdegeo:create-polygon(list(position(- 0(+ overlay_w(/ imp_w 2))))str_t 0)(position(- 0(+ overlay_w(+
      diag_w(/ imp_w 2))))str_t 0)(position(- 0(+ overlay_w(/ imp_w 2)))(+ str_t impvia)0)(position(- 0(+
      overlay_w(/ imp_w 2)))str_t 0))"Aluminum" "Strip_Diag_Left_1")
    (sdegeo:insert-vertex(position(/ imp_w 2)bulkstpos 0))
    (sdegeo:insert-vertex(position(- 0(/ imp_w 2))bulkstpos 0))
    (sdedr:define-refeval-window "Dop_Str_1" "Line"(position(- 0(/ imp_w 2))bulkstpos 0)(position(/ imp_w
      2)bulkstpos 0))
    (sdegeo:create-rectangle(position(-(- 0(/ str_w 2))nit_o)str_t 0)(position(-(-(- 0(/ imp_w
      2))overlay_w)diag_w)(+ nit_t str_t)0)"Si3N4" "Nitr11")
40  (sdegeo:create-polygon(list(position(- 0(+ overlay_w(/ imp_w 2)))(+ str_t impvia)0)(position(- 0(+
      overlay_w(+ diag_w(/ imp_w 2)))str_t 0)(position(- 0(+ overlay_w(+ diag_w(/ imp_w 2))))(+ str_t
      nit_t)0)(position(- 0(+ overlay_w(/ imp_w 2)))(+ str_t(+ impvia nit_t))0)(position(- 0(+ overlay_w(/
      imp_w 2)))(+ str_t impvia)0))"Si3N4" "Nitr12")
    (sdegeo:create-rectangle(position(-(- 0(/ imp_w 2))overlay_w)(+ str_t impvia)0)(position(+ overlay_w(/
      imp_w 2))(+ str_t(+ impvia nit_t))0)"Si3N4" "Nitr13")
```

```scheme
# Bias ring and guard ring
(sdegeo:create-rectangle(position(-(- 0(/ str_w 2))bias_s)0 0)(position(-(-(- 0(/ str_w
   2))bias_s)bias_w)str_t 0)"Aluminum" "Biasring_Top")
(sdegeo:create-rectangle(position(-(-(-(- 0(/ str_w 2))bias_s)bias_w)guard_s)0 0)(position(-(-(-(-(-
   0(/ str_w 2))bias_s)bias_w)guard_s)guard_w)str_t 0)"Aluminum" "Guardring_Top")
(sdegeo:create-rectangle(position(-(-(- 0(/ str_w 2))bias_s)bias_imp_s)str_t 0)(position(-(-(-(- 0(/
   str_w 2))bias_s)bias_imp_s)biasimp_w)(+ str_t ringviathickness)0)"Aluminum" "Biasring_Bottom")
(sdegeo:create-rectangle(position(-(-(-(-(- 0(/ str_w 2))bias_s)bias_w)guard_s)guar_imp_s)str_t
   0)(position(-(-(-(-(-(- 0(/ str_w 2))bias_s)bias_w)guard_s) guar_imp_s)guardimp_w)(+ str_t
   ringviathickness)0)"Aluminum" "Guardring_Bottom")
(sdegeo:insert-vertex(position(-(-(- 0(/ str_w 2))bias_s)bias_imp_s)bulkstpos 0))
(sdegeo:insert-vertex(position(-(-(-(-(- 0(/ str_w 2))bias_s)bias_w)bias_imp_s)biasimp_w)bulkstpos 0))
(sdegeo:insert-vertex(position(-(-(-(-(- 0(/ str_w 2))bias_s)bias_w)guard_s)guar_imp_s)bulkstpos 0))
(sdegeo:insert-vertex(position(-(-(-(-(-(- 0(/ str_w
   2))bias_s)bias_w)guard_s)guard_w)guar_imp_s)guardimp_w)bulkstpos 0))
(sdegeo:define-contact-set "Cont_AC_B" 4(color:rgb 1 1 1)"##")
(sdegeo:define-contact-set "Cont_AC_G" 4(color:rgb 1 1 1)"##")
(sdegeo:define-contact-set "Cont_DC_B" 4(color:rgb 1 1 1)"##")
(sdegeo:define-contact-set "Cont_DC_G" 4(color:rgb 1 1 1)"##")
(sdegeo:set-current-contact-set "Cont_AC_B")
(sdegeo:set-current-contact-set "Cont_AC_G")
(sdegeo:set-current-contact-set "Cont_DC_B")
(sdegeo:set-current-contact-set "Cont_DC_G")
(sdegeo:define-2d-contact(list(car(find-edge-id(position(-(-(- 0(/ str_w 2))bias_s)(/ bias_w 2))0
   0))))"Cont_AC_B")
(sdegeo:define-2d-contact(list(car(find-edge-id(position(-(-(-(- 0(/ str_w 2))bias_s)bias_imp_s)(/
   biasimp_w 2))bulkstpos 0))))"Cont_DC_B")
(sdegeo:define-2d-contact(list(car(find-edge-id(position(-(-(-(-(- 0(/ str_w
   2))bias_s)bias_w)guard_s)(/ guard_w 2))0 0))))"Cont_AC_G")
(sdegeo:define-2d-contact(list(car(find-edge-id(position(-(-(-(-(-(- 0(/ str_w
   2))bias_s)bias_w)guard_s)guar_imp_s)(/ guardimp_w 2))bulkstpos 0))))"Cont_DC_G")
(sdedr:define-refeval-window "Dop_Biasr" "Line"(position(-(-(- 0(/ str_w 2))bias_s)bias_imp_s)bulkstpos
   0)(position(-(-(-(- 0(/ str_w 2))bias_s)bias_imp_s)biasimp_w)bulkstpos 0))
(sdedr:define-refeval-window "Dop_Guar" "Line"(position(-(-(-(-(- 0(/ str_w
   2))bias_s)bias_w)guard_s)guar_imp_s)bulkstpos 0)(position(-(-(-(-(-(- 0(/ str_w
   2))bias_s)bias_w)guard_s)guar_imp_s)guardimp_w)bulkstpos 0))
(sdedr:define-analytical-profile-placement "Biasr_Dop" "Str_dop" "Dop_Biasr" "Both" "NoReplace" "Eval")
(sdedr:define-analytical-profile-placement "Guard_Dop" "Str_dop" "Dop_Guar" "Both" "NoReplace" "Eval")

# Isolation between strip 1 and the rings
(if(string=? sensortype "y")
  (begin
    (sdedr:define-refeval-window "Dop_Spr_0" "Line"(position(- 0(/ imp_w 2))bulkstpos 0)(position(-(-(-
       0(/ imp_w 2))bias_s)bias_imp_s)bulkstpos 0))
    (sdedr:define-analytical-profile-placement "Spr_dop_0" "Iso_dop" "Dop_Spr_0" "Both" "NoReplace"
       "Eval")
  )
)
(if(string=? sensortype "p")
  (begin
    (do((j 1(+ j 1)))((= j(+ pstopcount 1)))
      (begin
        (set! tmp2 "Dop_Stop_0")
        (set! tmp1(string-append tmp2(number->string j)))
        (set! tmp4 "Stop_dop_0")
        (set! tmp3(string-append tmp4(number->string j)))
        (sdedr:define-refeval-window tmp1 "Line"(position(+(-(- 0(/ pitch 2))(/(+(* stop_w
           pstopcount)(* stop_sp(- pstopcount 1)))2))(*(- j 1)(+ stop_w stop_sp)))bulkstpos
           0)(position(+(+(-(- 0(/ pitch 2))(/(+(* stop_w pstopcount)(* stop_sp(- pstopcount
           1)))2))(*(- j 1)(+ stop_w stop_sp)))stop_w)bulkstpos 0))
        (sdedr:define-analytical-profile-placement tmp3 "Iso_dop" tmp1 "Both" "NoReplace" "Eval")
      )
    )
  )
)

# Place electrical contacts, add doping
(sdedr:define-analytical-profile-placement "Dop_Def_Backp" "Dop_Def_Backp" "Dop_Backp" "Both"
   "NoReplace" "Eval")
(sdegeo:define-contact-set "Cont_Backp" 4(color:rgb 1 1 1)"##")
(sdegeo:set-current-contact-set "Cont_Backp")
(sdegeo:define-2d-contact(list(car(find-edge-id(position(/ sens_w 2)tot_t 0))))"Cont_Backp")
(sdedr:define-constant-profile-region "Dop_Bulk" "Dop_Bulk" "Bulk")
(sdegeo:create-polygon(list(position(+(/ imp_w 2)overlay_w)str_t 0)(position(+(+(/ imp_w
   2)overlay_w)diag_w)str_t 0)(position(+(/ imp_w 2)overlay_w)(+ impvia str_t)0)(position(+(/ imp_w
   2)overlay_w)str_t 0))"Aluminum" "Strip_Diag_Right_1")
(sdedr:define-analytical-profile-placement "Str_dop_1" "Str_dop" "Dop_Str_1" "Both" "NoReplace" "Eval")
(sdegeo:define-contact-set "Cont_AC_Str_1" 4(color:rgb 1 1 1)"##")
(sdegeo:set-current-contact-set "Cont_AC_Str_1")
(sdegeo:define-2d-contact(list(car(find-edge-id(position 1 0 0))))"Cont_AC_Str_1")
(sdegeo:define-contact-set "Cont_DC_Str1" 4(color:rgb 1 0 0)"##")
(sdegeo:set-current-contact-set "Cont_DC_Str1")
(sdegeo:define-2d-contact(list(car(find-edge-id(position 1 bulkstpos 0))))"Cont_DC_Str1")
(sdegeo:create-polygon(list(position(+(/ imp_w 2)overlay_w)(+ str_t impvia)0)(position(+(/ imp_w
   2)overlay_w)(+(+ str_t impvia)nit_t)0)(position(+(+(/ imp_w 2)overlay_w)diag_w)(+ str_t
   nit_t)0)(position(+(+(/ imp_w 2)overlay_w)diag_w)str_t 0)(position(+(/ imp_w 2)overlay_w)(+ str_t
   impvia)0))"Si3N4" "Nitr14")
(sdegeo:create-rectangle(position(+ diag_w(+ overlay_w(/ imp_w 2)))str_t 0)(position(+(/ str_w
   2)nit_o)(+ str_t nit_t)0)"Si3N4" "Nitr15")

# The last strip
```

```
    (set! tmp1 "StrTop_")
110 (set! tmp2(string-append tmp1(number->string stripcount)))
    (sdegeo:create-rectangle(position(- sens_w(/ str_w 2))0 0)(position sens_w str_t 0)"Aluminum" tmp2)
    (set! tmp1 "StrBot_")
    (set! tmp2(string-append tmp1(number->string stripcount)))
    (sdegeo:create-rectangle(position(- sens_w(+ overlay_w(/ imp_w 2)))str_t 0)(position sens_w(+ str_t
      impvia)0)"Aluminum" tmp2)
115 (set! tmp1 "StrDiL_")
    (set! tmp2(string-append tmp1(number->string stripcount)))
    (sdegeo:create-polygon(list(position(- sens_w(+ overlay_w(/ imp_w 2)))str_t 0)(position(- sens_w(+
      overlay_w(/ imp_w 2)))(+ str_t impvia)0)(position(- sens_w(+ overlay_w(+ diag_w(/ imp_w 2))))str_t
      0)(position(- sens_w(+ overlay_w(/ imp_w 2)))str_t 0))"Aluminum" tmp2)
    (sdegeo:insert-vertex(position(- sens_w(/ imp_w 2))bulkstpos 0))
    (set! tmp1 "Cont_AC_Str_")
120 (set! tmp2(string-append tmp1(number->string stripcount)))
    (sdegeo:define-contact-set tmp2 4(color:rgb 1 1 1)"##")
    (sdegeo:set-current-contact-set tmp2)
    (sdegeo:define-2d-contact(list(car(find-edge-id(position(- sens_w 1)0 0))))tmp2)
    (set! tmp1 "Cont_DC_Str")
125 (set! tmp2(string-append tmp1(number->string stripcount)))
    (sdegeo:define-contact-set tmp2 4(color:rgb 1 0 0)"##")
    (sdegeo:set-current-contact-set tmp2)
    (sdegeo:define-2d-contact(list(car(find-edge-id(position(- sens_w 1)bulkstpos 0))))tmp2)
    (set! tmp1 "Dop_Str_")
130 (set! tmp2(string-append tmp1(number->string stripcount)))
    (set! tmp3 "Str_dop_")
    (set! tmp4(string-append tmp3(number->string stripcount)))
    (sdedr:define-refeval-window tmp2 "Line"(position(- sens_w(/ imp_w 2))bulkstpos 0)(position sens_w
      bulkstpos 0))
    (sdedr:define-analytical-profile-placement tmp4 "Str_dop" tmp2 "Both" "NoReplace" "Eval")
135 (set! tmp1 "Nitr")
    (set! tmp2(string-append tmp1(number->string stripcount)))
    (set! tmp3(string-append tmp2(number->string 1)))
    (sdegeo:create-rectangle(position(- sens_w(+ diag_w(+ overlay_w(/ imp_w 2))))str_t 0)(position(-
      sens_w(+(/ str_w 2)nit_o))(+ str_t nit_t)0)"Si3N4" tmp3)
    (set! tmp2(string-append tmp1(number->string stripcount)))
140 (set! tmp3(string-append tmp2(number->string 2)))
    (sdegeo:create-polygon(list(position(- sens_w(+(+(/ imp_w 2)overlay_w)diag_w))str_t 0)(position(-
      sens_w(+(+(/ imp_w 2)overlay_w)diag_w))(+ str_t nit_t)0)(position(- sens_w(+(/ imp_w
      2)overlay_w))(+(+ str_t nit_t)impvia)0)(position(- sens_w(+(/ imp_w 2)overlay_w))(+ str_t
      impvia)0)(position(- sens_w(+(+(/ imp_w 2)overlay_w)diag_w))str_t 0))"Si3N4" tmp3)
    (set! tmp2(string-append tmp1(number->string stripcount)))
    (set! tmp3(string-append tmp2(number->string 3)))
    (sdegeo:create-rectangle(position sens_w(+ str_t impvia)0)(position(- sens_w(+ overlay_w(/ imp_w 2)))(+
      str_t(+ impvia nit_t))0)"Si3N4" tmp3)
```

Now the individual strips are added:

```
    # Implement remaining strip geometry, contacts and doping
    (do((i 2(+ i 1)))((= i stripcount))
      (begin
        (set! tmp1 "StrTop_")
150     (set! tmp2(string-append tmp1(number->string i)))
        (set! tmp3 "StrBot_")
        (set! tmp4(string-append tmp3(number->string i)))
        (sdegeo:create-rectangle(position(-(* pitch(- i 1))(/ str_w 2))0 0)(position(+(* pitch(- i 1))(/
          str_w 2))str_t 0)"Aluminum" tmp2)
        (sdegeo:create-rectangle(position(-(-(* pitch(- i 1))overlay_w)(/ imp_w 2))str_t 0)(position(+(+(*
          pitch(- i 1))overlay_w)(/ imp_w 2))(+ str_t impvia)0)"Aluminum" tmp4)
155     (set! tmp1 "StrDiL_")
        (set! tmp2 "StrDiR_")
        (set! tmp3(string-append tmp1(number->string i)))
        (set! tmp4(string-append tmp2(number->string i)))
        (sdegeo:create-polygon(list(position(-(* pitch(- i 1))(+ overlay_w(/ imp_w 2)))str_t
          0)(position(-(* pitch(- i 1))(+(+ overlay_w(/ imp_w 2))diag_w))str_t 0)(position(-(* pitch(- i
          1))(+ overlay_w(/ imp_w 2)))(+ str_t impvia)0)(position(-(* pitch(- i 1))(+ overlay_w(/ imp_w
          2)))str_t 0))"Aluminum" tmp3)
160     (sdegeo:create-polygon(list(position(+(* pitch(- i 1))(+ overlay_w(/ imp_w 2)))str_t
          0)(position(+(* pitch(- i 1))(+(+ overlay_w(/ imp_w 2))diag_w))str_t 0)(position(+(* pitch(- i
          1))(+ overlay_w(/ imp_w 2)))(+ str_t impvia)0)(position(+(* pitch(- i 1))(+ overlay_w(/ imp_w
          2)))str_t 0))"Aluminum" tmp4)
        (sdegeo:insert-vertex(position(-(* pitch(- i 1))(/ imp_w 2))bulkstpos 0))
        (sdegeo:insert-vertex(position(+(* pitch(- i 1))(/ imp_w 2))bulkstpos 0))
        (set! tmp1 "Cont_AC_Str_")
        (set! tmp2(string-append tmp1(number->string i)))
165     (sdegeo:define-contact-set tmp2 4(color:rgb 1 1 1)"##")
        (sdegeo:set-current-contact-set tmp2)
        (sdegeo:define-2d-contact(list(car(find-edge-id(position(* pitch(- i 1))0 0))))tmp2)
        (set! tmp1 "Cont_DC_Str")
        (set! tmp2(string-append tmp1(number->string i)))
170     (sdegeo:define-contact-set tmp2 4(color:rgb 1 0 0)"##")
        (sdegeo:set-current-contact-set tmp2)
        (sdegeo:define-2d-contact(list(car(find-edge-id(position(* pitch(- i 1))bulkstpos 0))))tmp2)
        (set! tmp1 "Dop_Str_")
        (set! tmp2(string-append tmp1(number->string i)))
175     (set! tmp3 "Str_dop_")
        (set! tmp4(string-append tmp3(number->string i)))
        (sdedr:define-refeval-window tmp2 "Line"(position(-(* pitch(- i 1))(/ imp_w 2))bulkstpos
          0)(position(+(* pitch(- i 1))(/ imp_w 2))bulkstpos 0))
```

```
        (sdedr:define-analytical-profile-placement tmp4 "Str_dop" tmp2 "Both" "NoReplace" "Eval")
        (set! tmp1 "Nitr")
180     (set! tmp2(string-append tmp1(number->string stripcount)))
        (set! tmp3(string-append tmp2(number->string 1)))
        (sdegeo:create-rectangle(position(-(-(* pitch(- i 1))(/ str_w 2))nit_o)str_t 0)(position(-(-(-(*
          pitch(- i 1))(/ imp_w 2))overlay_w)diag_w)(+ nit_t str_t)0)"Si3N4" tmp3)
        (set! tmp2(string-append tmp1(number->string stripcount)))
        (set! tmp3(string-append tmp2(number->string 2)))
185     (sdegeo:create-polygon(list(position(-(* pitch(- i 1))(+ overlay_w(/ imp_w 2)))(+ str_t
          impvia)0)(position(-(-(* pitch(- i 1))(+ overlay_w(+ diag_w(/ imp_w 2)))))str_t 0)(position(-(*
          pitch(- i 1))(+ overlay_w(+ diag_w(/ imp_w 2))))(+ str_t nit_t)0)(position(-(* pitch(- i 1))(+
          overlay_w(/ imp_w 2)))(+ str_t(+ impvia nit_t))0)(position(-(* pitch(- i 1))(+ overlay_w(/ imp_w
          2)))(+ str_t impvia)0))"Si3N4" tmp3)
        (set! tmp2(string-append tmp1(number->string stripcount)))
        (set! tmp3(string-append tmp2(number->string 3)))
        (sdegeo:create-rectangle(position(-(-(-(* pitch(- i 1))(/ imp_w 2))overlay_w)nit_t)(+ str_t
          impvia)0)(position(+(+(+(* pitch(- i 1))(/ imp_w 2))overlay_w)nit_t)(+ nit_t(+ str_t
          impvia))0)"Si3N4" tmp3)
190     (set! tmp2(string-append tmp1(number->string stripcount)))
        (set! tmp3(string-append tmp2(number->string 4)))
        (sdegeo:create-polygon(list(position(+(* pitch(- i 1))(+ overlay_w(/ imp_w 2)))(+ str_t
          impvia)0)(position(+(* pitch(- i 1))(+ overlay_w(+ diag_w(/ imp_w 2))))str_t 0)(position(+(*
          pitch(- i 1))(+ overlay_w(+ diag_w(/ imp_w 2))))(+ str_t nit_t)0)(position(+(* pitch(- i 1))(+
          overlay_w(/ imp_w 2)))(+ str_t(+ impvia nit_t))0)(position(+(* pitch(- i 1))(+ overlay_w(/ imp_w
          2)))(+ str_t impvia)0))"Si3N4" tmp3)
        (set! tmp2(string-append tmp1(number->string stripcount)))
        (set! tmp3(string-append tmp2(number->string 5)))
        (sdegeo:create-rectangle(position(+(+(* pitch(- i 1))(/ str_w 2))nit_o)str_t 0)(position(+(+(+(*
          pitch(- i 1))(/ imp_w 2))overlay_w)diag_w)(+ nit_t str_t)0)"Si3N4" tmp3)
195   )
)
```

Finally, a possible p-stop or p-spray isolation is added, the mesh size is refined, especially at the sensor surface and at the strip implants, and the mesh command is given:

```
# p-spray isolation
(if(string=? sensortype "y")
200   (begin
    (do((i 1(+ i 1)))((= i stripcount))
      (begin
        (set! tmp1 "Dop_Spr_")
        (set! tmp2(string-append tmp1(number->string i)))
205     (set! tmp3 "Spr_dop_")
        (set! tmp4(string-append tmp3(number->string i)))
        (sdedr:define-refeval-window tmp2 "Line"(position(+(* pitch(- i 1))(/ imp_w 2))bulkstpos
          0)(position(-(* pitch i)(/ imp_w 2))bulkstpos 0))
        (sdedr:define-analytical-profile-placement tmp4 "Iso_dop" tmp2 "Both" "NoReplace" "Eval")
      )
210   )
  )
)

# p-stop isolation
215 (if(string=? sensortype "p")
  (begin
    (do((i 1(+ i 1)))((= i stripcount))
      (begin
        (do((j 1(+ j 1)))((= j(+ pstopcount 1)))
220       (begin
            (set! tmp1 "Dop_Stop_")
            (set! tmp2(string-append tmp1(number->string i)))
            (set! tmp1(string-append tmp2(number->string j)))
            (set! tmp3 "Stop_dop_")
225         (set! tmp4(string-append tmp3(number->string i)))
            (set! tmp3(string-append tmp4(number->string j)))
            (sdedr:define-refeval-window tmp1 "Line"(position(+(-(+(*(- i 1)pitch)(/ pitch 2))(/(+(*
              stop_w pstopcount)(* stop_sp(- pstopcount 1)))2))(*(- j 1)(+ stop_w stop_sp)))bulkstpos
              0)(position(+(+(-(+(*(- i 1)pitch)(/ pitch 2))(/(+(* stop_w pstopcount)(* stop_sp(-
              pstopcount 1)))2))(*(- j 1)(+ stop_w stop_sp)))stop_w)bulkstpos 0))
            (sdedr:define-analytical-profile-placement tmp3 "Iso_dop" tmp1 "Both" "NoReplace" "Eval")
          )
230       )
        )
      )
    )
  )
)
235
# Mesh granularity
(sdedr:define-refinement-size "Si_Ref" refmaxsi_x refmaxsi_y refminsi_x refminsi_y)
(sdedr:define-refinement-material "Ref_Si" "Si_Ref" "Silicon")
(sdedr:define-refinement-function "Si_Ref" "DopingConcentration" "MaxTransDiff" 0.5)
240 (sdedr:define-refinement-size "Ox_Ref" refmaxox_x refmaxox_y refminox_x refminox_y)
(sdedr:define-refinement-material "Refinement_Oxide" "Ox_Ref" "SiO2")
(sdedr:define-refinement-function "Ox_Ref" "DopingConcentration" "MaxTransDiff" 0.5)
```

```
      (begin
245     (sdedr:define-refeval-window "Ref_Strs" "Rectangle"(position(-(-(-(-(- 0(/ str_w 2))bias_s)
            bias_w)guard_s)guard_w)bulkstpos 0)(position sens_w(/ sens_t 7.5)0))
      )
      (sdedr:define-refinement-size "Str_Ref" refmaxstr_x refmaxstr_y refminstr_x refminstr_y)
      (sdedr:define-refinement-placement "Ref_Str" "Str_Ref" "Ref_Strs")

250   # Build mesh and write files
      (sdeio:save-tdr-bnd(get-body-list)"n@node@_bnd.tdr")
      (sdedr:write-cmd-file "n@node@_msh.cmd")
      (system:command "snmesh tdr n@node@_msh")
      (sde:build-mesh "snmesh" " " "n@node@_msh")
```

A.1.3 *Device Simulation*

The device simulation shown here is also called from `swb` with specific variables
and parameters. It uses the mesh structure generated by the preceding commands.

First, the sensor polarity and, in the `File` section, the output paths are defined.
Following that, a device is defined in the `Device` section with the contacts as spec-
ified in the previous structure generation. The physical models are activated for
this device in the `Physics` subsection, a description of which is given in section 4.1.
In this example, the two-level radiation damage defect model described in sec-
tion 4.4.1.3 is included.

```
0   # Sensor polarity
    !( if { "@sensortype@" == "n" } {
       set sgn 1
       set sys_name "pnn"
    } else {
5      set sgn -1
       set sys_name "npp"
    } )!

    # Output files, directory "output" should be created manually
10  File {
       Plot = "output/FZ@activethickness@@sensortype@_@region@_n@node@"
       Output = "output/FZ@activethickness@@sensortype@_@region@_n@node@"
       Current = "output/FZ@activethickness@@sensortype@_@region@_n@node@"
       ACExtract = "output/FZ@activethickness@@sensortype@_@region@_n@node@"
15     Grid = "@tdr@"
       Parameter = "@parameter@"
    }

    # Device section
20  Device Stripsensor {
       Electrode {
          { Name = "Cont_Backp" voltage = 0 }
          !( for { set i 1 } { $i <= @stripcount@ } { incr i } {
             set tmp1 "{Name=\"Cont_AC_Str_"
25           set tmp2 "\" "
             set tmp3 "voltage=0}"
             set tmp4 $tmp1$i$tmp2$tmp3
             puts "$tmp4"
             set tmp1 "{Name=\"Cont_DC_Str_"
30           set tmp2 "\" "
             set tmp3 "voltage=0}"
             set tmp4 $tmp1$i$tmp2$tmp3
             puts "$tmp4"
          }
35        puts "{ Name = \"Cont_AC_B\" voltage = 0 }"
          puts "{ Name = \"Cont_DC_B\" voltage = 0 }"
          puts "{ Name = \"Cont_AC_G\" voltage = 0 }"
          puts "{ Name = \"Cont_DC_G\" voltage = 0 }"
       }
40     Physics {
          Temperature=@temperature@
          AreaFactor=@areafactor@
          Mobility (
             DopingDependence
45           eHighFieldSaturation
             hHighFieldSaturation
             CarrierCarrierScattering (
                ConwellWeisskopf
             )
50        )
```

```
         Recombination (
           SRH (
             DopingDependence
             TempDependence
55           ElectricField ( LifeTime = Hurkx DensityCorrection = none )
           )
           Auger
           eAvalanche ( vanOverstraeten Eparallel )
           hAvalanche ( vanOverstraeten Eparallel )
60         CDL
         )
         EffectiveIntrinsicDensity ( Slotboom )
         Fermi
       }
65   !( if { @fluence@ > 0 } {
         puts "Physics ( Material = \"Silicon\" ) {"
         if { "@irradiationmodel@" == "proton" } {
           puts "Traps ( ( Donor Level fromValBand"
           if { @fluence@ < 7.1e13 } {
70           puts "Conc = 0"
           }
           if { @fluence@ > 7.1e13 } {
             puts "Conc = [ expr @fluence@ * 5.598 - 3.959e14 ]"
           }
75         puts "EnergyMid = 0.48 eXsection = 1e-14 hXsection = 1e-14 ) ( Acceptor Level fromCondBand"
           if { @fluence@ < 7.1e13 } {
             puts "Conc = 0"
           }
           if { @fluence@ > 7.1e13 } {
80           puts "Conc = [ expr @fluence@ * 1.189 + 0.645e14 ]"
           }
           puts "EnergyMid = 0.525 eXsection = 1e-14 hXsection = 1e-14 ) )"
         }
         puts "}"
85   } )!
     Physics ( Material = "SiO2" ) { Traps ( FixedCharge Level Conc = @sio2_charge_conc@ ) }
     Physics ( MaterialInterface = "Silicon/Oxide" ) { Traps ( FixedCharge Level Conc =
       @interface_charge_conc@ ) }
     Physics ( MaterialInterface = "Nitride/Oxide" ) { Traps ( FixedCharge Level Conc =
       @interface_charge_conc@ ) }
   }
```

With the environment set, a SPICE network connecting the electrodes is defined in the System section of the file.

```
   System {
     Stripsensor !( puts $sys_name )!
     ( Cont_Backp = System_Cont_Backp
95   !( for { set i 1 } { $i <= @stripcount@ } { incr i } {
         set tmp1 "Cont_AC_Str_"
         set tmp2 " = System_Cont_AC_Str_"
         puts "$tmp1$i$tmp2$i"
         set tmp1 "Cont_DC_Str_"
100        set tmp2 " = System_Cont_DC_Str_"
         puts "$tmp1$i$tmp2$i"
       }
       puts "Cont_AC_B = System_Cont_AC_B"
       puts "Cont_DC_B = System_Cont_DC_B"
105      puts "Cont_AC_G = System_Cont_AC_G"
       puts "Cont_DC_G = System_Cont_DC_G"
       puts ")"
       puts "Vsource_pset v ( System_Cont_Backp System_Cont_DC_B ) { dc = 0 }"
       puts "Resistor_pset rg_ac ( System_Cont_AC_G 0 ) { resistance = 0.1 }"
110      puts "Resistor_pset rg_dc ( System_Cont_DC_G 0 ) { resistance = @biasresistor@ }"
       puts "Resistor_pset r0 ( System_Cont_DC_B 0 ) { resistance = 0.1 }"
       for { set i 1 } { $i <= @stripcount@ } { incr i } {
         set tmp1 "Resistor_pset r_ac_"
         set tmp2 " ( System_Cont_AC_Str_"
115        set tmp3 " 0 ) { resistance = 50 }"
         puts "$tmp1$i$tmp2$i$tmp3"
         set tmp1 "Resistor_pset r_dc_"
         set tmp2 " ( System_Cont_DC_Str_"
         set tmp3 " System_Cont_DC_B ) { resistance = @biasresistor@ }"
120        puts "$tmp1$i$tmp2$i$tmp3"
       }
     )!
   }
```

The Plot section lists the physical properties the user wishes to be written out.

```
125  Plot
   {
     eCurrent/Vector hCurrent/Vector Current/vector eDensity hDensity
     ElectricField ElectricField/Vector eEparallel hEparallel
```

```
     Potential SpaceCharge Doping DonorConcentration AcceptorConcentration
130  Auger eAvalanche hAvalanche AvalancheGeneration eMobility hMobility
     SRHRecombination BeamGeneration HeavyIonCharge HeavyIonGeneration
     eAlphaAvalanche hAlphaAvalanche CDL CDL1 CDL2 CDL3 eTrappedCharge hTrappedCharge
     eInterfaceTrappedCharge hInterfaceTrappedCharge eGapStatesRecombination hGapStatesRecombination
     }
```

It is followed by the `Math` section, in which the computational settings are defined.

```
     Math
     {
       Method = Pardiso
       Number_of_Threads = 16
140    Extrapolate
       Derivatives
       RelErrControl
       Digits = 4
       Notdamped = 50
145    Iterations = 25
       RecBoxIntegr ( 1e-2 10 1000 )
     }
```

The `Solve` section lists the simulations to perform. In this example, if the flags `ac_on` and `dc_on` are set, the applied bias voltage is ramped and a small-signal AC analysis is performed at each voltage step, from which the sensor capacitances can be calculated.

```
     Solve
150  {
       Save ( FilePrefix = "output/FZ@activethickness@@sensortype@_@region@" )
       Poisson Electron Hole Contact Circuit
       Coupled { Poisson }
       Coupled { Poisson Electron }
155    Coupled { Poisson Electron Hole }
       Coupled { Poisson Electron Hole Contact }
       Coupled { Poisson Electron Hole Contact Circuit }
       !(
         puts "QuasiStationary ( InitialStep = 1e-7 MinStep = 1e-15 MaxStep = 0.05 Increment = 4 Decrement =
           4 Goal { Parameter = v.dc Value = [ expr $sgn * @voltage_ramp@ ] } Plot { Range = ( 0 1 )
           Intervals = 10 } ) { Plugin ( Iterations = 0 BreakOnFailure ) {"
160      if { @ac_on@ == "yes" } {
           puts "ACCoupled ( StartFrequency = @ac_start_freq@ EndFrequency = @ac_end_freq@ NumberOfPoints =
             @ac_freq_steps@ Decade Iterations = 15 Node ( System_Cont_Backp "
           for { set i 1 } { $i <= @stripcount@ } { incr i } {
             set tmp1 "System_Cont_AC_Str_"
             puts "$tmp1$i"
165          set tmp1 "System_Cont_DC_Str_"
             puts "$tmp1$i"
           }
           puts ")"
           puts "ACMethod = Blocked ACSubMethod(\"1d\") = Pardiso ) { Poisson Electron Hole Contact Circuit
             }"
170      }
         if { @dc_on@ == "yes" } {
           puts " Coupled { Poisson Electron Hole Contact Circuit }"
         }
         puts "} }"
175    )!
     }
```

The resulting simulation output can then be analysed with the `inspect` and `svisual` tools, which can also be called from `swb` with `Tcl` scripts.

In this section, additional plots from chapter 5 are shown. For comparison, they contain all measurements of either p-bulk isolation type. The colour scheme used in chapter 5 to denote fluence levels is continued, but symbols are changed to encompass all incidence angles. For all epitaxial sensors, filled circles stand for measurements at 0 ° incidence, filled rectangles for 25 ° incidence. 51.3 ° incidence measurements are represented with filled triangles pointing upward. The p-stop sensor which was additionally measured at 38.6 ° is denoted by a filled cross. MCz sensors use the same legend, albeit with open symbols and 31.7 ° as the highest incidence angle. The different angular measurements of the Fth sensor are represented with an open cross, an open rhombus and an open triangle pointing downward. Some points are shifted on the x axis for legibility.

A.2.1   *Charge Collection Efficiencies*

The following figures summarise the measured charge collection efficiencies for all p-stop and p-spray sensors.
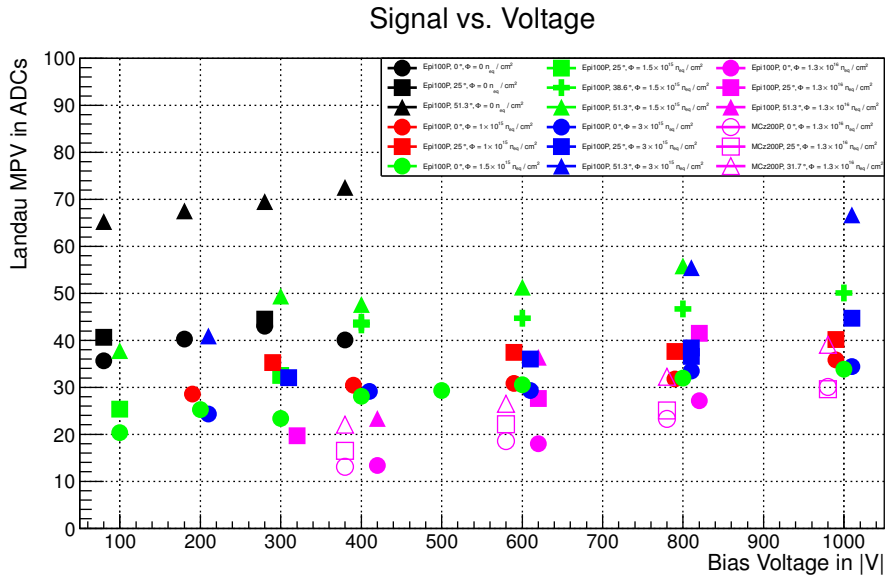
Figure A.1: The charges collected for all p-stop sensors. The colour and symbol scheme is explained in the text above.
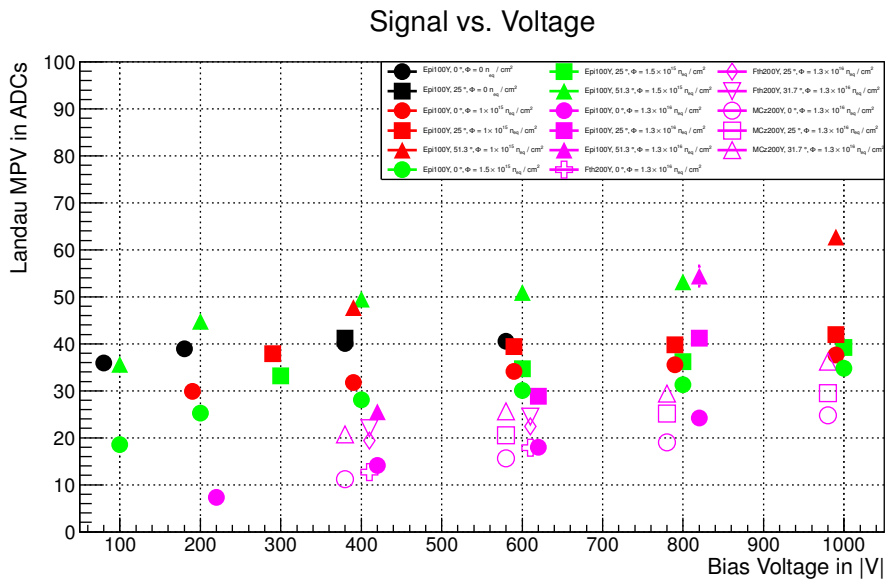
Figure A.2: The charges collected for all p-spray sensors.

Signal-To-Noise Ratios

The following figures summarise the measured signal-to-noise ratios for all p-stop and p-spray sensors.
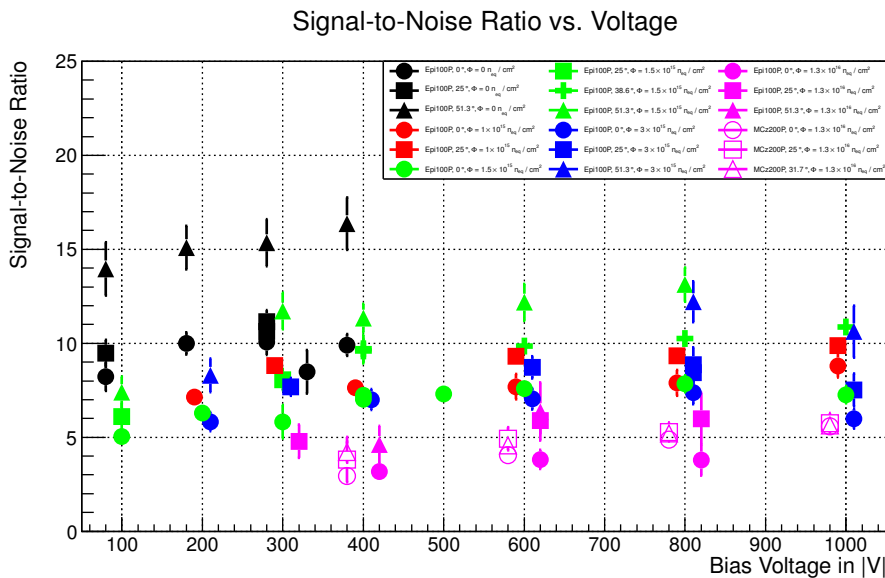
Figure A.3: The signal-to-noise ratios measured for all p-stop sensors.
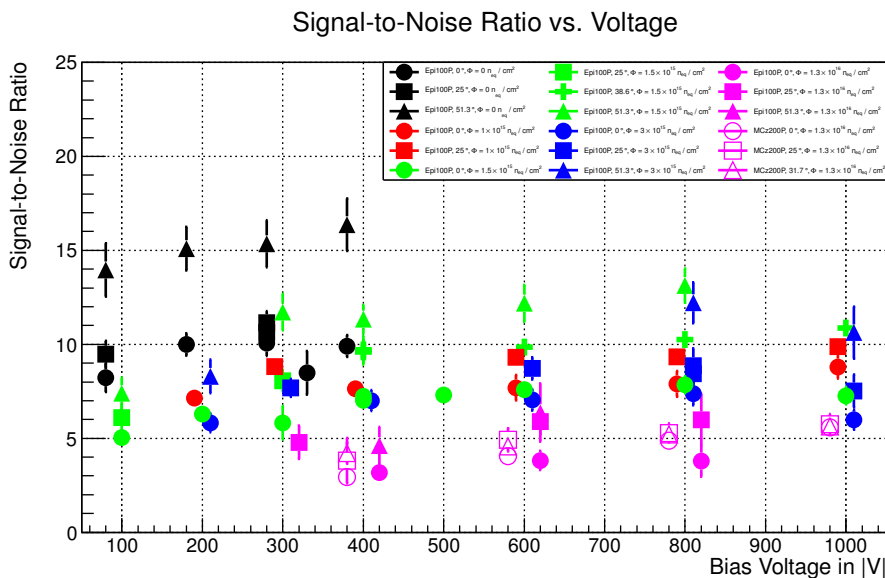
Figure A.4: The signal-to-noise ratios measured for all p-spray sensors.

A.2.3 *Charge Sharing*

The following figures summarise the measured charge sharing for all p-stop and
p-spray sensors, as calculated from the η-distributions.
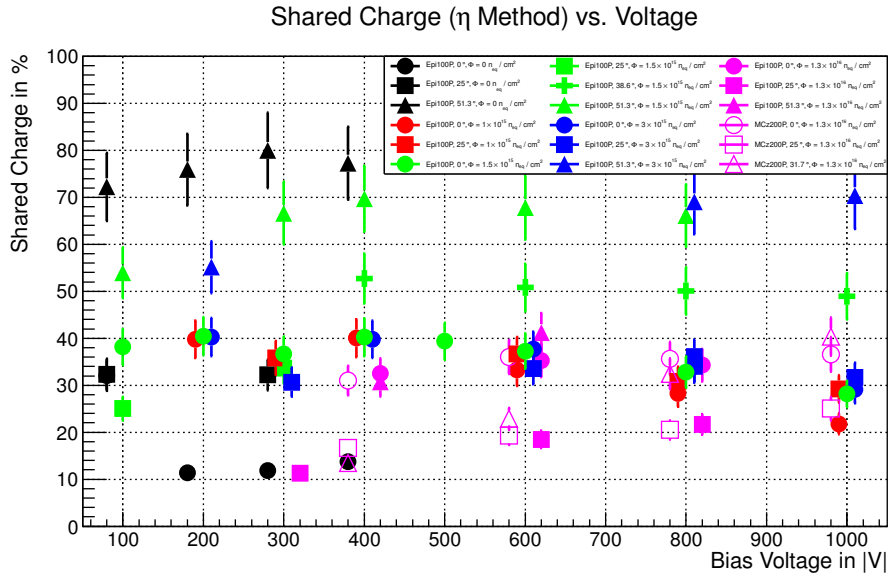
Figure A.5: Charge shared in all p-stop sensors as calculated from the η-distribution.
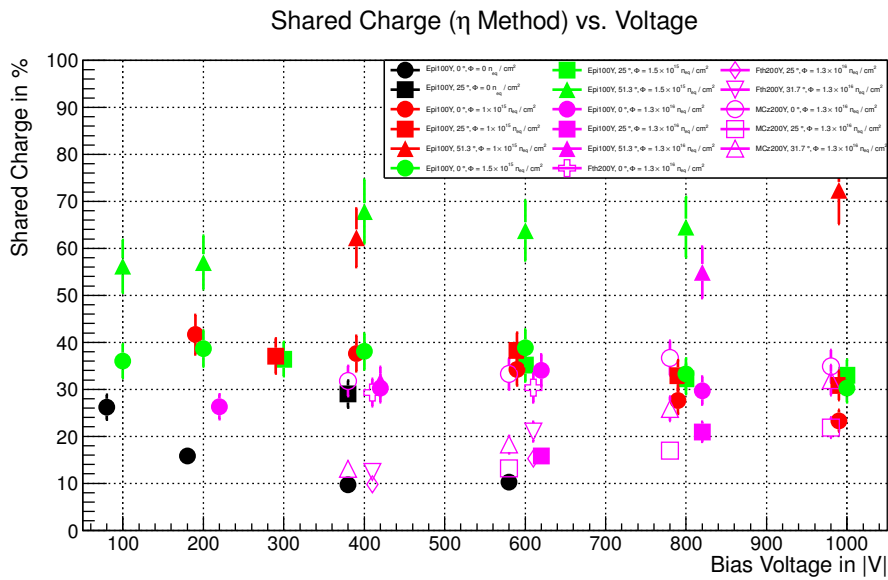
Figure A.6: Charge shared in all p-spray sensors as calculated from the η-distribution.

The following figures summarise the measured charge sharing for all p-stop and p-spray sensors, if a threshold cut of 1.5 times the individual channel noise is considered.
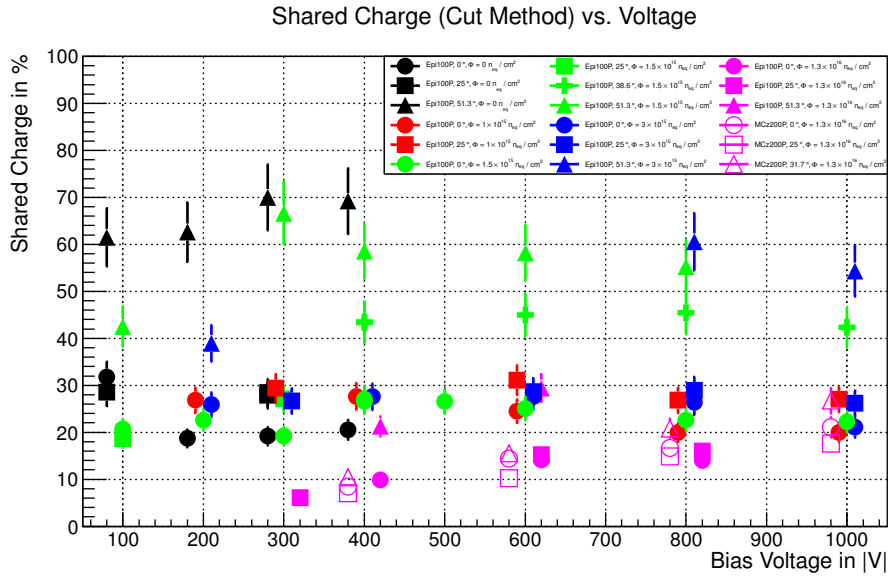
Figure A.7: Charge shared in all p-stop sensors if a threshold cut is considered.
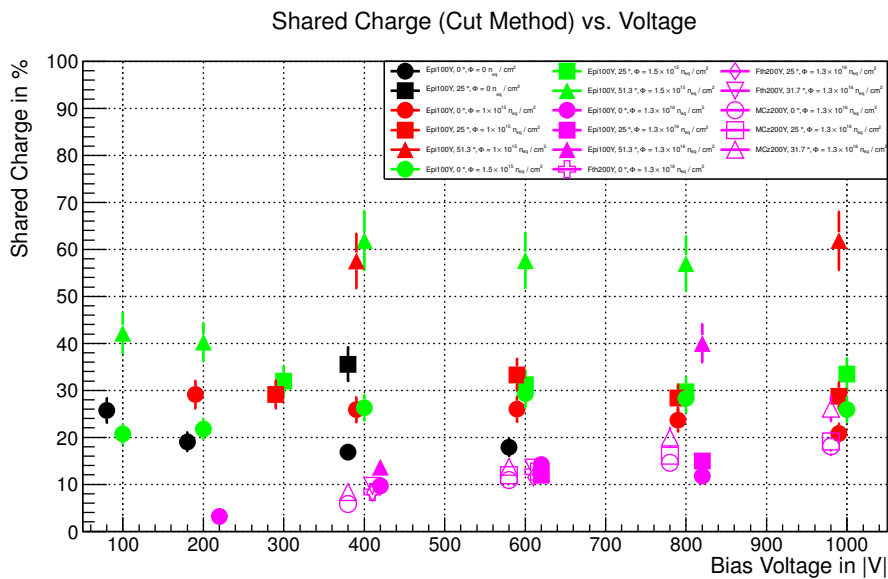
Figure A.8: Charge shared in all p-spray sensors if a threshold cut is considered.

PUBLICATIONS

Some ideas and figures presented in this thesis have been shown previously in the following publications:

[48] T. Eichhorn. *Simulationen bestrahlter Siliziumsensoren der Teilchenphysik.* Diplomarbeit, Karlsruhe Institute of Technology, Karlsruhe, 2011.

[49] T. Eichhorn (for the CMS Tracker Collaboration). *Silicon Strip Sensor Simulations for the CMS Phase-II Tracker Upgrade.* In *Nuclear Science Symposium and Medical Imaging Conference Record 2012*, 1664–1669. IEEE, 2012. doi:10.1109/NSSMIC.2012.6551395.

[50] T. Eichhorn, A. Bhardwaj, R. Dalal, R. Eber, K. Lalwani, A. Messineo, T. Peltola, M. Printz, and K. Ranjan. *Simulations of Inter-Strip Capacitance and Resistance for the Design of the CMS Tracker Upgrade.* In *PoS Proc. Sci.*, (TIPP2014)279, 2014.

[14] A. Bhardwaj, R. Dalal, R. Eber, T. Eichhorn, K. Lalwani, A. Messineo, T. Peltola, M. Printz, K. Ranjan. *Simulation of Silicon Devices for the CMS Phase II Tracker Upgrade.* Internal CMS Detector Note CMS DN-2014/016.

[1] I. Abt et al. (The H1 Collaboration). *The H1 detector at HERA*. In *Nucl. Instr. Meth. Phys. Res. A*, 386(2-3): 310–347, 1997. doi:10.1016/S0168-9002(96)00893-5.

[2] K. Akiba et al. *The algorithm for FIR corrections of the VELO analogue links and its performance*. Tech. Rep. LHCb-2008-015, CERN, Geneva, 2007.

[3] K. Akiba et al. *Charged particle tracking with the Timepix ASIC*. In *Nucl. Instr. Meth. Phys. Res. A*, 661(1): 31–49, 2012. doi:10.1016/j.nima.2011.09.021.

[4] A. Akkerman et al. *Updated NIEL calculations for estimating the damage induced by particles and γ-rays in Si and GaAs*. In *Radiat. Phys. Chem.*, 62(4): 301–310, 2001. doi:10.1016/S0969-806X(01)00207-9.

[5] L. Amaral et al. *The versatile link, a common project for super-LHC*. In *J. Instrum.*, 4(12): P12003, 2009. doi:10.1088/1748-0221/4/12/P12003.

[6] S. Aplin, J. Engels, and F. Gaede. *A production system for massive data processing in ILCSoft*. Tech. Rep. EUDET-Memo-2009-12, 2009.

[7] J. Baudot et al. *First test results of MIMOSA-26, a fast CMOS sensor with integrated zero suppression and digitized output*. In *Nuclear Science Symposium Conference Record 2009*, 1169–1173. IEEE, 2009. doi:10.1109/NSSMIC.2009.5402399.

[8] L. Bauerdick et al. *Beam test of silicon strip sensors for the ZEUS micro vertex detector*. In *Nucl. Instr. Meth. Phys. Res. A*, 501(2-3): 340–358, 2003. doi:10.1016/S0168-9002(03)00619-3.

[9] H. Behnamian (on behalf of the CMS Tracker Collaboration). *Sensor R&D for the CMS outer tracker upgrade for the HL-LHC*. In *J. Instrum.*, 9(04): C04033, 2014. doi:10.1088/1748-0221/9/04/C04033.

[10] T. Behnke et al. *Test Beams at DESY*. Tech. Rep. EUDET-Memo-2007-11, 2007.

[11] J. Behr. *Test Beam Measurements with the EUDET Pixel Telescope*. Tech. Rep. EUDET-Report-2010-01, 2010.

[12] E. Belau et al. *Charge collection in silicon strip detectors*. In *Nucl. Instr. Meth. Phys. Res.*, 214(2-3): 253–260, 1983. doi:10.1016/0167-5087(83)90591-4.

[13] M. Berger et al. *ESTAR, PSTAR, and ASTAR: Computer Programs for Calculating Stopping-Power and Range Tables for Electrons, Protons, and Helium Ions (version 1.2.3)*. http://physics.nist.gov/Star, National Institute of Standards and Technology, Gaithersburg, MD, USA. Accessed: 16.02.2015.

[14] A. Bhardwaj et al. *Simulation of Silicon Devices for the CMS Phase II Tracker Upgrade*. Internal CMS Detector Note CMS DN-2014/016, 2014.

[15] H. Bichsel. *Straggling in thin silicon detectors*. In *Rev. Mod. Phys.*, 60: 663–699, 1988. doi:10.1103/RevModPhys.60.663.

[16] R. Blair et al. (The CDF Collaboration). *The CDF-II detector: Technical design report*. FERMILAB-DESIGN-1996-01, FERMILAB-PUB-96-390-E, 1996.

[17] V. Blobel. *Software alignment for tracking detectors*. In *Nucl. Instr. Meth. Phys. Res. A*, 566(1): 5–13, 2006. doi:10.1016/j.nima.2006.05.157.

[18] A. Bulgheroni. *Results from the EUDET telescope with high resolution planes*. Tech. Rep. EUDET-Report-2009-02, 2009.

[19] E. Butz. *Calibration, Alignment and Long-Term Performance of the CMS Silicon Tracking Detector*. PhD thesis, Universität Hamburg, Hamburg, 2009.

[20] E. Butz (for the CMS Collaboration). *CMS Strip Detector: Operational Experience and Run1 to Run2 Transition*. Tech. Rep. CMS-CR-2014-390, CERN, Geneva, 2014.

[21] C. Canali et al. *Electron and Hole Drift Velocity Measurements in Silicon and Their Empirical Relation to Electric Field and Temperature*. In *IEEE Trans. Electron Devices*, 22(11): 1045–1047, 1975. doi:10.1109/T-ED.1975.18267.

[22] M. Centis Vignali. Private Communication.

[23] M. Centis Vignali. *PhD thesis in preparation*. PhD thesis, Universität Hamburg, Hamburg, 2015.

[24] M. Centis Vignali et al. *Characterization of thin irradiated epitaxial silicon sensors for the CMS phase II pixel upgrade*. Tech. Rep. CMS-CR-2014-364, CERN, Geneva, 2014.

[25] S. Chatrchyan et al. (The CMS Collaboration). *CMS Outreach*. http://cms.web.cern.ch/. Accessed: 03.09.2014.

[26] S. Chatrchyan et al. (The CMS Collaboration). *CMS Tracker Detector Performance Results*. https://twiki.cern.ch/twiki/bin/view/CMSPublic/DPGResultsTRK. Accessed: 21.03.2015.

[27] S. Chatrchyan et al. (The CMS Collaboration). *The CMS experiment at the CERN LHC*. In *J. Instrum.*, 3(08): S08004, 2008. doi:10.1088/1748-0221/3/08/S08004.

[28] S. Chatrchyan et al. (The CMS Collaboration). *Observation of a new boson at a mass of 125 GeV with the CMS experiment at the LHC*. In *Phys. Lett. B*, 716(1): 30–61, 2012. doi:10.1016/j.physletb.2012.08.021.

[29] S. Chatrchyan et al. (The CMS Collaboration). *Description and performance of track and primary-vertex reconstruction with the CMS tracker*. In *J. Instrum.*, 9(10): P10009, 2014. doi:10.1088/1748-0221/9/10/P10009.

[30] S. Chatterji et al. *Analysis of interstrip capacitance of Si microstrip detector using simulation approach*. In *Solid-State Electron.*, 47(9): 1491–1499, 2003. doi:10.1016/S0038-1101(03)00102-3.

[31] A. Chilingarov. *Temperature dependence of the current generated in Si bulk*. In *J. Instrum.*, 8(10): P10003, 2013. doi:10.1088/1748-0221/8/10/P10003.

[32] V. Chiochia et al. *A double junction model of irradiated silicon pixel sensors for LHC*. In *Nucl. Instr. Meth. Phys. Res. A*, 568(1): 51–55, 2006. doi:10.1016/j.nima.2006.05.199.

[33] CMS Collaboration. *Technical proposal for the upgrade of the CMS detector through 2020*. Tech. Rep. CERN-LHCC-2011-006. LHCC-P-004, CERN, Geneva, 2011.

[34] D. Contarato et al. *Beam-test of CMOS pixel sensors with 6 GeV electrons*. In *Nucl. Instr. Meth. Phys. Res. A*, 565(1): 119–125, 2006. doi:10.1016/j.nima.2006.04.068.

[35] E. Corrin. *EUDAQ Software User Manual*. Tech. Rep. EUDET-Memo-2010-1, 2010.

[36] N. Craig. *The State of Supersymmetry after Run I of the LHC*, 2014. arXiv: 1309.0528v2.

[37] D. Cussans. *Description of the JRA1 Trigger Logic Unit (TLU), v0.2c*. Tech. Rep. EUDET-Memo-2009-4, 2009.

[38] J. Czochralski. *Ein neues Verfahren zur Messung der Kristallisationsgeschwindigkeit der Metalle*. In *Z. Phys. Chem.*, 92: 219–221, 1918.

[39] R. Dalal et al. *Combined effect of bulk and surface damage on strip insulation properties of proton irradiated n^{+}-p silicon strip sensors*. In *J. Instrum.*, 9(04): P04007, 2014. doi:10.1088/1748-0221/9/04/P04007.

[40] R. Dalal et al. *Development of Radiation Damage Models for Irradiated Silicon Sensors Using TCAD Tools*. In *PoS Proc. Sci.*, (TIPP2014)276, 2014.

[41] DESY Test Beam Coordinators. *DESY Test Beam Description*. http://testbeam.desy.de. Accessed: 03.09.2014.

[42] A. Dierlamm. *Proton Irradiation in Karlsruhe*, 2010. 16th RD50 Workshop, URL http://indico.cern.ch/event/86625/session/3/contribution/19/material/slides/1.pdf.

[43] A. Dierlamm. *Characterisation of silicon sensor materials and designs for the CMS Tracker Upgrade*. In *PoS Proc. Sci.*, (Vertex 2012)016, 2012.

[44] A. Dominguez et al. *CMS Technical Design Report for the Pixel Detector Upgrade*. Tech. Rep. CERN-LHCC-2012-016. CMS-TDR-11, CERN, Geneva, 2012.

[45] R. Eber. *Lyon Tracker Upgrade Database*. http://ikcms02.fzk.de/probe/lyon2. Accessed: 23.02.2015.

[46] R. Eber. *Untersuchung neuartiger Sensorkonzepte und Entwicklung eines effektiven Modells der Strahlenschädigung für die Simulation hochbestrahlter Silizium-Teilchendetektoren*. PhD thesis, Karlsruhe Institute of Technology, Karlsruhe, 2013.

[47] D. Eckstein. *CMS outer tracker detector upgrade plans*. Tech. Rep. CMS-CR-2014-008, CERN, Geneva, 2014.

[48] T. Eichhorn. *Simulationen bestrahlter Siliziumsensoren der Teilchenphysik*. Diplomarbeit, Karlsruhe Institute of Technology, Karlsruhe, 2011.

[49] T. Eichhorn (for the CMS Tracker Collaboration). *Silicon Strip Sensor Simulations for the CMS Phase-II Tracker Upgrade.*. In *Nuclear Science Symposium and Medical Imaging Conference Record 2012*, 1664–1669. IEEE, 2012. doi:10.1109/NSSMIC.2012.6551395.

[50] T. Eichhorn et al. *Simulations of Inter-Strip Capacitance and Resistance for the Design of the CMS Tracker Upgrade*. In *PoS Proc. Sci.*, (TIPP2014)279, 2014.

[51] C. Eklund et al. *Silicon beam telescope for CMS detector tests*. In *Nucl. Instr. Meth. Phys. Res. A*, 430(2-3): 321–332, 1999. doi:10.1016/S0168-9002(99)00210-7.

[52] V. Eremin, E. Verbitskaya, and Z. Li. *The origin of double peak electric field distribution in heavily irradiated silicon detectors*. In *Nucl. Instr. Meth. Phys. Res. A*, 476(3): 556–564, 2002. doi:10.1016/S0168-9002(01)01642-4.

[53] J. Erfle. *Irradiation study of different silicon materials for the CMS tracker upgrade*. PhD thesis, Universität Hamburg, Hamburg, 2014.

[54] EUTelescope Software Developers. *EUTelescope Website*. http://eutelescope.desy.de. Accessed: 03.09.2014.

[55] S. Fartoukh and F. Zimmermann. *The HL-LHC accelerator physics challenges*. Tech. Rep. CERN-ACC-2014-0209, CERN, Geneva, 2014.

[56] W. Ferguson et al. *The CBC microstrip readout chip for CMS at the High Luminosity LHC*. In *J. Instrum.*, 7(08): C08006, 2012. doi:10.1088/1748-0221/7/08/C08006.

[57] K. Foraz et al. *LHC Long Shutdown: A Parenthesis for a Challenge*. In *Conf. Proc.*, no. CERN-ACC-2013-0276, TUPFI013. 2013.

[58] R. Frühwirth and A. Strandlie. *Track fitting with ambiguities and noise: A study of elastic tracking and nonlinear filters*. In *Comput. Phys. Commun.*, 120(2-3): 197–214, 1999. doi:10.1016/S0010-4655(99)00231-3.

[59] F. Gaede and J. Engels. *Marlin et al - A Software Framework for ILC detector R&D*. Tech. Rep. EUDET-Report-2007-11, 2007.

[60] F. Gaede et al. *LCIO - A persistency framework for linear collider simulation studies*, 2003. arXiv:physics/0306114.

[61] F. Gianotti et al. *Physics potential and experimental challenges of the LHC luminosity upgrade*. In *Eur. Phys. J. C*, 39(3): 293–333, 2005. doi:10.1140/epjc/s2004-02061-6.

[62] H. Gjersdal, A. Strandlie, and O. Røhne. *Straight line track reconstruction for the ATLAS IBL testbeam with the EUDET telescope*. Tech. Rep. ATL-INDET-PUB-2014-003, CERN, Geneva, 2014.

[63] M. Glaser, F. Ravotti, and M. Moll. *Dosimetry Assessments in the Irradiation Facilities at the CERN-PS Accelerator*. In *IEEE Trans. Nucl. Sci.*, 53(4): 2016–2022, 2006. doi:10.1109/TNS.2006.880569.

[64] G. Hall. *The upgrade programme of the CMS Tracker at SLHC*. In *PoS Proc. Sci.*, VERTEX 2008(CMS-CR-2009-053): 018, 2008.

[65] G. Hall (for the CMS collaboration). *Conceptual study of a trigger module for the CMS Tracker at SLHC*. In *Nucl. Instr. Meth. Phys. Res. A*, 636(1, Supplement): S201–S207, 2011. doi:10.1016/j.nima.2010.04.110.

[66] F. Hartmann. *Evolution of Silicon Sensor Technology in Particle Physics*. Springer-Verlag, Berlin, Heidelberg, 2009. ISBN 978-3-540-25094-4.

[67] P. Higgs. *Spontaneous Symmetry Breakdown without Massless Bosons*. In *Phys. Rev.*, 145: 1156–1163, 1966. doi:10.1103/PhysRev.145.1156.

[68] V. Highland. *Some practical remarks on multiple scattering*. In *Nucl. Instr. and Meth.*, 129(2): 497–499, 1975. doi:10.1016/0029-554X(75)90743-0.

[69] K.-H. Hoffmann. *Campaign to identify the future CMS tracker baseline*. In *Nucl. Instr. Meth. Phys. Res. A*, 658(1): 30–35, 2011. doi:10.1016/j.nima.2011.05.028.

[70] C. Honsberg and S. Bowden. *Photovoltaic Education Network*. http://pveducation.org/pvcdrom/manufacturing/float-zone-silicon. Accessed: 09.03.2015.

[71] M. Huhtinen. *Simulation of non-ionising energy loss and defect formation in silicon*. In *Nucl. Instr. Meth. Phys. Res. A*, 491(1-2): 194–215, 2002. doi:10.1016/S0168-9002(02)01227-5.

[72] H. Jansen. Private Communication.

[73] A. Junkes. Private Communication.

[74] A. Junkes. *Influence of radiation induced defect clusters on silicon particle detectors*. PhD thesis, Universität Hamburg, Hamburg, 2011.

[75] H. Kästli. *Frontend electronics development for the CMS pixel detector upgrade*. In *Nucl. Instr. Meth. Phys. Res. A*, 731(0): 88–91, 2013. doi:10.1016/j.nima.2013.05.056.

[76] V. Khachatryan et al. (The CMS Collaboration). *CMS tracking performance results from early LHC operation*. In *Eur. Phys. J. C*, 70(4): 1165–1192, 2010. doi:10.1140/epjc/s10052-010-1491-3.

[77] R. Klanner. *Impact of low-dose electron irradiation on n^+p silicon strip sensors*. Tech. Rep. CMS-CR-2014-131, CERN, Geneva, 2014.

[78] C. Kleinwort. *General Broken Lines as advanced track fitting method*. In *Nucl. Instr. Meth. Phys. Res. A*, 673(0): 107–110, 2012. doi:10.1016/j.nima.2012.01.024.

[79] G. Kramberger et al. *Investigation of Irradiated Silicon Detectors by Edge-TCT*. In *IEEE Trans. Nucl. Sci.*, 57(4): 2294–2302, 2010. doi:10.1109/TNS.2010.2051957.

[80] J. Lange. *Differential Top-Quark-Pair Cross Sections in pp Collisions at $\sqrt{s} = 7\,TeV$ with CMS and Charge Multiplication in Highly-Irradiated Silicon Sensors*. PhD thesis, Universität Hamburg, Hamburg, 2013.

[81] J. Lange et al. *Properties of a radiation-induced charge multiplication region in epitaxial silicon diodes*. In *Nucl. Instr. Meth. Phys. Res. A*, 622(1): 49–58, 2010. doi:10.1016/j.nima.2010.07.036.

[82] C. Lefevre. *LHC: the guide*, 2009.

[83] C. Leroy and P.-G. Rancoita. *Principles of Radiation Interaction in Matter and Detection*. World Scientific Publishing Co. Pte. Ltd., Singapore, 2009. ISBN 978-981-281-827-0.

[84] P. Lisowski and K. Schoenberg. *The Los Alamos Neutron Science Center*. In *Nucl. Instr. Meth. Phys. Res. A*, 562(2): 910–914, 2006. doi:10.1016/j.nima.2006.02.178.

[85] S. Löchner and M. Schmelling. *The Beetle Reference Manual - chip version 1.3, 1.4 and 1.5*. Tech. Rep. LHCb-2005-105, CERN, Geneva, 2006.

[86] G. Lutz. *Optimum track fitting in the presence of multiple scattering*. In *Nucl. Instr. Meth. Phys. Res. A*, 273(1): 349–361, 1988. doi:10.1016/0168-9002(88)90836-4.

[87] G. Lutz. *Semiconductor Radiation Detectors*. Springer-Verlag, Berlin, Heidelberg, 2007. ISBN 978-3-540-71678-5.

[88] A. Macchiolo et al. *Development of thin n-in-p planar pixel modules for the ATLAS upgrade at the HL-LHC*, 2015. 10th Trento Workshop on Advanced Silicon Radiation Detectors, URL https://indico.cern.ch/event/351695/session/1/contribution/5/material/slides/0.pdf.

[89] T. Mäenpää, M. Kortelainen, and T. Lampen. *Track-induced clustering in position sensitive detector characterization*. In *Nuclear Science Symposium Conference Record 2009*, 832–835. IEEE, 2009. doi:10.1109/NSSMIC.2009.5402394.

[90] R. Marco-Hernández. *A portable readout system for microstrip silicon sensors (ALIBAVA)*. In *Nuclear Science Symposium Conference Record 2008*, 3201–3208. IEEE, 2008. doi:10.1109/NSSMIC.2008.4775030.

[91] G. Masetti, M. Severi, and S. Solmi. *Modeling of carrier mobility against carrier concentration in arsenic-, phosphorus-, and boron-doped silicon*. In *IEEE Trans. Electron Devices*, 30(7): 764–769, 1983. doi:10.1109/T-ED.1983.21207.

[92] S. Mersi (for the CMS Collaboration). *CMS Silicon Tracker upgrade for HL-LHC*. Tech. Rep. CMS-CR-2012-137, CERN, Geneva, 2012.

[93] S. Mersi et al. *CMS Tracker Layout Studies for HL-LHC*. In *Phys. Procedia*, 37(0): 1070–1078, 2012. doi:10.1016/j.phpro.2012.03.729.

[94] M. Moll. *Radiation Damage in Silicon Particle Detectors - microscopic defects and macroscopic properties*. PhD thesis, Universität Hamburg, Hamburg, 1999.

[95] P. Moreira et al. *The GBT Project*. In *Conf. Proc. TWEPP 2009*. CERN, 2009. doi:10.5170/CERN-2009-006.342.

[96] M. Moritz. *Measurement of the High Q^2 Neutral Current DIS Cross Section at HERA*. PhD thesis, Universität Hamburg, Hamburg, 2001.

[97] F. Moscatelli et al. *An enhanced approach to numerical modeling of heavily irradiated silicon devices*. In *Nucl. Instr. Meth. Phys. Res. B*, 186(1-4): 171–175, 2002. doi:10.1016/S0168-583X(01)00899-0.

[98] S. Müller. *The Beam Condition Monitor 2 and the Radiation Environment of the CMS Detector at the LHC*. PhD thesis, Universität Karlsruhe (TH), Karlsruhe, 2011.

[99] A. Nürnberg. *Studien an bestrahlten Siliziumsensoren für den CMS Spurdetektor am HL-LHC*. PhD thesis, Karlsruhe Institute of Technology, Karlsruhe, 2014.

[100] K. Olive et al. (Particle Data Group). *Review of Particle Physics*. In *Chin. Phys. C*, 38: 090001, 2014. doi:10.1088/1674-1137/38/9/090001.

[101] Orange Tree Technologies Ltd. Didcot, UK.

[102] T. Peltola (for the CMS Collaboration). *Charge Collection Efficiency Simulations of Irradiated Silicon Strip Detectors*. Tech. Rep. CMS-CR-2014-255, CERN, Geneva, 2014.

[103] T. Peltola et al. *A Method to Simulate the Observed Surface Properties of Proton Irradiated Silicon Strip Sensors*, 2014. arXiv:1409.6956v3.

[104] H. Perrey (for the CMS Tracker Collaboration). *Plans and Status of the Phase I Upgrade of the CMS Pixel Tracker*. In *PoS Proc. Sci.*, (Vertex 2013)014, 2013.

[105] H. Perrey. *EUDAQ and EUTelescope - Software Frameworks for Testbeam Data Acquisition and Analysis*. In *PoS Proc. Sci.*, (TIPP2014)353, 2014.

[106] M. Petasecca et al. *Numerical simulation of radiation damage effects in p-type silicon detectors*. In *Nucl. Instr. Meth. Phys. Res. A*, 563(1): 192–195, 2006. doi:10.1016/j.nima.2006.01.093.

[107] B. Pifer et al. (The DØ Collaboration). *An Experiment at DØ to Study Antiproton - Proton Collisions at 2 TeV: Design Report*. FERMILAB-DESIGN-1983-02, FERMILAB-PUB-83-111-E, 1983.

[108] T. Pöhlsen. *Charge Losses in Silicon Sensors and Electric-Field Studies at the $Si - SiO_2$ Interface*. PhD thesis, Universität Hamburg, Hamburg, 2013.

[109] S. Ramo. *Currents Induced by Electron Motion*. In *Proc. IRE*, 27(9): 584–585, 1939. doi:10.1109/JRPROC.1939.228757.

[110] K. Ranjan. Private Communication.

[111] RD50 Collaboration. *RD50 - Radiation hard semiconductor devices for very high luminosity colliders*. http://rd50.web.cern.ch. Accessed: 03.09.2014.

[112] A. Richter et al. *Improved quantitative description of Auger recombination in crystalline silicon*. In *Phys. Rev. B*, 86: 165202, 2012. doi:10.1103/PhysRevB.86.165202.

[113] L. Rossi. *LHC Upgrade Plans: Options and Strategy*. Tech. Rep. CERN-ATS-2011-257, CERN, Geneva, 2011.

[114] I. Rubinskiy. Private Communication.

[115] I. Rubinskiy. *EUTelescope. Offline track reconstruction and DUT analysis software*. Tech. Rep. EUDET-Memo-2010-12, 2010.

[116] I. Rubinskiy. *An EUDET/AIDA Pixel Beam Telescope for Detector Development*. In *Phys. Procedia*, 37(0): 923–931, 2012. doi:10.1016/j.phpro.2012.02.434.

[117] P. Schütze. *Energy calibration of the DESY test beam in beamline 21*. DESY Summer Student Report, 2013.

[118] Silvaco Inc. Santa Clara, CA, USA.

[119] L. Snoj, G. Žerovnik, and A. Trkov. *Computational analysis of irradiation facilities at the JSI TRIGA reactor*. In *Appl. Radiat. Isot.*, 70(3): 483–488, 2012. doi:10.1016/j.apradiso.2011.11.042.

[120] S. Spannagel. Private Communication.

[121] S. Spannagel (for the CMS Collaboration). *Test Beam Campaigns for the CMS Phase I Upgrade Pixel Readout Chip*. In *J. Instrum.*, 9(12): C12001, 2014. doi:10.1088/1748-0221/9/12/C12001.

[122] H. Spieler. *Semiconductor Detector Systems*. Oxford University Press, Oxford, 2005. ISBN 978-0-19-852784-8.

[123] G. Steinbrück (for the CMS Tracker Collaboration). *The Upgrade of the CMS Outer Tracker*. Tech. Rep. CMS-CR-2014-421, CERN, Geneva, 2014.

[124] M. Swartz et al. *Simulation of Heavily Irradiated Silicon Pixel Detectors*, 2006. arXiv:physics/0605215v1.

[125] Synopsys Inc. Mountain View, CA, USA.

[126] Synopsys Inc. *Sentaurus Device Users Guide, Version G-2012.06*, 2012.

[127] S. Sze and K. Kwok. *Physics of Semiconductor Devices*. Wiley, Hoboken, 3rd ed., 2007. ISBN 978-0-471-14323-9.

[128] T. Szumlak and C. Parkes. *Application of the Beetle Header cross-talk correction algorithm for the VELO Detector*. Tech. Rep. LHCb-PUB-2009-006, CERN, Geneva, 2010.

[129] The ROOT Team. *ROOT Data Analysis Framework*. http://root.cern.ch. Accessed: 28.10.2014.

[130] H. Theuerer. *Method of processing semiconductive materials*, 1962. US Patent 3,060,123.

[131] W. Treberspurg. *Manufacturing Process of Silicon Strip Sensors and Analysis of Detector Structures*. Diplomarbeit, Vienna University of Technology, Vienna, 2011.

[132] A. Tricomi. *SLHC: The LHC luminosity upgrade*. In *Nucl. Instr. Meth. Phys. Res. A*, 596(1): 43–47, 2008. doi:10.1016/j.nima.2008.07.118.

[133] Y.-S. Tsai. *Pair production and bremsstrahlung of charged leptons*. In *Rev. Mod. Phys.*, 46: 815–851, 1974. doi:10.1103/RevModPhys.46.815.

[134] E. Yildirim. *PhD thesis in preparation*. PhD thesis, Universität Hamburg, Hamburg, 2015.

[135] T. Yunogami and T. Mizutani. *Radiation damage in SiO2/Si induced by low-energy electrons via plasmon excitation*. In *J. Appl. Phys.*, 73(12): 8184–8188, 1993. doi:10.1063/1.353433.

[136] A. Żarnecki and P. Nieżurawski. *EUDET Telescope Geometry and Resolution Studies*. Tech. Rep. EUDET-Report-2007-01, 2007.

[137] ZEUS Collaboration. *The ZEUS Detector, Status Report 1993*, 1993.

[138] J. Zhang. *X-ray Radiation Damage Studies and Design of a Silicon Pixel Sensor for Science at the XFEL*. PhD thesis, Universität Hamburg, Hamburg, 2013.

[139] J. Zhang et al. *Study of X-ray Radiation Damage in Silicon Sensors*, 2011. arXiv: 1111.1180v1.

ACKNOWLEDGEMENTS

EIDESSTATTLICHE VERSICHERUNG

Hiermit erkläre ich an Eides statt, dass ich die vorliegende Dissertationsschrift selbst verfasst und keine anderen als die angegebenen Quellen und Hilfsmittel benutzt habe.

Hamburg, den 21. April 2015

_____

Thomas Valentin Eichhorn